HELICAL MAGNETIC FIELDS IN SOLAR ACTIVE REGIONS: THEORY VS. OBSERVATIONS

Invited Talk

K. Petrovay[1], P. Chaterjee[2], A. Choudhuri[2]

[1] Eötvös University, Department of Astronomy, H-1518 Budapest, Pf. 32, Hungary
[2] Department of Physics, Indian Institute of Science, Bangalore 560012, India

E-mail: [1]K.Petrovay@astro.elte.hu

Abstract
The mean value of the normalized current helicity $\alpha_p = \mathbf{B} \cdot (\nabla \times \mathbf{B})/B^2$ in solar active regions is on the order of $10^{-8}\,\mathrm{m}^{-1}$, negative in the northern hemisphere, positive in the southern hemisphere. Observations indicate that this helicity has a subsurface origin. Possible mechanisms leading to a twist of this amplitude in magnetic flux tubes include the solar dynamo, convective buffeting of rising flux tubes, and the accretion of weak external poloidal flux by a rising toroidal flux tube. After briefly reviewing the observational and theoretical constraints on the origin of helicity, we present a recently developed detailed model for poloidal flux accretion.
Keywords: *Sun: active regions, Sun: magnetic fields, MHD*

1   Introduction

Three-dimensional vector fields may possess *chirality* (handedness), i.e. their structure may not be mirror symmetric. Concentrating on the magnetic field **B**, the simplest way to construct such a structure involves the superposition of a magnetic flux tube and a current tube. The result is a twisted tube where both the magnetic field lines and the current lines have a helical structure (Fig.1).
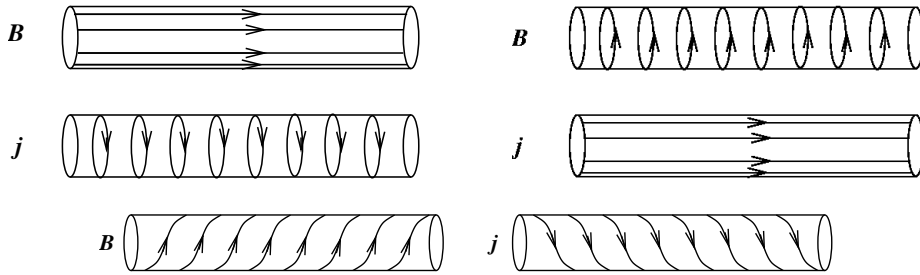
Figure 1: *As Maxwell's equations are linear, the solutions can be superposed. The superposition of a straight flux tube (top left) and a straight current tube (top right) results in a helical flux tube (bottom).*

This suggests that the helicity can be characterized by the scalar product of **B** and **j**; as the latter is proportional to $\nabla \times \mathbf{B}$, the *current helicity* is defined as

$$h_C = \mathbf{B} \cdot (\nabla \times \mathbf{B}) \tag{1}$$

Another quantity characterizing twist, often preferred for theoretical calculations is the *magnetic helicity*:

$$h_M = \mathbf{A} \cdot \mathbf{B} \equiv \mathbf{A} \cdot (\nabla \times \mathbf{A}) \tag{2}$$

(To be precise, the above defined h_C and h_M are helicity densities, helicity being their integral over a finite volume.)

Twist is just one form of helicity. As illustrated in Fig. 2, the twist of a tube or band can be converted into *writhe* or *kink:*
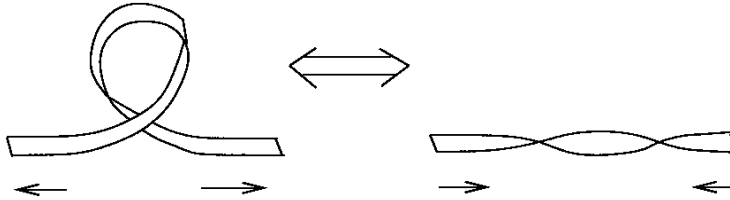
Figure 2: *Twist and kink of a magnetic flux tube can be converted into each other, as easily demonstrated by pulling the ends of a kinked paper tape, then pushing them together again.*

2   Observations of helical structure on the Sun

The apparent morphology of solar atmospheric structures, especially on H_α images, is often vortex-like, twisted or helical. Early claims by Hale (1927) and Richardson (1941) regarding the predominance of one chirality or another on a given hemisphere were hard to confirm owing to projection effects, a lack of information on 3D structure and large statistical scatter. In any case, the existence of a hemispheric rule of chirality was convincingly demonstrated at least in the case of quiescent prominences and interplanetary magnetic clouds (Zirker et al. 1997). Nevertheless, only direct magnetic measurements could provide convincing direct evidence for chirality rules in active regions.

Most determinations of current helicity rely on a constant-α force-free magnetic field model, constructed using the measured line-of-sight field component as lower boundary condition. Such models are based on the assumption that $\nabla \times \mathbf{B} = \alpha_p \mathbf{B}$ where α_p is constant. Multiplying this relation by $\mathbf{B}$, it is clear that $\alpha_p = h_C/B^2$ is a normalized measure of current helicity, with a dimension of 1/length. Its meaning is easy to visualize, as $1/\alpha_p$ is the length along a flux tube over which he field lines make a full circle around the tube.

Of the possible values of α_p, a best fit is then chosen by comparing the resulting magnetic field structure to either morphological features seen in solar images taken in H_α, EUV, etc. (Seehafer 1990) or, more recently, to the horizontal field components as measured by vector magnetographs (Pevtsov et al. 1995). A third method consists in simply taking the ratio $\alpha_p = (\nabla \times \mathbf{B})_n/B_n$, as measured by vector magnetographs, and averaging it over the active region. Results derived by different methods generally agree quite well (Leka & Skumanich 1999; Burnette et al. 2004).

Currently all these methods yield a single mean value of α_p over the whole active region. This is because the low S/N ratio of vector magnetograph measurements inhibits a reliable study of current helicity distribution across the plage; for the same reason, usually only pixels with relatively high field strength ($B > 100\,\mathrm{G}$ or so) are used in the determination. It is to be hoped that future improvements in magentograph sensibility will remedy this situation.

These studies have now firmly established that active region magnetic fields have helical structures, with a higher occurrence of negative helicity in the northern hemisphere. The observations show that the typical average value of the current helicity parameter α_p in an active region is on the order of $10^{-8}\,\mathrm{m^{-1}}$ (van Driel-Gesztelyi et al. 2003).

The tilt of the axis of bipolar active regions relative to the E-W direction is generally interpreted as evidence for writhe in the emerging flux tubes giving

rise to active regions. The origin of this writhe is well understood: it is the consequence of the Coriolis force acting on the downflows in the flux loop legs (D'Silva & Choudhuri 1993). The sign of current helicity implied by the observed tilts is positive on the northern hemisphere, i.e. opposite to the twist measured in the solar photosphere; its amplitude, however, remains well below the α_p values quoted above.

3   The origin of helicity

The basic question regarding the origin of the observed magnetic helicities is whether they are generated after the emergence of the flux loop or the flux emerges already in a helical form. Shearing of the photospheric footpoints of magnetic loops due to differential rotation or smaller scale granular and supergranular motions can, in principle, generate a helicity of right sign (DeVore 2000); however, the amount of helicity generated in this way seems to be insufficient to compensate for helicity losses in CME's (van Driel-Gesztelyi et al. 2003). In addition, in an important paper Pevtsov et al. (2003) studied the time development of the helicity in young, emerging active regions and found a good correlation between emergence rate and helicity increase. In particular, further increase of helicity ceases once the emergence of the loop, as measured by the increase in footpoint separation and area growth, comes to a halt. This observation seems to settle the issue in favor of a subsurface origin of the observed twist.

There are quite a few subsurface mechanisms which may naturally introduce twist in the structure of emerging flux loops. Such proposed mechanisms include helicity generation by the solar dynamo (Seehafer et al. 2003) and buffeting of the rising flux tubes by helical turbulent motions (Longcope et al. 1998). A further possibility is the effect of Coriolis force on flows in rising flux loops (Fan & Gong 2000). As we mentioned above, this process is responsible for the generation of positive writhe in active region flux tubes in the northern hemisphere, and thereby for the observed tilt of active regions. As magnetic helicity is conserved in ideal MHD (Berger 1999), the same process should then also give rise to a twist of opposite sense, so that the net helicity remains constant. The amount of helicity generated by this process, however, is too low to explain the observed values of α_p. On the other hand, a strongly twisted flux tube can develop a writhe by means of the kink instability. This mechanism should lead to a positive correlation of twist and writhe, in contrast to the helicity conservation argument above. Indeed, recent observations by López

Fuentes et al. (2003) and Holder et al. (2004) indicate that this mechanism may be important in the case of at least some active regions with unusually high tilt.
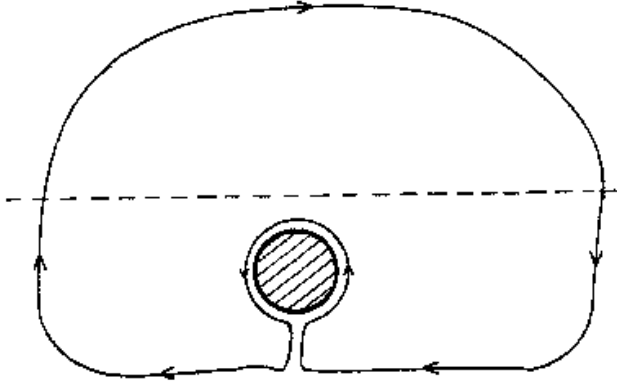
Figure 3: *During the rise of a toriodal flux tube (here shown in cross section, hatched) through the convective zone, field lines of the weak external poloidal field may get wrapped around it. After Choudhuri (2003).*

A further possible theoretical explanation of the observed helicity was proposed by Choudhuri (2003), who suggested that the poloidal flux in the solar convection zone (SCZ) gets wrapped around a rising flux tube, as sketched in Fig. 3. Choudhuri et al. (2004) later showed that this mechanism gives rise to helicity of the same order as what is observed. Choudhuri et al. (2004) also used their dynamo model to calculate the variation of helicity with latitude over a solar cycle and found that the latitudinal distribution of helicity from their theoretical model is in broad agreement with observational data.

If the magnetic flux in the rising flux tube is nearly frozen, then we expect that the poloidal flux collected by it during its rise through the SCZ would be confined in a narrow sheath at its outer periphery. In order to produce a twist in the flux tube, the poloidal field needs to diffuse from the sheath into the tube by turbulent diffusion. However, turbulent diffusion is strongly suppressed by the magnetic field in the tube. This nonlinear diffusion process was studied in an untwisted flux tube by Petrovay & Moreno-Insertis (1997). The model was subsequently successfully applied for sunspot decay (Petrovay & van Driel-Gesztelyi 1997). In a recent paper (Chatterjee et al. 2006) we extended this model by including the poloidal component of the magnetic field (i.e. the field which gets wrapped around the flux tube) and we studied the evolution of the
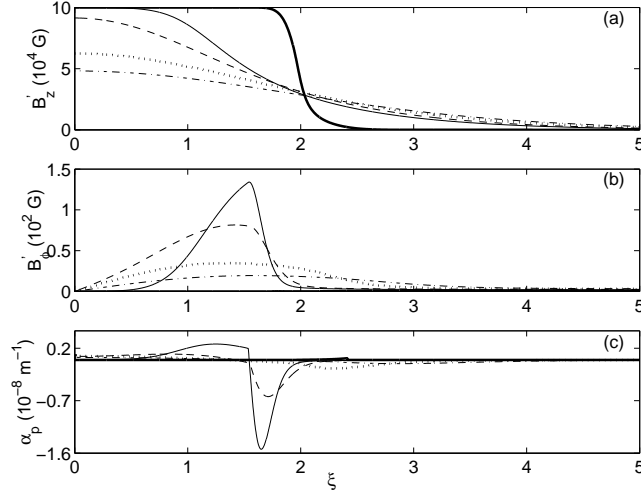
Figure 4: *Plots of B'_z, B'_ϕ and α_p as functions of ξ for a rising flux tube (case A). The different curves correspond to the profiles of these quantities at the following positions of the flux tube: $0.7R_\odot$ (thick solid), $0.85R_\odot$ (solid), $0.9R_\odot$ (dashed), $0.95R_\odot$ (dotted), $0.98R_\odot$ (dash-dotted).*

magnetic field in the rising flux tube, as it keeps collecting more poloidal flux during its rise and as turbulent diffusion keeps acting on it.

Consider a straight, cylindrical, horizontal magnetic flux tube rising through the solar convective zone. As all variables in this model depend only on the radial distance r from the tube axis and on time, we study the wrapping of the large-scale poloidal field around the flux tube by considering a radially symmetric accretion of azimuthal field by the flux tube. A further complication is the expansion of the flux tube during its rise, due to the decrease of the external pressure. This expansion is assumed to be self-similar, so that the Lagrangian radial coordinate ξ is related to the Eulerian radius r by $\xi = F(t)r$, where the expansion factor $F(t)$ was taken from thin flux tube emergence models. In the Lagrangian frame, flux density is rescaled as $B'_z = B_z/F^2$ and $B'_\phi = B_\phi/F$. With these notations and assumptions, the induction equation takes the form

$$\frac{\partial B'_z}{\partial t} = F^2 \frac{1}{\xi} \frac{\partial}{\partial \xi} \left(\eta \xi \frac{\partial B'_z}{\partial \xi} \right) \tag{3}$$
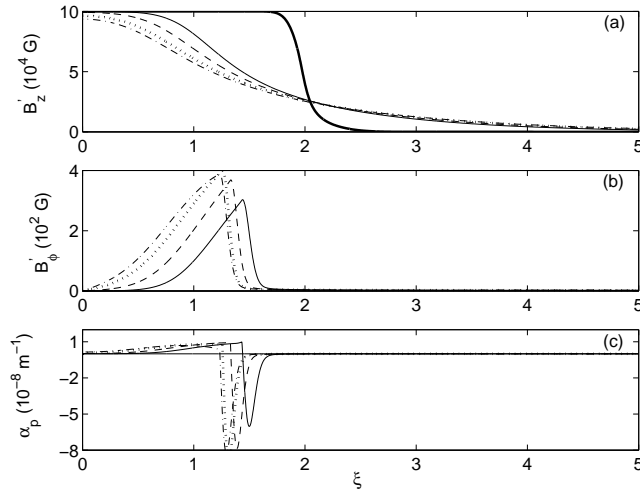
Figure 5: *Same as Fig. 4 but the field inside the flux tube is not allowed to decrease below $3B_e$ at any height. (Case B)*

$$\frac{\partial B'_\phi}{\partial t} = F^2 \frac{\partial}{\partial \xi}\left[\eta \frac{1}{\xi}\frac{\partial}{\partial \xi}(\xi B'_\phi)\right] - F\frac{\partial}{\partial \xi}(vB'_\phi). \tag{4}$$

(Note that the advection term appears in the ϕ component only, as it does not represent a truly radially symmetric inflow; instead, it is just designed to mimic the effect of the wrapping of poloidal field lines around the rising tube.) Following Petrovay & Moreno-Insertis (1997), the magnetic diffusivity η is specified in the form

$$\eta = \frac{\eta_0}{1 + (B/B_{eq})^2} \tag{5}$$

All our calculations are performed for a flux tube of flux 10^{22} Mx and initial field strength 10^5 G.

Numerical solutions of the equations are presented in Figures 4 and 5. The conclusions drawn from our model hinge on some assumptions, especially concerning the subsurface magnetic field structure in the last phases of the rise of the tube. The field strength in the rising tube, as calculated from thin flux tube emergence models, decreases well below the turbulent equipartition value B_e near the surface ($B_e^2/2\mu_0 = \rho\overline{v^2}/2$). The presence of 3000 G magnetic fields in sunspots is a compelling proof that magnetic fields may never fall to such low

values; in fact, at least in photospheric layers, they are at about $3B_e$. This is presumably the result of flux concentration processes such as turbulent pumping and convective collapse. Thus, it may be more realistic not to allow the magnetic field to fall below $3B_e$. Figures 4 and 5 present results without and with this constraint, respectively.

Inspecting the lower panels of Figures 4 and 5 one finds that the typical value of α_p in the internal parts of the flux tube is of order $\sim 10^{-8}\,\mathrm{m}^{-1}$ at a depth of $0.85R_\odot$ in both cases. However, as the flux reaches the solar surface, in case A the B_ϕ component spreads out due to diffusion and its gradient becomes smaller, reducing α_p by about one order of magnitude. Only if the magnetic field inside the flux tube remains stronger than the equipartition field (the case B represented in Figure 5) is the B_ϕ component unable to diffuse inside so that its gradient remains strong and α_p is of order $\sim 10^{-8}\,\mathrm{m}^{-1}$ even near the surface. This suggests that our case B may be closer to reality, i.e. during the rise of the flux tube from $0.9R_\odot$ to $0.98R_\odot$ effective flux concentration processes are at work, keeping the field strength at a value somewhat above the equipartition level.

Note, however, that in the calculations presented here the amplitude and sign of the poloidal field was assumed not to depend on depth. For alternative assumptions, significantly different current helicities may result, so the above conclusion should be treated with proper reservation. Details of the radial dependence of the poloidal field strength may strongly depend on the dynamo model.

A more robust feature of the current helicity distributions, present in all the lower panels of our plots, is the presence of a ring around the tube with a current helicity of the opposite sense. This is clearly the consequence of the fact that on the outer side of the accreted sheath the radial gradient of the azimuthal field, and thus the axial current, is negative. This is an inevitable corollary of the present mechanism of producing twist in active regions. A rather strong prediction of this model is, therefore, that a ring of reverse current helicity should be observed on the periphery of active regions, somewhere near the edge of the plage.

4   Conclusion

One rather strong prediction of our model is the existence of a ring of reverse current helicity on the periphery of active regions. On the other hand, the amplitude of the resulting twist (as measured by the mean current helicity in

the inner parts of the active region) depends sensitively on the assumed structure (diffuse vs. concentrated/intermittent) of the active region magnetic field right before its emergence, and on the assumed vertical profile of the poloidal field. Nevertheless, a mean twist comparable to the observations can result rather naturally in the model with the most plausible choice of assumptions (case B).

It is likely that the accretion of poloidal fields during the rise of a flux tube is just one contribution to the development of twist. Its importance may also be reduced by 3D effects: considering the rise of a finite flux loop instead of an infinite horizontal tube, the possibility exists for the poloidal field to "open up", giving way to the rising loop with less flux being wrapped around it. It is left for later multidimensional analyses of this problem to determine the importance of any such reduction. In any case, the results presented above indicate that the contribution of poloidal field accretion to the development of twist can be quite significant, and under favourable circumstances it can potentially account for most of the current helicity observed in active regions.

Acknowledgement

References

Berger, M. 1999, Plasma Phys. Contr. Fusion, 41, B167

Burnette, A. B., Canfield, R. C., Pevtsov, A. A. 2004, ApJ, 606, 565

Chatterjee, P., Choudhuri, A. R., Petrovay, K. 2006, A&A, 449, 781

Choudhuri, A. R. 2003, Sol. Phys., 215, 31

Choudhuri, A. R., Chatterjee, P., Nandy, D. 2004, ApJ, 615, L57

DeVore, C. R. 2000, ApJ, 539, 944

D'Silva, S., Choudhuri, A. R. 1993, A&A, 272, 621

Fan, Y., Gong, D. 2000, Sol. Phys., 192, 141

Hale, G. E. 1927, Nature, 119, 708

Holder, Z. A., Canfield, R. C., McMullen, R. A., Nandy, D., Howard, R. F., Pevtsov, A. A. 2004, ApJ, 661, 1149

Leka, K. D., Skumanich, A. 1999, Sol. Phys., 188, 3

Longcope, D. W., Fisher, G. H., Pevtsov, A. A. 1998, ApJ, 507, 417

López Fuentes, M. C., Démoulin, P., Mandrini, C. H., Pevtsov, A. A., van Driel-Gesztelyi, L. 2003, A&A, 397, 305

Petrovay, K., Moreno-Insertis, F. 1997, ApJ, 485, 398

Petrovay, K., van Driel-Gesztelyi, L. 1997, Sol. Phys., 176, 249

Pevtsov, A. A., Canfield, R. C., Metcalf, T. R. 1995, ApJ, 440, L109

Pevtsov, A. A., Maleev, V. M., Longcope, D. W. 2003, ApJ, 593, 1217

Richardson, R. S. 1941, ApJ, 93, 24

Seehafer, N. 1990, Sol. Phys., 125, 219

Seehafer, N., Gellert, M., Kuzanyan, K. M., Pipin, V. V. 2003, Advances in Space Research, 32, 1819

van Driel-Gesztelyi, L., Démoulin, P., Mandrini, C. H. 2003, Advances in Space Research, 32, 1855

Zirker, J. B., Martin, S. F., Harvey, K., Gaizauskas, V. 1997, Sol. Phys., 175, 27

East-West Asymmetry in the sunspot number distribution on the basis of different sunspots catalogues

G. Mező [1], T. Baranyi [2]

[1,2]Heliophysical Observatory, H-4010 Debrecen, P.O.B. 30, Hungary

E-mail: [1]`mezo@puma.unideb.hu`, [2]`baranyi@tigris.unideb.hu`

Abstract

The east-west asymmetry of the number of sunspots has been analyzed on the basis of the Debrecen Photoheliographic Data (DPD), the single spots of Greenwich Photoheliographic Results (GPHR), and the Sunspot Feature Catalogue (SFC). The DPD and SFC do not show E-W asymmetry in the number distribution of the spots for the spots with area of greater than 20 millionth of the solar hemisphere (MSH). The GPHR shows large E-W asymmetry. Its rate is increasing from center to limb while the area of the affected spots is also increasing from 10 to 50 MSH. The East-West asymmetry of the number of spots can be detected for small spots (<20 MSH) in all the three catalogues but its rate depends on the studied catalogue.

Keywords: *Sun: East-West asymmetry, Sun: Sunspot area distribution*

1 Introduction

The east-west asymmetry of sunspot groups was discovered by Maunder (1907). She found that there were more groups on the eastern than on the western half of the solar disc and also found eastern excess in the total area of spots. This "east effect" has been investigated by numerous astronomers since then, but the results are not concordant.

Maunder found the asymmetry by using of the data of one solar cycle (1889-1901) of the GPHR. However, Pajdušáková (1969) showed that there were cycles with western surplus of the number of sunspot groups in the GPHR, too.

This asymmetry was investigated on the function of the phase of development of groups (classification) (Bartsch, 1973) and the phase of the solar cycle (Pajdušáková, 1969).

Archenhold (1940) was the first who studied the distribution of individual spots to avoid the difficulties arising from the complexity of groups. He found that near the limb the asymmetry is about 20%. Gleissberg (1945) also counted individual spots on the Mount Wilson drawings. He established that the preceding spots show western excess while the following spots eastern excess.

Many hypothesis were born to explain this phenomenon: the unfavorable effect of the planets on solar activity (Maunder, 1907), the effect of faculae (Sawyer and Haurwitz, 1972), the inclination of spot axis (Minnaert, 1946), etc.

Earlier we investigated the E-W asymmetry of the spot number distribution taking into account how this distribution depends on the spot area using the data of the GPHR and DPD (Mező et al., 2005). Recently the SFC catalogue has become available, which contains the position and area of every observable sunspot similarly to DPD and the printed version of the GPHR (for the years 1884-1916). The SFC catalogue (Zharkova et al., 2005) was made automatically using the full disk continuum SOHO/MDI images. The SFC may help to decrease some possible effects affecting the detection E-W asymmetry.

The MDI images are free from the effects of the terrestrial atmosphere. The method of sunspot detection and area measurement is different from the previous ones. The larger time resolution may decrease the possible effect of time gaps.

2   The Observational Material

The data was taken from the DPD for the years of 1986-1989 and 1993-1998, from the electronic version of the GPHR (ftp:// ftp.ngdc.noaa.gov/STP/ SOLAR_DATA/SUNSPOT_REGIONS/GREENWICH/)

for the years of 1874-1974, and from the SFC for the years of 1996-2004. The electronic version of the GPHR gives only the position and area of the spot groups but it was also possible to select the single spots with the help the given classification of the groups.

The DPD contains about 140000 individual spot data, the SFC contains about 364000 individual spot data, and the GPHR contains about 47000 single spot data in the above mentioned time intervals.
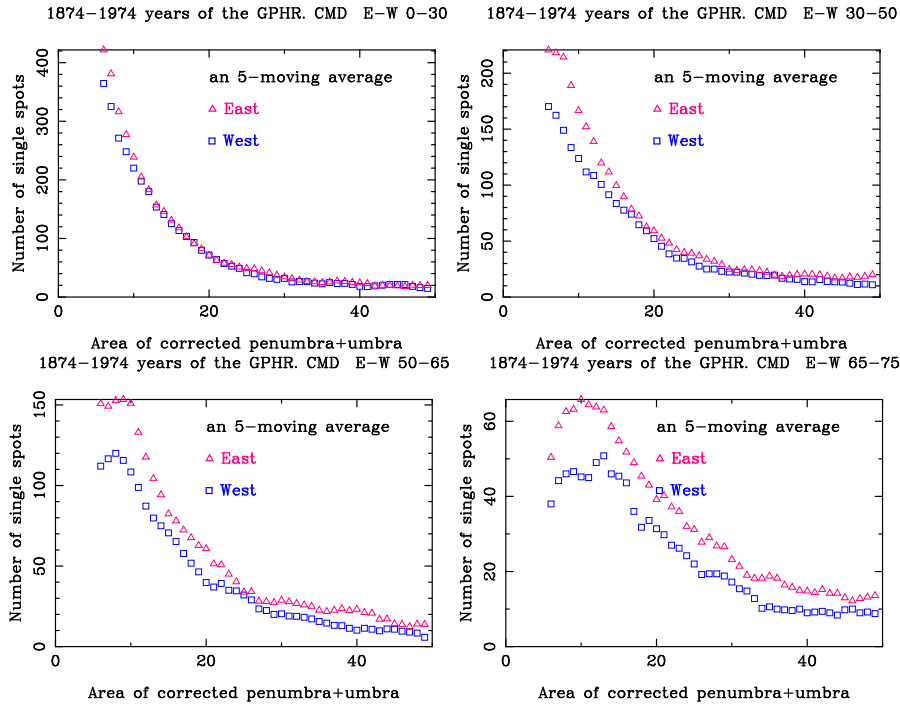
Figure 1: *Distribution of the number of the single spots of GPHR as a function of the corrected sunspot areas from the central meridian to the limb.*

The spatial resolution of the observations of the DPD and the GPHR is about $1''$ and of the SFC is about $2''$.

The time resolution of the DPD and GPHR is one day and the time resolution of the SFC is about 6 hours.

3   Distribution of the Number of Spots as a Function of the Corrected Sunspot Areas

We divided the solar hemisphere into zones from East to West. The zones were chosen symmetrically to the central meridian. The eastern zone was $[-L, -L + \Delta L]$ and the western zone was $[L - \Delta L, L]$ where L is the central
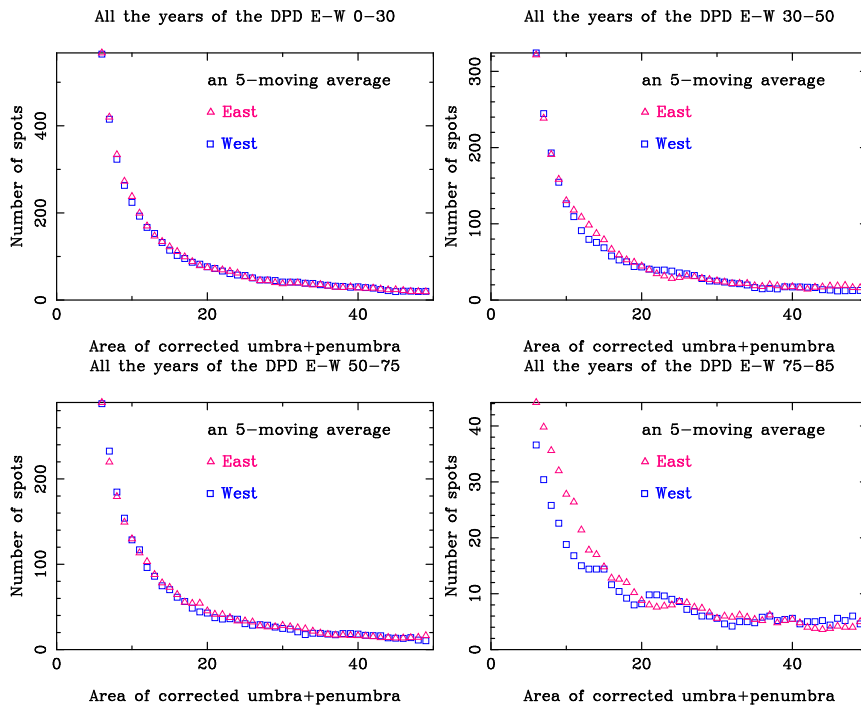
Figure 2: *Distribution of the number of the spots of DPD as a function of the corrected sunspot areas from the central meridian to the limb.*

meridian distance. We counted the spots in each zone with a given corrected area.

These numbers were displayed against the corrected area for the eastern and western halves on the same figure.

The spots of the corrected sunspot area being smaller than 6 millionth of the solar hemisphere ($A_c < 6\,MSH$) were omitted. In the case of the DPD and the GPHR it is to eliminate any visibility effect due to the tiny spots and solar pores but in the case of SFC it is to choose spots with more than two pixels near the limb in the observed images.

The results derived from the different catalogues are somewhat contradictory.

The GPHR shows large E-W asymmetry (Figure 1). The distribution of the GPHR single spots shows an increasing eastern excess from center to limb while

the maximum area of the affected spots is also increasing from 10 to 50.

The large spots ($\sim A_c > 20 \, MSH$) of the DPD (Figure 2) and the SFC (Figure 3) do not show any difference between their eastern and western distribution in any zone pair. However, in the case of spots of $A_c \leq 20 \, MSH$ the results are different.

The small spots of the DPD ($\sim A_c \leq 20 \, MSH$) have no E-W asymmetry between $0°$ and $75°$ but they show a small eastern excess observable in the zones very near the limb between $75°$ and $85°$.

The small spots of the SFC have a small eastern excess in the zones near the central meridian and no asymmetry or rather western excess in the zones near the limb.

4 Discussion

The DPD and SFC catalogue give the same result for the spots with area of greater than 20 MSH: there is not E-W asymmetry in the number distribution of the spots.

This questions the result derived from GPHR which shows eastern excess for spots of area >20 MSH.

Thus, the simple hypothesis of the inclination of spot axis cannot be maintained because in this model the inclination of spot axis independent of spot size.

The method used for calculation of the angle of spot axis by Minnaert (1946) is also questions his simple model. Minnaert used the corrected total spot area of the Table III of the Mrs. Maunder's article. He calculated the projected area of spots from the corrected area of spots of this table without taking into account the dependence of the projected area on the heliographic latitude of spots. It is easy to reproduce from the electronic version of the GPHR the Table III of the Mrs. Maunder's article and to collect the projected area of spots directly. The discrepancy between the projected area of electronic catalogue and the one calculated by Minnaert is large. However, the recent results do not exclude the validity of an improved version of this model.

Surprisingly, in the case of the small spots (<20 MSH) the results derived from DPD and SFC are opposite. The result from DPD could be explained with a small E-W inclination of spots, which could cause an observable effect only for small spots near the limb. The result from SFC seems to be the most difficult to explain at present. The found small E-W asymmetry may be a real effect but it cannot be excluded that it is only an artifact coming from the large
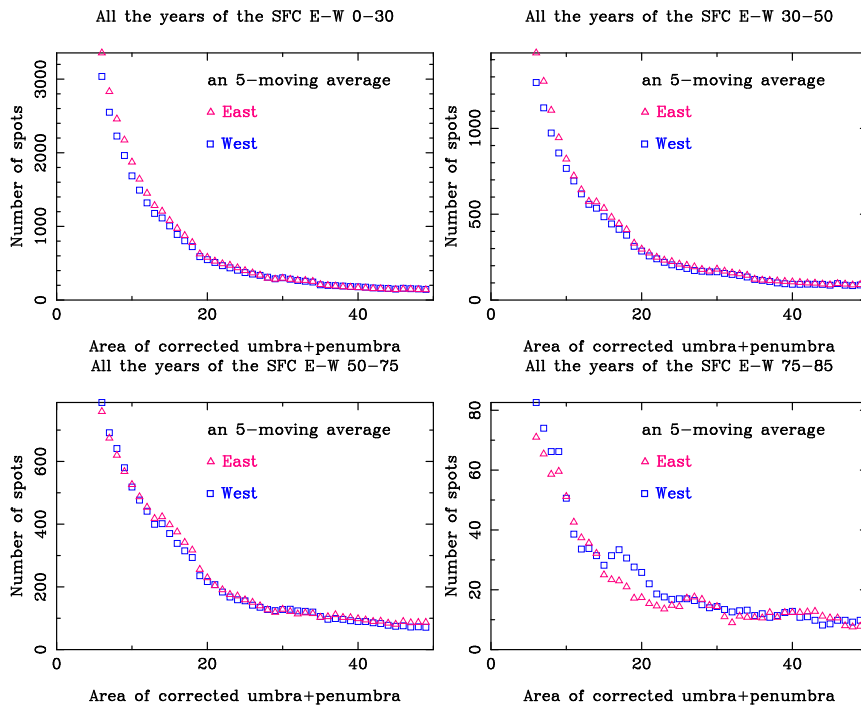
Figure 3: *Distribution of the number of the spots of SFC as a function of the corrected sunspot areas from the central meridian to the limb.*

scale intensity inhomogeneities of MDI continuum images.

On the basis of the present study the existence of East-West asymmetry of the number of small spots (<20 MSH) seems to be a real effect but its flavors cannot be determined exactly yet. If it exists,

this asymmetry is probably a weak effect, which requires further investigations.

Acknowledgement

References

Archenhold, G. H. A. 1940, MNRAS, 100, 645

Bartsch, R., 1973, Sol. Phys., 30, 93

Gleissberg, W. 1945, ApJ, 102, 133

Győri, L., Baranyi, T., et al. 2004,
  Debrecen Photoheliographic Data for 1993-1995 Publ. Debrecen Obs.
  Heliogr. Ser. 17-19.

Maunder, A. S. D. 1907, MNRAS, 67, 451

Mező, G., Muraközy, J., Baranyi, T., Győri, L. 2005, Hvar Obs. Bull., 29, 99

Minnaert, M. G. J. 1946, Mon. Not. R. Astron. Soc., 106, 98.

Pajdušáková, L. 1969, Contr. of the Astron. Obs. Skalnate Pleso, 4, 6

Sawyer, C., Haurwitz, M. W. 1972, Sol. Phys., 23, 429

Zharkova, V. V., Aboudarham, J., Zharkov, S., Ipson, S. S., Benkhalil A. K., Fuller,
  N. 2005, Sol. Phys., 228, 361

Connection of sunspot's distribution with the torsional wave

J. Muraközy, A. Ludmány

MTA KTMCsKI Heliophysical Observatory, H-4010 Debrecen, P.O.B. 30, Hungary

E-mail: `murakozyj@puma.unideb.hu`

Abstract
The torsional oscillation is a well-known observational fact, but its cause is unidentified yet. There were some theoretical assumptions for its reason, but no final solution has been accepted. Our work focuses on the study of correspondence between torsional waves and the distribution of several sunspot features which were based on the DPD (Debrecen Photoheliographic Data). Two of studied features show some spatial correlation with the shearing zones.
Keywords: *Sun, Torsional wave, Sunspot features*

1 Introduction

The torsional oscillation was discovered by Howard & LaBonte in 1980. They have recognized that the deviation (about 7 m/sec) from the differential rotation profile gives the so-called torsional oscillation pattern. Two waves exist on both hemispheres of the Sun which start from the poles and tend to the equator. These prograde (faster) and retrograde (slower) zones transit toward to the equator during about 22 years together with the magnetic activity. This was the reason that several authors expected some relation between the magnetic fields and the torsional oscillation.

There are no convincing evidences about the origin of torsional oscillation but there are several assumptions. Firstly, Howard & LaBonte (1982) investigated whether the torsional wave generates the magnetic activity or conversely,

the torsional wave is only an effect of the magnetic field of the activity cycle. In a recent model the presence of sunspots modify the turbulent viscosity in the convective zone which leads the modulation of the differential rotation (Petrovay & Forgács-Dajka 2002).

A question arises as to what is the depth of the torsional wave. It was determined from Doppler-measurements on the surface and from helioseismic observations (measurements of MDI and GONG) in the subsurface region (Howe et al., 2000, Zhao and Kosovichev, 2004). As a result it has been shown that the flows are detectable down to about 0.92 $R_\odot$.

We would like to find any spatial correlation between the torsional belts and any sunspot features. The solar latitudes have been divided into 1 degree stripes and the chosen parameters have been determined in each belt. The choice of the sunspot parameters to be studied is a matter of intuitive decision. Two choices may seem to be obvious: the total number and the area of the sunspots. The third parameter is somewhat more sophisticated, it also seems to be plausible that the complexity of the sunspot groups can also play a role in the interaction of the magnetic and velocity fields. This complexity was characterized by the third parameter: the mean number of spots within the groups of the given belt (number of all spots divided by the number of groups in the belt).

2 The method

2.1 The data

The data were taken from the Debrecen Photoheliographic Data (DPD) which is the most detailed sunspot catalogue. It contains data (area and position) for each sunspot group and for all observable (including even the smallest) sunspots on a daily basis. At the time of the present analysis the catalogue covered 10 years from 1986 until 1998 except of the years 1990-1992 (Győri et al. 1996 & Győri et al. 2004).

The sunspot features like the total and averaged number of sunspots as well as the total area of sunspots were added up for all stripes by three month periods. The total amount of considered sunspots is 8190 for the years 1986-1989 and 6443 for the period 1993-1998 as can be seen in the following table.

Table 1: *Sunspot's number*

year	total number of sunspots	consumed number of sunspots
1986	3060	398
1987	8592	1150
1988	26453	2840
1989	43012	3802
1993	16500	1823
1994	9057	1049
1995	6399	802
1996	2188	335
1997	5294	615
1998	17927	1819

To compare the obtained distribution with the torsional pattern one has to determine the latitudinal location of the torsional wave. For this purpose the most suitable data of the torsional wave were published by Ulrich (2001), see his Fig. 1, where the slow and fast belts as well as the shearing zones are well recognizable in this period.

2.2   Sunspot features

The first investigated candidate is the number of sunspots. All of the observed spots have been added up for three months in each 1° wide stripe. All groups were taken into account at the time of their largest extension. In this approach only the number of sunspots was considered with no regard to their size. All of the resulting distributions were plotted onto the simplified plot of the migrating zones, where grey/white stripes indicate the prograde/retrograde belts respectively.

The second targeted feature of the sunspots is their size. The method is the same as previously, the total area of sunspots has been added up for three month periods in all 1° wide latitudinal stripes and the obtained values were plotted onto the plot of migrating zones. The groups were considered at the moment when they had the largest extension during their passage through the solar disc.
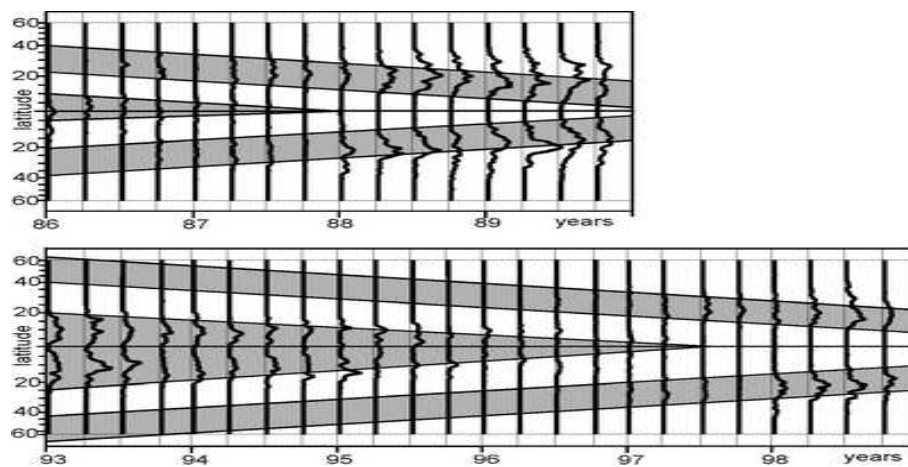
Figure 1: *Latitudinal distributions of the number of sunspots in comparison with the torsional belts.*
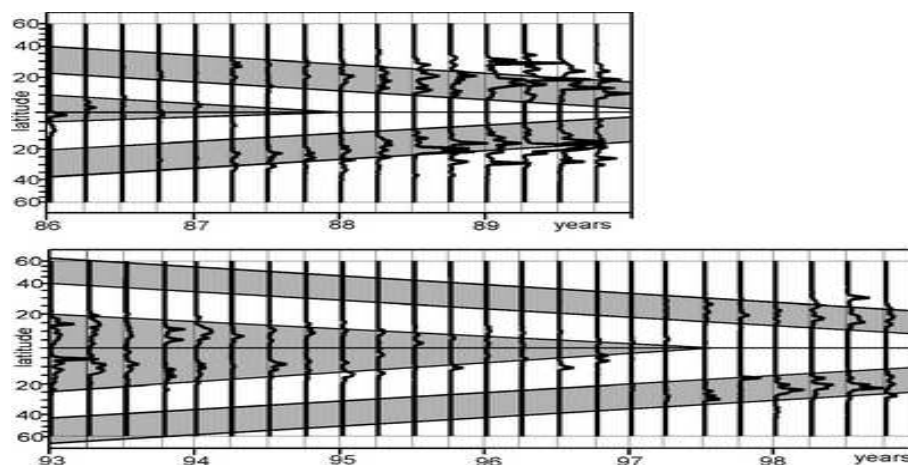
Figure 2: *Latitudinal distributions of the total area of sunspots in comparison with the torsional belts.*

The mean number of sunspots in the groups has also been studied. The procedure was the same as in the above cases but the total number of sunspots

in a stripe was averaged by the number of sunspot groups belonging to the same stripe. This parameter may be a measure of the sunspot group complexity.
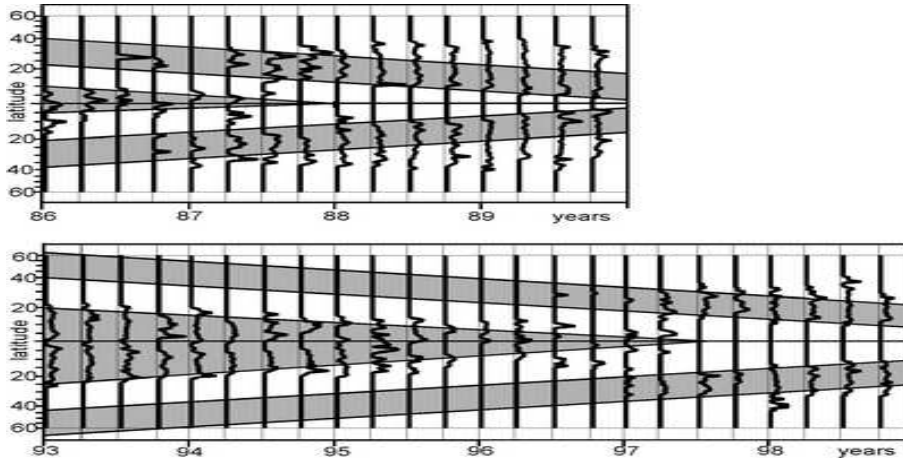
Figure 3: *Latitudinal distributions of the averaged number of sunspots in comparison with the torsional belts.*

3   Discussion

As can be seen in the above figures the total number and area of sunspots by stripes exhibit some spatial correlation with the torsional belts. It seems, that the bulges of the distributions coincide with the faster zones and their peaks are close to the poleward sides of the lower latitude borders of the faster zones. The complexity of the groups is apparently not remarkable from this view point, no trend can be recognized in the Figure 3 but the values of this parameter are also mostly situated in the faster belts.

These are preliminary results of this study, further details will be published elsewhere.

Acknowledgement

References

Godoli, G., Mazzucconi, F. 1982, A&A, 116, 88

Győri, L., Baranyi, T., Csepura, G., Gerlei, O., Ludmány A. 1996, Debrecen Photoheliographic Data for the year 1986 Publ. Debrecen Obs. Heliogr. Ser. 10, 1

Győri, L., Baranyi, T., Csepura, G., Gerlei, O., Ludmány A. 2001, Debrecen Photoheliographic Data for the year 1988 Publ. Debrecen Obs. Heliogr. Ser. 12, 1

Győri, L., Baranyi, T., Csepura, G., Gerlei, O., Ludmány A., Mezö G. 2004, Debrecen Photoheliographic Data for 1993-1995 Publ. Debrecen Obs. Heliogr. Ser. 17-19,

Howard, R., LaBonte, B. J. 1982, ApJ, 239, 33

Howard, R., LaBonte, B. J. 1982, Sol. Phys.75, 61

Howard, R., LaBonte, B. J. 1982, Sol. Phys.80, 73

Howe, R., et al. 2000, ApJ, 533, L163

Petrovay, K., Forgács-Dajka, E. 2002, Sol. Phys.205, 39

Ulrich, R. K. 2001, ApJ, 560, 466

Zhao, J., Kosovichev, A. G. 2004, ApJ, 603, 76

Hybrid Simulations of Hot Flow Anomalies in the Light of Cluster Measurements

G. Facskó, K. Kecskeméty, M. Tátrallyay

KFKI Research Institute for Particle and Nuclear Physics, H-1525 Budapest, POB 49, Hungary

E-mail: `gfacsko@rmki.kfki.hu`

Abstract
Known for about 20 years, the explanation of hot flow anomaly events is still far from being complete. Among the few hybrid simulations the results of Lin (2002) are cited frequently. We check some of its predictions using FGM and CIS measurements aboard Cluster. Several known geometrical features are verified and the average size of the affected determined. The results are confronted with the simulation.
Keywords: *hot flow anomaly, Earth's bow shock, tangential discontinuity, Cluster*

1 Introduction

Since their discovery (Schwartz et al., 1985; Thomsen et al., 1986), hot flow anomalies, these explosion-like events near the Earth's bow shock, still lack a complete theoretical explanation. Their main characteristics and development were described in a couple of papers (Burgess, 1989; Thomas et al., 1991; Sibeck et al., 1999; Schwartz et al., 2000; Lucek et al., 2004; Sibeck et al., 2002). The phenomenon is not uniquely Earth-related: similar events were identified at the bow-shock of the Mars (Øieroset et al., 2001) and probably present near the outer planets as well. Lin (1997, 2002, 2003) has developed a hybrid simulation code and published her simulation results. It was mentioned that her results

were in agreement with the observations but no particular experimental result was given thus offering an opportunity to check its predictions using the observations of Cluster. The predictions include that the size of the hot flow anomaly increases monotonically with the angle between the normal of the tangential discontinuity and the Earth-Sun direction until about 80° and then decreases. Another prediction of her theory to be checked is that the size of the hot flow anomalies is a monotone increasing function of $\Delta\Phi$, the magnetic field direction change angle within the tangential discontinuity (Lin, 2002). The purpose of this work is to verify such geometrical features of hot flow anomaly events in order to check the simulation results.

2   Description of the methods used

We used the minimum variance technique (Sonnerup and Ledley, 1974) as well as the cross-product method to determine the two angles using the measurements of the Cluster FGM[1] and ACE MAG[2] magnetic field measurements. The data series used of Cluster FGM were 1 sec averages while the ACE MAG data were 16 sec averages. We estimate the size of hot flow anomalies with a method developed previously (Facskó et al., 2005).

2.1   Determination of the angles

Among other features, there are two characteristic angles of tangential discontinuities (TD) which are important for hot flow anomaly events. One is the angle between the normal vector of the tangential discontinuity and the direction of the Earth-Sun line (γ), the other is the directional change of the magnetic field across the discontinuity ($\Delta\Phi$). Unfortunately, to calculate correlations are not viable due to the high level of fluctuations, therefore we determined the direction of the TD using both methods mentioned above. Our criterion for the minimum variance was that the fraction of the 2nd and 3rd eigenvalues be greater than 2 and the two vector point to the same direction within 15°, which usually provides reliable results.

The distributions of the number of events against γ and $\Delta\Phi$ are plotted in *Fig. 1*. One can see that both distributions differ from the distribution of TDs usually obtained and, particularly in the γ distribution, a wide empty cone can be observed around the Sun-Earth direction: no normal vector can

---

[1]Fluxgate Magnetometer

[2]ACE performs a halo orbit around the L1 LaGrange point.
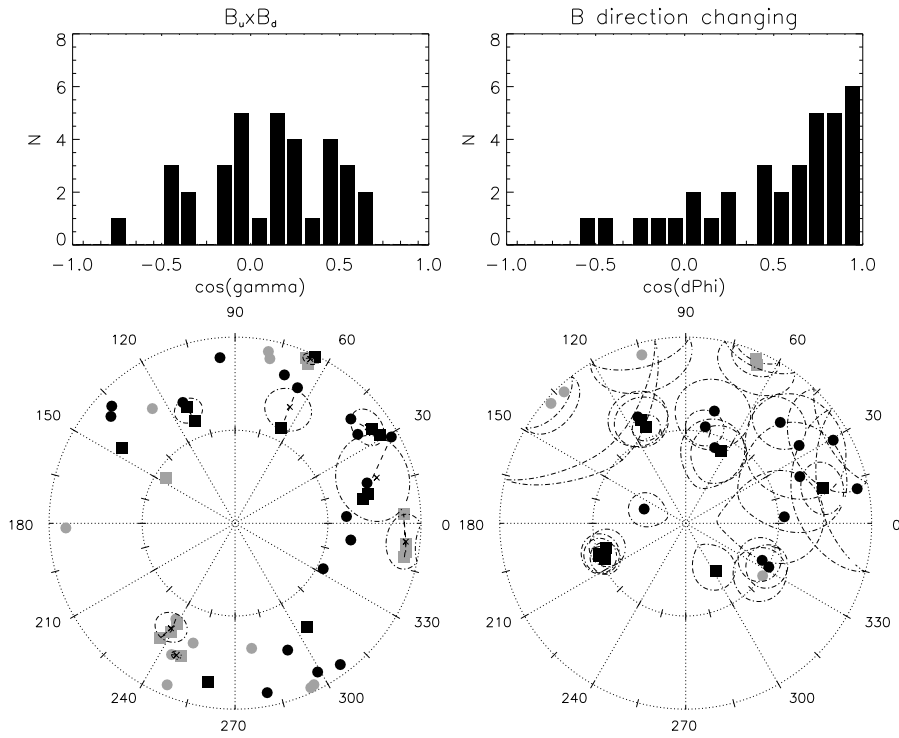
Figure 1: *Top panels: Distribution of* $\cos\gamma$ *and* $\cos\Delta\Phi$. *Bottom panels: Polar plots of the direction of the normal vectors of the TDs. The azimuthally angle is the angle between the GSE y direction and the projection of the normal vector to the GSE yz plane. The distance measured from the center is the cone angle of the normal vector of the TD determined by cross-product (left) and minimum variance method (right). The regions surrounded dashed line is the projection of error cones in both cases. Circles and squares symbolize ACE and Cluster data, respectively. Black and grey marks refer to positive and negative x values, respectively.*

be found within a 45° cone around it (*Fig. 1*). This feature was discovered in the distribution of γ determined by the cross-product method (*Fig. 1, bottom left*). Next we checked this result with the angles determined by the minimum variance method (*Fig. 1, bottom right*). The plot is significantly different so we calculated the projections of the error cones (dashed lines). This confirmed
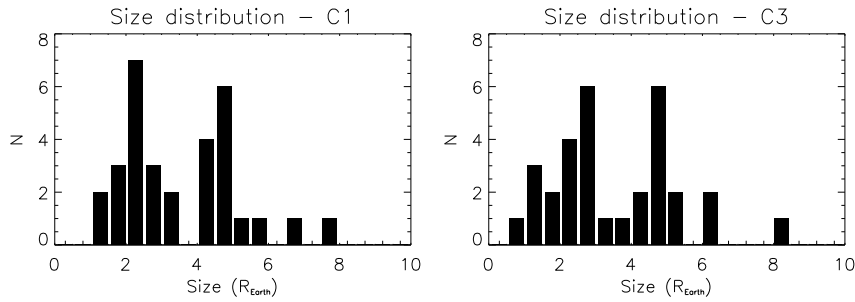
Figure 2: *Size distributions of the hot flow anomalies determined using measurements of FGM and CIS aboard Cluster. Left: Distributions based on the measurement of CIS aboard Cluster-1 and Right: Cluster-3.*

that the wide gap really exists, in accordance with the Lin (2002) results, which suggested that a hot flow anomaly can only form if $43^o \leq \gamma \leq 83^o$.

2.2   Estimation of the size of hot flow anomalies

We estimated the size and its error of hot flow anomalies with the method used in Facskó et al. (2005). This allows making a very rough estimation: we determined the length of the orbit within the hot flow anomaly event and added its time multiplied by the solar wind speed. The Cluster fleet consists of four spacecraft thus this method results in four different diameters. One can consider their average as size and the largest deviation from the average as its error. As the CIS[3] instrument works only aboard Cluster-1 and Cluster-3, we obtain two estimated sizes and errors. The size distribution is plotted (*Fig. 2*) and indicates that the distributions are similar at both spacecraft. The average calculated sizes are $4.52 \pm 1.26\,R_{Earth}$ and $4.54 \pm 1.30\,R_{Earth}$, respectively.

3   Results

Fig. 3 shows the main result of this study: the scatter plots of the sizes against the above angles. We used Cluster-1 CIS data for the top and Cluster-3 CIS data for the bottom panels: the size-γ plot is on the left and the size-$\Delta\Phi$ plot on the right. The angles are normal angles and the estimated error of the size is

---

[3]Cluster Ion Spectrometer.
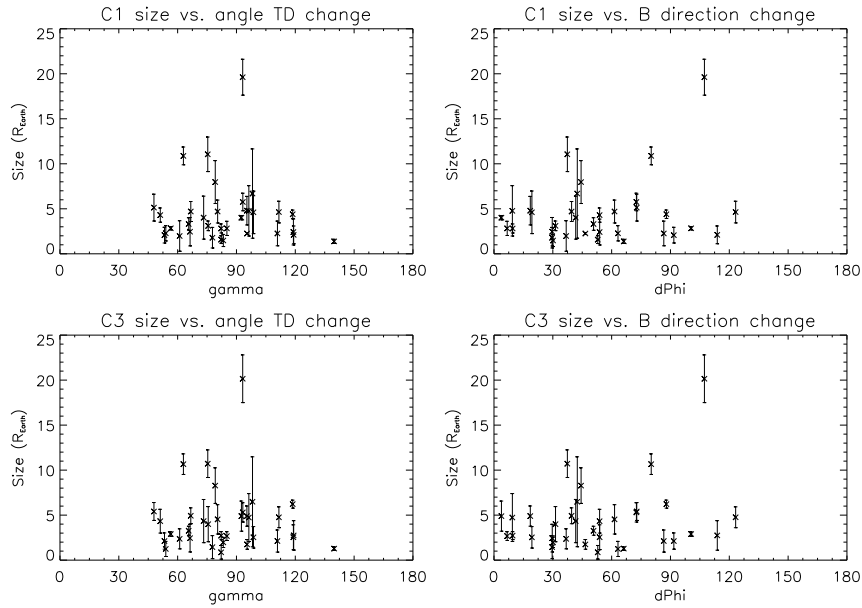
Figure 3: *Upper panels: The size vs. angle between the normal vector of the TD and the Sun-Earth direction. The size was determined using CIS solar wind speed measurements aboard Cluster-1 and Cluster-3. Lower panels: The same sizes as the function of the direction changing angle of the magnetic field within the tangential discontinuity.*

also plotted. Lin (2002) predicted that the size-γ function exhibits a maximum at 80° and our scatter plots seem to confirm this expectation. According to the prediction, the size of HFA is expected to be a monotone increasing function of $\Delta\Phi$. Unfortunately this is not seen on the size-$\Delta\Phi$ scattered plots.

4   Conclusions

We made size-angle scattered plots and they did not contradicted to the results of the hybrid simulations. We also determined the typical size of the hot flow anomalies and found a large (about 45° wide) empty cone around of the Sun-Earth direction. The estimated size is in accord with the values determined

by the simulations as well as the gap with the experimental γ values. One can conclude that the observations do not contradict to the theoretical works but we definitely need a larger sample of events to tell the final word. Also, more sophisticated size estimation should be performed and the total energy of the events determined using the measurements of RAPID aboard Cluster and compares the energy-angle scattered plot with the results of the simulation.

Acknowledgement

References

Burgess, D., J. Geophys. Res., 94, 472, 1989

Facskó, G. et al., PADEU, 15, 93, 2005

Lin, Y., J. Geophys. Res., 102, 24265, 1997

Lin, Y., Planet. Space Sci., 50, 577, 2002

Lin, Y., J. Geophys. Res., 108, doi:10.1029/2003JA009991, 2003

Lucek, E. A. et al., J. Geophys. Res., 109, 6207, 2004

Øieroset, M. et al., Geophys. Res. Lett., 28, 887, 2001

Schwartz, S. J. et al., Nature, 318, 269, 1985

Schwartz, S. J. et al., J. Geophys. Res., 105, 12639, 2000

Sibeck, D. G. et al., J. Geophys. Res., 104, 4577, 1999

Sibeck, D. G. et al., J. Geophys. Res., 107, doi:10.1029/2001JA007539, 2002

Sonnerup, B. U. O. and B. G. Ledley, J. Geophys. Res., 79, 4309, 1974

Thomas, V. A. et al., J. Geophys. Res., 96, 11625, 1991

Thomsen, M. F. et al., J. Geophys. Res., 91, 2961, 1986

A New Method for Determining the Equivalent Dose of Astronauts

A. Hirn[1], T. Pázmándi[1], S. Deme[1], I. Apáthy[1], A. Csőke[1], L. Bodnár[2]

[1] Hungarian Academy of Sciences KFKI Atomic Energy Research Institute, H-1525 Budapest, Pf. 49, Hungary

[2] BL-Electronics, H-2083 Solymár, Sport 5, Hungary

E-mail: [1]hirn@sunserv.kfki.hu, [1]pazmandi@sunserv.kfki.hu, [1]deme@sunserv.kfki.hu, [1]apathy@sunserv.kfki.hu, [1]csoke@sunserv.kfki.hu, [2]ble@axelero.hu

Abstract

One of the many risks of long-duration space flights is the excessive exposure to cosmic radiation, which has great importance particularly during solar flares and higher solar activity. Since space radiation mainly consists of charged heavy particles, the equivalent dose differs significantly from the absorbed dose. The objectives of this project are to develop and manufacture a three-axis silicon detector telescope, and to develop software for data evaluation of the measured energy deposition spectra. Research and development began in the KFKI Atomic Energy Research Institute several years ago. Elements of the 3D telescope system, issues of the electronic block diagram, requirements for the mechanical construction and possibilities of data handling and data evaluation are analyzed in this paper.

Keywords: *radiation, dosimetry, equivalent dose, LET telescope*

1 Introduction

The radiation field in space is a mixture of different particles differing in energy and varies considerably with time. Concerning the origin of the radiation two

components can be distinguished. One is the galactic component mostly consisting of energetic charged particles (protons, alpha particles, heavier ions and electrons in the energy range of 1 MeV – 10^{14} MeV) coming from the outside of the Solar System, the flux of which is almost constant and isotropic (Simonsen et al., 2000).

The other component is the solar cosmic radiation consisting of charged particles having a softer (eV - GeV) energy spectrum and most of the time a very low intensity. However, in case of solar flers its intensity can be orders of magnitude higher than that of the galactic component.

On orbits around the Earth the radiation environment is even more complicated. Due to the interaction between the magnetic field of the Earth and the solar wind the originally dipole field is distorted and torodial radiation belts are formed by the trapping of charged particles (in particular electrons and protons).

In Low Earth Orbit (LEO) the astronauts suffer twice as much equivalent dose when passing the South Atlantic region as along other regions of the orbit. This phenomenon is called the South Atlantic Anomaly (SAA) and caused by an offset and tilt of the magnetic axis with respect to the Earth's axis of rotation. Due to that asymmetry the lower radiation belt protrudes into LEO and therefore the radiation field is mainly determined by the trapped particles within this region (Kivelson, 1995).

2   Dosimetry terminology

In order to describe the effects of radiation on humans various terms have been defined. The absorbed dose D describes the amount of energy (dE) absorbed in mass dm:

$$D = dE/dm$$

Since the stochastic biological effect of particles of different type and energy are different, the term of equivalent dose was introduced in the recommendation of the ICRP (International Commission on Radiological Protection), which takes into account the ionisation density as well:

$$H_{T,R} = \sum_R D_{T,R} \cdot w_R,$$

where $H_{T,R}$ is the equivalent dose, $D_{T,R}$ is the absorbed dose in tissue T and w_R is the radiation weighting factor of radiation R. The values of w_R are broadly

compatible with the values of Q, which are related (Fig. 1) to the Linear Energy Transfer (LET):

$$LET = dE/dx,$$

where dE is the average energy locally imparted to the material by an incoming charged particle of a specified energy over a dx path length (ICRP 60, 1990).
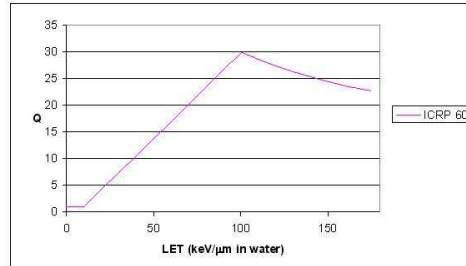
Figure 1: *The quality factor as a function of the LET (ICRP 60, 1990)*

3   Instrumentation

Since space radiation mainly consists of charged heavy particles the equivalent dose differs significantly from the absorbed dose. In order to determine the average w_R of these particles the development of a three-axis silicon detector telescope, called Tritel began in the KFKI Atomic Energy Research Institute several years ago. The main benefit of the three-axis arrangement is that it is going to exclude mostly the highly anisotropic sensitivity of the recently used one-dimensional silicon telescopes.

The geometric parameters (Fig. 2) of the 3D silicon LET telescope were defined, results of previous measurements were used as a benchmark. Features of various types and sizes of telescopes were analyzed (Pázmándi, 2004).

Tritel (Fig. 3) is based on six identical passivated implanted planar silicon detectors having a thickness of 300 μm and a sensitive area of 450 mm^2. The detector chips of each axis are mounted at a distance of 12 mm, which means an opening angle of 120°, and connected as AND gate in coincidence. The instrument cannot provide the primary energy spectrum only the energy deposit of charged particles coming from a certain solid angle. Thus the absorbed dose, LET spectrum, w_R and equivalent dose can be determined for different regions of the orbit (Pázmándi, 2004).
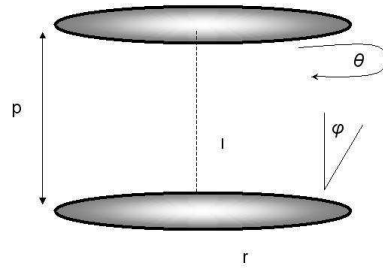
Figure 2: *The main geometric parameters of the telescope (r is the radius of the detector and p is the distance between the detector chips) (Pázmándi, 2004)*
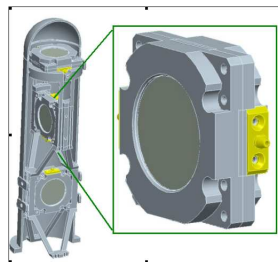
Figure 3: *The arrangement of the telescopes (x, y and z axis) in the external unit*

Fig. 4 shows the simplified block diagram of Tritel: Each detector of the 3D silicon LET telescope is connected to a charge sensitive preamplifier. After initial amplification and pulse shaping the pulses are amplified and connected to a coincidence circuit in each axis. The pulses of the measuring detector and the signal of the coincidence circuit (the last as a flag) are then fed to a peak detector. The analogue outputs of each peak detectors are sent to a flash amplitude analyser. The address of the channel together with the coincidence flags are sent to a digital multiplexer.

The energy spectrum can be used to obtain the LET spectrum because of the pathlength limitation due to the telescope geometry. The evaluation software will convert the LET spectrum to an average w_R. The final output of the system - including ground evaluation as well – will be the equivalent dose on board International Space Station (ISS).

Since the radiation environment in the SAA differs so much from that of the rest of the orbit it is worth considering the two segments separately. The
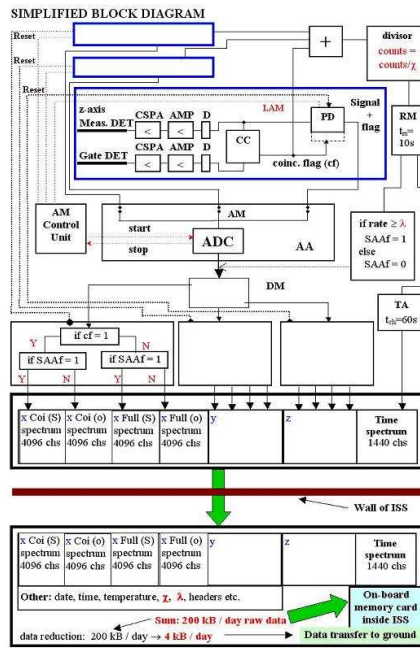
Figure 4: *Simplified block diagram of Tritel three-axis silicon detector telescope*

two regions differ not only in the LET spectrum of the particles but in intensity as well, which makes differentiation between them possible on the basis of measuring count rates in the detectors. The rate of the signals coming from the coincidence circuits (CC) of the three axes is measured with a ratemeter (RM). From the consecutive 10-second-long measurements a time analyser (TA) will produce a time spectrum from which the rate at the boundary of the SAA (λ) can be determined.

Every 24 hours the multi–channel analyzer provides altogether 12 different primary spectra (for each axis two gated and two full spectra, one taken in the South Atlantic Anomaly and the other in the rest of the orbit).

4   The Mechanical Construction

The Tritel 3D telescope system onboard ISS will consist of two units: an external unit (Fig. 5), which comprises the three silicon detector telescopes and the signal processing units and a unit located inside ISS where all the onboard digital data processing take place.
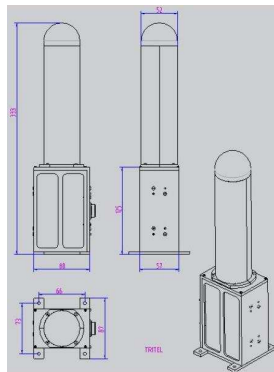
Figure 5: *Technical drawings of the external unit of Tritel*

The external unit will be attached to the zenith side of ISS by means of a 30-centimeter-long boom. In this way the axis of the unit can be adjusted to the zenith and the degree of hiding by the other instruments located on the platform can be reduced, as well.

Data of the measurements are stored in the memory of the internal unit and can be saved to a memory stick. A menu-driven graphical interface will help the astronauts to change the settings, download data or update the software. Crew change onboard the ISS takes place once every six month, hence the memory stick may be returned to Earth only at that time. Another possibility of data transfer is the data transmission to ground by using the data transfer system of the space station. This solution is independent of ISS crew change but it has an important drawback: due to the limitations of data transmission only a limited amount of data can be transferred to ground therefore the measurement data must be reduced to some extent.

Table 1: *The reverse current of the detector in original and telescope mounting (the measured data and data calculated from datasheet values)*

Detector mounting	U [V]	spec.(20°) U_{max} [V]	I_{rev} [nA]	T [°C]	measured I_{rev} [nA]	calculated I_{rev} [nA]
original:	70	90	36	25±1	67±1	72±10
telescope:				23±1	56±1	55±8

5   Measurements

Testing of the detectors and the analog circuits has already begun. The reverse current measurements have shown that the Canberra FD450-24-300RM detectors are suitable for Tritel telescopes because of their relatively low and constant reverse current in the operating point of the device ($U = 70V$). After mounting the detector chip in the prototype of the telescope, its parameters were checked (Fig. 6).
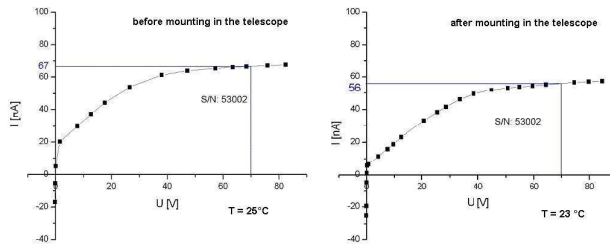
Figure 6: *The reverse current of Canberra silicon detector as a function of the bias*

Table 1 shows the reverse current measured in the operating point of the detector before and after mounting in the telescope. The values were also calculated form the data given in the datasheets of the detector. From the results it can be noticed that the difference in the reverse current can be attributed to the temperature difference of the two measurements.

The construction of the first model of the analog signal processing chain (preamplifier - shaping circuit - amplifiers) has been finished as well. The final optimization of the parameters of the system - among others the improvement

of the signal-to-noise ration - is under way.

6   The future of Tritel

In the near future the Institute of Biomedical Problems (IBMP), Moscow is
going to provide us the opportunity to carry out measurements on the Russian
platform of the International Space Station.

Within the framework of the Student Space Exploration and Technology
Initiative (SSETI) created by the ESA Education Department, a more com-
pact version of Tritel (Tritel-S) will be operated onboard the European Student
Earth Orbiter (ESEO) in Geostacionary Transfer Orbit. The device may be a
precursor of a subsequent version of Tritel planned for a future Mars probe, too.

7   Conclusions

The elements of the Tritel device together with the mechanical and electrical
requirements for the mechanical construction and the possibilities of data han-
dling and data evaluation were analyzed. The construction of the telescope
prototype and the first model of the analog signal processing chain has been fin-
ished. Further optimization of the parameters and the calibration of the system
are under way.

The 3D silicon detector telescope would provide the environmental infor-
mation for the absorbed dose, LET spectrum, w_R and equivalent dose as well
and should be the first such device used for measuring the dose astronauts are
subjected to.

References

ICRP 60, 1990 Recommendations of the International Commission on Radiological
    Protection, Publication No. 60, Pergamon Press, Oxford and New York, 1991

Kivelson, M. G., Russel, C. T.: Introduction to Space Physics, Cambridge University
    Press, 1995

Pázmándi, T., Deme, S.: Space Dosimetry with the Application of 3D Silicon Telescope
    and Pille Onboard TLD Device, Proceedings of the International Youth Nuclear
    Congress, Toronto, May 9 - 13, 2004, Canada

Simonsen, L. C., Wilson, J. W., Kim, M. H., Cucinotta, F. A.: Radiation exposure
    for human Mars exploration, Health Phys. 79(5):515-525, 2000

Motion indicators in the 2D standard map

Á. Süli[1]

[1] Eötvös University, Department of Astronomy, H-1518 Budapest, Pf. 32, Hungary

E-mail: [1]a.suli@astro.elte.hu

Abstract

In this article four motion (chaos) indicators were analyzed and compared using the framework of the 2D standard map. These indicators, namely the LCE, FLI, RLI and SALI may provide a global picture of the phase space. Until now a detailed comparison of these methods have not been performed. To supersede this imperfection is the aim of the present paper.

Keywords: *LCE, FLI, RLI & SALI – 2D standard map*

1 Introduction

The numerous experiments conducted in the last decades show that that chaotic behaviour is typical and already occurs in simple but nonlinear systems. This finding throw completely new light upon these systems and the study of chaotic behaviour become of high concern. A major part of the frontline research focuses on the structure of the phase space, therefore the problem to separate ordered and chaotic motion in systems, which posses only a few degrees of freedom and are described by ordinary differential equations, has become a fundamental task in a wide area of modern research. The phase space of these nonlinear systems can not be described by the known mathematical tools. To map the phase space and study the chaotic behaviour of a given system fast and reliable numerical tools are needed. These tools are extremely useful in those cases when the inspected dynamical system has more than two degrees of freedom and

accordingly it's phase space can't be explored in a direct way or the classical method of surface of section can not be applied which is widely used in the case of conservative systems with two degrees and freedom. The basic idea of the method of surface of section (SoS) was invented by Poincaré (1899) and it's application was renewed by Henon & Heiles (1964).

The mathematical foundation of the theory of Lyapunov characteristic exponents (LCE) is approximately of the same age as the SoS and arose progressively in the literature. The use of such exponents dates back to Lyapunov (1907), but was firstly applied by Oseledec (1968) to characterize trajectories. Henon & Heiles (1964) found that in an integrable region of the phase space of a dynamical system nearby orbits diverge linearly whereas in a chaotic region they diverge exponentially. The LCEs express these facts in a precise form and many papers were devoted to the application of LCEs in several nonlinear problems.

Unfortunately both methods have a serious drawback. To compute the LCEs the equations have to integrate for infinity, which is numerically impossible. The SoS method becomes very difficult and greatly deceiving for systems with more than two degrees of freedom. To overcome these problems was the main motivation that initiated the research to develop new numerical methods to characterize the stochasticity of the trajectories in the phase space in short timespan and in arbitrary dimension in the 1980s. The developed methods can be classified in two groups: one group consists of the methods which are based on the analysis of the orbits, (e.g. SoS or frequency analysis see Laskar (1990)), the other one is based on the time evolution of the tangent vector i.e. the solution of the linearized equations of motion (e.g. LCE). For a detailed list of the methods see Table 1. of Süli. (2006).

In this paper the LCE, Fast Lyapunov Indicator (FLI), Relative Lyapunov Indicator (RLI) and Smaller Alignment Index (SALI) methods are investigated and compared in the framework of the 2D standard map. In the literature the above quantities are commonly referred to as chaos indicators. This terminology may be misleading since these quantities indicates not only chaotic motion but also regular one. Already in Froeschlé et al. (2000) new terms such as indicators of complexity and methods of analysis have been introduced to replace the inappropriate terminology. In the spirit of this effort the (MI) is used in this paper. These quantities are inherently connected to the motion itself and indicates whether the phase trajectory lies in the regular or in the chaotic domain of the phase space. This terminology was already used by Nagy et al. (2006).

The paper is organized as follows. In Section 2 the 2D standard map is described and the initial conditions of the orbits are given. In Section 3 the definition of the MIs are given and their behaviour is shortly described. In Section
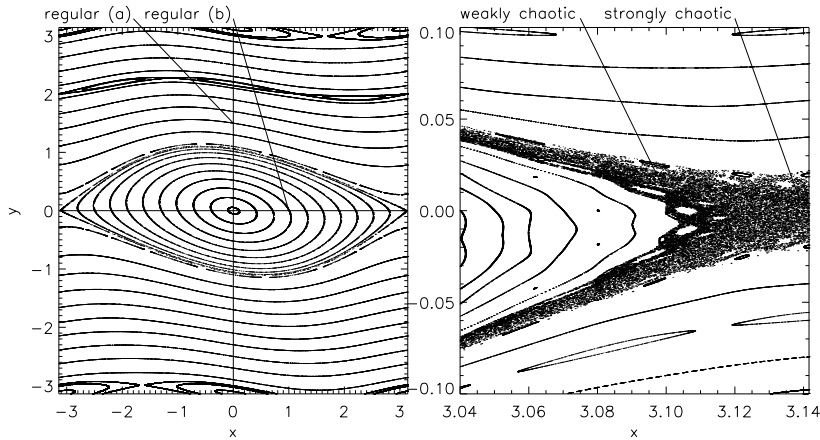
Figure 1: *The phase space of the standard map for K = 0.3. The vicinity of the hyperbolic point (π, 0) is enlarged to visualize the initial condition of the weakly chaotic orbit.*

4 the results, such as the efficiency, the dependence and the confidence of the methods are presented and compared. In Section 5 the results are summarized.

2   Model and initial conditions

The dynamical system we use to demonstrate and compare the methods is the 2D standard map, defined by

$$
\begin{aligned}
x_{i+1} &= x_i + y_i, \\
y_{i+1} &= y_i - K\sin(x_i + y_i),
\end{aligned}
\qquad \texttt{mod } 2\pi \qquad (1)
$$

where $K \geq 0$ is the non-linearity parameter. This map has been widely used since it shows the essence of chaos. In addition it's phase space is two dimensional which allows to verify the results directly and many authors used this simple mapping to introduce and test new chaos indicators.

Throughout the paper the $K = 0.3$ case is considered. For this value of the nonlinearity parameter the complete phase space of the system and the vicinity of the hyperbolic point (π,0) is depicted in Fig. 1. Different kinds of structures can be discerned: (i) islands or chains of islands (librational tori)

Table 1: *Initial conditions.*

(x_0, y_0)	type	appearance
(0,1.5)	quasi-periodic	invariant curve (rotational torus)
(1,0)	quasi-periodic	invariant (closed) curve (librational torus)
(3.14,0)	strongly chaotic	clouds of points
(3.1024048,0)	weakly chaotic	clouds of points

surrounding elliptic periodic orbits; (ii) clouds of points centered at hyperbolic periodic orbits and surrounding the islands; (iii) invariant lines extending from left to right (rotational tori).

In this work the MIs for four different kind of orbits were calculated and analyzed. An orbit can be classified as regular or chaotic. A regular orbit is quasi-periodic or periodic depending on the ratios of the frequencies of the motion. If all the frequencies are linearly independent than the motion takes place on an invariant torus, otherwise it takes place on a resonant one. When only one linearly independent frequency exist than the motion is periodic. A chaotic orbit may be further classified, accordingly to the rate of divergence of nearby orbits. In this context, one can speak about strongly and weakly chaotic orbits. If two initially nearby trajectories diverge fast, the orbit is strongly chaotic, if the divergence is slow (comparing to the previous case), we speak about weakly chaotic or sticky orbit. The initial conditions for four orbits of the standard map are listed in Table 1 with their type and appearance on the phase space (see Fig. 1).

3   Motion indicators

Let us briefly review the definition of the different methods! Given a mapping M from $\Re^n$ to $\Re^n$, an initial condition $\vec{x}_0 \in \Re^n$, and an initial vector $\vec{\xi}_0 \in \Re^n$ of norm 1. The definition of the largest LCE (Benettin et al. (1980)):

$$\text{LCE}\left(\vec{x}_0, \vec{\xi}_0\right) = \lim_{k \to \infty} \frac{1}{k} \log \|\vec{\xi}_k\| = \lim_{k \to \infty} \gamma(k, \vec{x}_0, \vec{\xi}_0), \tag{2}$$

the definition of the FLI (Froeschlé et al. (1997):

$$\text{FLI}\left(\vec{x}_0, \vec{\xi}_{10}, \ldots, \vec{\xi}_{n0}\right) = \sup_{j=1,\ldots,n} \|\xi_j(t)\|, \tag{3}$$

the definition of the RLI (Sándor, Érdi & Efthymiopoulos (2000)):

$$\text{RLI}(\vec{x}_0, \vec{\xi}_0, \Delta\vec{x}_0) = \frac{1}{t}|\text{LCI}(\vec{x}_0, \vec{\xi}_0) - \text{LCI}(\vec{x}_0 + \Delta\vec{x}_0, \vec{\xi}_0)|, \tag{4}$$

and the definition of the SALI (Skokos (2001)):

$$\text{SALI}(\vec{x}_0, \vec{\xi}_{10}, \vec{\xi}_{20}) = \min\left(\|\vec{\xi}_1 + \vec{\xi}_2\|, \|\vec{\xi}_1 - \vec{\xi}_2\|\right), \tag{5}$$

where the evolution of the vector $\vec{\xi}_i$ $i = 1, 2$ is given by the set of coupled equations

$$\begin{aligned} \vec{x}_{k+1} &= M\vec{x}_k, \\ \vec{\xi}_{k+1} &= \frac{\partial M}{\partial \vec{x}}(\vec{x}_k)\vec{\xi}_k, \end{aligned} \tag{6}$$

The second equation of Eq. 6 is the first order variational (i.e. linearized) equation. The function $\gamma(t, \vec{x}_0, \xi_0)$ measures the mean rate of divergence of the orbits.

The value of the LCE measures the sensitivity of the given trajectory to the initial conditions. The problem is that it is defined as a limit, which can not be calculated numerically. Therefore the function $\gamma(k, \vec{x}_0, \vec{\xi}_0)$ is used as the Lyapunov characteristic indicator (LCI), which is a finite estimate of the LCE. In practice the evolution of LCI is followed up and $\log(\text{LCI})$ versus $\log k$ is plotted. If the curve has a negative constant slope, the trajectory is ordered; if it exhibits an inflection of the slope, which comes close to 0 and the function converges to a certain value, the orbit is chaotic (see Fig. 2). This plotting technique is used in the cases of the other three MIs.

The FLI, RLI and SALI curves behave differently as the number of iterations increases, which makes it possible to separate the phase space. The MIs and their properties are summarized in Table 2.

Table 2: *Summary and properties of the MIs for different type of orbits.*

MI	LCI	FLI	RLI	SALI
	$\vec{x}_0, \vec{\xi}$	$\vec{x}_0, \vec{\xi}_1, \dots, \vec{\xi}_n$	$\vec{x}_0, \vec{\xi}, \Delta x$	$\vec{x}_0, \vec{\xi}_1, \vec{\xi}_2$
regular	$\longrightarrow 0$	$\longrightarrow \infty$	$\longrightarrow 0$	$\longrightarrow > 0$
chaotic	$\longrightarrow > 0$	$\longrightarrow \infty$	$\longrightarrow \geq 0$	$\longrightarrow 0$

4   Results

The efficiency or speed of the methods was study in the case of four different kind of orbits whose initial conditions are given in Table 1 and the corresponding orbits are plotted on Fig. 1. The efficiency is measured by the minimum number of iterations needed to establish with certainty the nature of an orbit.

In Fig. 2 the time evolution of the four indicators are plotted for the different kinds of orbits. The stopping time was set to 10^9 iterations. In the case of FLI, RLI and SALI an additional stopping criteria was used: whenever the running average of FLI, RLI or SALI (see definition later) reached 10^{20}, 10^{-14} or 10^{-16}, respectively the computation was stopped.

Between 1 and some times 10 iterations none of the methods is capable to establish the type of the orbit: all four curves are overlapping each other inhibiting the classification. Inspecting the LCI panel of Fig. 2 it is evident that after 10^3 the chaotic and regular curve are well separated. In the case of the other MIs the separation is possible after 10^2 iterations.

In the case of LCI, FLI and SALI the indicator corresponding to the weakly chaotic orbit (dotted line) follows exactly the curve belonging to the strongly chaotic orbit (solid line) for the first 10 iterations. Afterwards the weakly chaotic curve essentially follows the curves corresponding to the ordered orbits for approximately 10^6 iterations. Using LCI the classification is only possible after approximately 10^6 iterations, when the curve has a turning point, and its slope becomes zero. It is worth noting, that after some 10^8 iterations the LCI suddenly jumps form 1.21×10^{-5} to 6.03×10^{-3}, than it climbs to 2.55×10^{-2} which is very close to the value belonging to the strongly chaotic orbit (3.45×10^{-2}). This is a numerical evidence, that both orbits originate in the same chaotic domain. The FLI needs approximately 2×10^6 iterations, whereas in the case of the SALI about 9×10^5 iterations must be performed for the assignment.

In the case of the RLI, the weakly chaotic curve does not follow any other, but it wildly oscillates around 10^{-12}. Between 10^2 and 10^3 iterations it overlaps for short intervals with the ordered curves, beyond 10^6 it goes close to the strongly chaotic curve. The classification is possible after 10^3 iterations. It is worth noting that in all four cases the curve associated with the weakly chaotic curve is very irregular.

The LCI curves for regular orbits of different origin merge after a certain number of iteration inhibiting the distinction between the orbits. The RLI curves overlap each other from the beginning of the computations. An examination of the FLI and SALI curves in Fig. 2 allows one to distinguish also between resonant and non-resonant motion. Although the corresponding FLI
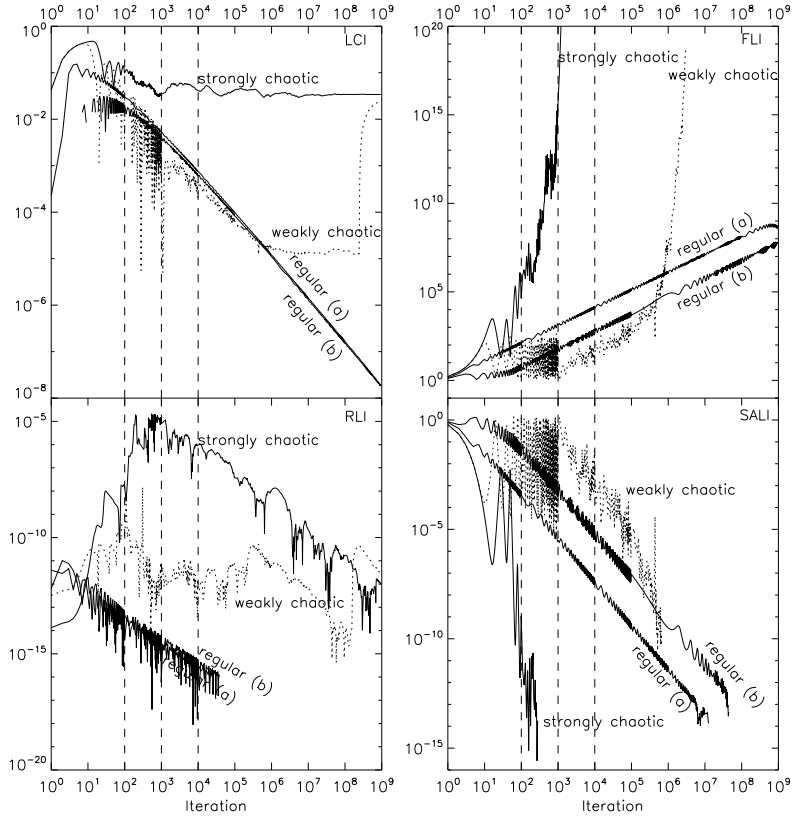
Figure 2: *Variation of the MIs with the number of iterations for four kinds of orbits of the standard map. The dotted curves correspond to the weakly chaotic orbit.*

and SALI curves are separated for these initial condition but this is in principle not true. Generally the oscillations prevent definite distinction between the two cases. Therefore, following the idea of Froeschlé et al. (2000), the definitions are replaced by their running average

$$\overline{\mathrm{MI}}_i = \frac{1}{2N} \sum_{k=i-N}^{i+N} \mathrm{MI}_k, \tag{7}$$

where MI denotes one of the methods and $2N$ is the width of the running

window. In the following $N = 50$ was used. The running average on a set of $2N$ data was introduced in order to smooth the oscillations of the FLI.

In Fig. 3 the running average of the MIs are shown. In the case of LCI the two curves can not be distinguished from each other, whilst the FLI and SALI curves are well separated. It appears clearly that using $\overline{\mathrm{FLI}}(t)$ and $\overline{\mathrm{SALI}}(t)$ resonant and non-resonant motion are clearly separated. We note that the curves appear to be precisely parallel. The $\overline{\mathrm{RLI}}(t)$ curves run close to each other. This averaging technique does not influence the behaviour of the indicators in the case of chaos.
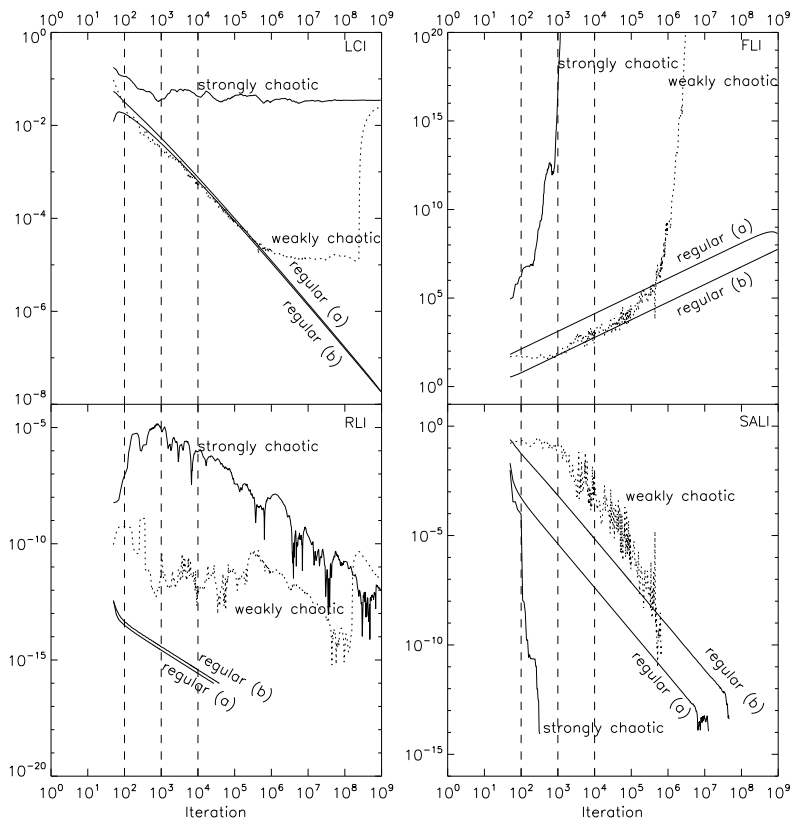
Figure 3: *Variation of the $\overline{\mathrm{MI}}(t)s$ with the number of iterations for four kinds of orbit of the standard map.*

It is only natural that the methods are sensitive to the initial direction of the tangent vector $\vec{\xi}_0$. To quantify the dependence of the $\overline{MI}$s on the direction of the tangent vector, $\vec{\xi}_0$ is rotated by $\phi \in [0, 2\pi]$ with stepsize $0°.5$, and the $\overline{MI}$s are calculated. The result is presented in Fig. 4 in which the values of the $\overline{MI}$s are plotted against the angle ϕ, for the regular (a) and for the weakly chaotic orbits. The ϕ is the angle between $\vec{\xi}_0$ and the $(1, 0)$ vector (x-axis). The calculation was performed for $N = 10^3$ iterations for the top and middle panel and for $N = 10^4$ iterations for the bottom panel to visualize the dependence on N in the case of the weakly chaotic orbit. From Fig. 4 it is obvious that these values are far from being constant when varying the angle ϕ. In order to plot all four curves together, a normalization was performed, i.e. the $\overline{MI}$ values were divided by their maximum value (see Table 3).

The normalized curves have extremum at the same ϕ, which is a natural consequence of that, that all four methods are based on the evolution of the tangent vector. The LCI and RLI are periodic with $90°$, since these methods are based on one tangent vector, while the FLI and SALI are periodic with $180°$, because they are based on two tangent vectors which are initially perpendicular to each other.

Table 3: *Dependence and relative variation for the regular (a) orbit ($N = 10^3$).*

	LCI	FLI	RLI	SALI
max	7.5809e-3	1.268e3	1.29182e-14	1.31788e-1
min	4.1322e-4	8.980e2	2.76197e-15	6.25438e-4
$\Delta_{\overline{MI}}$	1.26	0.145	0.669	2.32
ϕ_{max}	$81°.5$ $(261°.5)$	$81°.5$ $(171°.5)$	$171°.5$ $(351°.5)$	$28°$ $(118°)$
ϕ_{min}	$171°.5$ $(351°.5)$	$36°.5$ $(126°.5)$	$170°$ $(350°)$	$73°$ $(163°)$
$\Delta\phi$	$180°$	$90°$	$180°$	$90°$

In Table 3 the maximum and minimum values for the resonant orbit are listed. Introducing the quantity

$$\Delta_{\overline{MI}} = \log_{10}\left(\frac{\max(\overline{MI})}{\min(\overline{MI})}\right), \qquad (8)$$

also the measure of dependence was determinded. According to the third line of Table 3, we see that the SALI has the largest, and the FLI has the smallest value which could already be observed in Fig. 4.
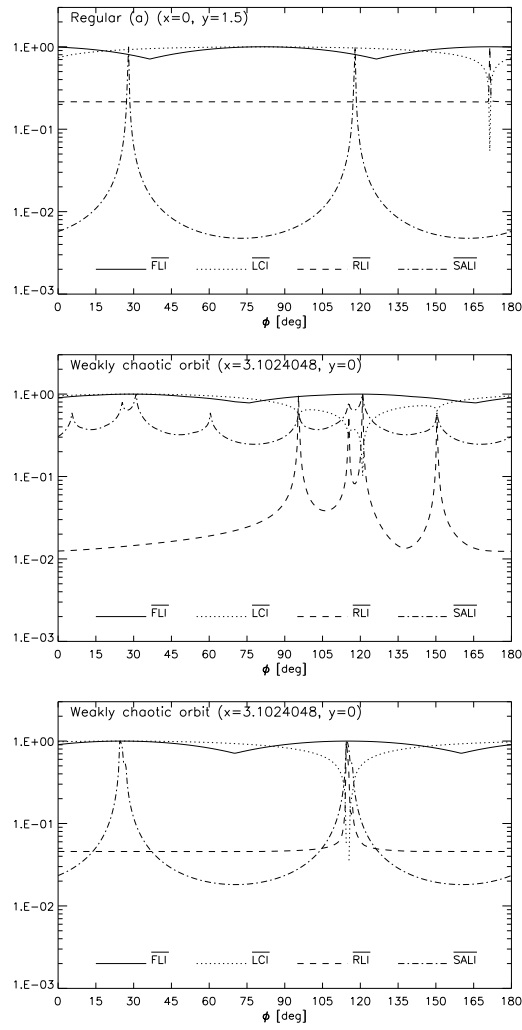
Figure 4: *Variation of the $\overline{MI}s$ as a function of the initial direction of the tangent vector(s) for the regular (a) (top) and for the weakly chaotic orbit (middle $N = 10^3$), bottom $N = 10^4$).*

To compare the $\overline{MI}$s confidence I have started computing their values for a set of 1001×1001 initial conditions regularly spaced on the (x, y)-plane in the region $[0, \pi] \times [0, \pi]$. According to the previous results the values of the $\overline{MI}$s depend on the direction of $\vec{\xi}_0$ and therefore it is important to take the same $\vec{\xi}_0$ for the whole set of orbits in order to compare their dynamical character. Fig. 5 shows the 2D $\overline{MI}$ map, that is the value of LCI, FLI, RLI and SALI after 10^3 iterations on the (x, y)-plane, $\vec{\xi}_0$ was always set in the direction of the x-axis. To demonstrate the advantage of the running average of the MIs in Fig. 5 the MIs displayed while in Fig. 6 the $\overline{MI}$s.

The most striking feature in Fig. 5 is the structure that appears on the LCI, RLI and SALI map but absent on the FLI map. This structure consits of a line that connects the $(\pi/2, \pi)$ and the $(\pi, 0)$ points. Along this line the values of the corresponding indicators are approximately equal to those around the elliptic fix point (0,0). The advantage of our simple model is now undeniable: this structure is not real it is an artifact of the methods LCI, RLI and SALI. Apart from this significant difference, the maps are in excellent agreement with Fig. 1. Islands are distinct from tori and the chaotic zone between them are well visible.

Table 4: *The initial tanget vectors $\vec{\xi}_{10}, \vec{\xi}_{20}$, number of iterations N and separation vector $\Delta\vec{x}_0$ for which the confidence tests were done.*

$\overline{MI}$	$[\vec{\xi}_{10}, \vec{\xi}_{20}]$	N	$\Delta\vec{x}_0$
LCI	$[(1,0),–], [(0,1),–]$	$10^3, 10^4$	–
FLI & SALI	$[(1,0),(0,1)],[(1,1),(-1,1)]$	$10^3, 10^4$	–
RLI	$[(1,0),–], [(0,1),–]$	$10^3, 10^4$	$(10^{-10}, 0), (0, 10^{-10})$

As it was shown the running average smooth the oscillations of the MIs which is evident by comparing Fig. 5 with Fig. 6. In other words this technique filters out the noise. Of course the false structure is a consequence of the dependence of the $\overline{MI}$s on the initial $\vec{\xi}_{10}, \vec{\xi}_{20}$ and therefore it is still present in Fig. 6.

In order to get rid of the unreal structure several different initial tanget and separation vectors were used to compute the 2D maps for 10^3 and 10^4 iterations (see Table 4). Increasing the number of iterations by a factor of 10 reduced the size of the false structure in the case of the LCI and SALI but not for the RLI. An adequate choice of the tangent and separation vectors resulted in perfect 2D maps for all MIs as shown in Fig. 7. The tangent vector was $(0, 1)$ for the LCI and RLI and $(1, 1)$, $(-1, 1)$ for the FLI and SALI, and in the case of the RLI
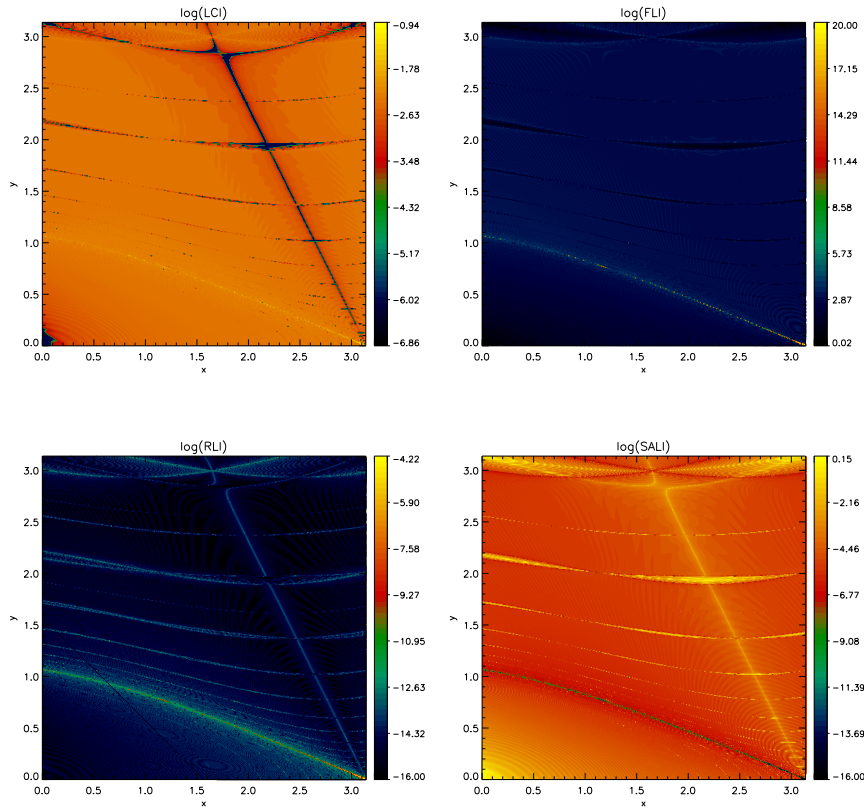
Figure 5: *Values of the MIs on the (x, y)-plane after 10^3 iterations. The tangent vectors were $\vec{\xi}_{10} = (1, 0)$ and $\vec{\xi}_{20} = (0, 1)$ and the separation vector was $\Delta \vec{x}_0 = (10^{-10}, 0)$. The color code for the values are given on the right of each panel.*

the separation vector was set to $(0, 10^{-10})$.
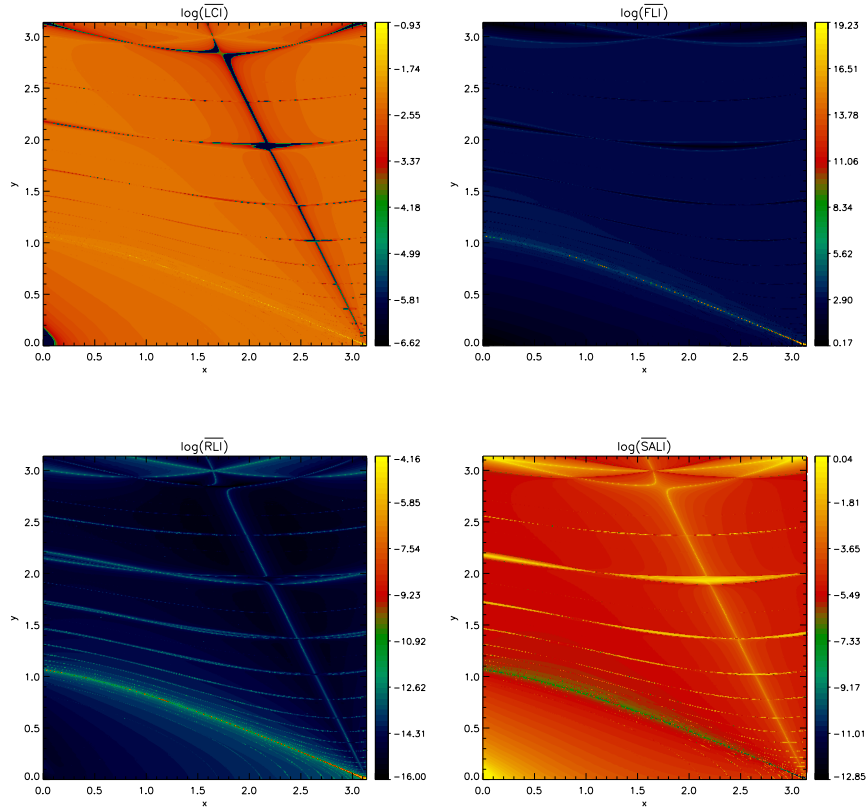
Figure 6: *Values of the MIs on the (x, y)-plane after 10^3 iterations. The tangent vectors were $\vec{\xi}_{10} = (1, 0)$ and $\vec{\xi}_{20} = (0, 1)$ and the separation vector was $\Delta \vec{x}_0 = (10^{-10}, 0)$.*

5   Summary

In this article four motion (chaos) indicators, namely the LCI, FLI, RLI and SALI were briefly described in Section 2. These methods were compared using the 2D standard map. The efficiency of these techniques was tested via applying them to four different types of orbits. It was shown that the distinction between strongly chaotic and regular orbit is possible after 10^2 iterations using the FLI,
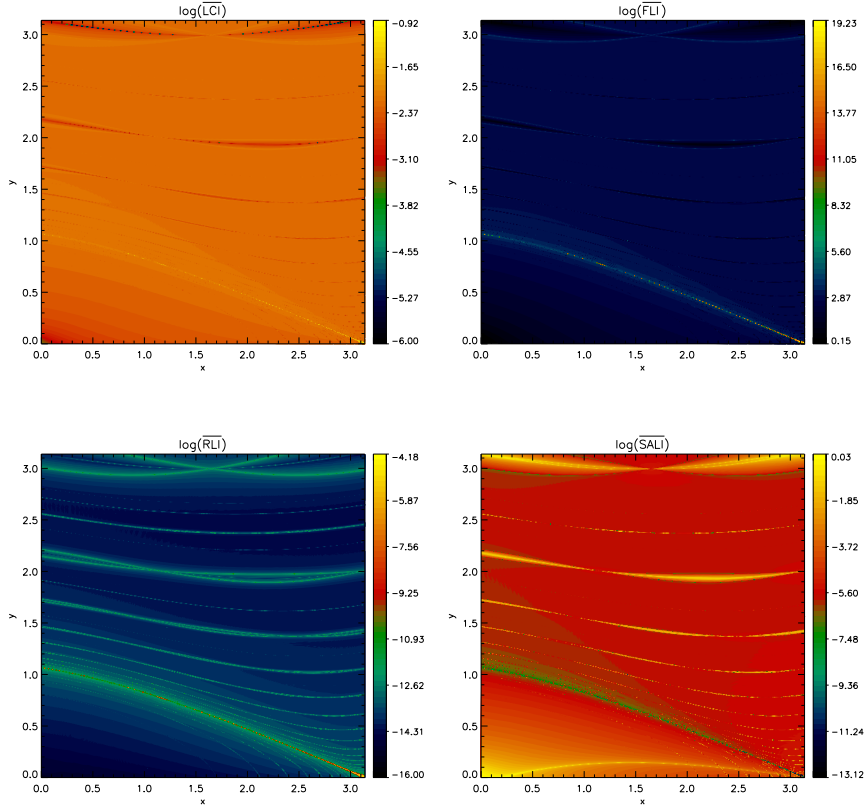
Figure 7: *Values of the $\overline{MI}s$ on the (x, y)-plane after 10^3 iterations. The tangent vectors were $\vec{\xi}_0 = (0, 1)$ for the LCI and RLI and $\vec{\xi}_{10} = (1, 1)$ $\vec{\xi}_{20} = (-1, 1)$ and the separation vector was $\Delta\vec{x}_0 = (0, 10^{-10})$.*

RLI and SALI, for the LCI 10^3 iterations are needed. To reveal the true nature of a weakly chaotic orbit, it turned out that the new methods are somewhat more efficient than the classical method of LCI. It is worth noting that in short time interval ($N \leq 10^3$) they failed to properly classify this orbit. This is because the weakly chaotic orbit pretends regular behaviour for a priori unknown time interval. The length of this time interval may be considered as the measure of

chaos: the longer the interval the weaker the chaos is.

Generally the oscillations prevent definite distinction between regular orbits with different origin. Following the idea of Froeschlé et al. (2000), the definitions are replaced by their running average. The running average on a set of $2N$ data smooth the oscillations of the MIs. This improvement is very useful when making 2D maps as it was shown in Fig. 5 and Fig. 6.

The sensitivity of the MIs to the initial direction of the tangent vector $|vec\xi_0$ was demonstrated and compared. It was shown that the MIs have extremum at the same angle ϕ, which is the angle between $\vec{\xi_0}$ and the x-axis. The LCI and RLI are periodic with π, while the FLI and SALI are periodic with $\pi/2$. With the definition of Δ_{MI} the dependence of the methods were quantitatively also characterized. The least sensitive is the FLI and the RLI the most one is the SALI.

The confidence of these methods were tested on a large portion of the phase space. The most striking feature in Fig. 5 and is the appearance of a false structure on the LCI, RLI and SALI map. This is structure is absent on the FLI map. The false structure is the result of the initial tangent vector(s) and separation vector, therefore the use of the running average technique or the increase of the maximum number of iterations did not removed it. Using adequate tangent vectors and separation vector this false structure is completely removed and the results are in perfect agreement with the real phase space structure as a comparison of Fig. 7 with Fig. 1 shows.

References

Benettin, G., Galgani, L., Giorgilli, A., Streclyn, J. M.: 1980, Meccanica, **15**: Part I: Theory, 9-20 – Part II: Numerical applications, 21-30

Froeschl, C., Lega, E., Gonczi, R.: 1997 "Fast Lyapunov Indicators. Application to Asteroidal Motion" *Celest. Mech. & Dyn. Astron.* **67**, 41.

Froeschl, Claude; Lega, Elena: On the Structure of Symplectic Mappings. The Fast Lyapunov Indicator: a Very Sensitive Tool Celestial Mechanics and Dynamical Astronomy, v. 78, Issue 1/4, p. 167-195 (2000)

Henon, M., Heiles, C.: The applicability of the third integral of motion: Some numerical experiments Astronomical Journal, Vol. 69, p. 73, 1964

Laskar, J.: 1990, "The chaotic motion of the Solar System: A numerical estimate of the size of the chaotic zones", *Icarus* **88**, 266-291.

Lyapunov A. M.: (1907) Ann. Math. Studies 17, Princeton, 1947

Nagy, I., Sli, A., rdi, B.: 2006 MNRAS in press

Oseledec V. I.: Trans. Moscow Math. Soc. 19, 197, 1968

H. Poincaré, Méthodes nouvelles de la mécanique céleste, Tome 3 (Gauthier Villars, Paris 1899)

Sándor, Zs., Érdi, B., Efthymiopoulos, C.: 2000 "The Phase Space Structure Around L4 in the Restricted Three-Body Problem", *Cel. Mech. & Dyn. Astron* **78**, 113.

Süli. Á.: 2006 4th AHW

Skokos, Ch.: 2001 "Alignment indices: a new, simple method for determining the ordered or chaotic nature of orbits" *Journal of Physics A*, **34**, 10029.

Generalized eccentric vs. true anomaly parametrizations in the perturbed Keplerian motion

Balázs Mikóczi[1]**, Zoltán Keresztes**[2]

Departments of Theoretical and Experimental Physics, University of Szeged, 6720 Szeged, Dóm tér 9, Hungary

E-mail: [1]`mikoczi@titan.physx.u-szeged.hu`, [2]`zkeresztes@titan.physx.u-szeged.hu`

Abstract
The angular and the radial parts of the dynamics of the perturbed Kepler motion are separable in many important cases. In this paper we study the radial motion and its parametrizations. We develop in detail a generalized eccentric anomaly parametrization and a procedure of computing a generic class of integrals based on the residue theorem. We apply the formalism to determine various contributions to the luminosity of a compact binary.

1 Introduction

The main sources of the gravitational radiation to be detected by Earth-based observatories (LIGO, VIRGO, TAMA and GEO) are compact binaries. The Laser Interferometer Space Antenna (LISA) will also detect gravitational waves from colliding galactic black holes. Compact binaries are composed of black holes and/or neutron stars. In such systems, a highly accurate description would include the spin-spin (SS) interaction [Barker & O'Connell (1979)], the magnetic dipole-magnetic dipole moments (DD) contribution [Ioka & Taniguchi (2000)] and the quadrupole-monopole effect (QM) [Poisson (1998)]. The parametrization of the radial motion for them are presented in [Gergely (2000)], [Vasúth, Keresztes, Mihály, Gergely (2003)], and [Gergely & Keresztes (2003)].

The method for solving a wide class of the perturbed Keplerian radial motions is worked out in [Gergely, Perjés, Vasúth (2000)]. For this purpose two (the true and eccentric anomaly) parametrization were introduced. The method can be further generalized for an even wider class of perturbed Keplerian radial motions (see: [Gergely, Keresztes, Mikóczi (2006)]).

2   The perturbed Kepler motion

The so-called radial equations for SS, DD and QM interactions are given in [Keresztes, Mikóczi , Gergely (2005)]. The radial equation of the generalized perturbed Kepler motion we consider here [Gergely, Keresztes, Mikóczi (2006)] is

$$\dot{r}^2 = \frac{2E}{\mu} + \frac{2Gm}{r} - \frac{L^2}{\mu^2 r^2} + \sum_{i=0}^{p} \frac{\varphi_i(\chi)}{\mu^2 r^i} \tag{1}$$

where $\varphi_i(\chi)$ characterize the perturbative terms and they are periodic functions of the true anomaly:

$$\varphi_i(\chi) = \sum_{j=0}^{\infty} (f_{ij} + g_{ij} \cos \chi) \sin^j \chi . \tag{2}$$

The expression $\varphi_i(\chi)$ given above is equivalent with a generic Fourier series [Gergely, Keresztes, Mikóczi (2006)]. The coefficients f_{ij} and g_{ij} can be expressed in terms of the coefficients of the Fourier expansion as well. The last term in Eq. (5) contains the generic perturbing Brumberg force [Brumberg (1991)], the spin-orbit interaction for compact binaries [Rieth and Schafer (1997); Gergely, Perjés, Vasúth (1998)], and the SS, DD and QM contributions. The energy E and angular momentum L refer to the perturbed motion. From the condition $\dot{r}^2 = 0$ we find the turning points $r_{\max}_{\min}$:

$$r_{\max}_{\min} = \frac{Gm\mu \pm A_0}{-2E} \pm \frac{1}{2\mu A_0} \sum_{i=0}^{p} \varphi_i^{\pm}(\chi) \left[\frac{\mu(Gm\mu \mp A_0)}{L^2} \right]^{i-2} , \tag{3}$$

where $A_0 = \left(G^2 m^2 \mu^2 + 2EL^2/\mu \right)^{1/2}$ is the magnitude of the Laplace-Runge-Lenz vector belonging to the perturbed motion characterized by E and L. $\varphi_i^- = \varphi_i(0)$, $\varphi_i^+ = \varphi_i(\pi)$ are small coefficients. With these turning points is possible to introduce the generalized true anomaly parametrization of the radial motion,

$r(\chi)$ as

$$\frac{2}{r} = \frac{1 + \cos\chi}{r_{\min}} + \frac{1 - \cos\chi}{r_{\max}} \ . \tag{4}$$

Integrals of the type

$$\int_0^T \frac{\omega(\chi)}{r^{2+n}} dt \tag{5}$$

frequently occur. Here $\omega(\chi)$ is the same type of periodic function of the true anomaly as $\varphi_i(\chi)$, and T is the radial period of the motion.

For constant values of φ_i and $n \geq 0$ these integrals can be evaluated in terms of a complex true anomaly variable $z = \exp(i\chi)$ by using the residue theorem. The only pole is in the origin ($z = 0$) [Gergely, Perjés, Vasúth (2000)]. For the class $n < 0$ a complex eccentric anomaly parameter can be used and then the poles are in the origin and in

$$w_1 = \left(\frac{Gm\mu^2 - \sqrt{-2\mu EL^2}}{Gm\mu^2 + \sqrt{-2\mu EL^2}} \right)^{1/2} , \tag{6}$$

however the latter occurs only rarely in physical applications (see:[Gergely, Perjés, Vasúth (2000)]).

3   Generalized perturbed Kepler motion with the eccentric anomaly parametrization

We introduce the $r(\xi)$ eccentric anomaly parametrization in the same way as in [Gergely, Perjés, Vasúth (2000)]:

$$2r = (1 + \cos\xi)r_{\min} + (1 - \cos\xi)r_{\max} \ . \tag{7}$$

We use the relations between the true and eccentric anomaly (4), (7)

$$\cos\chi = \frac{Gm\mu\cos\xi - A_0}{Gm\mu - A_0\cos\xi} \ , \qquad \sin\chi = \frac{\sqrt{\frac{-2EL^2}{\mu}}\sin\xi}{Gm\mu - A_0\cos\xi} \ . \tag{8}$$

Thus we can express φ_i as the function of ξ:

$$\varphi_i(\xi) = \sum_{j=0}^{\infty} \left(f_{ij} + g_{ij}\frac{Gm\mu\cos\xi - A_0}{Gm\mu - A_0\cos\xi} \right) \left(\frac{-2EL^2\sin\xi}{Gm\mu^2 - A_0\mu\cos\xi} \right)^j \ . \tag{9}$$

Employing the eccentric anomaly parametrization (7), the integrals (5) could be evaluated as

$$\int_0^{2\pi} \frac{\omega(\xi)}{r^{n+1}} \left(\frac{1}{r} \frac{dt}{d\xi} \right) d\xi \ . \tag{10}$$

For $n' \equiv -n - 1 \geq 0$ we apply the binomial expansion

$$(2r)^{n'} = \sum_{k=0}^{n'} \binom{k}{n'} r_{\min}^k r_{\max}^{n'-k} (1 + \cos \xi)^k (1 - \cos \xi)^{n'-k} \ , \tag{11}$$

leading to a polynomial in $\cos \xi$. From the radial equation (5) using the eccentric anomaly parametrization (7) to leading order we obtain:

$$\frac{1}{r} \frac{dt}{d\xi} = \sqrt{\frac{\mu}{-2E}} \left[1 - \frac{E}{2\mu A_0^2 \sin^2 \xi} \sum_{i=0}^p \left(\Omega_+^i - \Omega_-^i \cos \xi - \frac{2\varphi_i(\xi)}{r^{i-2}} \right) \right] , \tag{12}$$

with

$$\Omega_\pm^i = \left(\frac{\mu}{L^2} \right)^{i-2} \left[\varphi_i^+ (Gm\mu - A_0)^{i-2} \pm \varphi_i^- (Gm\mu + A_0)^{i-2} \right] \ . \tag{13}$$

The bracket becomes proportional to $\sin^2 \xi$ in (12) if the following two conditions are satisfied:

$$\sum_{i=0}^p \frac{\mu^i}{L^{2i}} (Gm\mu \pm A_0)^i (f_{i1} \pm g_{i1}) = 0 \ . \tag{14}$$

With conditions (14) satisfied, using the parametrization (7), the integrand of (10) becomes regular. The conditions are fulfilled in the case of the SS, DD and QM interactions. Introducing the complex variable $w = \exp(i\xi)$, the integral of (10) contains only two poles: the origin and the w_1 (see:[Gergely, Perjés, Vasúth (2000)]). We have proven for the $n < 0$ case:

Theorem: *For all perturbed Kepler motions characterized by the radial equation (5), with periodic perturbing functions $\varphi_i(\xi)$ obeying the conditions (14), and for arbitrary periodic functions $\omega(\xi)$, the integrals (10) are given by the residue in the origin and in the w_1 [Gergely, Perjés, Vasúth (2000)]. on w complex plane.*

In the next section we apply the above method for computing different contributions to the luminosity of compact binaries.

4 Application for some compact binaries

Peters and Mathews [Peters and Mathews (1963)] computed the luminosity of the compact binaries in the Kepler motion (Newtonian case) with orbital parameters:

$$\mathcal{L}_N = \frac{G^4 m^3 \mu^2}{15 c^5 a^5 (1-e^2)^{7/2}} \left(37 e^4 + 292 e^2 + 96\right) \ , \tag{15}$$

where a the semi-major axis and e the eccentricity. The form of $\varphi_i(\xi)$ can be derived for all of the SS, QM and DD contributions. We can then compute the various contributions to the luminosity ($-\langle dE/dt \rangle$, the time-averaged energy loss over one radial period). These are:

$$
\begin{aligned}
\mathcal{L}_{S_1 S_1} &= \frac{G^4 m^2 \mu S_1 S_2}{480 c^7 a^7 (1-e^2)^{10/2}} \bigg[c_1 \sin \kappa_1 \sin \kappa_2 \cos 2(\psi_0 - \bar{\psi}) \\
&\quad + c_2 \cos \kappa_1 \cos \kappa_2 + c_3 \cos \gamma \bigg] \ , \\
\mathcal{L}_{QM} &= \frac{G^4 m^5 \mu}{60 c^5 a^7 (1-e^2)^{10/2}} \\
&\quad \times \sum_{i=1}^{2} p_i \left[\left(c_4 (3 \sin^2 \kappa_i - 2) + c_5 \sin^2 \kappa_i \cos \delta_i \right) \right] \ , \\
\mathcal{L}_{DD} &= \frac{G^3 m^2 \mu d_1 d_2}{30 c^5 a^7 (1-e^2)^{10/2}} [c_4 \mathcal{A}_0 - c_5 \mathcal{B}_0] \ ,
\end{aligned}
\tag{16}
$$

where we have denoted by S_i the spin magnitudes, by d_i the magnitudes of the magetic dipoles, by p_i the quadrupole moment scalars and by $\mathcal{A}_0$, $\mathcal{B}_0$, δ_i, γ, ψ_0, $\bar{\psi}$, κ_i auxiliary angular quantities defined in [Gergely (2000)], [Vasúth, Keresztes, Mihály, Gergely (2003)] and [Gergely & Keresztes (2003)]. The constants $c_{1..5}$ are

$$c_i = \sum_{j=0}^{3} C_{ij} e^{2j} \ , \tag{17}$$

with coefficients C_{ij} given in Tab. 1.

5 Summary

We have introduced a generalized eccentric anomaly parametrization for the perturbed Kepler motion. We have proved that even for the generic perturbation

Table 1: *The coefficients in the C_{ij}.*

$_i\backslash^j$	0	1	2	3
1	0	131344	127888	7593
2	-124864	-450656	-215544	-8532
3	42048	154272	75528	3084
4	0	8208	7988	474
5	2600	9376	4479	-177

functions $\varphi_i(\xi)$ there are no new poles as compared to [Gergely, Perjés, Vasúth (2000)]. The method of integration can be widely employed in the case of compact binaries. We have applied the procedure to compute the SS, QM and DD contributions to the luminosity of a compact binary.

6   Acknowledgements

7   References

References

Barker, B. M., O'Connell, R. F. 1979, Gen.Relativ.Gravit. D2, 1428

Brumberg, V. A. 1991. Essential Relativistic Celestial Mechanics. Adam Hilger, Bristol

Gergely, L. Á., Perjés, Z. I., Vasúth, M. 2000, ApJS. 126, 79

Gergely, L. Á. 2000, Phys. Rev. D61, 024035; ibid. 024007

Gergely, L. Á., Perjés, Z. I., Vasúth, M. 1998 Phys. Rev. D57, 876; ibid. D57, 3423; ibid. D58, 124001

Gergely, L. Á., Keresztes, Z. 2003, Phys. Rev. D67, 024020

Gergely, L. Á., Keresztes, Z., Mikóczi, B., in preparation

Ioka, K., Taniguchi, T. 2000, ApJ. 537, 327

Keresztes, Z., Mikóczi, B., M., Gergely, L. Á. 2005, Phys. Rev. D72 104022

Peters, P. C., Mathews, J. 1963, Phys. Rev. 131, 435

Poisson, E. 1998, Phys. Rev. D57, 5287

Rieth, R. & Schafer, G. 1997, Class. Quantum Grav, 14, 2357

Vasúth, M., Keresztes, Z., Mihály, A., Gergely, L. Á. 2003, Phys. Rev. D68, 124006

P–type orbits in the Pluto–Charon system

I. Nagy[1], Á. Süli[2], B. Érdi[3]

[1,2,3] Eötvös University, Department of Astronomy, H-1518 Budapest, Pf. 32, Hungary

E-mail: [1]I.Nagy@astro.elte.hu, [2]A.Suli@astro.elte.hu,
[3]B.Erdi@astro.elte.hu

Abstract
The dynamical structure of the phase space of the Pluto–Charon system is studied in the model of the spatial circular restricted three-body problem by using numerical methods. With the newly discovered two small satellites S/2005 P1 and S/2005 P2, the Pluto–Charon system can be considered as the first known binary system in which celestial bodies move in P-type orbits. It is shown that the two satellites are in the stable region of the phase space and their origin by capture is unlikely.
Keywords: *celestial mechanics – planets and satellites: general – Kuiper Belt –*

methods: numerical

1   Introduction

In 1930 C. Tombaugh discovered Pluto, the ninth planet of the Solar system. Pluto's first moon, Charon was found by Christy & Harrington (1978). The Pluto–Charon system is remarkable, since in the Solar system Charon is the largest moon relative to its primary, with the highest mass-ratio 0.130137. Subsequent searches for other satellites around Pluto had been unsuccessful until mid May 2005, when two small satellites were discovered (Stern et al., 2005) provisionally designated as S/2005 P1 and S/2005 P2 (henceforth P1 and P2). With this observation Pluto became the first Kuiper Belt object known to have multiple satellites. These new satellites are much smaller than Charon, with

diameters 61-167 km (P1) and 46-137 km (P2) depending on the albedo. Both satellites appear to be moving in nearly circular orbits in the same orbital plane as Charon, with orbital periods 38 days (P1) and 25 days (P2).

From a dynamical point of view the Pluto–Charon system corresponds to such a binary system whose mass parameter is approximately one tenth. The phase space of binaries and the Pluto–Charon system can be studied simultaneously. To survey the phase space of binaries is a fundamental task, since more and more exoplanetary systems are being discovered. The great majority of exoplanets have been observed around single stars, but more than 15 planets are already known to orbit one of the stellar components in binary systems (this type of motion is referred to as satellite or S-type motion).

There are some studies on planetary orbits in binaries. The so far discovered planets in binaries move in S-type orbits. Theoretically there is another possible type of motion, the so-called planetary or P-type, where a planet moves around both stars. There are several studies on S- and P-type motions using the model of the planar elliptic restricted three-body problem see e.g. (Dvorak, 1984, 1986; Holman & Wiegert, 1999; Pilat-Lohinger & Dvorak, 2002) and references therein. The three-dimensional case, that is the effect of the inclination was studied by Pilat-Lohinger, Funk & Dvorak (2003) for P-type orbits in equal-mass binary models.

The main goal of this paper is to investigate the dynamical structure of the phase space of the Pluto–Charon system which can be considered as the first known binary system in which celestial bodies, namely P1 and P2 move in P-type orbits. In Section 2 we describe the investigated model and give the initial conditions used in the integrations. The applied numerical methods are briefly explained in Section 3. The results are shown in Section 4. Section 5 is devoted to some conclusions.

2   Model and initial conditions

To study the structure of the phase space of the Pluto–Charon system we applied the model of the spatial circular restricted three-body problem. We integrated the equations of motion by using a Bulirsch–Stoer integrator with adaptive stepsize control. The orbits of the primaries were considered circular and their mutual distance A was taken as unit distance. The orbital plane of the primaries was used as reference plane, in which the line connecting the primaries at $t = 0$ defines a reference x-axis. We assume that the line of nodes of the orbital plane of the massless test particle (i.e. P1 or P2) coincides with the x-axis at

$t = 0$, thus the ascending node $\Omega = 0°$. The pericenter of the test particle's orbit is also assumed to be on the x-axis at $t = 0$, thus the argument of the pericenter $\omega = 0°$. Though P1 and P2 are in the orbital plane of Charon, still we study the problem more generally by considering the effect of non-zero inclinations on the orbital stability. Thus our results are applicable to a wider class of satellite or planetary systems around binaries for the mass parameter $\mu = m_2/(m_1 + m_2) = 0.130137$, corresponding to the Pluto–Charon system (m_1 and m_2 being the mass of Pluto and Charon, respectively).

To examine the phase space and the stability properties of P-type orbits, we varied the initial orbital elements of the test particle in the following way (see Table 1):

- the semimajor axis a is measured from the barycentre of Pluto and Charon and it is varied from 1 to 5 A with stepsize $\Delta a = 0.005\ A$,

- the eccentricity e is varied from 0 to 0.3 with stepsize $\Delta e = 0.05$ ($\Delta e = 0.002$ in Fig. 2),

- the inclination i is varied from $0°$ to $180°$ with stepsize $\Delta i = 1°$,

- the mean anomaly M is given the values: $0°$, $45°$, $90°$, $135°$, and $180°$.

The above orbital elements refer to a barycentric reference frame, where the mass of the barycentre is $m_1 + m_2$. By the usual procedure we calculated the barycentric coordinates and velocities of the test particle and then transformed them to a reference frame with Pluto in the origin. In the numerical integrations we used the latter coordinates and velocities.

In total almost six million orbits were integrated for 10^3 Charon's period (hereafter T_C) and approximately 500 thousand for $10^5\ T_C$.

3   Methods

To determine the dynamical character of orbits we used three methods. The method of the relative Lyapunov indicator (RLI) was introduced by Sándor, Érdi & Efthymiopoulos (2000) for a particular problem, and its efficiency was demonstrated in a later paper (Sándor et al., 2004) for 2D and 4D symplectic mappings and for Hamiltonian systems. This method is extremely fast to determine the ordered or chaotic nature of orbits.

For an indication of stability a straightforward check based on the eccentricity was used. This action-like variable shows the probability of orbital crossing

Table 1: *In the first three rows the orbital elements from unrestricted fits (epoch = 2452600.5) are listed (Buie et al., 2005): a, e, i, ω, Ω and M denote the semimajor axis, eccentricity, inclination, argument of the pericenter, longitude of the ascending node, and mean anomaly. In the last column the orbital periods are given in days. The orbital elements for P-type orbits are given with the corresponding stepsizes.*

Object	$a\,[A]$	e	$i[°]$	$\omega[°]$	$\Omega[°]$	$M[°]$	T [day]
Charon	1.0	0	96.145	–	223.046	257.946	6.387
P2	2.487	0.0023	96.18	352.86	223.14	267.14	25
P1	3.31	0.0052	96.36	336.827	223.173	122.71	38
P-type	0.55–5	0–0.3	0–180	0	0	0–180	
Δ	0.005	0.05	1	–	–	45	

and close encounter of two planets, and therefore its value provides information on the stability of orbits. We examined the behaviour of the eccentricity of the orbit of the test particle along the integration, and used its largest value ME as a stability indicator; in the following we call it the maximum eccentricity method (hereafter MEM). This simple check was already used in several stability investigations, and was found to be a powerful indicator of the stability character of orbits (Dvorak et al., 2003; Süli, Dvorak & Freistetter, 2005).

THE MAXIMUM DIFFERENCE OF THE ECCENTRICITIES METHOD (MDEM). We developed this new method and applied it for the first time in this investigation. Two initially nearby trajectories emanating from a chaotic domain of the phase space will diverge according to the strength of chaos. The divergence manifests itself in the differences between the eccentricities of the orbits and in the angle variables. The more chaotic the system is, the faster the difference in the eccentricities grows. This difference is sensible to the variations around the running average of the eccentricity and depends also on the position along the orbit. Thus if the positions along the two orbits change chaotically, the eccentricities of the two orbits also behave differently and their momentary differences can be large even if the average value of the eccentricity of each orbit remains small. This method characterises the stability in the phase space, whereas the MEM does it in the space of orbital elements. We define the stability indicator MDE as:

$$\mathtt{MDE}(t) = \mathtt{max}|e(t, x_0) - e(t, x_0 + \Delta x)|, \tag{1}$$

where x_0 is the initial condition of the orbit and Δx is the distance of the

nearby orbit in the phase space. The method of the MDE has the advantage with respect to the MEM that in the case of chaotic orbits the MDE grows more rapidly than the ME, and while the difference between the ME for regular and chaotic motions is only 1-2 orders of magnitude, this can be 4-7 orders of magnitude for the MDE and therefore can be detected more easily.

4   Results

We show the results of our investigations in Figs. 1 – 2. These were obtained as follows. By varying the initial orbital elements as described in Section 2, we performed the integration of each orbit for five different initial values of the mean anomaly: $M = 0°$, $45°$, $90°$, $135°$, and $180°$. For each M the indicators $I^{(M)}(a, e, i)$ were determined, where $I^{(M)}$ stands for RLI, ME, and MDE, respectively. Any value, plotted in the figures, is an average over M:

$$\bar{I}(a, e, i) = \frac{1}{5} \sum_M I^{(M)}(a, e, i).$$ (2)

We note, that this averaging in the case of the RLI and the MDE emphasises the chaotic behaviour of an orbit, while in the case of the ME is not so drastic.

The three methods are not equivalent, however they complete each other. The ME detects macroscopic instability (which may even result in an escape from the system), whereas the RLI and the MDE are capable to indicate microscopic instability.

In most of the simulations the $I^{(M)}$ values were calculated for $10^3 \, T_C$. To decide whether this time interval is enough to map the real structure of the phase space, several test runs were done for a much longer time span, for $10^5 \, T_C$.

We found that the maps obtained from simulations for a time span of $10^5 \, T_C$ and $10^3 \, T_C$ are in a close agreement. Thus we can conclude that the phase space of the Pluto–Charon system can be surveyed in a reliable way by using a time span of $10^3 \, T_C$.

4.1   The phase space of the Pluto–Charon system

We investigated the behaviour of P-type orbits systematically by changing the initial orbital elements of the test particle as described in Section 2 (see also Table 1). Beside direct orbits ($i < 90°$) we studied also retrograd P-type motion ($i > 90°$) of the test particle. All the integrations were made for $10^3 \, T_C$. The
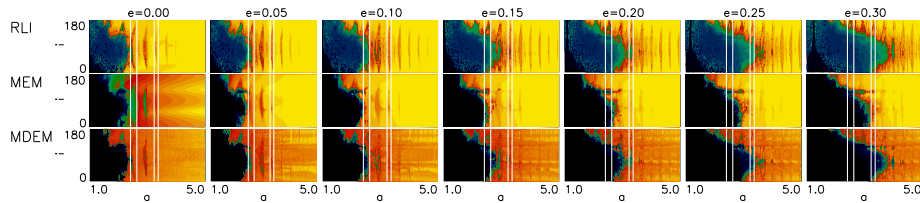
Figure 1: *The results of the 10^3 T_C simulations for $e = 0, \ldots, 0.3$ in the a, i plane. The dark area is unstable, the grey regions are stable. See text for details.*

results are shown in Fig. 1, where the indicators $\bar{I}$ are plotted on the a, i plane for different values of e.

In general, the results show an increase of the chaotic area for higher eccentricities: for $i < 160°$ the chaotic region grows with e. However, the rate of the increase strongly varies with the inclination. It can also be seen that the resonant islands (4:1 at $a = 2.52$ A, 5:1 at $a = 2.92$ A etc.) merge with the growing chaotic zone. The most striking feature is that the stability of the retrograd P-type motion practically does not depend on e. Inspecting Fig. 1 it is evident that the border of the chaotic zone for $i > 160°$ stay almost constantly at $a \approx 1.7$ A.

4.2   Stability of the satellites P1 and P2

We have addressed the problem of stability of the recently discovered satellites of Pluto. The results are shown in Fig. 2, where the values of the MDE (computed for 10^3 T_C and averaged over for the mean anomalies) are plotted on the a, e plane for the planar case ($i = 0°$). Below $a = 2.15$ A the system is unstable for all e, above $a = 2.15$ A there is a stable region depending on e. The two satellites are situated here, in the small rectangles, indicating their dynamically possible most probable places of occurance. These rectangles are defined by the ME, computed in the vicinity of each satellite. This means that we took a grid around the present value of a of each satellite with a stepsize $\Delta a = 0.005$ A, $\Delta i = 1.25°$ in the interval $i = 0 - 180°$, and with initial $e = 0$ we computed the largest ME_{max} during 10^5 T_C (including averaging over the five values of M). We obtained that $\text{ME}_{max} = 0.045$ for P2 and $\text{ME}_{max} = 0.02$ for P1. In Fig. 2 these values give the height of the rectangles. We computed the possible minimal $r_p = a(1 - \text{ME}_{max})$ pericenter and maximal $r_a = a(1 + \text{ME}_{max})$ apocenter
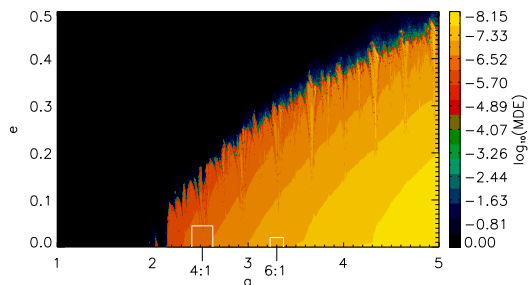
Figure 2: *Stability map in the a, e plane.*

distances of the satellites, these are 2.41 and 2.63 A for P2 and 3.23 and 3.37 A for P1. These values define the horizontal limits of the rectangles in Fig. 2, and also the places of the vertical lines in Figs. 1.

From Fig. 2 it can be seen that the determined orbital elements of the two satellites are well in the stable domain of the phase space. If P2 and P1 move in the orbital plane of Charon, their eccentricities cannot be larger than 0.17 and 0.31, respectively. The present semimajor axis a of P2 is very close to the 4:1 resonance, whereas that of P1 is close to 6:1. The locations of the exact resonances are well inside the small rectangles. We presume that these satellites probably move in resonant orbits. This could be confirmed by new observations.

5   Conclusions

Up to now the Pluto–Charon system is the only known binary system which has a relatively large mass-ratio and celestial bodies revolve around it in P-type orbits. This circumstance and the high ratio of binary stellar systems among stars make it important to study the stability properties of P-type orbits in binaries and particularly in the Pluto–Charon system. Our investigations show that the stable region is wider for retrograd than for direct P-type orbits. With the increase of the eccentricity the chaotic region becomes larger, and because of it the eccentricities of the two satellites, at their present semi-major axis, cannot be higher than 0.17 for P2 and 0.31 for P1. Below $a = 2.15$ A orbits are unstable for all eccentricities, thus no satellite could exist here.

Stern et al. (2005) has shown that P1 and P2 were very likely formed together with Charon, due to a collision of a large body with Pluto, from material ejected

from Pluto and/or the Charon progenitor. This is based on the facts that P1 and P2 move close to Pluto and Charon in nearly circular orbits in the same orbital plane as Charon, and they are also in or close to higher-order mean motion resonances.

Our results are also against the capture origin of these satellites. Firstly, since the stability region for retrograd orbits is wider, it would have been more probable for the satellites to be captured into retrograd than for direct orbits. Secondly, capture into orbits close to the Pluto–Charon binary cannot be with high eccentricity ($e > 0.17$ and 0.31 at the present semimajor axis of P2 and P1), since these orbits become unstable on a timescale of $10^3 \, T_C$. On the other hand, for eccentric capture orbits the tidal circularisation time for P1 and P2 is much longer than the age of the Solar System as Stern et al. (2005) pointed out.

Acknowledgement

References

Christy, J. W., Harrington, R. S., 1978, AJ, 83, 1005

Dvorak, R., 1984, Celest. Mech., 34, 369

Dvorak, R., 1986, A&A, 167, 379

Dvorak, R., Pilat-Lohinger, E., Funk, B., Freistetter, F., 2003, A&A, 398, L1

Holman, M. J., Wiegert, P. A., 1999, AJ, 367, 943

Pilat-Lohinger, E., Dvorak, R., 2002, Celest. Mech. & Dyn. Astron., 82, 143

Pilat-Lohinger, E., Funk, B., Dvorak, R., 2003, A&A, 400, 1085

Sándor, Zs., Érdi, B., Efthymiopoulos, C., 2000, Celest. Mech. & Dyn. Astron., 78, 113

Sándor, Zs., Érdi, B., Széll, A., Funk, B., 2004, Celest. Mech. & Dyn. Astron., 90, 127

Süli, Á., Dvorak, R., Freistetter, F., 2005, MNRAS 363, 241

Stern, S. A., Weaver, H. A., Steffl, A. J., Mutchler, M. J., Merline, W. J., Buie, M. W., Young, E. F., Young, L. A., et al., 2005, (astro-ph/0512599)

Buie, M. W., Grundy, W. M., Young, E. F., Young, L. A., Stern, S. A., 2005, (astro-ph/0512591)

Activity on single dwarf stars

Invited Talk

K. Oláh[1]

[1] Konkoly Observatory of HAS, H-1525 Budapest, Pf. 67, Hungary

E-mail: [1]`olah2@konkoly.hu`

Abstract
The importance of studies of late-type, low-mass active stars is discussed, with emphasis on the possible dynamo mechanisms that can be constrained through observing results.
Keywords: *Stars: activity, Stars: late-type, Stars: imaging*

1 Introduction

In close binaries the magnetic activity is influenced by the other component from the weak gravitational influence to the common magnetic fields of the components depending on several factors (e.g. masses of the two stars, orbits, age). Although there are several advantages of observing close binaries, like the precise orbital - and thus a good approximation of the rotational - period, precise inclination value (in case of eclipses) or a good estimate of it (in case of no eclipses), precise stellar parameters of the components etc., but on return there are the proximity effects that may modify the work of the dynamo. In single active stars the strength of the activity and its manifestations are not affected by the common gravitational field of the binary system, and by all what follows from that. For this reason, to study such stars is important for understanding the stellar magnetic activity. The different types of possible dynamo mechanisms can also be studied on low-mass single active stars.
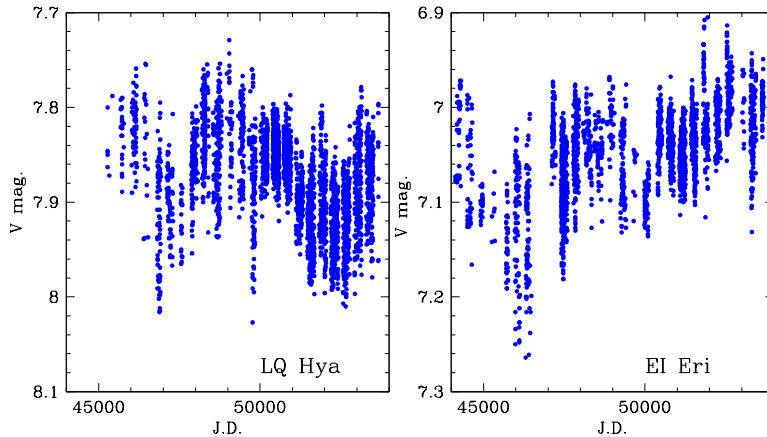
Figure 1: *Long-term photometric variability of two active stars, plotted on the same time and magnitude scales. Left: LQ Hya, single star, P_{rot}=1.67 days. Right: EI Eri, binary,$P_{rot,orb}$=1.95 days. The long-term changes are similar for both the single and the binary star. See Oláh et al. (2000) and Oláh & Strassmeier (2002) for more.*

2   Observations: single or binary?

From photometric observations alone it is not easy (if at all possible) to distinguish between single and binary stars, if no eclipse is observed. Fig. 1 shows long-term photometric measurements of one single (LQ Hya, see Kővári (2002)) and one binary (EI Eri) star for similar time intervals. The rotational periods and the magnitudes of the observed activity are also similar. Both objects show cyclic magnetic activity, evident from Fig. 1. Knowing just the long-term photometry one cannot distinguish between the single and the binary: the appearance of activity is the same.

Figure 2 shows Doppler images of one single and one binary dwarf stars. It is well seen that the surface structures are similar. This case of couse we *know* which is the binary. On the other hand, there are *effectively* single stars, just like the well-known young solar proxy EK Dra, with a secondary component in a 45 years long orbit. For the details see König et al. (2005). These wide binaries evolve like single stars, since the effects of the secondaries are negligible because of their distances.

Figure 2: *Left: HD 171488, P_{rot}=1.34 days, single star surface. Right: $\sigma^2 CrB$, $P_{rot,orb}$=1.16 days, surface of both components of a binary. The surface structures are similar in the two cases (see: http://www.aip.de/groups/activity/DI/results.html).*

3 Rotation-activity connection

The strength of activity grows with faster rotation. Numerous rotation-activity studies were published in the past decades. One of the most powerful activity index is the X-ray to bolometric luminosity ratio. Pizzolato et al. (2003) finds that from 5 days down to 0.4 days rotational periods the activity index is constant: $\log(L_X/L_{bol}) \approx -3$, and they claimed that the activity of stars with these periods are saturated. However, Mullan & MacDonald (2001) find that the saturation limit is around $\log(L_X/L_{bol}) = -1.8$. Earlier James et al (2000) using the same activity index for only M dwarf stars showed that althought the index is flat between 5-0.4 periods, but it may *decrease* later, for even shorter periods. The correlations are plotted in Fig. 3, where the place of two active single dwarfs EY Dra (Vida, 2006) and LO Peg (Csorvási, 2006) are given.

The existence or not-existence of the saturation limit, and the question until how short rotational period is the activity index constant, and what happens at even shorter periods, leads us to the next question about the stellar dynamo(s) operating in active stars.

4 Cyclic and turbulent dynamos

Two basic types of stellar dynamos are known: the interface or shell dynamo (operates near the interface between the radiative core and the convective envelope of the star) and the distributive dynamo (driven by the turbulence in the convective zone). It is quite a possible scenario if we consider the two types
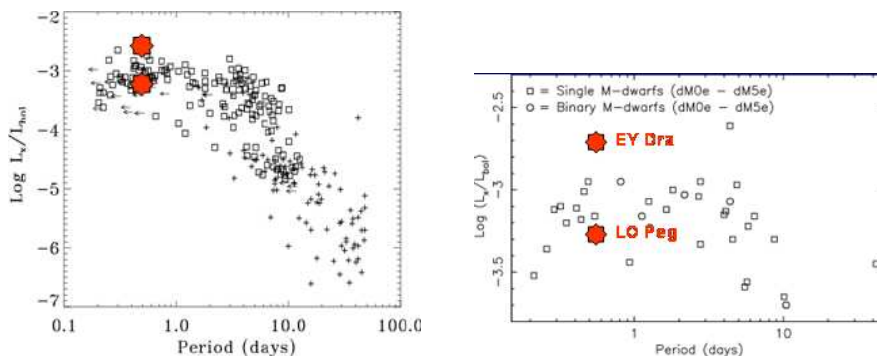
Figure 3: *Left: Rotation-activity connection of dwarf stars from Pizzolato et al. (2003). Right: Rotation-activity connection of M dwarfs from James et al (2000). In both figures positions of two single dwarf stars EY Dra and LO Peg are marked.*

of dynamos existing together in the stellar interiors. The question is, how it is possible to distinguish between these two dynamo types? Magnetic measurements show that the strength of the flux depends on the rotation (as discussed in the previous section about the X-ray flux), but there exist the so-called "flat-activity" stars that do now show variation in the strength of activity (which is low) with the rotation. Those stars that obey the rotation-activity relation should have an interface dynamo (besides a possible distributive one), whereas whose magnetic flux is lower and do not depend on rotation may held just a distributive dynamo. See Saar (1996, 1998) for more on this subject.

Another difference is, that the interface dynamo shows cycles ($\alpha - \Omega$ dynamo), while the distributive dynamo does not. Observations show that the stellar cycle lengths correlate with the rotational rates, as Fig. 4 displays. Studying active stars with very short periods is thus of fundamental importance. In Fig. 4 the possible position of cycles are plotted for two single, fast rotating active stars, that have rotational period of less than 0.5 day, EY Dra and LO Peg. New photometric observations and modelling of these two stars are published in the present volume by Vida (2006) for EY Dra and by Csorvási (2006) for LO Peg. These stars are near the border where the transition occurs to complete convection, and in the fully convective stars, evidently, the interface dynamo cannot work.

Figure 5 shows the position of active dwarf stars in the radius-effective temperature diagram. Theoratical results from Baraffe & Chabrier (1997) are plot-
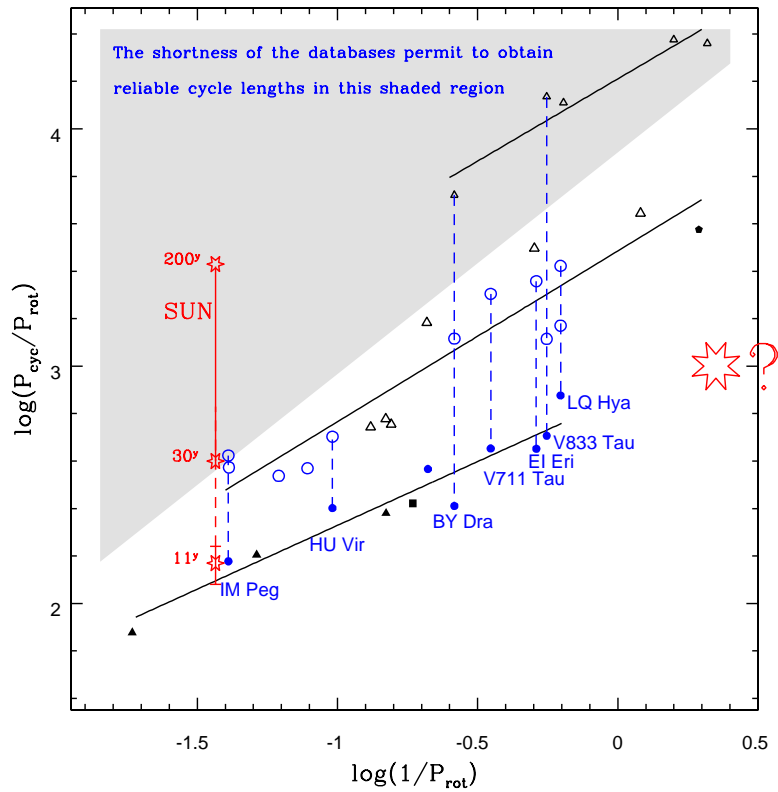
Figure 4: *Normalised cycle lengths in the function of inverse rotational periods, in logarithmic scales. Faster rotating stars have shorter cycles. Note the multiple cycles in several cases. The red star on the right shows the hypothetic position of the shortest cycle lengths of EY Dra and LO Peg, which remains to be verified or rejected.*

ted with dashed and dotted lines, for different metallicities. The observed radii and temperatures put the active stars to the right and lower than the theory predicts: they seem to be cooler and bigger than suspected. The cause of this discrepancy possibly is, that no magnetic field was taken into account in the modelling. Mullan & MacDonald (2001) in their enlightening paper show evidence that if strong magnetic fields are taken into acoount in the modelling, than the observed and theoretical positions of the stars in the radius-effective tem-
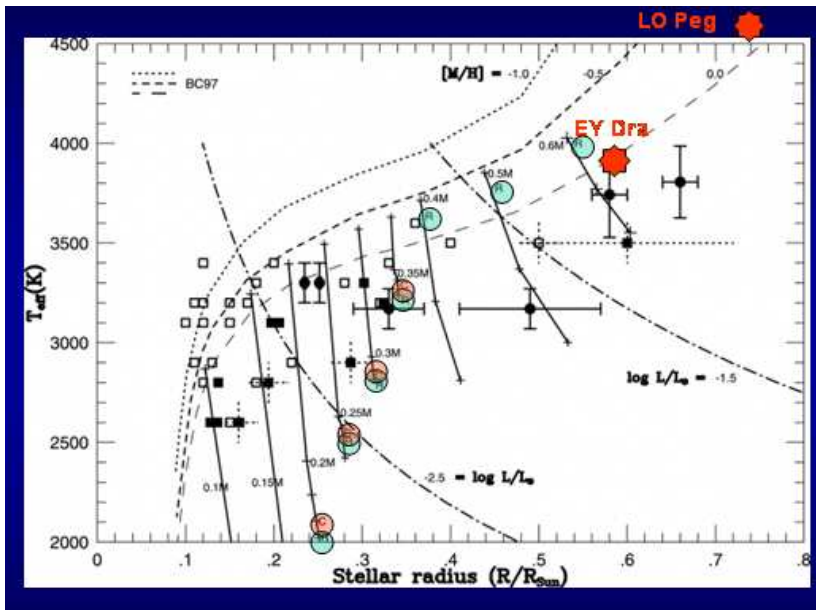
Figure 5: *The effective temperatures of M dwarf stars in the function of stellar radius. Filled squares mark known variable stars (flare stars, spotted stars) and filled circles denote eclipsing binaries. Theoretical models are plotted by dotted and dashed lines, solid lines connect positions of modelled stars with the same masses but with different magnetic parameters. Green circles show the models with radiative cores (R), pink circles show where the model is completely convective (C). The positions of EY Dra and LO Peg are indicated. From Mullan & MacDonald (2001).*

perature diagram can be reconciled, their model result in bigger, cooler stars. Another important result is, that Mullan & MacDonald (2001) find radiative core down to about 0.2 solar masses, which makes possible to held an interface dynamo, in the corresponding spectral types of about M5-M6, and complete convection stars afterwards.

Thus, we showed, that monitoring of very low mass, late type stars is of fundamental importance. See also Bartus et al. (2006), in this volume. Unfortunately, though these stars make up more than half of the galactic stellar population, but their low luminosity makes most of them invisible, and there are only a few which can be studied in sufficient details.

Acknowledgement

5 References

References

Baraffe, I., Chabrier, G. 1997, A&A327, 1054

Bartus, J., Kővári, Zs., Oláh, K., Granzer, Th., Strassmeier, K.G., Weber, M. 2006, in: PADEU 17 (this volume)

Csorvási, R. 2006, in: PADEU 17 (this volume)

James, D.J., Jardine, M.M., Jeffries, R.D., Randich, S., Collier Cameron, A., Ferreira, M. 2000, MNRAS318, 1217

König, B., Guenther, E.W., Woitas, J., Hatzes, A.P. 2005, A&A435, 215

Kővári, Zs. 2002, in: 2nd Workshop of Young Researchers in Astronomy & Astrophysics, Eötvös University, 10-11 Jan, 2002, Budapest, Hungary, Publ. Astron. Dept. Eötvös University Vol. 12, E. Forgács-Dajka (ed), p. 123

Mullan, D.J, MacDonald, J. 2001, ApJ559, 353

Oláh, K., Kolláth, Z., Strassmeier, K. G. 2000, A&A, 356, 643

Oláh, K., Strassmeier, K.G. 2001, AN 323, 3/4, 361

Pizzolato, N., Maggio, A., Micela, G., Sciortino, S., Ventura, P. 2003, A&A, 397, 147

Saar, S.N. 1996, in: Stellar Surface Structure, ed. K.G. Strassmeier and J.L. Linsky (Dordrecht:Kluwer) p. 237

Saar, S.N. 1998, in: ASP Conf. Ser. 154, Cool Stars, Stellar Systems and the Sun, ed. R. Donahue and J. Bookbinder, p.21

Vida, K. 2006, in: PADEU 17 (this volume)

http://www.aip.de/groups/activity/DI/results.html

Papers for further reading on the subject:

Barnes, J.R., 2005, MNRAS364, 137

Cardini, D. 2005, A&A430, 303

Delfosse, X., Forveille, T., Perrier, C., Mayor, M. 1998, A&A331, 581

Dunstone, N.J., Barnes, J.R., Collier Cameron, A. Jardine, M., 2006, MN-RAS365, 530

Gizis, J.E., Reid, I.N., Hawley, S.L., 2002, AJ123, 3356

Granzer, T., Caligari, P., Schüssler, M., Strassmeier, K.G., 2000, A&A, 355, 1087

Kafka, S., Honeycutt, R.K., 2004, AN, 325, 413

Messina, S., Guinan, E.F., 2002, A&A393, 25

Messina, S., Guinan, E.F., 2003, A&A409, 1017

Kővári, Zs., Strassmeier, K.G., Granzer, T., Weber, M., Oláh, K., Rice, J. B. 2004, A&A417, 1047

Rice, J.B., Strassmeier, K.G., 2001, A&A377, 264

Scholz, A., Eislöffel, J. 2004, A&A421, 259

Strassmeier, K.G., 2002, AN 323, 309

Strassmeier, K.G., Rice, J. 2003, A&A, 399, 315

Walkowicz, L.M., Hawley, S.L., West, A.A., 2004, PASP116, 1105

Wolter, U., Schmitt, J.H.M.M., van Wyk, F., 2005, A&A435, 261

http://solarphysics.livingreviews.org/

Four-colour photometry of the spotted dMe-star EY Draconis

K. Vida[1]

[1] Eötvös University, Department of Astronomy, H-1518 Budapest, Pf. 32, Hungary

E-mail: [1]`vidakris@elte.hu`

Abstract

We present the first four-colour photometry and spot modelling of the fast-rotating active star EY Draconis. In the result of the modelling possible spot evolution can be seen. The observed light curve appeared to be stable through 118 rotational cycles.

Keywords: *starspots – stars:activity – stars:atmospheres – stars:late-type – stars:imaging – stars:individual:EY Dra*

1 Introduction

The history of EY Draconis as an active star dates back until 1991, when the ROSAT X-ray/EUV satellite completed its all-sky survey. One of the WFC sources was RE 1816 + 541, which optical counterpart was identified as EY Draconis. Jeffries et al. (1994) presented spectroscopic measurements, and classified the object as a rapidly rotating dM1-2e star with chromospheric and coronal activity, based on the observed Hα and Ca H & K emission lines. Eibe (1998) studied the Hα line, and detected the presence of plage areas, and a flare. Barnes et al. (2001) presented Doppler imaging based on high-resolution spectroscopy, and derived stellar parameters as well as the image of the stellar surface, where starspots mainly at high latitudes can be seen.

The only photometry published up to now was made by Robb et al. (1995). The Johnson V-band measurements covered 8 days. From the observed light

curve – which appeared to be stable through the time of the observations – they concluded that the variations are caused by at least two large spots or spot groups. The authors found a period of 0.459 days in the light variability. Stellar parameters obtained from the mentioned articles are summarised in Table 1.

Table 1: *Stellar parameters of EY Draconis*

spectral type	dM1-2e	Jeffries et al. (1994)
$v \sin i$	61 km s^{-1}	Jeffries et al. (1994)
P	0.459 d	Robb et al. (1995)
distance	45.5 $\pm$2.1 pc	Barnes et al. (2001)
M_V	8.54 $\pm$ 0.12	Barnes et al. (2001)
$r \sin i$	0.549 $\pm$ 0.002 R$_\odot$	Barnes et al. (2001)
i	70°	Barnes et al. (2001)

2 Observations and data reduction

New observations were made with the 60 cm automatic Cassegrain telescope of the Konkoly Observatory in Svábhegy, Budapest, equipped with a Wright 750x1100 CCD using $BV(RI)_C$ filters, between 8 August and 28 September, 2005 (JD 2 453 584 – 2 453 642), on 33 nights. More than 1000 frames were obtained in each passband. We used GSC 03904-00259 as comparison and GSC 03904-00645 as check star. The images were bias subtracted and flat fielded using IRAF. Magnitudes were retrieved from differential aperture photometry using standard IRAF packages.

We calculated the principal and secondary extinction coefficients based on the work of Hardie (1962) using the star field of EY Draconis, TZ Aurigæ and SS Cancri. The correct determining of the extinction coefficients are badly needed, because only a few thousandths of magnitude errors could cause inconsistent results in the spot temperature modelling. Our analysis showed that the primary extinction coefficient do not play a role because of the small chip size and the proximity of the observed stars, however, we cannot forget about the colour extinction, which appears to be significant only in $B - V$, and its value is $k'' = -0.027$. The constants for transforming to the international Johnson–Cousins system for $B - V$, $V - R_C$, $V - I_C$ and V are 0.90, 1.077, 1.103, 0.092, respectively. The resulting light curves and colour index curves can be seen on Figure 1 (note the small amplitudes!).
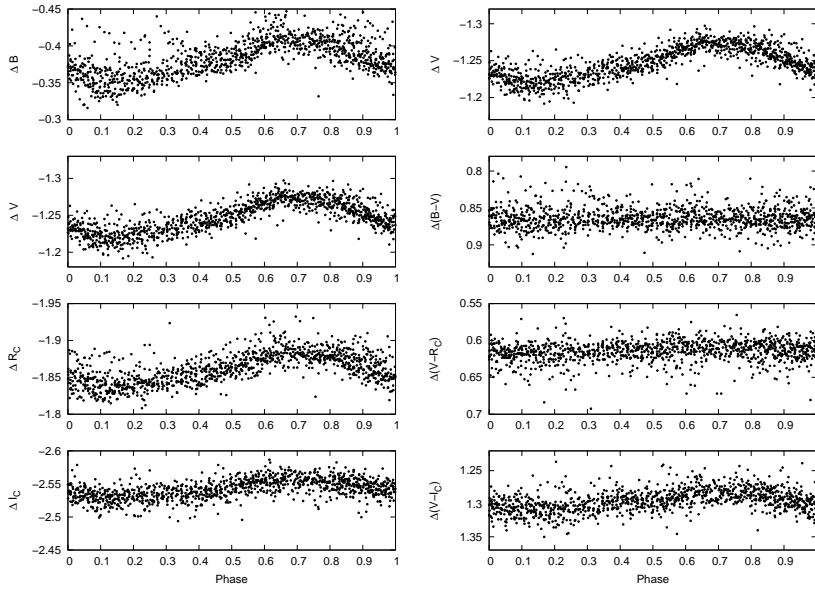
Figure 1: *Light curves and colour index curves of EY Draconis*

3   Spot modelling

The spot modelling was performed using the program SpotModeL (Ribárik et al., 2003). This program is able to determine the position, temperature and size of up to three circular spots with the analytical formulæ from Budding (1977) and Dorren (1987) using multi-bandpass data. The fixed values of some input parameters of the supposed spots (see Table 2) were determined using the Doppler images made by Barnes et al. (2001). Modelling was carried out using four consecutive day's observation blocks covering full rotational light curves, simultaneously in B and V and also in V and I_C, adjusting the spot parameters together with the spot temperature. One of those fits is displayed on Figure 2. As one can see, the fit follows the measurements well in all colours. The modelling results originating from the two different colour sets (B, V and V, I_C) agree with each other usually within 1σ (see Figure 2). The variability of the spot parameters (longitude, latitude and size) in time is plotted on Figure 2. A strong anticorrelation is clearly seen between the spot temperature and size, and the observed magnitudes. Comparing the spot coverage (Figure 3) to the
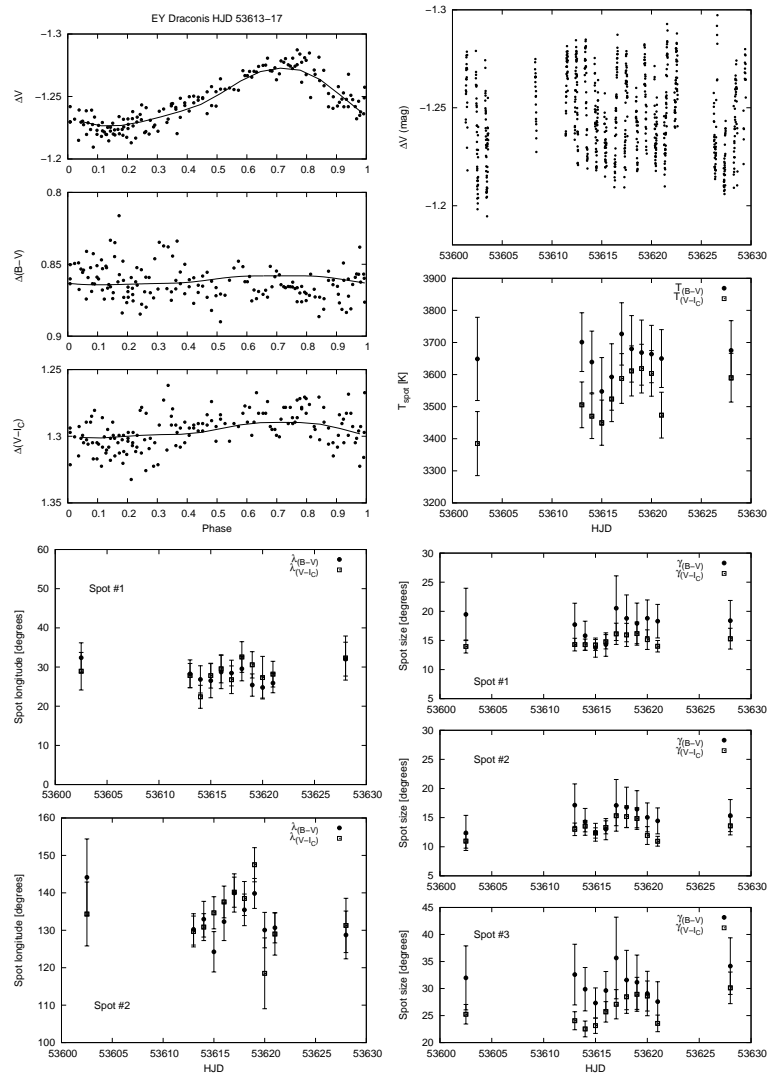
Figure 2: *Result of spot modelling: fitting and the spot parameters*

Table 2: *Input parameters for SpotModeL*

	V	I_C	B
Unspotted intensity (USI)*	−1.3	−2.585	−0.455
Limb darkening (u)**	0.670	0.509	0.763
	Spot #1	Spot #2	Spot #3
Spot longitude (λ) [°]	30	130	360***
Spot latitude (β) [°]	45***	45***	90***
Spot size (γ) [°]	20	20	10
T_{spot}	3900K		

* all fixed

** all fixed (van Hamme, 1993)

*** fixed

spot temperature, it seems that as the temperature grows, so does the spot coverage. This can be explained by the disappearance of a spot or a spot group so that the spot-to-plage ratio decreases, similar to those results in Ribárik et al. (2003).

Looking at Figure 3 one can see that the light curves are stable through the whole set of observations – over 118 rotational phases. This phenomenon is more interesting since, considering the fast stellar rotation, one would suspect, that the evolution of starspots and spot groups are faster – just like in BO (Speedy) Mic (Walter et al., 2005) which shows strongly variable light curves on the timescale of 1-2 stellar rotations. This stability we find on EY Draconis could be explained if we assume that the object is an unresolved binary and the tidal effect forces the activity to appeat at certain positions (see eg. Oláh (2006)), or there may be some other stabilising process present, such as a strong frozen-in magnetic field. The object is worth of further studying as a representative of the rare single, ultra-fast rotating low-mass field stars.

In order to study the stability of the light curve – and so the starspots, additional observations are needed on a longer timescale.
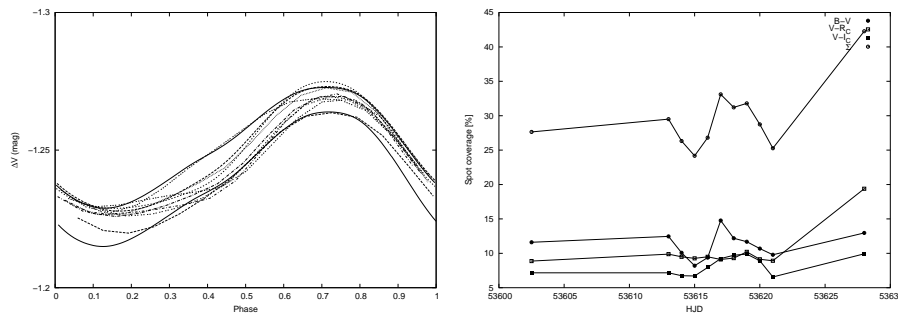
Figure 3: *The stability of the light curve; only the fits to the lisht curves are plotted for clarity (left), and spot coverage from the modelling (right)*

Acknowledgement

References

Barnes J. R., Collier Cameron A., 2001, MNRAS, 326, 950

Budding, E., 1977, Ap&SS, 48,207

Dorren, J. D., 1987, ApJ, 320, 756

Eibe M. T., 1998, A&A, 337, 757

van Hamme, W. 1993, AJ, 106, 2096

Hardie, R. H. 1962, in Stars and Stellar Systems, vol. II: Astronomical Techniques, ed. G. P. Kuiper, & B. M. Middlehurst (Univ. of Chicago Press, Chicago, USA), 178

Jeffries R. D., James D.J., Bromage G. E., 1994, MNRAS, 271, 476

Oláh, K., 2006, in: proc. Close Binaries in the 21th Century, June 27–30, Syros, Greece, submitted to Ap&SS

Ribárik, G, Oláh, K., Strassmeier, K. G., 2003, Astronomische Nachrichten, 324,202

Robb R.M., Cardinal R.D. 1995, Informational Bulletin on Variable Stars, 4270, 1

Walter, U., Schmitt, H. H. M. M., van Wyk, F., 2005, A&A435, 261

Photometry of LO Pegasi in B, V, R colors

Róbert Csorvási[1],

[1] Szeged University, Department of Physics, H-1518 Szeged, Dóm tér 9., Hungary

E-mail: [1]`csorvasi@titan.physx.u-szeged.hu`,

Abstract

Variable magnetic activity manifested by starspot distribution is investigated on the single K5-K7 dwarf LO Peg, using one month long photometric observations. We supposed three circular spots for light curve solution. We find variable spot temperature, whose average is 3960 K. The sizes of spots were stable for two spots and one spot showed a significant decrease. Different migration periods on two spots indicate differential rotation, the magnitude of the migration is slow. During the measured 90 stellar rotations (38.5 days) the location of the activity remained on the same hemisphere of the star.

Keywords: *starspots – stars:activity – stars:atmospheres – stars:late-type – stars:imaging – stars:individual:LO Peg*

1   Introduction

LO Peg (BD+22° 4409) is among the least massive stars of the young rapid rotators in the solar neighbourhood. It was detected by the ROSAT Wide Field Camera (WFC) extreme ultraviolet (EUV) all sky survey as the source RE J2131+23, and by the Extrem Ultraviolet Explorer survey as the source EUVE J2131+23.3 (Malina et al., 1994). Jeffries & Jewell (1993) identified LO Peg as a member of the Local Association on the basis of its galactic space motions and a large EUV to bolometric flux ratio. LO Peg was first studied in detail

by Jeffries et al. (1994) who determined an axial rotation period of 0.42375 d from V-band photometric observations. Photometry yielded a visual magnitude of V=9.19±0.05 and colours (B−V) = 1.08±0.02, (V−R) = 0.59±0.02. Jeffries et al. (1994) also obtained a model fit to the spectrum of LO Peg, and found a spectral type of K5-K7 and an age slightly over 30 Myr. At this spectral type, the radiative core decreases in size as the star approaches the fully convective regime at spectral type early to mid-M. If a solar like interface dynamo is at work, according to Schüssler et al. (1994) and Granzer et al. (2000) we may expect only intermediate to high latitude eruption of magnetic flux. The K5V-K7V spectral type makes LO Pegasi an important object because not very much single stars of this late spectral type have been studied.

2   Observations and data reduction

CCD photometric observations of LO Peg were obtained at the Baja Astronomical Observatory using a 0.5-m Ritchey-Chrétien telescope on twenty-one night in Summer 2005. The detectors were an Apogee Alta U16 camera (Kodak chip, 4096x4096 pixels, field of view ∼ 30'x30') and an Apogee AP7 camera (SiTe Si-502A chip, 512x512 pixels, field of view ∼ 10'x10'). All photometric reductions (image processing, digital photometry) were done with the corresponding IRAF tasks. TYC 2188-1288-1 was used as comparison star and GSC 02188-00700 was used as check star. The magnitude differences between the comparison star and check star was constant during the time of the measurements (Figure 1, left side, lower panel). The determined calibrated differential magnitudes of the comparison and check stars are $\triangle$B=−0.090±0.001, $\triangle$V=−0.988±0.001 and $\triangle$R=−1.474±0.001. For both cameras photometric calibration were made. LO Peg was also observed for photometric calibration using PG 2213-006 (Landolt, 1992) and EF Peg (Henden) standard fields on 2005 July 15 and July 29 in the B,V and R bands. The determined transformation constants are given in Table 1.

Table 1: *Determined transformation constans for B−V (μ), V−R (ν), V (ϵ).*

Camera	μ	ν	ϵ
Apogee Alta U16	1.143±0.025	0.976±0.039	−0.052±0.012
Apogee AP7	1.018±0.082	1.002±0.109	−0.023±0.052
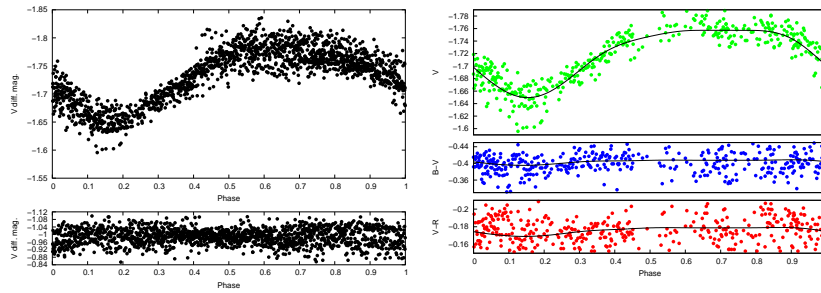
Figure 1: *(left) V light curve of the variable (upper panel) and the corresponding comparison-check data (lower panel); and example fit to the data observed between 53576 HJD - 53582 HJD (right).*

3   Modelling

For starspot modelling we used the SpotModeL program (Ribárik et al., 2003). Table 2. shows the fixed parameters and the starting values of the free parameters. As unspotted brightness, in lack of long-term data, the maximum measured values were used. We supposed three circular spots for the light curve solutions. One spot was fixed on the pole of the star on the basis of Doppler Imaging results (Barnes et al., 2004). The other two spots were fixed at $+10^o$ latitude to ensure, that spots do not overlap each other during the modelling. The spot coordinates and temperatures were simultaneously fitted in two different bandpasses (B,V and V,R). Figure 1 (right panel) shows the result of such a fit.

Table 2: *Starting values of spot parameters.*

	1. spot	2. spot	3. spot
α	30° free	130° free	360° fix
β	10° fix	10° fix	90° fix
γ	20° free	20° free	20° free

Table 3: *Wavelength dependent fixed parameters.*

	B band	V band	R band
Limb darkening (van Hamme, 1993)	0.906	0.763	0.658
Unspotted brightness (mag)	−2.255	−1.840	−1.655

Table 4: *Fixed parameters of LO Peg.*

T_{eff} (K)	4750 ± 250	(Pandey et al., 2005)
log g	4.5 ± 0.5	(Pandey et al., 2005)
Axial inclination (deg)	45.0 ± 2.5	(Barnes et al., 2004)
P (d)	0.423229 ± 0.000048	(Barnes et al., 2004)
Epocha (HJD)	2 453 540	

4   Results

The folded light curves for the data observed between 53545 and 53576 shows, that the maxima are at phases 0.6 and 0.8. Comparing this to the phased light curve obtained between 53582.5 and 53585 it is well seen (Figure 2), that the spot maxima are shifted to phases 0.4 and 0.6 while the light curve minima did not change much. This indicates, that the spots/spot groups moved or the sizes of spots/spot groups decreased and other spots/spot groups increased or emerged.

Figure 3, left panel, shows the results of spot temperature variations. At the beginning of the observations, higher brightness and hotter spot temperature is found, which indicates more hotter plages and less dark spots. The spot temperature relaxed to a constant value by the end of the measurements. The average spot temperature is about 3960 K, which is 790 K cooler than the effective temperature of the star. From the B−V and V−R color indicies the values of the derived spot temperatures agree within the errorbars except two points.

Figure 3, right panel, shows the variation of spot's sizes and the spot coverage. Spot 1 and spot 3 showed stable spot sizes, while spot 2 showed a significant decrease.

Figure 4 displays the time behaviour of the spot's longitudes. Slow migration is observed in the longitude positions of the two low-latitude spots as 0.96±0.26 ^{o}/days and 1.74±0.49 ^{o}/days. The calculeted migration periods are about 374 days and 205 days for the two spots. This indicates the presence of differential rotation and that the spots are at different latitudes.
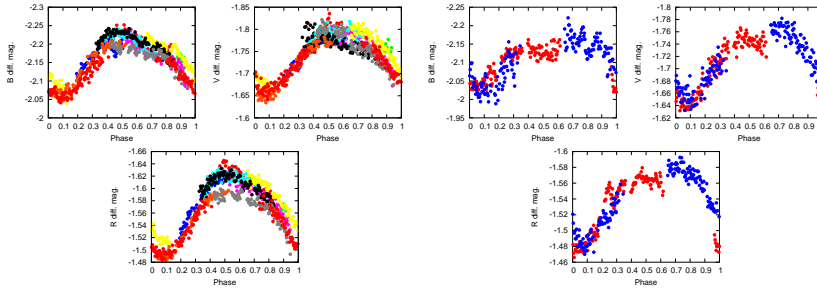
Figure 2: *Light curves observed between 53545 HJD - 53576 HJD (left) and 53582.5 HJD - 53585 HJD (right) of LO Peg. Different colors mark observations obtained on different nights.*
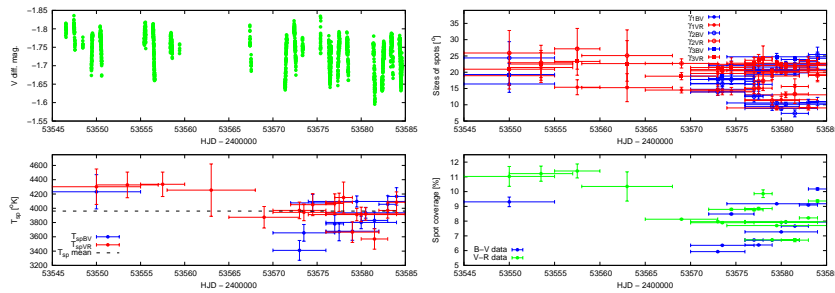
Figure 3: *V observations and variations of spot the temperature (left) and variation of spot sizes and spot coverage (right). Vertical bars give the errors of the results, horizontal bars show the time intervals of the observations that were used together for the modelled, folded light curves.*
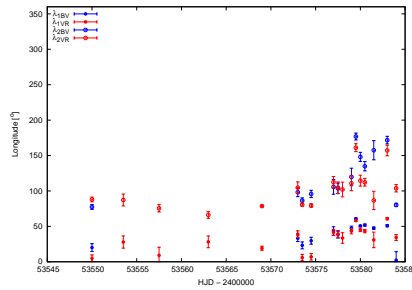
Figure 4: *Time behavior of spot's longitudes.*

Acknowledgement

References

Barnes J.R., Collier Cameron A., Lister T.A., Pointer G.R. and Still M.D., 2004, MNRAS, 356, 1501

Granzer T., Schüssler M., Caligari P., Strassmeier K. G., 2000, A&A, 355, 1087

Henden, A. ftp://ftp.nofs.navy.mil/pub/outgoing/aah/sequence/efpeg.dat

Jeffries R.D., Jewell S.J., 1993, MNRAS, 264, 106

Jeffries R.D., Byrne P.B., Doyle J.G., Anders G.J., James D.J., Lanzafame A.C., 1994, MNRAS, 270, 153

Landolt, A.U. 1992, AJ, 104, 340

Malina R.F. et al., 1994, AJ, 107, 751

Pandey, J.C., Singh, K.P., Drake, S. A., Sagar, R. 2005, AJ, 130, 1231

Ribárik, G, Oláh, K., Strassmeier, K. G., 2003, Astronomische Nachrichten, 324,202

Schüssler M., Caligari P., Ferriz-Mas A., Solanki S.K., Stix M., 1996, A&A, 314, 503

van Hamme, W. 1993, AJ, 106, 2096

STELLA Robotic Observatory for Stellar Activity Research

J. Bartus[1], Zs. Kővári[2], K. Oláh[2], T. Granzer[1], K.G. Strassmeier[1], M. Weber[1]

[1] Astrophysical Institute Potsdam, An der Sternwarte 16, D-14482 Potsdam, Germany
[2] Konkoly Observatory, Box 67, H-1525 Budapest, Hungary

E-mail: [1]jbartus@aip.de, [2]kovari@konkoly.hu, [2]olah@konkoly.hu, [1]tgranzer@aip.de, [1]kstrassmeier@aip.de, [1]mweber@aip.de

Abstract
The STELLA Robotic Observatory (abbreviation for STELLar Activity) is a long-term project for observing and monitoring activity tracers on cool stars with two robotic telescopes: STELLA-I equipped with a high resolution echelle spectrograph, a large-format CCD imager and photometer, and STELLA-II also equipped with an optical CCD imager and photometer. After listing the most important technical details we focus on some of the scientific programs planned for routine observations of active stars by STELLA.
Keywords: *Stars: imaging - Stars: activity - Starspots - Instrumentation: spectrographs - Instrumentation: photometers*

1   What makes STELLA robotic?

Automated photoelectric telescopes (APTs) have been widely used in observational astronomy for decades. However, when optimizing the scientific output the automation must not stop at a level, where a single observation is performed by the robotic telescope. The STELLA Robotic Observatory is a long-term project of the Astrophysical Institute Potsdam (AIP) in collaboration with the Instituto de Astrofísica de Canarias (IAC) located at the Teide Observatory

in Tenerife, Spain, at 2400 m above sea-level, (in the longitude of 16^h 30^m 35^s west and in the latitude of $28°$ 18^m 00^s north). Its main scientific objective is the spectroscopic and photometric monitoring of activity tracers on cool stars. STELLA is organized to operate fully automatically, i.e., not only the two telescopes are automatic but also the entire observatory, no human presence is needed for observing - not even in remote control.

STELLA is controlled by the STELLA Control System (SCS). Its duty is the delivery of commands in a correct timing sequence to all other subsystems. SCS is fed by numerous sensors and cameras throughout the building, watching the status of the scientific instruments and their auxiliary equipment, as well as the current environmental conditions, local climate, humidity, cloud positions and other secondary systems like air conditioner.
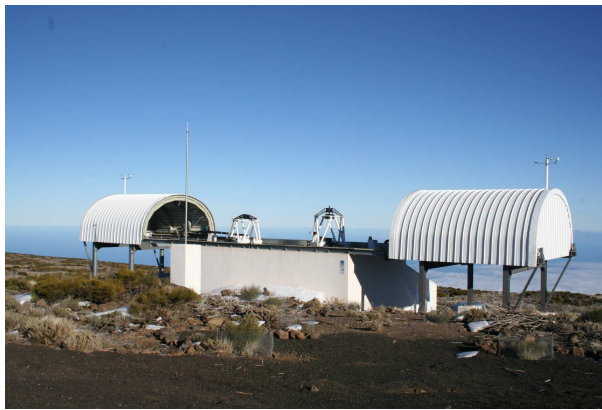
Figure 1: *The view of the STELLA building in Jan 2006. The building itself is automatic, the two roof halves are opened in the evening as ordered by SCS after evaluating the data of the two weather stations.*

2   The telescopes

The STELLA Robotic Observatory consists of two fully automated telescopes. STELLA-I is a 1.2 m diameter f/8 Cassegrain system with a Zeiss Zerodur mirror, an Alt/Az mount, and two Nasmyth foci. The telescope fiberfeeds an echelle spectrograph (SES) and hosts a wide field optical CCD imager and photometer (Wide Field STELLA Imaging Photometer-WIFSIP). The spectrograph has a

fixed format to cover the wavelength range 380-860 nm in a single exposure. The 2-pixel resolution is 50,000 with a 50-micron fiber attached to a high-curvature microlens. A pair of 100-micron fibers for resolutions of approximately 25,000 will be available initially. The detector is a 2k×2k back-illuminated thinned CCD with 13.5μm pixels. The STELLA echelle spectrograph (SES) has seen first calibration light from Aldebaran on June 28, 2005.

STELLA-II is also a 1.2 m telescope, f/10, Alt/Az mount, Newton focus, also hosts an optical CCD imager and photometer (WIFSIP-II) and an adaptive optics testbed. WIFSIP-II is based on a large format CCD (22'×22') at a scale of 0.32"/pixel. The detector is a single 4096x4096 back-illuminated thinned CCD with 15μm pixels. Available filters are Strömgren *uvby*, narrow and wide H_α and H_β, Johnson-Bessell *UBVRI* and the Sloan-filterset.

3   Target selection strategy: dispatch-scheduling

STELLA schedules observing targets according to astronomical conditions, weather and other constraints like the scientific needs of the different science programs. The scheduling schema is the so called dispatch-scheduling, i.e., at any given time all targets are queried for their actual merit and the target with the highest merit is selected.
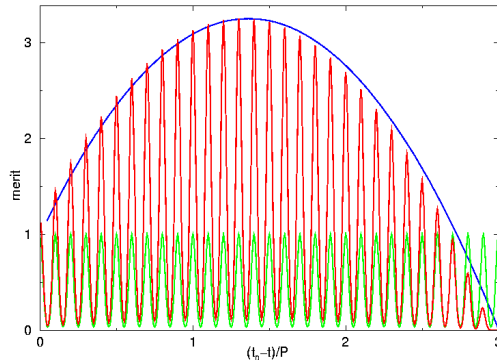
Figure 2: *Target specific merit for Doppler-imaging: taking spectra near peak values of evenly spaced selection windows ensures good phase coverage while the modulator Gaussian keeps observations within a reasonable duration (e.g., in a few rotation periods).*

The merit function $m(t)$ of a certain target is built from two different parts, a slowly varying "time-slot" $s(t)$ and a possibly fast changing "gain" $g(t)$:

$$m(t) = \prod_j s_j(t) \cdot \sum_i g_i(t) \tag{1}$$

Gains are used e.g., to reflect priority of a target, to force observation at culmination (airmass gain) to minimize the telescope slew-time between targets (slew-time gain), to incorporate user fairness (user-gain), to reflect time remaining to observe a given target (window gain), etc. On the other hand, time-slots are used to pick up a target e.g., at regular intervals or only at a certain time, or (not) after/before a certain time, etc. As an example a possible combination of time-slots is shown in Fig. 2.

4   Scientific objectives

In this section we show two examples of studying stellar activity on a shorter and on a longer term. In such studies, in the nearest future, a great help could come from STELLA when performing routine photometric and spectroscopic observations for a large sample of active stars.

4.1   Measuring differential rotation from time-series Doppler images

The surface differential rotation, one key ingredient of dynamo theory, can be measured by tracing spot positions. Doppler imaging technique uses the rotation-induced Doppler-broadening of spectral lines to compute the surface distribution of the temperature. To obtain the surface image of a star, high-resolution spectroscopic observations, evenly distributed over one stellar rotation period, are needed. This turns out to be quite complicated for long period stars. STELLA addresses this problem with a dedicated scheduling routine, which is tailored for Doppler imaging targets. This will make observations for Doppler imaging not only easier, but also more efficient. As a preview of what can be done with STELLA, we present preliminary results of a Doppler imaging study for the giant component of the long period RS CVn star ζ Andromedae.

In our example we use a total of 54 Ca I 6439-Å spectra covering ≈ 3.8 rotations, collected at NSO between Nov/96-Jan/97. From the spectra we built 36 data subsets with 17 spectra in each in the way, that the first subset consists of the first 17 observations, the next subset is formed from omitting the

first spectrum and adding the subsequent one to the end, etc., until the last 17 spectra are included. For each subset Doppler image reconstruction technique is performed using our image reconstruction code `TempMap`$_\epsilon$ originally written by Rice et al. (1989). The result is a time series of altogether 36 Doppler-maps. Then the consecutive but contiguous maps are cross-correlated and the resulting correlation maps are averaged. For the details of this method see Kővári et al. (2004). The resulting ccf map is shown in Fig. 3, where the best fit continuous line represents a weak solar-type differential rotation. The resulting differential rotation parameter $\Delta\Omega/\Omega_{\mathrm{eq}}$ of 0.061 ± 0.026 is about one-third of the solar value.
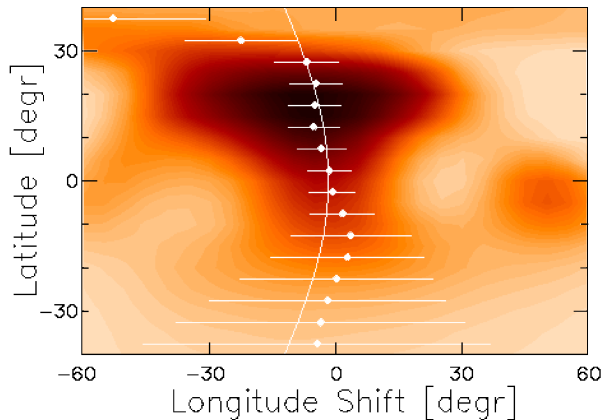
Figure 3: *Average cross-correlation map from the time-series Doppler maps, where the better the correlation, the darker the shade. For each latitude strip the maximum correlation is represented by the Gaussian peaks (dots) and the corresponding FWHMs (bars). The solid line is the best-fit solar-type differential rotation law.*

4.2 Activity cycles from long-term photometric monitoring

Since long-term photometric variations of active stars are known to be governed by changing their overall spot coverage, long-term monitoring can help us in extending our input knowledge for dynamo theory. The relation between activity cycle lenghts and rotational rates can be measured by long-term monitoring of different types of active stars (Oláh et al., 2000; Oláh & Strassmeier, 2002).

An example is given in Fig. 4, showing 23-year long photometric dataset of the single, rapidly rotating solar-like star LQ Hya. Data were collected between 1982-2005 mostly by the Vienna automated photoelectric telescopes, Wolfgang and Amadeus (`www.aip.de/groups/activity/APT/`). The existence of cycles in the stellar brightness in the order of several years is evident, in a good agreement with the cycle period derived from dynamo modelling of this star by Kitchatinov et al. (2000). Photometry, on the other hand, has limited information content: e.g., no butterfly diagram can be constructed from the data in lack of latitude information. On the other hand, simultaneous use of long-term photometry with time-series spectra from the automatic spectroscopic telescope STELLA-I would help in constructing butterfly diagrams for stars, too.
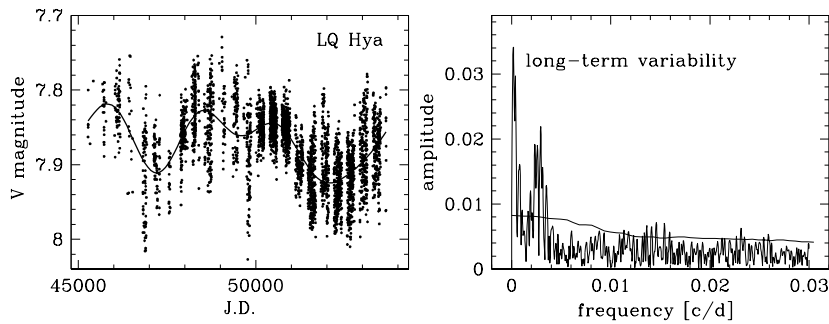
Figure 4: *Long-term monitoring of LQ Hya. Left: 23-year long photometric data fitted with two long-term cycle periods, right: the respective amplitude spectrum.*

Acknowledgement

References

Oláh, K., Kolláth, Z., Strassmeier, K. G. 2000, A&A 356, 643

Oláh, K., Strassmeier, K. G. 2002, AN 323, 3/4, 361

Kitchatinov, L. L., Jardine, M., Donati, J.-F. 2000, MNRAS318, 1171

Kővári, Zs., Strassmeier, K. G., Granzer, T., Weber, M., Oláh, K., Rice, J. B. 2004, A&A 417, 1047

Rice, J. B., Wehlau, W. H., Khokhlova, V. L. 1989, A&A 208, 179

PADEU

Indirect evidence for short period magnetic cycles in overcontact binary stars

T. Borkovits[1], Sz. Csizmadia[2], J. Nuspl[2], I.B. Bíró[1]

[1] Baja Astronomical Observatory of Bács-Kiskun County, H-6500 Baja, Szegedi út, Kt. 766, Hungary

[2] Konkoly Observatory of HAS, H-1525 Budapest, Pf. 67, Hungary

E-mail: [1]`[borko;barna]@alcyone.bajaobs.hu`, [2]`[csizmadia;nuspl]@konkoly.hu`

Abstract
Complex period variations of five W UMa type binaries (AB And, OO Aql, DK Cyg, V566 Oph, U Peg) were investigated by the analysis of their O–C diagrams, and several common features were found. Four of the five systems show secular period variations at a constant rate in the order of $|\dot{P}_{\mathrm{sec}}/P| \sim 10^{-7}$ y^{-1}. In the case of AB And, OO Aql and U Peg a high-amplitude, nearly one-century long quasi-sinusoidal pattern was also found. It might be explained as light-time effect, or by some magnetic phenomena. The most interesting feature of the studied O–C diagrams is a low amplitude ($\sim 2 - 4 \times 10^{-3}$ d) modulation with a period around 18–20 yr in four of the five cases. This phenomenon might be an indirect evidence of some magnetic cycle in late-type overcontact binaries as an analog to the observed activity cycles in RS CVn systems.
Keywords: *binaries: close, binaries: eclipsing, stars: activity*

1 Introduction

The moments of minima are one of the most fundamental observables of eclipsing binary systems and, due to their relatively easy measurement, a huge pile of data of this type was collected by observers during the last century. However, so far

there is no a commonly accepted and straightforward interpretation of the O–C diagrams constructed from them.

These observed variations can be classified into two subsets: (i) in the first part are the apparent period variations due to light-time effect (LITE) caused by a distant third or further body, or apsidal motion in eccentric systems, and (ii) the second part comprises the inherent physical period variations.

The latter may also be of various types, e. g. caused by the evolution of the system, mechanical and/or thermodynamical effects, or due to variable magnetic activity. Of course, a mixture of the different sources can be active at the same time, generating a very complex variation of the orbital period.

With respect to the involved time scales we can distinguish the long-term variations (on a nuclear or thermal time scale) from the short-term variations characterised by a decade long cycle length. In our recent study we are focusing onto the short–term orbital period variations of several W UMa systems, because the real O–C observations can reveal these effects only, while the long–term ones require a different (statistical) approach.

2 General remarks on the analysis

We concentrated mainly on systems whose observations cover more than half, or even a complete century. As in several cases the earlier observations are photographic or more frequently less accurate patrol measurements or visual observations, they were taken into account as well (at least at the first step of our analysis), but with different weights. We used four different weights: 1: visually observed minima; 2: plate minima; 5: photographic normal minima; and 10: photoelectric observations (both photomultiplier tube and CCD). The data series were analysed in a similar manner was described e.g. in Borkovits et al. (2002), i. e. after the calculation of the O–C curve with a preliminary linear ephemeris, the final representation of the O–C was searched for by a weighted linear least-squares fit in the form:

$$f = c_0 + c_1 E + c_2 E^2 + \sum_{i,j} a_{ij} \sin j\nu_i E + b_{ij} \cos j\nu_i E, \tag{1}$$

where $0 \leq i \leq 5$, $1 \leq j \leq 4$. The frequencies ν_i were kept fixed during the individual LSQ runs but an interval of frequencies was scanned and the best parameter set was selected according to the smallest χ^2 test. Then the astrophysical parameters were calculated from the corresponding coefficients of the equation above by the use of well-known physical relations.

Table 1: *Main parameters of the investigated stars. (The spectral types are taken from SIMBAD.)*

Name	Sp	P	T	M_1	M_2	R_1	R_2	T_1	T_2	A	refs
		d		$M_\odot$	$M_\odot$	$R_\odot$	$R_\odot$	K	K	$R_\odot$	
AB And	$G5V^a$	0.33	W	0.60	1.04	0.78	1.03	5450	5798	2.37	1
OO Aql	$G5V$	0.51	A	1.04	0.88	1.39	1.29	5700	5560	3.33	2
DK Cyg	$A6V$	0.47	A	1.74	0.53	1.71	0.99	7351	7200	3.34	1
V566 Oph	$F4V$	0.41	A	1.56	0.41	1.51	0.86	6700	6618	2.91	3
U Peg	$G2V$	0.37	W	1.15	0.38	1.22	0.74	5860	5785	2.52	4

1: Baran et al. (2004); 2: Hrivnak (1989); 3: Niarchos et al. (1993); 4: Pribulla & Vaňko (2002)

a: More recently Pych et al. (2004) found a mean spectral type of G8V

3 Discussion

The five investigated systems are distributed in the range of effective temperatures from $T_{\mathrm{eff}} = 7400$ down to $T_{\mathrm{eff}} = 5400$, which is the transition region where a convection zone develops in the envelope of the stars toward the lower temperatures. The most important parameters are listed in Table 1. The analysis of the O–C diagrams of the systems has revealed in four cases different periodic variations beside the secular development of the orbital period.

3.1 Secular period changes

Four of the five O–C curves show evidence of continuous orbital period change with a constant rate during the total observing interval. The only exception was OO Aql, although it is possible that in this system only one (or two) abrupt period jump(s) obscure this behaviour.

The most usual explanation of this kind of secular period variation is mass exchange in the system. The widely used approximating formulae for the calculation of the mass exchange rate is as follows:

$$\dot{m} = -m_{12}\frac{q}{1-q^2}\frac{\dot{P}}{3P} \approx -m_{12}\frac{q}{1-q^2}\frac{2}{3}\frac{c_2}{c_1^2}, \tag{2}$$

Table 2: *Derived parameters from the period variations*

Name	$\dot{P}_{\mathrm{sec}}/P$	$|\dot{m}|$	P_{mod}	A_{mod}
	$\times 10^{-7}$ (y^{-1})	$\times 10^{-7}$ (M$_\odot$ y^{-1})	(d)	(d)
AB And	2.65	1.25	6 695	0.0020
OO Aql	−	−	7 467	0.0036
DK Cyg	1.93	0.49	−	−
V566 Oph	6.76	1.25	7 250	0.0035
U Peg	−1.88	0.36	6 544	0.0016

where c_1, c_2 directly come from the O–C ephemerides in the form of Eq. (1). Note that the equation requires constancy of the total mass, as well as of the total angular momentum. The rate of the secular period change, as well as the calculated mass exchange rate are tabulated in Table 2.

Nevertheless, it is necessary to note that in the case of AB And and U Peg the coefficients of the quadratic terms, and the period and amplitude of the longer period quasi-sinusoidal period variations are not independent from each other as we will see later.

3.2   Longer period cyclic variations

In three cases (AB And, OO Aql, U Peg) the simultaneous fitting gave longer as well as shorter period cycles. These longer scale variations are roughly 62, 75 and 85 years long, respectively, and naturally might be identified as a LITE, i. e. effect due to the presence of a third body. The corresponding LITE solution parameters are listed in Borkovits et al. (2005). However, we have to note that e. g. in the case of OO Aql the calculated minimal mass of the tertiary component seems to be unrealistically large. Hence, the identification of these periods as LITE solution can be considered only as a simple designation and their real origin should require yet a careful analysis in all cases. It should also be emphasised that these periods are in the same order as the total interval of the observations and the separation of the different effects in the analysis are doubtful.

3.3 Shorter period cyclic variations - manifestation of magnetic activity cycles?

It is an interesting fact that four of our five systems show small amplitude cyclic fluctuations with very similar periods (see Cols. 4-5 in Table 2). The only exception is DK Cyg, the hottest in the sample, with A8 spectral-type components, whilst the other four are later than F0 down to G5 in the case of AB And.

These modulation periods range from $6\,500$ to $7\,500$ days (18–20 years) that are quite similar to those one observed in other types of stars showing magnetic activity. The startling resemblance of orbital period variations in these more or less similar systems suggests some parallelism in their origin and makes likely some common physical explanations. According to our opinion this feature might be an indirect evidence of similar magnetic cycles in the investigated binaries and the detected variations might caused by it. We mainly refer to Lanza & Rodonó (1999) who found a relation between the orbital period of a binary system and the magnetic activity cycle assuming synchronisation between the orbital motion and rotation of the member stars:

$$\log P_{\mathrm{mod}} \ [\mathrm{yr}] = 0.018 - 0.36(\pm 0.10) \log \frac{2\pi}{P_{\mathrm{orb}}} [\mathrm{sec}]. \tag{3}$$

For the binaries studied here, this formula predicts $P_{\mathrm{mod}} \approx 7\,900,\, 9\,200,\, 8\,500,$ and $8\,200$ days, respectively. (Note that these values are very close to the length of the Sun's magnetic cycle). These values are in the same order of magnitude as the observed ones. This supports our conjecture that magnetic activity cycles are able to explain the observed short term orbital period variations.

From the period of the modulation (P_{mod}) and the amplitude of the O–C ($A_{\mathrm{O-C}}$) the rate of the period variation can be expressed easily. Using this the variation of the gravitational quadrupole momentum is (Applegate, 1992):

$$\Delta Q = -\frac{2\pi}{9} M R^2 \left(R/a \right)^{-2} \frac{A_{\mathrm{O-C}}}{P_{\mathrm{mod}}} \tag{4}$$

where M is the mass of the active star, R is the radius of the active star and $a = 2A$, the separation between the components. (A is the semi-major axis and note that in contact binaries the orbit is circular.) A calculation with the parameters of the primary and the secondary (see Table 1) gives $\Delta Q_1 = 4.02 \times 10^{42} \mathrm{kgm}^2$, and $\Delta Q_2 = 6.97 \times 10^{42} \mathrm{kgm}^2$, respectively. These values correspond to the typical values in active binary stars (Lanza & Rodonó, 1999). Due to the similar

absolute dimensions of the other investigated binaries, the same calculations give physically realistic results for them as well.

As it was mentioned already, the spectral type of the systems showing short period variations in the O–C diagrams is later than F0, while the earlier type DK Cyg does not show this feature. This type of behaviour is pretty similar to the observed one among the Algol-type RS CVn systems (see Hall, 1989) that the magnetic activity can be observed only in systems later than F5, as the magnetic dynamo theories are based on a strong connection with the presence of a convection zone in the outer envelope predicting magnetic activity for them. Since the convection zones in the envelope appear in lower mass MS and cooler stars, this type of relation is a trivial requirement but, of course, the strict border lines can be different. Although our sample is not a systematic one, however, it indicates the existence of a separation border somewhere around the spectral type F0.

Acknowledgement

References

Applegate, J.H., 1992, ApJ, 385, 621

Baran, A, Zola, S, Rucinski, S.M. et al., 2004, AcA, 54, 195

Borkovits, T., Csizmadia, Sz., Hegedüs, T. et al., 2002, A&A, 392, 895

Borkovits, T., Elkhateeb, M.M., Csizmadia, Sz. et al., 2005, A&A, 441, 1087

Hall, D.S., 1989, Space Sci. Rev., 50, 219

Hrivnak, B.J., 1989, ApJ, 340, 458

Lanza, A. F., & Rodonó, M., 1999, A&A, 349, 887

Niarchos, P.G., Rovithis-Livaniou, H., & Rovithis, P., 1993, Ap&SS, 203, 197

Pribulla, T., & Vaňko, M., 2002, Contrib. Astron. Obs. Skalnaté Pleso, 32, 79

Pych, W., Rucinski, S.M., DeBond, H., et al., 2004, AJ, 127, 1712

The long term behaviour of RR Gem

Ádám Sódor[1]

[1] Konkoly Observatory of HAS, H-1525 Budapest, Pf. 67, Hungary

E-mail: [1]`sodor@konkoly.hu`

Abstract

The photometric observations of RR Gem obtained at the Konkoly Observatory during the last 70 years have been analysed in search of the signs of Blazhko modulation. The analysis showed that RR Gem was modulated nearly all the time with the same 7.21 d period as nowadays. The amplitude of the modulation varied inversely with the variation of the pulsation period.

Keywords: *Stars: individual: RR Gem, Stars: variables: RR Lyr*

1 Introduction

The phenomenon of the periodic light curve variation of some fraction of the RR Lyrae stars is known for about a century. Blazhko (1907) and Shapley (1916) discovered that RW Dra and RR Lyr showed periodic oscillation in the phase and height of light maxima on a timescale of tens of days. Nowadays the light curve modulation of RR Lyrae stars is called Blazhko effect.

There are signs suggesting that the Blazhko modulation changes in time. For example the most extensively studied Blazhko star, RR Lyr itself, changes the modulation amplitude with about a 4 year long period (Detre & Szeidl, 1973). Unfortunately, there are only a few Blazhko stars for which long term photometry are available. RR Gem is one of these stars. At the Konkoly Observatory RR Gem has been observed more or less continuously since 1935. The most accurate photometric technique of the time was always applied. Between 1935 and 1953 photographic, from 1954 to 1983 photoelectric, and in 2004 and 2005 CCD observations were made.

Considering its modulation properties, RR Gem is a peculiar Blazhko star. Detre (1970) found that it showed Blazhko modulation with a period of 37 days in the 1930s from photographic observations. The modulation had, however, disappeared for the 40s. Based on CCD observations Jurcsik et al. (2005) have found recently that the true modulation period of RR Gem is 7.2 d. This was the shortest Blazhko period known and the 0.1 mag B band amplitude of the modulation was also the lowest observed. On the ground of these surprising results it seemed worthwhile to reinvestigate the long term behaviour of the modulation of RR Gem, i.e., to reanalyse the photographic and photoelectric data collected at the Konkoly Observatory with the help of new computer aided techniques.

2 The data

In this paper we report the results of the analysis of the photographic, photo-electric and CCD light curves obtained at the Konkoly Observatory in the last 70 years. We also used about 300 published times of maxima from different authors collected in the GEOS[1] database.

The photographic observations. More than 1000 exposures were taken on more than 100 photographic plates. Unfortunately, many of the plates have been damaged or disappeared. We could measure 671 data points from 37 nights, 20 of them covered phases around light maximum.

The photoelectric observations were obtained and reduced by Béla Szeidl. No filter was used before 1958. At that time the new photometer was in test phase and due to the different settings these observations were too inhomogeneous to study the low amplitude Blazhko modulation. More than 1000 data points covering 31 maxima were obtained in B and V colours on 41 nights after 1958.

The CCD observations were obtained with a Wright CCD camera attached to the refurbished and automated 60 cm Heyde telescope of the Konkoly Observatory, Budapest. We obtained more than 3200 frames in each passbands of the $BV(RI)_c$ filters. Altogether 32 light maxima were observed on 63 nights. The analysis of the CCD light curve from 2004 has been already published (Jurcsik et al., 2005). In 2005 we continued the observations to refine the pulsation and modulation periods.

---

[1]Groupe Europen d'Observation Stellaire
http://webast.ast.obs-mip.fr/people/leborgne/dbRR/

3   The $O - C$ diagram

The variation of the pulsation period during the last 115 years is presented on the $O - C$ diagram shown in Fig. 1. We determined the maximum times for the observations by polynomial fit to the data points around the maxima. These fits also yielded the magnitudes of maximum brightnesses. We corrected some mistyped GEOS data according to the original publications and left out a few outlying points where no cause of the deviation was found. We have also found additional published maximum times from two authors (Waterfield, 1927; Graff, 1906). The $O - C$ diagram shown in the top panel of Fig. 1 was constructed using the following ephemeris:

$$t_{\max} = 2412077.521\,[\text{HJD}] + 0.397291066 \cdot E.$$

This period is the average pulsation period of RR Gem over the last 115 years.

The diagram shows many changes in the pulsation period, among them the most abrupt and the most remarkable happened just at the middle of the Konkoly photographic observations, around 1938. This section of the $O - C$ is enlarged in the lower left panel of Fig. 1. During the photoelectric observations a slow and nearly constant period decrease occurred. This linear period change is demonstrated in the lower right panel of Fig. 1. The fitted parabolic curve is also drawn. To plot this diagram we used a different ephemeris:

$$t_{\max} = 2435062.216\,[\text{HJD}] + 0.3973106 \cdot E.$$
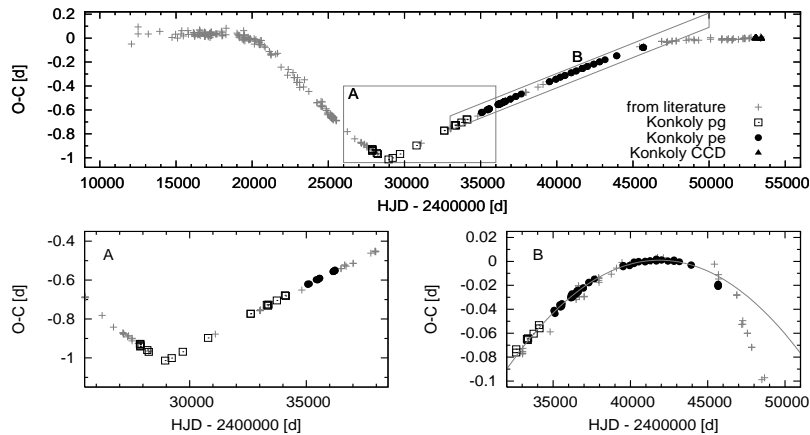
Figure 1: *The $O - C$ diagram of RR Gem for the last 115 years.*

4   Light curve analysis

4.1   The CCD light curve

A detailed study of the CCD photometry from the 2004 season has been published by Jurcsik et al. (2005). We give here the refined parameters of the modulation and the pulsation based on the light curve from 2004 and 2005.

The pulsation period was determined from nonlinear Fourier fit of the light curve with 15 harmonics. The yielded period is $P_{\mathrm{puls}} = 0.39728930 \pm 2.4 \cdot 10^{-7}$ d.

After the removal of the pulsation frequencies the prewhitened Fourier spectra showed the modulation peaks clearly, symmetrically around the pulsation frequencies (see Fig. 2 in Jurcsik et al. (2005)). The frequency separation of the modulation and pulsation peaks corresponds to a modulation period of $P_{\mathrm{Bl}} = 7.216$ d.

As the modulation of the maximum light is nearly sinusoidal, the amplitude and period of the maximum light modulation can be determined from a simple sine fit to the maximum points. Data folded with the modulation period and the fit are shown in Fig. 2. The maximum magnitude modulation in B band has an amplitude of $A_{\mathrm{m}} = 0.114 \pm 0.004$ mag, with a period of $P_{\mathrm{Bl}} = 7.214 \pm 0.0025$ d.

We derived the following normal maxima times for the two observing seasons:

$$t_{\mathrm{max}}^{(2004)} = 2453063.6492 \pm 0.0007 \,\mathrm{HJD}, \qquad t_{\mathrm{max}}^{(2005)} = 2453424.4003 \pm 0.0016 \,\mathrm{HJD}.$$
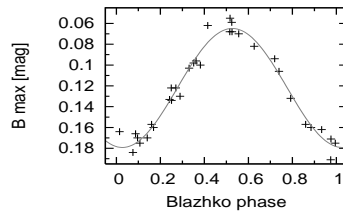
Figure 2: *The maximum magnitudes of the CCD B observations folded with the 7.214 d modulation period.*

4.2   The photoelectric light curve

Due to the period change and the uneven data distribution of the photoelectric observations we analysed only the data of the first 3 seasons in search for the signs of modulation. About the half of the observations were obtained during this time, which covered 15 light maxima. In the next 18 years altogether 16

maxima were only observed. The effect of period change was negligible in the first 3 years of the photoelectric observations. The B and V observations were made simultaneously, however, we analysed only the B light curve as its S/N ratio was better.

The observations were made only around rising branch and maximum brightness what makes Fourier analysis difficult. To stabilize the Fourier fit and to reduce the $\pm f_p$ aliases in the amplitude spectrum we inserted 2 synthetic descending branches based on the CCD B mean light curve. The analysis of the CCD light curve which showed that the modulation practically has no effect on the descending branch (see Fig. 9 in Jurcsik et al. (2005)) validates this procedure.

As the modulation peaks in the Fourier spectra of the light curves of Blazhko stars follow the same pattern around the harmonics of the pulsation frequency, the S/N ratio can be improved if we sum up the appropriate sections of the spectrum around the harmonics of the pulsation frequencies. The formula to calculate this *aggregated spectrum*, $A'(f)$ for n harmonics is:

$$A'(f) = \sum_{i=1}^{n} A(f + i \cdot f_{\mathrm{p}}), \text{ where } -\Delta f > f > \Delta f, \ \Delta f > f_{\mathrm{mod}},$$

f_{p} is the pulsation frequency, $A(f)$ is the original amplitude spectrum and the examined range extends to $2 \cdot \Delta f$ symmetrically around the pulsation peaks.

The Fourier analysis of the photoelectric B light curve and of the B maximum points showed that RR Gem was modulated at this time also, but the modulation was even weaker than today.

4.3 The photographic light curve

The available photographic plates were digitized and aperture photometry was applied. To construct the density–magnitude curves for every exposure we used the Johnson B magnitudes of 16 comparison stars measured with the Wright CCD camera on the 60 cm telescope. As the sensitivity range of the photographic emulsion is near to the B band this way we transformed the photographic measurements to B magnitudes.

Due to the abrupt period change during the time of the photographic observations the photographic light curve had to be divided into two parts before the analysis.

We had 8 light maxima from the first 2 seasons and 12 maxima from the next 15 years. The modulation was detected in the first part of the data in

spite of the large uncertainty of the photographic observations. Its amplitude was much larger than today, 0.25 mag in the B passband while the modulation period was the same as today. On the other hand no sign of the modulation was found in the second part of the data. As the observations at this period were very sparse and the period of the modulation was very short it does not mean that RR Gem was not modulated then. We estimate the upper limit of the modulation amplitude to be 0.06 mag in B band from the scatter of the maximum points of this dataset.

5   Discussion

The analysis of the light curves from the last 70 years showed that RR Gem was modulated nearly all the time. When modulation was detected, its period was always the same as recently, 7.21 d. The amplitude of the modulation, however, changed significantly from the undetectable level to 0.25 mag amplitude in the maximum brightness in the B passband. The modulation amplitude changed in reverse to the pulsation period.

Acknowledgement

References

Blazhko, S. 1907, Astron. Nachr., 173, 325

Detre, L. 1970, Transactions of the IAU XIV A, Rep. Astron., 259

Detre, L. & Szeidl, B. 1973, in IAU Coll. 21, Variable Stars in Globular Clusters and Related Systems, ed. J. D. Fernie (Dordrecht: Reidel), 31

Graff, K. 1906, AN, 173, 55

Jurcsik, J., Sódor, Á., Váradi, M., Szeidl, B., Washüettl, A., Weber, M., Dékány, I., Hurta, Zs., Lakatos, B., Posztobányi, K., Szing, A., Vida, K. 2005, A&A, 430, 1049

Shapley, H. 1916, ApJ, 43, 217

Waterfield, R. L. 1927, Bulletin of the Harvard College Observatory, 848, 25

Metallicity dependence of some parameters of Cepheids

P. Klagyivik[1], L. Szabados[2]

[1] Eötvös University, Department of Astronomy, H-1518 Budapest, Pf. 32, Hungary
[2] Konkoly Observatory of HAS, H-1525 Budapest, Pf. 67, Hungary

E-mail: [1]P.Klagyivik@astro.elte.hu, [2]szabados@konkoly.hu

Abstract
Dependence of phenomenological properties of Cepheids on the heavy element abundance is studied. It is found that the amplitude of the pulsation depends on the metallicity of the stellar atmosphere.
Keywords: *Cepheid variable, pulsation, metallicity*

1   Introduction

Metallicity has a very important role in Cepheids. Nowadays its influence on the PLC relation is a frequently discussed topic of research papers. But we only know little or nothing about other effects of metallicity. Kovács and Zsoldos (1995) and Jurcsik and Kovács (1996) worked out a method to determine the value of $[Fe/H]$ from the shape of the light curves of RR Lyrae stars. Zsoldos (1995) tested this method for Cepheids too, and found a similar relation.

An extensive project has been initiated for studying the effect of heavy element abundance of Cepheids on various pulsational properties of these radially oscillating stars. Here we present the first results on the metallicity dependence of the photometric and radial velocity amplitudes.

2 Data collection

We collected the periods, the amplitudes of the light curves in different colours, radial velocity curves and metallicity of galactic Cepheids. Thanks to the recently aroused great interest there are about 150 Cepheids in our galaxy with known $[Fe/H]$ value. The periods were taken from the DDO Database (Fernie et al., 1995), the amplitudes from three catalogues (Fernie et al. (1995), Szabados (1997), Berdnikov et al. (2000)) and the metallicities from the following publications: Eggen (1985), Giridhar (1986), Fry and Carney (1997) , Groenewegen et al. (2004), Andrievsky et al. (2002a, 2002b, 2002c) , Andrievsky et al. (2004, 2005), Luck et al. (2003), Kovtyukh et al. (2005).

In some cases the amplitudes of the light curves had quite different values as determined by different authors. Thus we omitted the stars, if the differences were larger than 0.1 mag. For stars having several published metallicity values, we averaged these data.

3 Metallicity dependence

3.1 Photometric amplitude – [Fe/H]

First we studied the period–amplitude diagram. Kraft (1960) explored first this relation and he determined an upper envelope to the points on the $\log P$ – ΔB and $\log P$ – ΔV diagrams. Eichendorf and Reinhardt (1977) derived a method for constructing envelopes to point diagrams and calculated an upper envelope for ΔB. Their sample contained 255 galactic Cepheids.

Because more comprehensive catalogues have been published since then, we could repeat this study by fitting two parabolae (Fig. 1). These curves fitted better the dip near $\log P = 1$ than polynomials. The equations of the parabolae are given in Eq.(1) and (2). There are three stars (FF Aur, AC Cam, SU Sct) that lie far above the envelope. It is possible, that they are not classical Cepheids.

$$A_B = 1.41 - 5.5 \times (\log P - 0.73)^2 \qquad \log P < 1 \qquad (1)$$

$$A_B = 2.15 - 10.0 \times (\log P - 1.3)^2 \qquad \log P > 1 \qquad (2)$$

We investigated the metallicity dependence of the deviation of the amplitudes from the estimated maximum amplitude ($\Delta B_{max} - \Delta B_*$) for the given period. If a star has a companion, its light variation decreases because of the
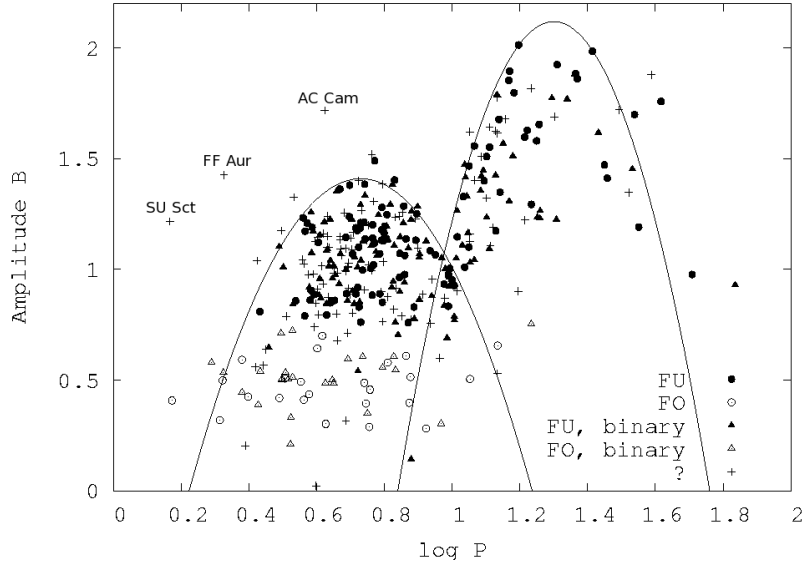
Figure 1: *Upper envelope for ΔB. The two curves are the fitted parabolas. FU: fundamental mode, FO: first overtone, ?: we have no information about pulsation mode. The three stars marked with their names may not be classical Cepheids.*

smaller variation of the intensity ratios. First overtone pulsators also have lower amplitudes. If only the solitary Cepheids (at least those without any known companion), pulsating in the fundamental mode are plotted, there is a definite trend (Figure 2). In the case of higher metallicity the amplitude decreases compared to the upper envelope (i.e. the maximum possible value). The equation of the straight line fit is given in Eq.(3) where DEV is the deviation from the upper envelope.

$$[Fe/H] = -0.09(\pm 0.03) + 0.27(\pm 0.10) \times DEV \qquad (3)$$
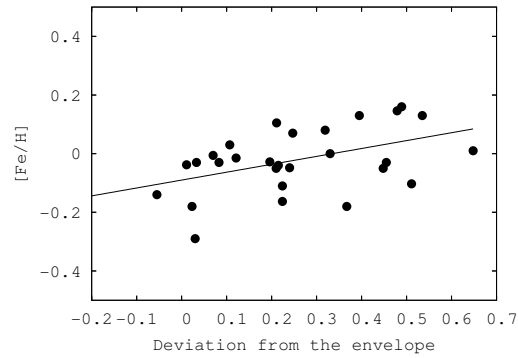
Figure 2: *Deviation from the envelope for solitary, fundamental mode Cepheids.*

3.2   Amplitude ratio − [Fe/H]

We defined the amplitude ratio as the ratio of the radial velocity and the B band photometric amplitude ($AR = \Delta V_{rad}/\Delta B$). The relation between metallicity and AR and the linear fit is presented in Figure 3 and Eq.(4). The fit applies only to the solitary and fundamental mode Cepheids, but all the other groups show similar relation.
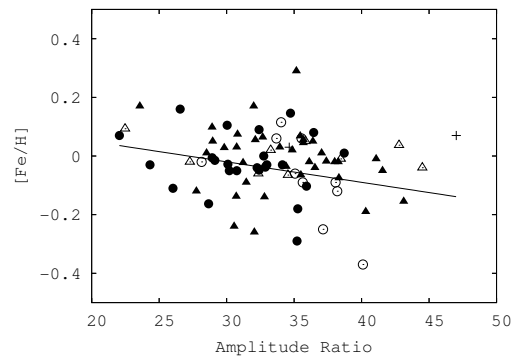
Figure 3: *Metallicity dependence of the amplitude ratio. Symbols are the same as in Fig. 1.*

$$[Fe/H] = 0.19(\pm 0.10) - 0.007(\pm 0.003) \times AR \tag{4}$$

3.3 Slope parameter – [Fe/H]

If we plot the amplitude of the light variations in different colors compared to the amplitude measured in B band vs. $(1/\lambda)$, the distribution of the points will be roughly linear (Fernie, 1979). Szabados (1997) defined the slope parameter as the slope of the straight line fitted to these points.
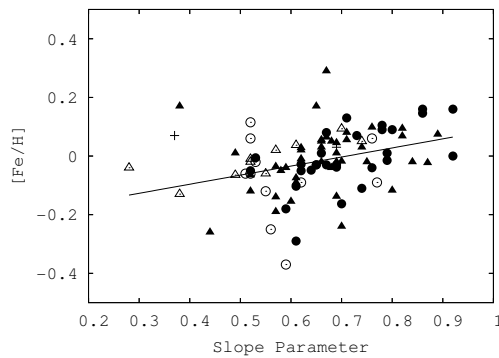
Figure 4: *Metallicity dependence of the slope parameter. Symbols are the same as before.*

Fig. 4 shows the relation between metallicity and the slope parameter. It is visible that the metallicity affects the slope of the line. The higher the [Fe/H] the larger the slope parameter, i.e. the amplitude decreases quicker with the increase of the wavelength. Probably this is due to the change (of the strength) of the mechanisms that govern the pulsation. The result of the linear fit is given in Eq.(5).

$$[Fe/H] = -0.22(\pm 0.06) + 0.31(\pm 0.10) \times SP \tag{5}$$

where SP is the slope parameter. The fit applies only to the solitary and fundamental mode Cepheids again, but all the other groups show similar behaviour and the differences are not significant.

4   Summary

We analysed the metallicity dependence of three parameters related to the light variation and radial velocity amplitudes of galactic Cepheids. We showed that all these parameters (deviation from the upper envelope on the $\log P$–ΔB diagram, amplitude ratio and slope parameter) show a definite relation with $[Fe/H]$. These are not exactly defined relations, rather tendencies (note that the errors of $[Fe/H]$ are generally $0.05 - 0.10$). A deeper analysis of metallicity dependence on pulsation properties of Cepheids is in progress.

Acknowledgement

References

Andrievsky, S. M., Kovtyukh, V. V., Luck, R. E., et al. 2002a, A&A, 381, 32

Andrievsky, S. M., Bersier, D., Kovtyukh, V. V., et al. 2002b, A&A, 384, 140

Andrievsky, S. M., Kovtyukh, V. V., Luck, R. E., et al. 2002c, A&A, 392, 491

Andrievsky, S. M., Luck, R. E., Martin, P., et al. 2004, A&A, 413, 159

Andrievsky, S. M., Luck, R. E., and Kovtyukh, V. V. 2005, AJ, 130, 1880

Berdnikov, L. N., Dambis, A. K., and Vozyakova, O. V. 2000, A&AS 143, 211

Eggen, O. J. 1985, AJ, 90, 1278

Eichendorf, M., and Reinhardt, M. 1977, A&A, 61, 827

Fernie, J. D. 1979, PASP, 91, 67

Fernie, J. D., Beattie, B., Evans, N. R., and Seager, S. 1995, IBVS 4148

Fry, A. M., and Carney, B. W. 1997 AJ, 113, 1073

Giridhar, S. 1986, JApA, 7, 83

Groenewegen, M. A. T., Romaniello, M., Primas, F., et al. 2004, A&A, 420, 655

Jurcsik, J., and Kovács, G. 1996, A&A, 312, 111

Kovács, G., and Zsoldos, E. 1995, A&A, 293, 55L

Kovtyukh, V. V., Andrievsky, S. M., Belik, S. I., et al. 2005, AJ, 129, 433

Kraft, R. P. 1960, ApJ, 132, 404

Luck, R. E., Gieren, W. P., Andrievsky, S. M., et al. 2003, A&A, 401, 939

Szabados, L. 1997, DSc Thesis

Zsoldos, E. 1995, ASPC, 83, 351

A survey of variable stars in the globular cluster NGC 362

P. Székely[1], R. Jackson[2], L. L. Kiss[1,2], K. Szatmáry[1]

[1] University of Szeged, Department of Experimental Physics and Astronomical Observatory, H-6720 Szeged, Dóm tér 9., Hungary
[2] University of Sydney, School of Physics, NSW 2006, Australia

E-mail: [1]`pierre@physx.u-szeged.hu`

Abstract
We present the first results of our survey in NGC 362 globular cluster. We found numerous variable stars in the field: 38 RR Lyr stars, 5 eclipsing binaries and 13 other pulsating stars. Five RR Lyrae stars can be member of the halo/SMC population.
Keywords: *Stars: variables: general - Stars: variables: RR Lyr - globular clusters: individual: NGC 362*

1 Introduction

Although globular clusters are primary testbeds of modern astrophysics due to large number of stars with the same age and composition, there are still a number of unstudied clusters, mostly in the southern hemisphere. We have been carrying out a CCD photometric survey project of southern globular clusters since mid-2003. Here we present the first (and still preliminary) results for NGC 362, which is one of the brightest unstudied southern clusters, located in front of the outer edge of the Small Magellanic Cloud.

2 Observations and data analysis

Our V-filtered photometric observations were carried out between July 2003 and October 2004 on 17 nights at Siding Spring Observatory, Australia. We used the 1m ANU telescope equipped with the Wide Field Imager; three chips of the WFI gave $\sim 40' \times 26'$ field of view. In addition to the photometry, we measured radial velocities for the brightest RR Lyrae stars from medium-resolution spectra, taken with the 2.3m ANU telescope. All data were processed with standard IRAF routines, including bias and flat-field corrections. Instrumental magnitudes were obtained via a semi-automatic pipeline using daophot tasks for PSF photometry. Another method of data reduction was applying image substraction using ISIS 2.1 package (Alard, 2000).

After a careful selection of ensemble comparison stars, variables were identified with visual inspection of the resulting light curves. Periods were determined with a combination of Fourier analysis, phase dispersion minimization (Stellingwerf, 1978) and string-length minimization (Lafler & Kinman, 1965).

3 Variable stars

Our results regarding variable stars can be summarized as follows.

- From the ensemble photometry of over 10,000 stars, we found 38 RR Lyr variables in the cluster, of which 31 are new discoveries.

- We found 8 long period (>1 d) RR Lyr-like variables, which are either candidate above-horizontal-branch stars (AHB stars, Diethelm (1990)) or short-period Type II Cepheids.

- We also discovered several short-period eclipsing binaries, most likely in the galactic foreground of the cluster.

- A number of stars on the red giant branch showed evidence for variability on a time-scale of 10-50 days, suggesting the presence of RGB pulsations predicted by Kiss & Bedding (2003).

- We have tried to find faint RR Lyr stars in the halo of the SMC, but the results so far are not fully conclusive.

3.1   Regular RR Lyr stars

We identified 33 RRab/RRc variable stars with very similar mean apparent brightnesses, so that they are all members of the cluster. The measured radial velocities for 5 RR Lyr stars supported this conclusion for having the same ∼200 km/s mean velocity as the cluster itself (Fischer, 1993). The two light curves below show the light curve shape changes with the increasing period. Current data include some of the non-photometric nights, which is why there is increased scatter in the light curves.
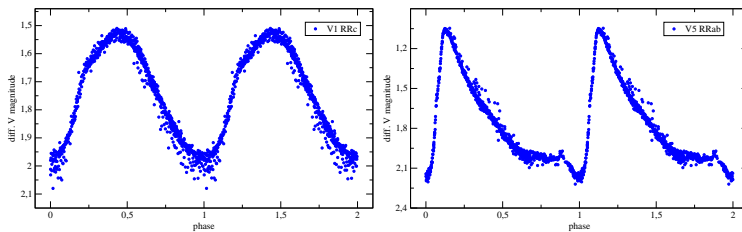
Figure 1: *Light curves of regular RR Lyr stars. Left: V1, P=0.342d. Right: V5, P=0.528d.*

3.2   Blazhko RR Lyr stars

A large fraction of RR Lyr stars show periodic amplitude and/or phase modulations, the so-called Blazhko-effect, which is still one of the greatest mysteries in classical pulsating stars, e.g. Chadid et al. (2004). In our sample, two variables, V6 and V18, have the strongest light curve modulations, while further five stars (V9, V12, V13, V19 and V31) exhibited only subtle changes during the 15 months of observations. The phase diagrams of V6 and V18 can be seen in Fig. 2.

3.3   Other short-period variable stars

We found, of course, a large number of variable stars belonging to other classes. Interestingly, we also identified a few RR Lyr stars that are several magnitudes fainter than those in the cluster. We suspect these to belong to the outer halo of the Small Magellanic Cloud; a more secure membership investigation is in progress. It is worth mentioning that some of the field variable stars (V4, V7, V21, V26, V29) have particularly RR Lyr-like light curve shape but with periods
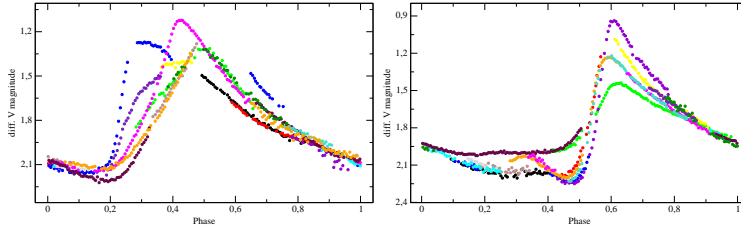
Figure 2: *RR Lyr stars with Blazhko-effect. Left: Phase diagram of V6. Right: Phase diagram of V18.*

greater than 1 day; one of them (V7) has almost 4 days period. Depending on their position in the colour-magnitude diagram, these stars can be either above-horizontal-branch (AHB) variables (Diethelm, 1990) or Type II Cepheid. V21 showed a peculiar bump on the descending branch of the light curve. Its origin is not clear yet.

4   Other results

In order to determine the metallicities and from those parameters the absolute magnitudes of some of the RR Lyr stars we applied the equations Nr. 3 of Jurcsik & Kovács (1996), $[Fe/H] = -5.038 - 5.394P + 1.345\phi_{31}$ and Nr. 5 of Kovács & Jurcsik (1996), $M_V = 0.19[Fe/H] + 1.04$, respectively. The results of the calculations can be seen in Tab. 1.

The colour-magnitude diagrams shown in Fig. 3 are produced with rejecting the stars which positions fall off from a given radii fixed on the center of NGC 362, $\alpha_{2000.0} = 1^h3^m14^s.3$, $\delta_{2000.0} = -70^o50'54''$ (Dorman et al., 1997). The applied radii are $3'$, $5'$, $10'$ and $30'$, respectively. The CMDs show increasing field contamination, a noticeable feature is a somewhat dimmer secondary RGB of the Small Magellanic Cloud (SMC) which is in the line of sight of NGC 362. The presence of stars from the SMC contaminates the CMDs which involve greater number of stars (N) so we used the second diagram (N=4060) in order to determine the properties of NGC 362.

To determine the distance modulus, age, metallicity and reddening of the cluster we fitted the VI Padova isochrones (Girardi et al., 2000). To fit the isochrones we have attempted to match the slope of the RGB to fit metallicity, fit the RGB tip for distance, the SGB for age and the position of the base of
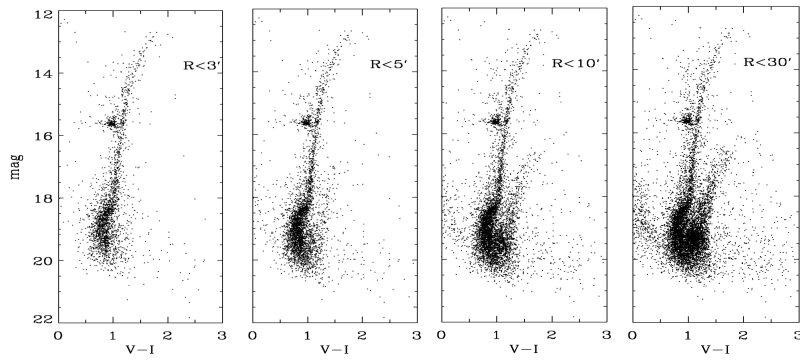
Figure 3: *CMDs of the central regions with different radii.*

the RGB for reddening. As the best fit we found the 8.9 Gyr isochrone with metallicity $Z = 0.001$ and it gives an apparent distance modulus of $\mu = 15.2 \pm 0.4$ and $E(V - I) = 0.19$. The next best fit is also shown in the left side panel of Fig. 4 which gives the same metallicity, distance and reddening but an age of 10 Gyr. The right side panel of Fig. 4 shows a surface density profile of the cluster. This diagram clearly shows a very high density of stars in the centre of the cluster. This plot however, does not show any evidence for the existence of tidal tails caused by the cluster's motion around the galaxy.
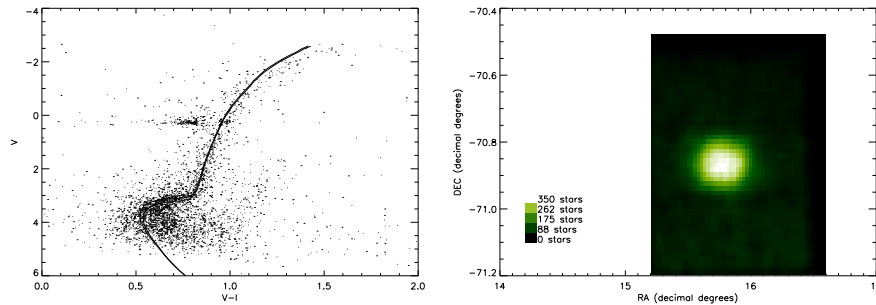
Figure 4: *Left: Isochrone fitting. Right: Surface densities of NGC 362*

Table 1: *Metallicities of the RR Lyrae Stars.* [†] *Blazhko effect present.* [*] *Outliers?*

Star	Period	ϕ_{31}	$[Fe/H]$	M_V	Distance(pc)
V1	0.3425	4.1616	−1.28	0.79	8354
V3	0.4901	4.6615	−1.44	0.77	7820
V5	0.5286	4.9274	−1.26	0.80	7946
V8	0.3333	3.8357	−1.67	0.72	7890
V9	0.5851	5.3094	−1.05	0.84	9238
V11	0.5146	5.1881	−0.83	0.88	10601
V12[†]	0.4202	4.4477	−1.32	0.78	9312
V16	0.5098	4.6814	−1.49	0.75	6526
V31[*]	0.4708	4.6953	−1.26	0.79	29308
V32[*]	0.5757	4.1546	−2.55	0.55	24271
V34	0.6271	5.6164	−0.86	0.87	8078
Average	0.4907	4.6981	−1.37	0.78	8418

Acknowledgement

References

Alard, C., 2000, A&AS, 144, 363

Chadid, M. et al., 2004, A&A, 413, 1087

Diethelm, R., 1990, A&A, 239, 186

Dorman, B. et al., 1997, ApJ, 480, 31

Fischer, P. et al., 1993, AJ, 106, 1508

Girardi, L. et al., 2000, A&AS, 141, 371

Jurcsik, J., Kovács, G., 1996, A&A, 312, 111

Kovács, G., Jurcsik, J., 1996, ApJ, 466, 17

Kiss, L.L., Bedding, T.R., 2003, MNRAS, 343, L79

Lafler, J., Kinman, T. D., 1965, ApJS, 11, 216

Stellingwerf, R. F., 1978, ApJ, 224, 953

PADEU

AN ASTEROID MODEL OF THE MID- AND FAR-INFRARED SKY

Cs. Kiss[1], A. Pál[2], Th. Müller[3], P. Ábrahám[1]

[1]Konkoly Observatory, PO Box 67, H-1525 Budapest, Hungary
[2]Eötvös University, Department of Astronomy, H-1518 Budapest, Pf. 32, Hungary
[3]Max-Planck-Institut für extraterrestrische Physik, Giessenbachstrasse, D-85748 Garching, Germany

E-mail: `pkisscs@konkoly.hu`

Abstract
We developed a statistical model for the asteroid component of the far-infrared sky for wavelengths $5\,\mu\mathrm{m} \leq \lambda \leq 1000\,\mu\mathrm{m}$ based on the Statistical Asteroid Model (Tedesco et al., 2005). Far-infrared fluxes of ∼1.9 million asteroids are used to calculate confusion noise values and expected asteroid counts for space IR instruments in operation or in the near future. Our results show that the confusion noise due to asteroids will not increase the detection threshold for most of the sky. However, there are specific areas near the ecliptic plane where the effect of asteroids can be comparable to the contribution of Galactic cirrus emission and of the extragalactic background.
Keywords: *Infrared: Solar System, Asteroids*

1 Introduction

Currently, 329 777 minor planets are known[1] (as of March 16, 2006) in our Solar System, of which about 99% are located in the main belt. On the plane of the sky the vast majority of main-belt asteroids (MBA) are found at ecliptic latitudes beween ±20°. Their sizes range from a few ten meters up to about 1000 km. With temperatures between 200 and 300 K, the asteroids emit predominantly at thermal wavelengths between $5\,\mu$m and the millimetre range.

---

[1]http://cfa-www.harvard.edu/iau/lists/ArchiveStatistics.html

Deep infrared observations close to the ecliptic will therefore always include some of these moving targets (e.g. Tedesco & Désert 2002; Meadows et al. 2004). Such observations also show that only a small fraction of the existing minor body population is currently known and that this population might cause a non-negligible confusion noise contribution at certain wavelengths for specific instruments.

Recently several authors calculated confusion noise and detection limits for current/future infrared (IR) space missions (Spitzer, Akari, Herschel and SPICA). These papers focus on the two major confusion noise components: the extragalactic background (e.g. Negrello et al., 2004), the Galactic cirrus emission (Kiss et al., 2005; Jeong et al., 2005), or the combination of the two (Jeong et al., 2006).

It is an important question whether faint asteroids, which are individually below the detection limits, could contribute significantly to the confusion noise of these instruments. In order to take into accound these asteroids, a reliable statistical model is needed, which also includes minor bodies smaller than a few kilometers in diameter. Recently, Tedesco et al. (2005) presented the "Statistical Asteroid Model" (hereafter SAM). This model is based on a population of $\sim 1.9 \times 10^6$ asteroids obtained from the complete known asteroid sample (as of 1999), plus extrapolation of the size-frequency distribution (SFD) of 15 asteroid dynamical families and three background populations, to a diameter limit of 1 km. The main belt asteroid SFD can be described by a power law where the cumulative number of asteroids smaller than a given size $N(> D)$ is proportional to $D^{-\gamma}$. The SAM uses a value of $\gamma \simeq 2.8$ down to $D \approx 1$ km. The validity of the SAM was demonstrated by comparing SAM predictions with ISO measurements at $12\,\mu$m (Tedesco and Desert, 2002) and Spitzer measurements at the 8 and $24\,\mu$m bands (Meadows et al., 2004). Asteroid counts from both surveys show good agreement with the SAM predictions.

For our calculations we used the *Statistical Asteroid Module* file from the SAM database[2], containing orbital elements, absolute magnitudes (H_{mag}), diameters and albedos for 1 880 987 objects. The tabulated values form the basis to calculate i) the position of each asteroid in the sky for a given epoch ii) the brightness of each asteroid at any given wavelength. For practical purposes we limited the position calculations to the time period between July 1, 1999 and June 30th 2000, and the wavelength range from $5\,\mu$m (where the thermal emission starts to dominate the spectral energy distribution) to about 1 mm (to cover future far-IR/sub-mm space instruments).

---

[2]http://www.psi.edu/pds/SAM-I/

2   Data processing

POSITION CALCULATION: Orbital elements of all SAM asteroids, including real and artifical ones were calculated for different epochs between the time span July 1999 and June 2000 with the average step size of 5 days. This step size is sufficient for yielding a good solar elongation coverage during one year. The orbital elements were obtained using accurate numerical integrations including the effect of all inner and outer planets (except for Pluto). From the orbital parameters the apparent ecliptical coordinates, distances and magnitudes were derived using the spatial coordinates of the Earth itself and the absolute magnitudes (which are known from the SAM database). The difference between the spatial position of the barycenter of the Earth-Moon system and the prospective position of the satellites is negligable for the apparent distribution of the asteroids.

THERMAL BRIGHTNESS CALCULATION: For the brightness calculations we applied the Standard Thermal Model (STM; Lebofsky et al. 1986). This model uses the true observing geometry for a given epoch, based on the heliocentric and geocentric distances and the phase angle. The asteroids are described as smooth, spherical and non-rotating bodies in instantaneous equilibrium with the solar radiation, no heat conduction into the surface is considered. The correction for beaming, shape and conductivity effects is done via the η-parameter with a value of $\eta = 0.756$. Furthermore, the flux at non-zero solar phase angles is obtained by applying an empirical phase correction of $0.01\,\mathrm{mag/deg}$ to the flux calculated at opposition. The STM has clear limitations with respect to flux accuracy (e.g., Müller & Blommaert 2004) or for modelling of minor bodies outside the main-belt (e.g., Harris 1998), but highly accurate flux predictions are not mandatory for our project. The STM predictions fulfill our needs to estimate fluxes for all objects in the specified time period and wavelength range.

CONFUSION NOISE CALCULATION: A grid of $0.5' \times 0.5'$ cells was defined in the sky (in ecliptic coordinates). We determined the asteroid counts above specific flux limits for each cell, as well as the confusion noise due to asteroids in that particular cell. The confusion noise was calculated from the 'observed' distribution of all asteroids in that specific cell for each wavelength λ_i:

$$\sigma_a(\lambda_i)^2 = \left(\frac{\Omega_c}{\Omega_p}\right) \sum_j S_j^2(\lambda_i) \tag{1}$$

where Ω_c and Ω_p are the effective solid angle of the counting cell and the pixel of the observer instrument, respectively, and S_j is the observed flux of the asteroid

at λ_i. Note, that Ω_p is not necessarily the geometrical size of an instrument pixel but is modified by the properties of the optical system (like beam size). The sum runs over all asteroids in a counting cell.

These σ_a confusion noise values are *lower limits*, since there is an unknown contribtuion of small (fainter) asteroids, which is not considered here. However, bright asteroids are the dominant sources of confusion and asteroids smaller than $\sim 1\,\mathrm{km}$ in diameter would not contribute to the confusion noise significantly. We also note, that this confusion noise value is *per pixel* confusion noise. The confusion noise applicable for e.g. detection limits of point sources depends on the method used to extract/reconstruct the point source flux.

3   Results

Using these model calculations we have constructed all-sky confusion noise maps and calculated expected number counts for the sensitivity limits of several IR instruments. These results can be found under the URL: "*http://kisag.konkoly.hu/confnoise*".

Our general results are summarized as follows: (I) The main trend shows a strong concentration of asteroids and a corresponding peak of confusion noise at the local anti-solar point and an extended "cloud" is present around the current maximum (see the example in Fig. 1). Seasonal variations are also not negligible. (II) Survey instruments working in the mid-infrared domain (like Spitzer/MIPS at $24\,\mu\mathrm{m}$ and Akari/IRC) may be strongly affected by confusion noise in the vicinity of the ecliptic plane. Such surveys should have already detected many faint asteroids serendipitously. (III) For $3\,\mathrm{m}$-class IR telescopes, like Herschel or SPICA, asteroid confusion would not be negligible in anti-solar direction, however, solar aspect constraints for satellites usually do not allow to observe towards opposition targets.

4   Limitations of the model

The SAM is limited to asteroids with a lower limit in size of $\sim 1\,\mathrm{km}$ in diameter, but there is a population of asteroids with sizes below this limit. As can be verified with Eq. 1, the impact of very small bodies (a few hundred meters in diameter and below) is minor to the confusion noise.

In our model we considered only asteroid families covered in the SAM, i.e. most of our asteroids are MBAs, with typical temperatures in the order of
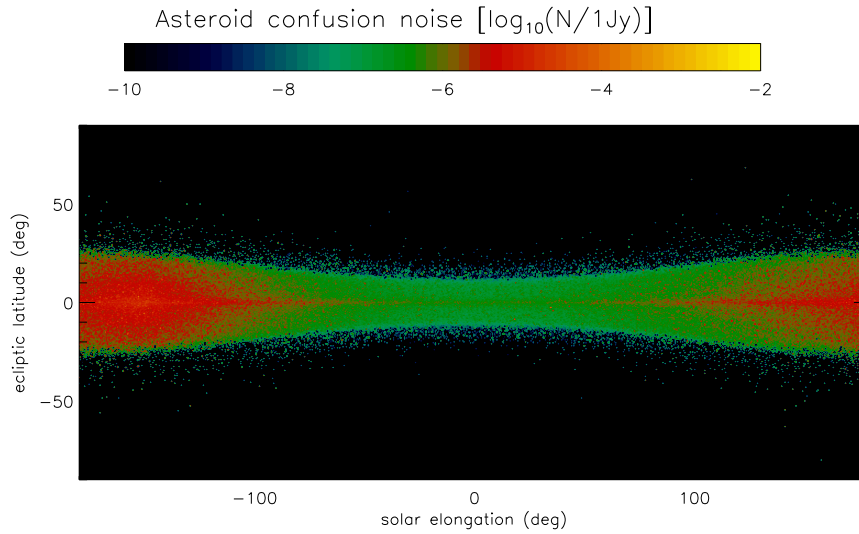
Figure 1: *Asteroid confusion noise (1σ per pixel) in the 18.3 μm (L18W) of the Akari/IRC instrument (former ASTRO-F). The Sun is located in the figure at (0,0) and the highest confusion noise can be seen in the anti-solar direction ($\lambda - \lambda_\odot = 180°$). The asteroid component dominates the confusion noise in the ecliptic plane at solar elongations $|\lambda - \lambda_\odot| \geq 30°$. Akari observations take place at $|\lambda - \lambda_\odot| = 90° \pm 1°$.*

few hundred Kelvin. With these temperatures, most of the heat is emitted at mid-IR wavelengths. Asteroids further out in the Solar System (e.g. in the Kuiper belt) have lower temperatures, therefore have their peak emission at far-IR wavelengths. However, due to geometry effects, the absolute flux drops quadratically with the distance from the observer. We demonstrate this effect in Fig. 2 where the spectral energy distribution of the same asteroid is plotted, if placed at different Earth/Sun distances in the Solar System.

The observed far-IR flux at longer wavelengths is decreasing rapidly despite the fact that the emission peaks shift to longer wavelengths as the target moves further from the Sun. E.g. at 70 μm 100 asteroids at 2 AU would produce roughly the same confusion contribution as 10^{10} (!) asteroids of similar size at 50 AU. Therefore an enormous population of relatively large bodies would be needed to have an effect comparable to that of main belt asteroids on the far-infrared confusion noise and expected counts of asteroids.
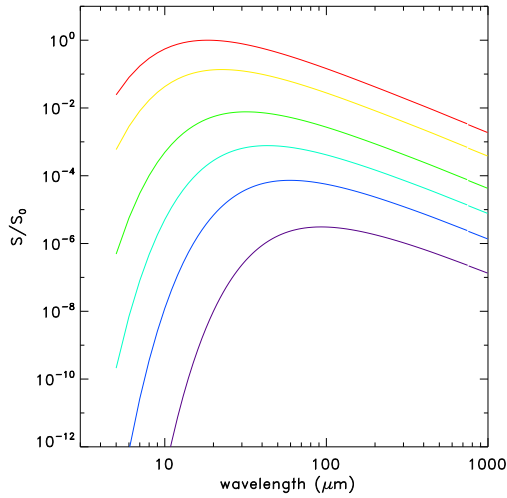
Figure 2: *Demonstration of the effect of the increasing Earth/Sun distance on the observed fluxes of the asteroids. S/S_0 is the ratio of measured S flux value at a specific wavelength and the reference flux value S_0 (the maximum value of the spectral energy distribution at $\Delta = 1\,AU$). The curves correspond to $\Delta = 1$, 2, 5, 10, 20 and 50 AU, from top to bottom, respectively and $r_\odot = \Delta + 1\,AU$ in all cases.*

Acknowledgement

References

Harris, A. W. 1998, Icarus 131, 291

Jeong, W.S., Lee, H.M., Pak, S., et al., 2005, MNRAS, 357, 535

Jeong, W.S., Pearson, C.P., Lee, H.M., Pak, S., Nakagawa, T., 2006, MNRAS, in press [astro-ph/0603163]

Kiss, Cs., Klaas, U., Lemke, D., 2005, A&A 430, 343

Lebofsky, L. A., Sykes, M. V., Tedesco, E. F. et al. 1986, Icarus 68, 239

Meadows, V.S., Bhattacharya, B., Reach, W.T. et al., 2004, ApJS 154, 469

Müller, T. G., Blommaert, J. A. D. L. 2004, A&A 418, 347

Negrello, M., Magliocchetti, M., Moscardini, L., 2004, MNRAS 352, 493

Tedesco, E.F., Désert, F.-X., 2002, AJ 123, 2070

Tedesco, E.F., Cellino, A.; Zappalá, V., 2005, AJ 129, 2869

PARSAMIAN 21: A FUOR SURROUNDED BY AN EDGE-ON DISC

Á. Kóspál[1], D. Apai[2,3], P. Ábrahám[1]

[1] Konkoly Observatory of the HAS, P.O.Box 67, H1525 Budapest, Hungary
[2] Steward Observatory, University of Arizona, 933 N. Cherry Avenue, Tucson, AZ 85721, USA
[3] NASA Astrobiology Institute

E-mail: [1]`kospal@konkoly.hu`

Abstract

FU Orionis objects (FUors) are young stars that have recently undergone major outbursts, probably powered by enhanced accretion from the circumstellar disc to the star. Parsamian 21 is a unique FUor, as it is thought to be surrounded by an edge-on circumstellar disc, making it an ideal case for studying the geometry and structure of the circumstellar material. In this paper we report on new adaptive optics assisted near-infrared direct and polarimetric measurements of Parsamian 21 taken with the NaCO instrument on the VLT. With the help of these observations, we search for companions and study the innermost part of the circumstellar disc with an unprecedented resolution and contrast.

Keywords: *stars: circumstellar matter, stars: individual: Parsamian 21*

1 Introduction

Parsamian 21 is a young star situated close to the Galactic plane, in the constellation Aquila. The star (also known as HBC 687) is located at the apex of a bright cometary nebula, which was first mentioned in the catalogue of Parsamian (1965). The estimated distance of the object is 400 pc (Neckel & Staude, 1984; Hillenbrand et al., 1992; Pezzuto et al., 1997). Taking into account that its radial velocity is $+27 \pm 15\,\mathrm{km\,s^{-1}}$ (Staude & Neckel, 1992), Parsamian 21 appears

to be related to "Cloud A", a molecular cloud in the Galactic plane (Henning et al., 1998).

Although no eruption has been observed, because of its spectral characteristics Parsamian 21 is thought to be an FU Orionis-type star (FUor) surrounded by a circumstellar disc (Staude & Neckel, 1992). Polarimetric observations by Draper et al. (1985) and Hajjar et al. (1997) also suggest that the star is surrounded by a flat, disc-like structure. Bastien & Ménard (1990) interpreted the polarization maps of Parsamian 21 in terms of multiple scattering in flattened, optically thick structures and derived an inclination angle of 80-85° and a size of 12 000 AU × 3200 AU. From 1.3 mm measurements Sandell & Weintraub (2001) derived a mass of $0.3\,M_\odot$ for the circumstellar material. Staude & Neckel (1992) identified bipolar Herbig-Haro outflows along the polar axis of the nebula.

In this paper we report on new near-infrared direct and polarimetric measurements of Parsamian 21 taken with the NaCO instrument on the VLT. Due to the combination of adaptive optics and the new technique of differential polarimetric imaging, these measurements allow us to investigate the size and geometry of the circumstellar material at small spatial scales ($\sim 30\,\mathrm{AU}$), as well as to search for close low-mass companions that are often suggested to be the outburst triggers for FUors.

2   Observations and data reduction

Table 1 lists the observations of Parsamian 21 used in this paper. We have obtained near-infrared imaging and polarimetric observations using the NaCO instrument on the UT4 of ESO's Very Large Telescope at Cerro Paranal, Chile, on 18 June 2004. NaCO consist of the NAOS adaptive optics system and the CONICA near-infrared camera. Direct imaging was obtained through H ($\lambda_c = 1.66\,\mu$m), K$_S$ ($\lambda_c = 2.18\,\mu$m) and L' ($\lambda_c = 3.8\,\mu$m) filters; Tab. 1 shows the pixel scales and exposure times used for each filter.

Polarimetric observations were obtained using the polarimetric differential imaging technique (DPI, Kuhn et al., 2001; Apai et al., 2004). The basic idea of this method is to take the difference of two orthogonally polarized, simultaneously acquired images of the same object in order to remove all non-polarized light. As the non-polarized light mainly comes from the central star, after subtraction only the polarized light, such as the scattered light from the circumstellar material remains. We obtained polarimetric images with NaCO through the H filter, using a Wollaston prism with a 2″ Wollaston mask. Parsamian 21 was observed at four different rotator angles of 0°, 45°, 90° and 135°. At each

Table 1: *Log of VLT/NaCO and HST/WFPC2 observations of Parsamian 21*

Instrum.	Filter	Mode	Pixel scale mas/pixel	Exp. Time	Sky mag/□″	Limiting mag
NaCO	H	Imag.	13	8×30 s	13.6	22.8
NaCO	K_S	Imag.	13	8×20 s	12.4	21.6
NaCO	L′	Imag.	27	48×0.2 s	2.7	15.2
NaCO	H	Pol.	27	72×10 s, 24×80 s		
WFPC2	F814W	Imag.	100	2×500 s		23.5

angle a 3-point dithering was applied.

In case of the VLT/NaCO images, data reduction was done with self-developed idl routines. Raw images were flat fielded using lamp-flats in case of H and Ks filters and sky-flats in case of L′ filter. Sky frames were calculated by taking the median of all images taken with the same filter, then images were sky-subtracted. Since a 4-point dithering was applied, individual frames were shifted and co-added to obtain a final mosaic. This resulted in an image of 21″4×21″4 in case of H and Ks filters, and 43″8×43″8 in L′. VLT/NaCO polarimetric measurements were reduced using a previously developed software which is described in detail in Apai et al. (2004).

In addition to the VLT/NaCO observations, there are archival HST/WFPC2 images on Parsamian 21. These images were obtained on 30 July 2001, with the broadband F814W filter ($\lambda_{\mathrm{pivot}} = 0.801\,\mu$m). High-Level Science Products based on these images can be downloaded from the HST Archive.

3 Results

3.1 Large-scale structure of the nebula

Figure 1 displays the central part of the VLT/NaCO and the HST/WFPC2 images. The appearance of the nebula can be understood in the following way: the star drives a bipolar outflow (Staude & Neckel, 1992), which had excavated a conical cavity in the dense circumstellar material. The star illuminates this cavity and the light is scattered towards us mainly from the walls of the cavity. Since the scattering is more efficient at shorter wavelengths, the nebula seems
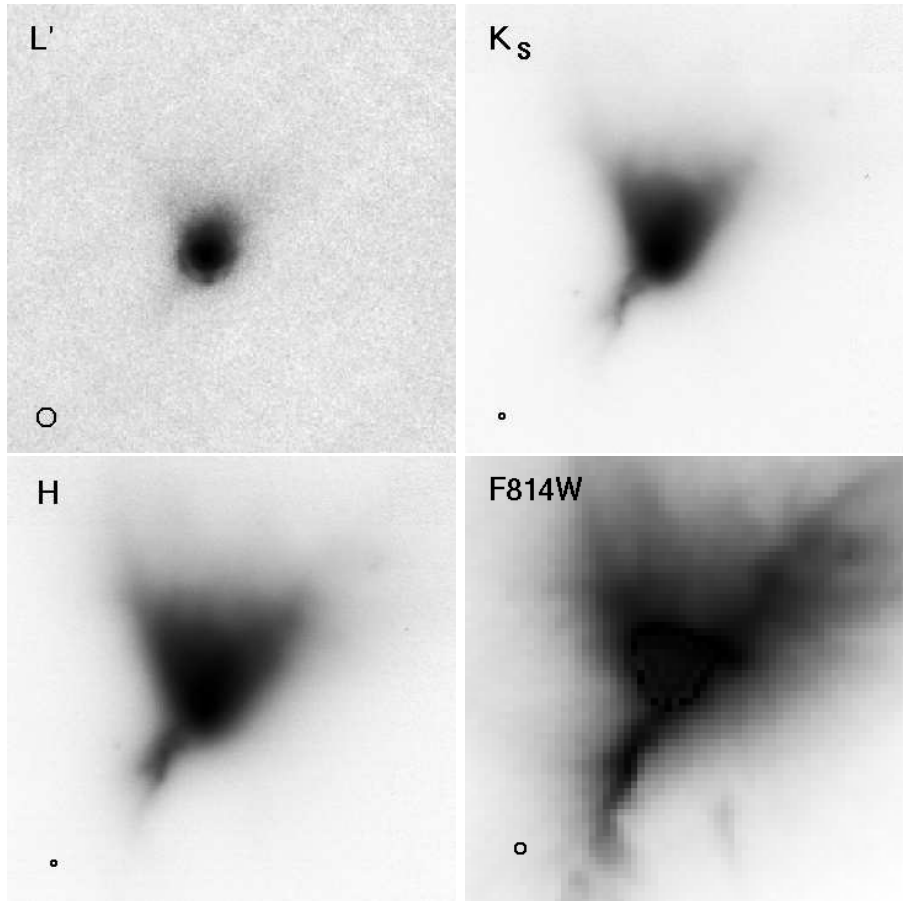
Figure 1: *VLT/NaCO (with filters and L′, K_S and H) and HST/WFPC2 (with filter F814W) images of Parsamian 21. Circles at the left bottom corners indicate the FWHM at the centre of the corresponding image. The displayed area is 6.″5 × 6.″5.*
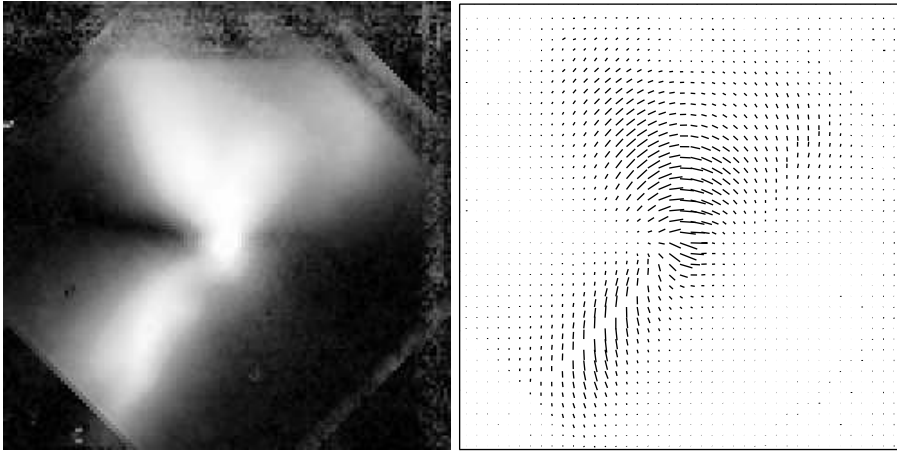
Figure 2: *Polarized intensity (left), and polarization map (vectors are displayed in arbitrary units) of Parsamian 21 (right). The displayed area is approximately* $3'' \times 3''$.

to be more extended at these wavelengths (see Fig. 1). It is worth to notice that the source is extended even in the L′-band. In the K_S and H bands, mainly the northern lobe of the reflection nebula can be seen, but at $0.814\,\mu$m the southern part is also visible, suggesting that it is rather a bipolar than a cometary nebula as stated previously.

3.2   Small-scale structure of the nebula

The spectral energy distribution (SED) of FUors are usually flat, which cannot be explained by a simple flat accretion disc model. Instead a flared disc and/or an extended envelope is necessary to reproduce the SED (Hartmann & Kenyon, 1996; Turner et al., 1997). This assumption, however, has never been observationally proven.

During the VLT/NaCO observations, we obtained H-band images of the scattering circumstellar material around Parsamian 21. Due to the DPI technique, unprecedented contrast and resolution could be achieved, enabling us to probe the disc structure closer to the star than any previous observation.

Fig. 2 displays the polarized intensity as well as the polarization map of the surroundings of Parsamian 21. On both panels of Fig. 2 a horizontal weakly polarized band can be seen across the star. This can be interpreted as the

signature of an edge-on disc, since the reduced polarization is due to multiple scattering in the optically thick disc (Draper et al., 1985). On the polarized intensity image, this band clearly has a flaring shape indicating a flared disc geometry. The disc can be followed as close as $0''\!.15$ (60 AU) to the star.

3.3 Possible companions

Close companions are often suggested as possible outburst triggers for FUors (eg. Hartmann & Kenyon, 1996). However, to date only a couple of FUors are proved binaries. The majority of FUors have not been studied with sufficiently high resolution and contrast to verify if all of them have companions.

We have searched for possible companions in all four direct images. In order to establish a detection limit for source detection, we measured the sky brightness on the VLT/NaCO images (before sky-subtraction), and estimated a limiting magnitude for each filter. The resulting values can be seen in the last two columns of Tab. 1. In case of the HST/WFPC2 image, the larger $(75'' \times 75'')$ field of view made it possible to estimate a limiting magnitude using star counts. Due to the bright reflection nebula, the detection limit is somewhat less sensitive close to the star.

The two closest objects we found are the following: one star to the east, at a distance of $1''\!.4$ (560 AU at 400 pc), which has an $H - K = 1.2 \pm 0.2$ mag; and another one to the northwest, at a distance of $3''\!.3$ (1320 AU at 400 pc), which has an $H - K = 1.1 \pm 0.1$ mag. Neither of these stars are visible at 3.8 or 0.801 μm. As they are very red, they can equally be heavily reddened field stars, or stars with infrared excess (indicating that they might be associated with Parsamian 21). Further multifilter observations may help to clarify the nature of these objects.

4   Summary

In this paper we report on new adaptive optics assisted near-infrared measurements of Parsamian 21, an FU Orionis-type young star in Aquila. We present VLT/NaCO L$'$, K$_S$ and H images, as well as archival HST/WFPC2 F814W images, and we discuss the morphology of the reflection nebula around the star. We have also obtained H-band polarimetric images of Parsamian 21 using the differential polarimetric imaging technique. Polarization measurements indicate that the circumstellar disc around the star is seen edge-on, shows a flaring shape, and can be discerned even as close as 60 AU to the star. The high resolution

observations presented here will allow for the first time the characterisation of the geometry of an FU Orionis-type disc on a $\sim 30\,$AU spatial scale providing a direct observational test to the accretion disc models.

Acknowledgement

References

Apai, D., Pascucci, I., Brandner, W., et al. 2004, A&A, 415, 671

Bastien, P., Ménard, F. 1990, ApJ, 364, 232

Draper, P.W., Warren-Smith, R.F., Scarrott, S.M. 1985, MNRAS, 212, 1P

Hajjar, R., Bastien, P, Nadeau, D. 1997, CFHT Information Bulletin, Number 37

Hartmann, L., Kenyon, S.J. 1996, ARA&A, 34, 207

Henning, Th., Burkert, A., Launhardt, R., Leinert, Ch., Stecklum, B. 1998, A&A, 336, 565

Hillenbrand, L.A., Strom, S.E., Vrba, F.J., Keene, J. 1992, ApJ, 397, 613

Kuhn, J.R., Potter, D., Parise, B. 2001, ApJ, 553, L189

Neckel, T., Staude, H.J. 1984, A&A, 131, 200

Parsamian, E. 1965, Izv. Akad. Nauk Armyan. SSR., Ser., 18, 146

Pezzuto, S., Strafella, F., Lorenzetti, D. 1997, ApJ, 485, 290

Sandell, G., Weintraub, D.A. 2001, ApJ, 134, 115

Staude, H.J., Neckel, T. 1992, ApJ, 400, 556

Turner, N. J. J., Bodenheimer, P., Bell, K. R. 1997, ApJ, 480, 754

Celestial positions in radio and optical

S. Frey[1], P. Veres[2], K. Vida[2]

[1] FÖMI Satellite Geodetic Observatory, P.O. Box 585, H-1592 Budapest, Hungary
[2] Eötvös University, Department of Astronomy, P.O. Box 32, H-1518 Budapest, Hungary

E-mail: `frey@sgo.fomi.hu`

Abstract
We discuss the importance of the direct link between the most accurate radio and optical reference frames that will become possible with the next-generation space astrometry missions in about a decade. The positions of more than 500 active galactic nuclei that are common in the precise Very Long Baseline Interferometry (VLBI) catalogues and the Sloan Digital Sky Survey (SDSS) Data Release 4 (DR4) are compared. While obtaining an "independent" estimate for the SDSS coordinate accuracies, we find indications that the assumption of spatially coincident brightness peaks for the same objects in radio and optical does not hold for each object.
Keywords: *celestial reference frames, astrometry, quasars, VLBI, SDSS, surveys*

1 Introduction

From 1998, the International Astronomical Union (IAU) adopted the International Celestial Reference Frame (ICRF) as the fundamental celestial reference frame (Ma et al., 1998). The ICRF is defined by the positions of 212 compact extragalactic *radio* sources (active galactic nuclei, AGNs) regularly observed with Very Long Baseline Interferometry (VLBI) over a long period of time. In the *optical*, the HIPPARCOS catalogue (Perryman et al., 1997) is the most accurate available to date. It is linked to the ICRF with a variety of observing techniques

but mainly through relative astrometry with respect to nearby radio-loud AGNs using radio interferometric observations of twelve radio stars (Kovalevsky et al., 1997). The coordinate axes were aligned with the extragalactic radio frame to within ±0.6 milli-arcseconds (mas) at the epoch 1991.25, with a non-rotation within ±0.25 mas/yr. The quality of this link is known to degrade with time, due to e.g. the uncertainties in the measured stellar proper motions.

With a sensitive next-generation space astrometry mission – like the European Space Agency's Gaia spacecraft to be lauched in 2011 (Perryman, 2005), or the U.S. Space Interferometry Mission (SIM) PlanetQuest (Marr, 2003) – a quasi-inertial reference frame can directly be established in the optical as well. Gaia will detect $\sim$500 000 quasars brighter than the limiting magnitude $G = 20^{\mathrm{m}}$. Its celestial reference frame will be defined by a sample of at least $\sim 10\ 000$ clearly detected quasars expected to be observed during the mission (e.g. Mignard, 2002). In terms of precision, the Gaia optical reference frame will supersede the current radio ICRF. However, the latter will retain its importance at least because the Earth rotation and orientation are uniquely measured with VLBI by linking the terrestrial reference frame defined by the radio antenna locations and the quasi-inertial celestial reference frame defined by the extragalactic radio sources (Fey et al., 2004).

2   Direct link between reference frames

The space- and ground-based optical astometric sky surveys conducted to date are not sensitive enough to detect the faint optical counterparts of the distant radio-loud AGNs routinely observed with VLBI. An extensive astometric program is going on at the U.S. Naval Observatory to construct an optical extragalactic reference frame (e.g. Zacharias, 2003; Assafin et al., 2003).

The limiting visual magnitude of Gaia will enable observing the optical couterparts of practically all the ICRF defining radio-loud AGNs (their median visual magnitude is $V = 18.1$, Fey et al., 2001), allowing in principle an accurate *direct* link between the radio and optical reference frames. This link is essential not only for astrometry, but for astrophysical applications as well. The high-resolution stucture of the AGNs observed at different electromagnetic wavelengths can only be registered correctly if the coordinates are expressed in consistent systems. The quality of such a link is enhanced with the increasing number of common objects in both the optical and the radio. Any survey that offers an extensive list of suitable link sources is valuable for improving the tie between the radio and optical reference frames, even if the individual positional

accuracy of the sources is somewhat worse than that of the reference frame defining objects. Once completed, e.g. the Deep Extragalactic VLBI–Optical Survey (DEVOS, Mosoni et al., 2006) could provide a sizeable set of additional useful link sources (Frey, 2005).

3   A case study: SDSS coordinates

The imaging catalogue of the 4th Data Release[1] (DR4, Adelman-McCarthy et al., 2006) of the Sloan Digital Sky Survey (SDSS) covers almost 6700 square degrees of the sky, mainly on the Northern hemisphere and around the Equator. Although SDSS is of course not an astrometric sky survey, the positions of its objects are thoroughly calibrated using the USNO CCD Astrograph Catalogue (UCAC, Zacharias et al., 2000) and the Tycho-2 catalogue (Høg et al., 2000), with a declared absolute rms accuracy better than 100 mas per coordinate (Pier et al., 2003). The large sky coverage and the $R \sim 22^{\mathrm{m}}$ magnitude limit of SDSS make possible to identify the counterparts of many radio-loud AGNs that have accurate radio positions available. We compared the ICRF (Ma et al., 1998; Fey et al., 2004) and the VLBA Calibrators Survey[2] (VCS, Beasley et al., 2002; Fomalont et al., 2003; Petrov et al., 2005, 2006) catalogues with the SDSS DR4. We looked for optical cross-identifications of radio sources that have 10 mas formal positional accuracy or better in both right ascension (α) and declination (δ) coordinates. (The average values are actually below 1 mas.) This way the source positions in the sample are at least an order of magnitude more accurate than in the optical. Among the all-sky set of 2628 ICRF and VCS sources satifying the above criteria, optical counterparts of 524 were found in the SDSS within a search radius of 300 mas. The majority of our sources are in the range $7^{\mathrm{h}} < \alpha < 18^{\mathrm{h}}$ and $-5° < \delta < +70°$, with a few additional sources well distributed in right ascension at $-15° < \delta < +15°$. The distribution of the SDSS–VLBI position differences for these objects is shown in a histogram in Fig. 1.

One may suspect that the "outliers" seen at the tail of the distribution that represent SDSS–VLBI cross-identifications well beyond the expected radial distance are *chance coincidences*. To test this hypothesis, we constructed four "false" radio source lists by shifting the right ascension or declination coordinates of all the ICRF sources by a large amount ($\pm 1°$). We then tried to find SDSS optical counterparts within 300 mas radius for these "objects" (over

---

[1]http://www.sdss.org/dr4
[2]http://www.vlba.nrao.edu/astro/calib
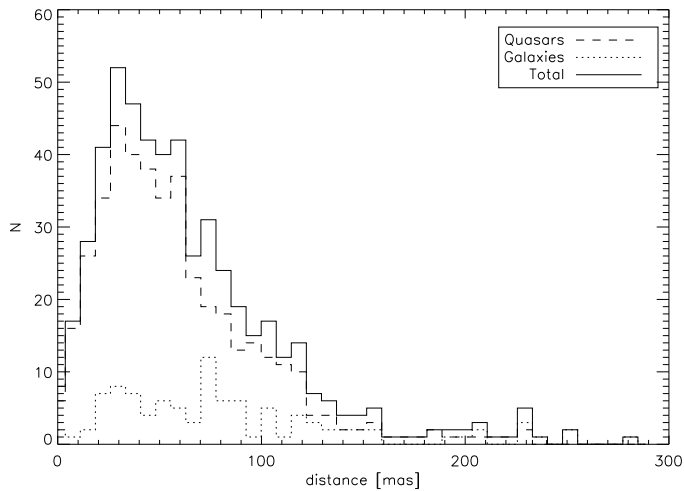
Figure 1: *Histogram of optical–VLBI radial position differences for 524 ICRF and/or VCS sources that are also identified in SDSS DR4 as quasars or galaxies. The distribution is consistent with ~ 60 mas (1σ) accuracy in both right ascension and declination in SDSS.*

10 000 in total). Only two chance coincidences were found, suggesting that most if not all of our outliers (21 AGNs with optical–radio separation larger than 180 mas) in Fig. 1 are *real identifications.* This result can be considered as a sign of warning. When comparing directly the radio and optical positions, we naturally assume that the optical and radio emission peaks physically coincide. Because the activity of these AGNs is driven by their central supermassive black holes, this assumption seems plausible in general. However, there are objects for which it is not necessarily true. Such objects should be avoided when the radio and optical reference frames are linked. (On the other hand, these AGNs may well be interesting from an astrophysical point of view.) Although the optical images – at least for the quasars – are unresolved, earlier studies of ICRF radio sources with extended (~ 10 mas) VLBI structure also found evidence of non-coincidence between the radio and optical centers (da Silva Neto et al., 2002).

The distribution in Fig. 1 is generally consistent with ~ 60 mas positional uncertainty per coordinate, in a good agreement with the values determined for SDSS (Pier et al., 2003). The *optical minus radio* right ascension

($\Delta\alpha\cos\delta$) differences have $\sigma_{\Delta\alpha} = 58.3$ mas standard deviation and a negligible $\langle\Delta\alpha\cos\delta\rangle = 0.4$ mas mean value. While the declination differences have similar standard deviation ($\sigma_{\Delta\delta} = 59.9$ mas), there appears to be an average offset of $\langle\Delta\delta\rangle = 12.3$ mas. As expected, the coordinate differences for optically resolved SDSS galaxies (102 in the sample) show larger standard deviation ($\sigma \approx 80$ mas) than for the quasars alone ($\sigma \approx 53$ mas).

To see if there is a set of rotations which could transform the system defined by the SDSS optical positions to the radio system, a three-parameter least-squares adjustment was performed. (The uncertainties of the individual points were not considered here.) The estimates for the rotation angles around two of the Cartesian coordinate axes (x: $\alpha = 0$, $\delta = 0$ and z: $\alpha = 0$, $\delta = \pi/2$) were insignificant: (-5.7 ± 3.1) mas and (3.0 ± 2.7) mas, respectively. The (14.6 ± 2.4) mas rotation obtained around the y axis ($\alpha = \pi/2$, $\delta = 0$), although small compared to the individual coordianate uncertainties, may be an indication for a small systematic difference in the SDSS positions with respect to the ICRF. Notably, a -15 mas mean declination offset (i.e. similar in extent but with an opposite sign) was found by Assafin et al. (2003), who determined the UCAC optical positons of 172 ICRF sources in the range $-30° < \delta < +25°$ and compared them with the radio positions. In our case, after transforming the SDSS coordinates using the rotation angles estimated above, the mean optical–radio differences became small: $\langle\Delta\alpha\cos\delta\rangle = -0.3$ mas and $\langle\Delta\delta\rangle = 3.2$ mas.

4   Conclusions

SDSS, although not an astrometric survey, could be used to compare optical and radio coordinates of 524 AGNs, all with accurate positions determined with VLBI at the mas or sub-mas level. We confirmed that the SDSS coordinates of these objects agree in both right ascension and declination with $\sigma \approx 60$ mas. There may be a small (~ 15 mas) systematic rotation between the reference frame of the SDSS and the ICRF. We found that the radio and optical brightness peaks do not necessarily coincide in the sky for each object. It is therefore essential to identify these "outliers" before high-precision refererence frame connections are made in the future.

Acknowledgement

References

Adelman-McCarthy, J.K., Agüeros, M.A., Allam, S.S., et al. 2006, ApJS, 162, 38

Assafin, M., Zacharias, N., Rafferty, T.J., et al. 2003, AJ, 125, 2728

Beasley, A.J., Gordon, D., Peck, A.B., et al. 2002, ApJS, 141, 13

da Silva Neto, D.N., Andrei, A.H., Vieira Martins, R., Assafin, M. 2002, AJ, 124, 612

Fey, A.L., Boboltz, D.A., Gaume, R.A., et al. 2001, AJ, 121, 1741

Fey, A.L., Ma, C., Arias, E.F., et al. 2004, AJ, 127, 3587

Fomalont, E.B., Petrov, L., McMillan, D.S., Gordon, D., Ma, C. 2003, AJ, 126, 2562

Frey, S. 2005, in The Three-Dimensional Universe with Gaia, ed. C. Turon, K.S. O'Flaherty, M.A.C. Perryman, European Space Agency, ESA SP-576, p. 683

Høg, E., Fabricius, C., Makarov, V.V., et al. 2000, A&A, 355, L27

Kovalevsky, J., Lindegren, L., Perryman, M.A.C., et al. 1997, A&A, 323, 620

Ma, C., Arias, E.F., Eubanks, T.M., et al. 1998, AJ, 116, 516

Marr, J.C. 2003, in Interferometry in Space, ed. M. Shao, Proc. SPIE, Vol. 4852, p. 1

Mignard, F. 2002, in GAIA: A European Space Project, EAS Publ. Ser., Vol. 2, ed. O. Bienaymé, C. Turon, p. 327

Mosoni, L., Frey, S., Gurvits, L.I., et al. 2006, A&A, 445, 413

Perryman, M.A.C. 2005, in The Three-Dimensional Universe with Gaia, ed. C. Turon, K.S. O'Flaherty, M.A.C. Perryman, European Space Agency, ESA SP-576, p. 15

Perryman, M.A.C., Lindegren, L., Kovalevsky, J., et al. 1997, A&A, 323, L49

Petrov, L., Kovalev, Y. Y., Fomalont, E.B., Gordon, D. 2005, AJ, 129, 1163

Petrov, L., Kovalev, Y. Y., Fomalont, E.B., Gordon, D. 2006, AJ, 131, in press (astro-ph/0508506)

Pier, J.R., Munn, J.A., Hindsley, R.B., et al. 2003, AJ, 125, 1559

Zacharias, N. 2003, in Astrometry in Latin America, ed. R. Teixeira, N.V. Leister, V.A.F. Martin, P. Benevides-Soares, ADeLA Publ. Ser., Vol. 1, p. 123

Zacharias, N., Urban, S.E., Zacharias, M.I., et al. 2000, AJ, 120, 2131

Interferometry in radio and infrared

L. Mosoni[1]

[1] Konkoly Observatory of HAS, H-1525 Budapest, Pf. 67, Hungary

E-mail: [1]mosoni@konkoly.hu

Abstract
In this paper I give three brief examples, two astrophysical applications and an image reconstruction study for a future instrument, of interferometric projects in which Hungarian groups are involved.

Keywords: *technique: interferometric, galaxies: active, stars: individual: V1647 Ori*

1 The Deep Extragalactic VLBI-Optical Survey

Pilot results of an ambitious programme, the Deep Extragalactic VLBI-Optical Survey (DEVOS, Mosoni et al. 2006) is presented first. Our ultimate aim is to collect information on compact structures in a large sample of extragalactic radio sources ($\sim 10^4$ objects) up to two orders of magnitude fainter than those studied in typical imaging Very Long Baseline Interferometry (VLBI) surveys up until now. In order to place the objects in the cosmological context, DEVOS will match the sky coverage of large optical surveys (e.g. the Sloan Digital Sky Survey, SDSS, Abazajian et al. 2004) which provide the necessary redshifts. This would lead to an unprecedented data base for various applications: 1. Study the cosmological evolution of radio-loud active galaxy population, 2. Study gravitational lensing, 3. Estimate fundamental cosmological parameters, such as the density parameters Ω_m and Ω_Λ (Gurvits 2003 and references therein), 4. Position of μJy-sources (Garrett et al. 2005) can be determined, 5. Provides an essential supplement to and basis for future development of the astrometric VLBI data bases (e.g. Ma et al. 1998). The sensitive next-generation

space-borne optical astrometry missions (e.g. Gaia) would provide a possibility to directly link the radio and optical reference frames using a large number of AGNs observed also with VLBI (Frey et al. and references therein, in these proceedings).

The primary goal of the DEVOS pilot project was to verify and adjust sample selection criteria, observing strategies and data reduction procedures before the full survey has started. We conducted MERLIN (Multi-Element Radio Linked Interferometer Network) and global VLBI observations of a sample of 47 radio sources selected from the FIRST (Faint Images of the Radio Sky at Twenty-centimeters, White et al. 1997) survey with integrated flux density $S > 30$ mJy and angular size $\theta < 5$", within $2°$ separation from the phase-reference calibrator source J1257+3229. We detected 37 sources at 5 GHz with MERLIN observations at a peak brightness of at least ~ 2 mJy/beam, filtering out extended radio structures not detected with MERLIN. Subsequent 5-GHz observations with the global VLBI network revealed that 19 of the sources are stronger than ~ 1 mJy at an angular resolution of ~ 1 mas. Tools are available for efficient data reduction in a highly automated way for the full survey. We were able to identify 34% of the pilot source sample with SDSS-detected sources. All of these sources were detected with MERLIN and 11 with VLBI. All sources with unresolved optical structure were detected with VLBI.

With the typically $0.3 - 0.7$ mJy/beam (3σ) VLBI image noise achieved, we could determine the mas-scale brightness distribution of sources with rest-frame brightness temperatures of at least $\sim 5 \times 10^6$ K. Hence the objects detected are likely to be powered by AGN rather than starburst activity (e.g. Condon 1992). In DEVOS, we are probing the same AGN population, but one or two orders of magnitude fainter than traditionally surveyed with imaging VLBI. The results of this pilot study can already be valuable in their own right since there are a couple of individual sources that may be worth studying further (e.g. J125858.6+325738 and J130129.1+333700).

DEVOS is a very demanding project in terms of network resources. With a detection rate of $\sim 40\%$, VLBI imaging of $10\,000$ objects implies $25\,000$ sources in the parent FIRST-based sample to be observed with MERLIN. The full SDSS-FIRST spectroscopic quasar sample will contain ~ 15000 objects (Ivezić et al. 2002). Our experience shows that a significant fraction of these is expected to have compact radio structure and could be detected with VLBI. With the technical capabilities available for the pilot experiment presented here, such a full survey would require approximately 600 days of MERLIN and 450 days of VLBI time. The time required can be significantly reduced with the perspective of further developments in the radio interferometric technique and an increased

detection rate of the VLBI observations by "fine-tuning" the selection and filter criteria based on our pilot experience. After completing this pilot study, we initiated further VLBI and target-finding filter observations.

2 First AU-scale observations of V1647 Ori

In January 2004 a new reflection nebula (McNeil's Nebula) appeared in the LDN 1640 dark cloud of the Orion B molecular cloud complex (McNeil et al. 2004). V1647 Ori, whose outburst apparently caused the appearance of McNeil's Nebula, is a low-mass pre-main sequence object. Near-infrared colour maps show that the source is embedded in an elongated disk-like structure, whose size is approximately 7000 AU (Acosta-Pulido et al., in prep.). Since the object had been gradually fading until Oct 2005, when the eruption rapidly ended (Kóspál et al. 2005), it seems to be pausible that V1647 Ori is an intermediate-type object between FU Orionis and EX Lupi-type (Muzerolle et al. 2005 and references therein).

V1647 Ori was observed with MIDI, the mid-infrared interferometric instrument at the Very Large Telescope Interferometer (VLTI) with two 8-m Unit Telescopes (UT3 nd UT4), in Dec 2004 and March 2005 (Ábrahám et al. 2006). The obtained data set consists of acquisition images, 8–$13\,\mu$m low resolution spectra (R=30), and interferometric measurements. Some of our results are summarised in the following.

1. The calibrated visibilities (Fig. 1) show that the source is resolved by MIDI on the UT3-UT4 baseline. The visibility curve suggests a non-uniform temperature distribution of the emitting material. The size of the mid-infrared emitting region is $\approx 7\,$AU at $10\,\mu$m.

2. The $8-13\,\mu$m spectrum *i*) exhibit no obvious spectral features thus cannot support models consisting of optically thin components; *ii*) the source faded in the N-band significantly between March (Andrews et al. 2004) and December 2004 but afterwards it exhibited an approximately constant spectral shape between December 2004 and March 2005; *iii*) the main fraction of the mid-infrared flux ($\approx 70\%$) is emitted in the innermost regions.

3. A simple disk model is able to fit both the spectral energy distribution and the observed visibility values simultaneously (Fig. 1). Model parameters for the disk were the following: $T(1\,\mathrm{AU}) = 680\,$K and $T \sim r^{-0.53}$, inner and

outer disk radii $7R_\odot$ and 100 AU, respectively, surface density $\Sigma \sim r^{-1.5}$, disk mass $M_d = 0.05\,\mathrm{M}_\odot$, inclination angle $60°$.

3   Image reconstruction in the mid-infrared

The *Multi-AperTure mid-Infrared SpectroScopic Experiment* (*MATISSE*), designed as a beam combiner for 3 and 4-telescope arrays, will enable image reconstruction in the mid-infrared wavelength regime at the VLTI. It will overcome the ambiguities often existing in the interpretation of simple visibility measurements. We investigated image reconstruction methods of the Very Long Baseline Interferometry (VLBI) and the possible gains for *MATISSE* (Mosoni et al. 2005). The *MATISSE* image reconstruction studies show that 3-7 nights of observations with 3-4 ATs (1.8-m Auxiliary Telescopes) at varying locations will result in an uv-coverage which is sufficient in order to reconstruct images which allow to address profound science questions.

Different methods have been developed to handle the image reconstruction problem, e.g. deficiencies of the Fourier-plane sampling and the limited phase information. We applied phase self-calibartion algorithms and compared the results to the reconstructed images obtained with a bispectrum algorithm (i.e. Building Block Method, Hofmann & Weigelt 1993). We considered two different scenarios for our image reconstruction study: The availability of 1. closure phases and 2. Fourier-phases.

In the first case, phase self-calibration methods, which correct the Fourier-phases taking the measured closure phases into account, need a starting model. In some cases, even with complex source structure, this model can be a point source and so the procedure is model-independent. But in general, the starting model consists of some model components (point source, Gaussian distribution, etc.) in order to obtain a reconstructed image which fits to the visibility data well. In this case, the model-independent Building Block Method is more favourable. But in some cases, the bispectrum or the closure phase information were not sufficient for succesful image reconstruction. In most of these cases, the image reconstruction was succesful with radio interferometric techniques because the Fourier-phase information can be considered. In a 3 or 4-telescope configuration the closure-phases and the bispectrum contain much less information on the source structure than the Fourier-phases.

Bispectrum and phase self-calibration methods are available, the image reconstruction will depend on the VLTI infrastructure and instrumentation – what observables will be measured.
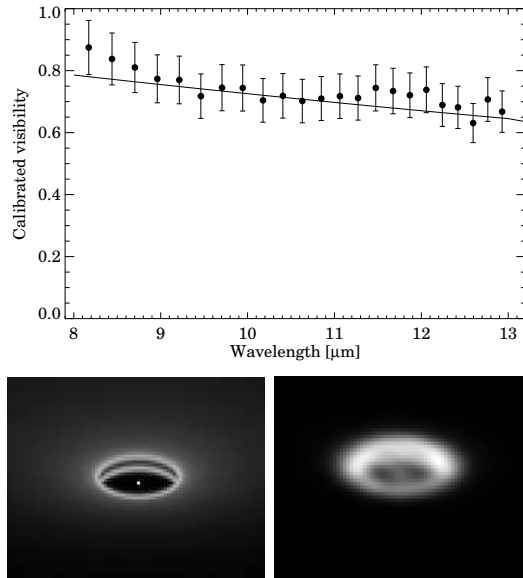
Figure 1: *A comparison of the outputs of present and future infrared interferometers. On the top panel the calibrated visibilities obtained with MIDI for V1647 Ori are plotted as a function of wavelength. The uniform error bars of 10% reflect our conservative estimate of the uncertainties. The solid line represents the model visibility curve of V1647 Ori. An example of MATISSE image reconstruction test results is shown below: the model image (bottom left) and a reconstructed image (bottom right). The model image, created with the radiative transfer code MC3D (Wolf et al. 1999), is a circumstellar disk around a T Tauri star with an inner hole up to 4 AU at the distance of 140 pc.*

Acknowledgement

References

Abazajian, K., Adelman-McCarthy, J.K., Agüeros, M.A., et al. 2004, AJ, 128, 502

Ábrahám, P., Mosoni, L., Henning, Th., et al. 2006, A&A accepted

Andrews, S.M., Rothberg, B., Simon, Th. 2004, ApJ 610, L45

Condon, J.J. 1992, ARA&A, 30, 575

Garrett, M.A., Wrobel, J.M., & Morganti, R. 2005, ApJ, 619, 105

Gurvits, L.I. 2003, in ASP Conf. Ser. 300, 285

Hofmann, K.-H., & Weigelt, G., 1993, A&A 278, 328

Ivezić, Ž., Menou, K., Knapp, G.R., et al. 2002, AJ, 124, 2364

Kóspál, Á., Ábrahám, P., Acosta-Pulido, J., et al. 2005, IBVS, 5661, 1

Ma, C., Arias, E.F., Eubanks, T.M., et al. 1998, AJ, 116, 516

McNeil, J.W., Reipurth, B., Meeck, K., 2004, IAUC 8284, 1

Mosoni, L., Frey, S., Gurvits, L.I., et al. 2006, A&A 445, 413

Mosoni, L., Wolf, S. Lopez, B., et al. 2005, Astr. Nachr. 326, 566

Muzerolle, J., Megeath, S.T., et al. 2005, ApJ 620, L107

Reipurth, B., Aspin, C., 2004b, ApJ 608, L65

White, R.L., Becker, R.H., Helfand, D.J., & Gregg, M.D. 1997, ApJ, 475, 479

S. Wolf, Th. Henning & B. Stecklum, 1999, A&A 349, 839

Test of the Infrared Wide-Field Camera OMEGA2000 and its Application for an Extragalactic Survey

Zoltán Kovács

Max-Planck-Institut für Astronomie, Königstuhl 17. D-69117 Heidelberg, Germany

E-mail: kovacs@mpia-hd.mpg.de

Abstract
The near-infrared wide-field camera OMEGA2000, mounted on the 3.5m telescope at Calar Alto is presented here. We give an overview on the first results of its scientific operation for the MANOS project. We discuss briefly the redshift and spectral energy distribution of the red bright galaxy sample detected in one of the COMBO-17 fields.
Keywords: *OMEGA2000, HAWAII-2, COMBO-17, MANOS*

1 Introduction

OMEGA2000 is a prime-focus, near-infrared (NIR), wide-field camera, mounted on the 3.5m telescope at Calar Alto. The camera uses a 2k×2k HAWAII-2 Focal plane array with a sensitivity from z to K band. Here we present the the camera system and give a short overview on its performance test. We also report the preliminary results of the MANOS project (**MPIA NIR and Optical Survey**), a scientific application using the OMEGA2000 instrument. Then we discuss the improvement in the measurement of the astrophysical properties of its galaxy sample due to the application of the NIR data besides a pre-existing optical data base. The first results of bright infrared galaxies observed in one of the field

of the COMBO-17 project are described. We present the redshift distribution, clustering properties and real nature of the Extremely Red Objects (EROs) detected in this field as well.

2   OMEGA2000

The optics and the detector of OMEGA2000 are enclosed in a cryostat which cools these parts to the operating temperature of 77 K with liquid nitrogen and insulates them from the warm telescope mirrors, structure and dome [Baumeister et al. (2002)]. The complete camera system consists of this cryostat, the detector with its mount plate, the optics with the filter wheels, the baffle system and the readout electronics.

The OMEGA2000 instrument uses a HAWAII-2 2kx2k Focal Plane Array (FPA), which belongs to the new generation of the large format NIR image sensors developed by the Rockwell company. It is a low-capacitance HgCdTe detector array mated to a low-noise CMOS silicon multiplexer via indium interconnects. The quantum efficiency of the detector is high enough for scientific purposes in the wavelength range 0.8-2.5 μm. The image sensor is built up in electrically independent quadrants, which are controlled in parallel. We implemented various readout modes with correlated double sampling for the FPA and optimized them to obtain the best image quality with a high frame rate [Kovács et al. (2004)]. We tested the operation of three specimen from the HAWAII-2 family in these readout modes and compared their performances with each other. We determined the typical characteristics of the FPAs which were similar for each of them. We measured low readout noise of 10 e^- on the average and gains of about 5 e^-/ADU by plotting their photon transfer curves. The low readout noise allowed us to operate the camera with background noise limited performance (BLIP). The number of dead pixels were under 2 % of the total pixel number for each FPA and they could be masked out from the science frames. We found the low dark current to be dominated by the noise of the readout electronics. We determined the linearity of the FPAs and measured their full well capacities to be about 200,000 e^-.

Since the primary science goal was for OMEGA2000 to be a NIR wide field imager, producing high quality images with the largest reasonable pixel scale, it is placed at the prime focus of the telescope. The optics of the camera consists of a cryogenic focal reducer providing a $15.4'' \times 15.4''$ field of view with a resolution of $0.45''$/pixel [Baumeister et al. (2002)]. The center to corner image distortion was measured to be $0.12''$ for the maximum distance of $600''$, which is less than

one pixel.

The OMEGA2000 camera contains 17 filters of 3 inch diameter for wavelengths between 0.8 and 2.4 μm and one closed blank, which are distributed over three filter wheels. The filter unit containing the wheels, the cryogenic stepper motors and the locking/cooling mechanisms is placed between the detector and the focal reducer.

OMEGA2000 is equipped with a baffle system to minimize the amount of background radiation reaching the detector in the K band (Baumeister et al., 2002). The baffle system consists of one cold and two warm mirror baffles. They prevent the detector from seeing the warm surroundings, which improves the S/N ratio in the K band. For J and H band observations, one of the mirror baffles can be moved closer to the dewar to a position where it does not vignette at all [Bailer et al. (2000)].

3 Scientific Applications

One of the first scientific applications if the OMEGA2000 camera is the MANOS Deep Field Survey, called COMBO-17+4 NIR, which was planned to extend the results of the COMBO-17 project to higher redshifts. The NIR extension of the COMBO-17 survey is to produce multi-band data in 4 NIR filters for three equatorial fields covering 0.77 deg^2 already observed by COMBO-17 [Wolf et al. (2003)]. The survey is designed to use a filter set of the medium-band Y, J_1(1190/130nm), J_2(1320/130nm), and the broad-band filter H. In order to combine the existing optical database from COMBO-17 with observations in the four NIR bands, 10σ magnitudes in the four NIR bands with $Y = 22.0$, $J_1 = 21.2$, $J_2 = 21.0$, and $H = 20.5$ (Vega mag.) have to be obtained.

Although the first observations of this survey produced only J_1- and H-band imaging in the COMBO S11 field, restricting the original project to the COMBO-17+2 NIR, the enlarged color space of the measurement allowed us to derive redshifts for the galaxies detected in this field up to $z \sim 2.1$. We studied the improvement in the redshift determination and the quality of fittings of the COMBO-17+4 NIR spectral template library on the measured fluxes for galaxies due to the supplement of the optical data with the NIR-band colors. We chose a population from the R- and H-band selected galaxy sample in the COMBO S11 field for which the variation in the astrophysical properties derived from the optical and the optical+NIR data sets was significant. We studied the differences between the photometric redshifts derived from the optical and NIR-supplemented optical fluxes and analyzed the results of the SED and extinction

evaluation for the original and the extended data set. We found the galaxies with the 4000 Å break in their spectra redshifted to the redward end or even out of the optical regime, i.e., at $z > 1.2$, had a significant improvement in the redshift and SED determination. The measurement based on only optical bands could not detect the spectral features of their old stellar content at these redshifts. These galaxies were identified mainly as actively star-forming systems with large variations in their dust reddening and some of them were dusty early-type or evolved spiral galaxies at redshifts between 0.7 and 1. By including the NIR colors in optical ones, we detected mainly advanced spiral galaxies from Sa to Sbc with low extinction at higher redshifts and some starburst galaxies with more dust as well.

By extrapolating this preliminary analysis to the total planned survey data, we expect the extension of wavelength coverage and the increase of the number of bands will have a deep impact in the redshift and SED determination for at least 15% of the entire galaxy population detected in the COMBO-17 fields.

4   Preliminary Results

We investigated how the relative fractions of the spectral types in our bright infrared galaxy sample ($H < 21.4$) with $M_B < -20 + 5 \log h$ has been evolving from $z \sim 2$ to present, comparing with the development of the morphological distribution observed in other surveys at $z \sim 0$, and how this is related to the structure formation history. We determined the redshift distribution of bright infrared galaxies observed in the COMBO S11 field and analyzed the evolution of their number counts for four classes of galaxies defined by their restframe colors. A decline in the number of the old elliptical and evolved spiral galaxies at $z > 1.5$ was found, whereas the actively star-forming galaxies become the dominating population at $z > 1$. This is in a broad agreement with earlier results. In the analysis of the galaxy population with $M_B < -20$ in the Hubble Deep Field North and South, Conselice et al. (2005) recognized similar tendencies in the evolution of the co-moving densities of ellipticals, spirals, and peculiars to those we found in the case of four spectral types originally defined in the COMBO-17 survey [Wolf et al. (2003)]. They showed a gradual decrease of peculiar galaxies at the expense of the normal Hubble types and considered it as circumstantial evidence that at least some fraction of ellipticals and spirals at lower redshifts originate from peculiar galaxies. The change of the relative fraction of E-Sb-type galaxies and the actively star-forming systems defined via their bluer rest-frame colors probably indicates that some massive early-type galaxies originate from

peculiars at high redshifts. The dramatic decline of the E-Sb type systems with increasing redshift also demonstrates the important role of the passive evolution of galaxy colors besides the merging processes in the variation of the relative fractions of different spectral types.

The NIR-band-extended wavelength range of the measurement between 700 nm and 1300 nm covers the most interesting part of the spectra for EROs, which may help to answer the question of whether the extreme colors of these objects can be attributed to the dust-extinction in starburst galaxies or the EROs are early-type galaxies dominated by an old stellar population. For the EROs in our galaxy sample selected with $R-H < 4$, we measured similar redshift distribution and clustering properties to those derived in other NIR surveys. The sharply peaked redshift distribution we obtained might suggest that our color cut selects mainly early-type galaxies with advanced stellar population. The high clustering amplitude, $A(1'') = 0.33$, we derived for $H < 20$ shows that our EROs are much more positively correlated than expected for blue galaxies at high redshifts. This indicates that they are indeed early-type galaxies at $z \sim 1$. As a result of the multi color classification, we find that our ERO sample does not contain starburst galaxies at all, confirming the results of earlier observations in the Las Campanas Survey [Firth et al. (2002)]. This is in good agrement with the two-color separation methods we applied as well. However, the total absence of the star-forming systems may also be attributed to the spectral template library used in the COMBO-17+2 NIR multi-color classification.

5   Summary and Outlook

We have given a brief overview on the OMEGA2000 instrument and the first results of the MANOS project using this camera. We described the improvement in the measurement of the astrophysical properties of galaxies achieved in this survey by applying the NIR data produced in a COMBO-17 field. Then we presented the redshift evolution of the number counts for bright infrared galaxies and studied the nature of EROs in our galaxy sample. We obtained similar results for the both types of galaxy samples to those derived in other surveys.

Besides the extention of the redsift regime available for optical galaxy surveys, there are other promising advantages of the supplement of the COMBO-17 data set in NIR regime. We expect a considerable improvement of the stellar mass estimation in galaxies. Even in the redshift range $0.7 < z < 1.1$, the old stars have a dominant contribution for galaxy spectra only in the NIR regime. Therefore, the data provided in COMBO-17+4 NIR will significantly improve

the determination of the stellar mass in galaxies. The NIR-band filters with the broad I-band filter seem useful for searching AGNs at redshits $z > 6.5$ as well, and measure their rest-frame B-band and 250 nm luminosity functions out to $z \simeq 2.6$ and 5.5. This will be useful for studying the redshift evolution of AGNs in the Universe. The COMBO-17+4 NIR survey has also prospects for the detection of extremely red stars (brown dwarfs), as a consequence of the improvement in the object classification due to inclusion of the NIR bands.

Acknowledgement

References

C. A. Bailer-Jones, P. Bizenberger, and C. Storz, "Achieving a wide field infrared camera for the Calar Alto 3.5m telescope," in *Optical and IR Telescope Instrumentation and Detectors*, M. Iye and A. F. Moorwood, eds., *Proc. SPIE* **4008**, pp. 1305–1316, 2000.

H. Baumeister, P. Bizenberger, C.A. Bailer-Jones, Z. Kovács, H.-J. Röser, and R.-R. Rohloff, "Cryogenic engineering for Omega 2000: Desig n and performance," in *Instrument Design and Performance for Optical/Infrared Ground-based Telescopes*, *Proc. SPIE* **4842**, pp. 343–354, 2002.

C. J. Conselice, J. A. Blackburne, and C. Papovich: 2005. The luminosity, stellar mass, and number density evolution of field galaxies of known morphology from $z = 0.5 - 3$. *Astrophysical Journal* **620**, 564-583

A. E. Firth, R. S. Somerville, R. G. McMahon, O. Lahav, R. S. Ellis, C. N. Sabbey, P. J. McCarthy, H.-W. Chen, R. O. Marzke, J. Wilson, R. G. Abraham, M. G. Beckett, R. G. Carlberg, J. R. Lewis, C. D. Mackay, D. C. Murphy, A. E. Oemler, and S. E. Persson: 2002. Las Campanas IR Survey. II. Photometric redshifts, comparison with models and clustering evolution. *Monthly Notes R. Astron. Soc.* **332**, 617+

Z. Kovács, U. Mall, P. Bizenberger, H. Baumeister, H.-J. Röser Characterization, testing, and operation of Omega2000 wide-field infrared camera: in *Optical and Infrared Detectors for Astronomy*, J. D. Garnett, J. W. Beletic, Eds. *Proc. SPIE* **5499**, 432-441, 2004

C. Wolf, K. Meisenheimer, H.-W. Rix, A. Borch, S. Dye, and M. Kleinheinrich: 2003. The COMBO-17 survey: Evolution of the galaxy luminosity function from 25,000 galaxies with $0.2 < z < 1.2$ *Astronomy and Astrophysics* **401**, 73+

STATISTICAL PHENOMENA IN ASTRONOMY

Invited Talk

L.G. Balázs

Konkoly Observatory of HAS, H-1525 Budapest, Pf. 67, Hungary

E-mail: `balazs@konkoly.hu`

Abstract
This paper represents the short version of the author's DSc theses. The whole text is available at the web site of http://www.konkoly.hu/staff/balazs/dissertation.pdf

1 Mathematical introduction

1.1 Nature of astronomical information

Observing and storing the photons of the incoming radiation from the Cosmos typically gives a data cube defined by $(\alpha, \delta, \lambda)$. It is easy to translate this data structure into the formalism of multivariate statistics. A common problem is in the multivariate statistics whether the stochastic variables described by observed properties are statistically independent or can be described by a less number of hidden variables. This is the task of factor analysis. Forming groups from cases having similar properties according to the measures of similarities or the distances is the task of cluster analysis. I demonstrated in several particular cases how these technics can be used for studying structures in the $(\alpha, \delta, \lambda)$ data cube and how to translate the statistical results into true physical quantities.

1.2 The basic equation of stellar statistics

The basic equation of stellar statistics connects the probability density function of a measurable quantity with the probability density of two variables, which can

not be observed directly, by the law of full probabilities. The resulting relation is a Fredholm type integral equation of the first kind. If the two background variables are statistically independent we recover the convolution equation. The analytical solution based on the Fourier transformation is very sensitive to high frequency noise. Eddington's solution attempts to find the unknown function in form of a series $\sum \gamma_j h^{(j)}(z)$. Malmquist's method computes the conditional probability of the unknown variable assuming that the observed variable is given. The statistical aspect of the problem is expressed if one uses the Lucy's algorithm which is a particular form of the more general EM algorithm. Dolan's matrix method solves numerically the matrix equation which approximates the integral equation. Methods are superior which retain the true statistical nature of the problem.

2   Statistical study of extended sources

2.1   Separation of Components

Separation of the Zodiacal and Galactic Light.

Principal components analysis and k-means clustering was utilized to identify different components of cosmic dust. Applying these techniques on the PL51 IRAS maps I recognized two main components with temperatures of about $200\,K$ (Zodiacal Light) and $40\,K$ (Galactic dust).

Structure and Dynamics of the Cepheus Bubble.

The Cepheus Bubble is a giant (10° in angular diameter) dust ring around the Cep OB2 association. Performing factor analysis on HI 21 cm data, taken from the Leiden/Dwingeloo survey, reveals HI structures in the [-14,+2] kms^{-1} velocity range which can be associated with prominent parts of the dust ring. In the same area the HI maps also show an expanding shell with a well-defined approaching side at VLSR=-37 kms^{-1} and a less well-defined receding side at VLSR=-4 kms^{-1}. The kinematics and size of this shell are best modelled by a supernova explosion, occurring in Cep OB2a at about 1.7 $Myrs$ ago. Since the ages of several parts of the Cepheus Bubble are considerably higher than the age of the expanding shell, the supernova probably exploded in a pre-existing cavity, and its shock front might have interacted with the already existing star forming regions Sh2-140, IC 1396, and NGC 7129, leading to a new wave of star formation there.

2.2   Star count study of the extinction

I studied the ISM distribution in and around the star forming cloud L1251 with optical star counts. A careful calculation with a maximum likelihood based statistical approach resulted in *B, V, R, I* extinction distributions from the star count maps. A distance of 330±30pc was derived. The extinction maps revealed an elongated dense cloud with a bow shock at its eastern side. I estimated a Mach number of $M \approx 2$ for the bow shock. A variation of the apparent dust properties is detected, i.e. the $R_V = A_V/E_{B-V}$ total to selective extinction ratio varies from 3 to 5.5, peaking at the densest part of L1251. The spatial structure of the head of L1251 is well modelled with a Schuster-sphere (i.e. n=5 polytropic sphere). The observed radial distribution of mass fits the model with high accuracy out to $2.5pc$ distance from the assumed center. Unexpectedly, the distribution of NH_3 1.3 cm line widths is also well matched by the Schuster solution even in the tail of the cloud. Since the elongated head-tail structure of L1251 is far from the spherical symmetry the good fit of the linewidths in the tail makes reasonable to assume that the present cloud structure has been formed by isothermal contraction.

3   Statistics of point sources

3.1   Classification of stellar spectra

I made medium resolution ($100\mathring{A}/mm$) spectroscopy of 35 stars, picked up as suspected $H\alpha$ emission objects on small scale spectra, in the IC1396 star-forming region. Statistical studies based on factor analysis and k-means clustering yielded templates for further classification. Using proper motion data published in the literature I suggested that the vast majority of our objects belong to IC1396. Plotting the program stars, along with theoretical evolutionary tracks, onto the $\{Log(L); Log(T_{eff})\}$ plane I concluded that they are pre-main sequence objects of $0.5M_\odot < M < 3M_\odot$ masses and $10^5 < t < 10^7$ years age.

3.2   Angular distribution of GRBs

The isotropy of gamma-ray bursts collected in current BATSE catalog was studied. I showed that the quadrupole term being proportional to $\sin 2b \sin l$ was non-zero with a probability of 99.9%. The occurrence of this anisotropy term was then confirmed by the binomial test even with the probability of 99.97%. Hence, the sky distribution of all known gamma-ray bursts is anisotropic. I

also argued that this anisotropy cannot be caused exclusively by instrumental effects due to the nonuniform sky exposure of BATSE instrument. Separating the GRBs into short and long subclasses, I showed that the short ones are distributed anisotropically, but the long ones seem to be distributed still isotropically. The character of anisotropy suggests that the cosmological origin of short GRBs further holds, and there is no evidence for their Galactic origin.

3.3 Classification of GRBs

The gamma-ray bursts can be divided into three subgroups ("short", "intermediate", "long") with respect to their durations. This classification is somewhat unclear, since the subgroup of the intermediate durations has an admixture of both short and long bursts. A physically more reasonable definition of the intermediate subgroup was presented using also the hardness of the bursts. I showed that the existence of the three subgroups is real, and it was shown that no further subgroups are needed. According to the result the intermediate subgroup is the softest one. From this new definition it follows that 11% of all bursts belong to this subgroup. The intermediate subgroup shows furthermore an anisotropic distribution on the sky. A strong anticorrelation between the hardness and the duration was found - contrary to the short and long subgroups - for this subclass. Despite this difference it is not clear yet whether this subgroup represents a physically different phenomenon.

3.4 Physical difference between GRBs

I argued that the distributions of both the intrinsic fluence and the intrinsic duration of the gamma -ray emission in gamma-ray bursts from the BATSE sample are well represented by log-normal distributions, in which the intrinsic dispersion is much larger than the cosmological time dilatation and redshift effects. I performed separate bivariate log-normal distribution fits to the BATSE short and long burst samples. The bivariate log-normal behavior results in an ellipsoidal distribution, whose major axis determines an overall statistical relation between the fluence and the duration. I showed that this fit provides evidence for a power-law dependence between the fluence and the duration, with a statistically significant different index for the long and short groups. I discuss possible biases, which might affect this result, and argue that the effect is probably real. This may provide a potentially useful constraint for models of long and short bursts.

The distribution of photometrically selected T Tauri candidates in the outer Galaxy

Z. T. Kiss[1,2], L. V. Tóth[2], L. G. Balázs[3] V. Könyves[2]

[1] Baja Astronomical Observatory, H-6500 Baja, Pf. 766, Hungary
[2] Eötvös University, Department of Astronomy, H-1518 Budapest, Pf. 32, Hungary
[3] Konkoly Observatory of HAS, H-1525 Budapest, Pf. 67, Hungary

E-mail: [1]`kissz@alcyone.bajaobs.hu`, [2]`L.V.Toth@astro.elte.hu`,
`V.Konyves@astro.elte.hu`, [3]`balazs@konkoly.hu`

Abstract
We mapped the NIR extinction in the 2nd and 3rd galactic quadrant in the $\pm 30\deg$ latitude range covering a $\approx$10300 square degree area based on the 2MASS Point Source Catalogue. We selected the sources with T Tauri like NIR colours, and investigated their distribution. We describe the variation of the CTT candidate number density as function of galactic latitude and longitude. We searched for CTT candidate clustering and compiled a catalogue of associations found. We found that significant fraction of clusters found are situated in the shells of GIRLs.
Keywords: *dust, extinction – ISM: bubbles – Stars: formation*

1 Introduction

Star formation efficiency is considered to be in close relation with the column density of the ISM, however, the role of other factors such as triggering could not be ignored. Studying the occurrence of possible triggers in the vicinity of newly formed stars or stellar clusters can give answer how important is the role of triggers in star formation.

For finding young stars one can use different methods based on either Hα (Kun et al., 2000) emission far (Beichman et al., 1986; Kun et al., 2000) or near (Meyer et al., 1997) infrared colours of sources, however, to confirm the young stellar nature of the candidates found with these methods spectroscopic examination would be desirable.

Clustering of young star candidates in Orion was studied on a sample assembled based on Hα emission using statistical methods by Balázs (1995). A recently studied manifestation of star forming triggers is the phenomenon of the loop-like galactic structures seen in far infrared referred as Galactic Infrared Loops (GIRLS, Kiss et al., 2004).

In this paper we present a near infrared extinction map of a wide area of the galactic plane in the 2nd and 3rd quadrant, search for young stellar objects and describe their distribution versus galactic latitude and longitude, detect clustering of objects using statistical method based on that of Balázs (1995), and compile a catalogue of candidate young clusters found. We compare the distribution of T Tau candidate clusters and their richness to those of extinction A_V mapped based on 2MASS (Cutri et al., 2003) data and also checked the relation between clusters found and Galactic Infrared Loop shells.

2 Input data and data processing

2.1 Extinction map

The near infrared extinction map of a $\approx$10300 square degree area in the 2nd and 3rd galactic quadrant within $\pm$30 deg around the galactic plane was created based on 2MASS photometric data using the method described by Lombardi&Alves (2001). We used gaussian smoothing with a beam FWHM=4.5 arcmin on a 1.5 arcmin rectangular grid. The extinction can be traced reliably up to $\approx$8 mag.

2.2 Selection of CTTs

We carried out a rough classification based on $J - H$ vs. $H - K$ colour-colour diagram of sources in the 2nd and 3rd galactic quadrant at low and medium galactic latitudes ($90 \deg < l < 270 \deg$, $-30 \deg < b < 30 \deg$) using the data of the 2MASS point source catalogue (Cutri et al., 2003). Sources located between the reddened main sequence and the T Tauri line with at least 1σ reliability, having good detection quality ("A", "B" or "C") and photometric error less

than 0.1 mag were considered as classical T Tauri candidates. Sources coinciding galaxies of HYPERLEDA (Paturel et al., 2003) catalogue were removed from the sample.

2.3 Finding clusters

The distribution of the sample of T Tau candidates in the region examined were homogenized in galactic longitude and latitude independently, using the functions fitted to their empirical distribution. The homogenized distribution was compared to the expected poissonian distribution using 768×256 sized equidistant rectangular grid following Balázs (1995).

Clustering was defined by the following criteria: $P_m^{n_{sq}} < P_{lim}$ and $p < n_{sq}^{-1}$; where $P_m^{n_{sq}}$ is the probability of a poissonian distribution sample to contain m different cells among the n_{sq} with more objects than a given t, $P_{lim} = 10^{-4}$ is the $P_m^{n_{sq}}$ probability accompanied to the highest value occurred in the randomly generated poissonian samples; n_{sq} is the number of cells and p is the sum of the Poisson probabilities for the number of counts above the given t. For more detailed description see Balázs (1995).

Each cell meeting these criteria was considered as a cluster or a part of a cluster. In case of two or more neighboring cells meet the criteria, those cells were merged into one cluster.

3 Results

3.1 Global description of CTT distribution

As many as 3872 T Tauri like point sources have been found in the field. The empirical distribution function of CTTs versus the longitude and latitude was approximated as the followings: $D(l) = \frac{1}{7.8069}(exp(6.4111 \times 10^{-3}|l - 180|) - 1)$ and $D(b) = \frac{1}{1.4690} arctan(3.2626|b|)$.

3.2 Clustering

We found 26 and 38 clusters of T Tauri candidates in the 2nd and 3rd galactic quadrant, respectively, from which 27 (42%) has not been catalogued previously. We determined the number of stars N_{cl}, defined an effective radius r_{eff} as the mean angular distance of cluster members from the center, and an effective surface density $n_{eff} = r_{eff}^2 \pi / N$ for all clusters found. Among the 3872 candidate
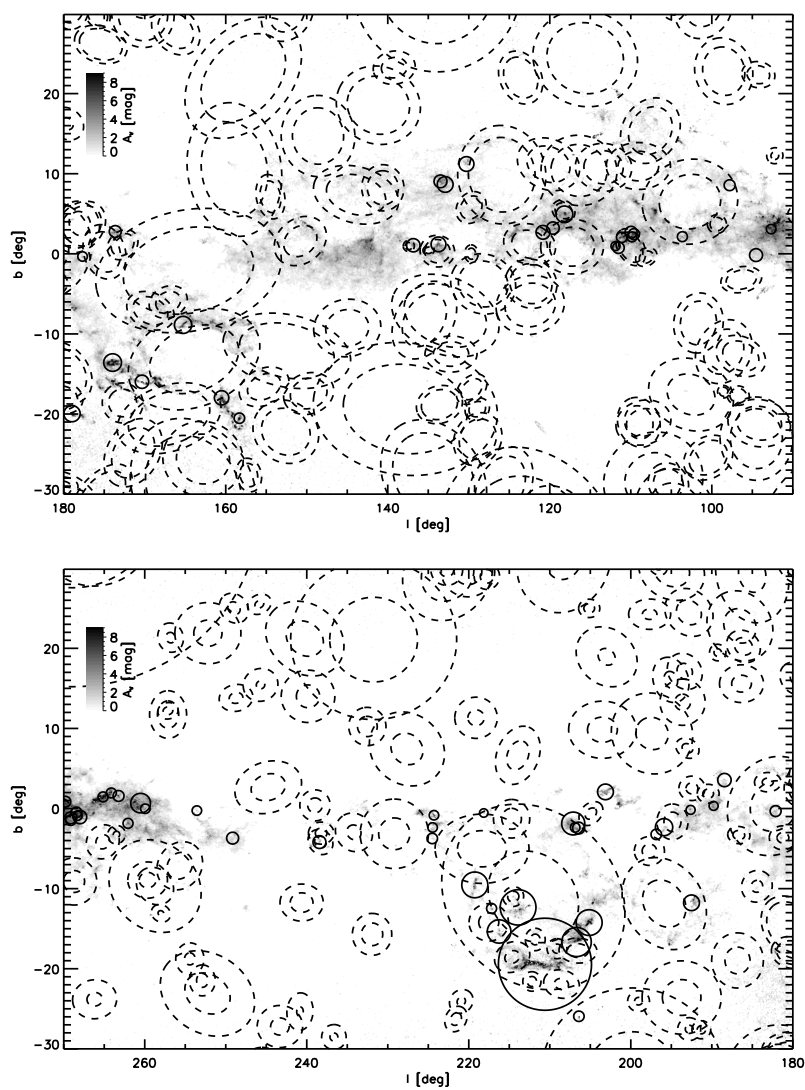
Figure 1: *Clusters of T Tauri stars (solid circles) and the distribution of visual extinction A_V in the 2nd and 3rd quadrant. Boundaries of FIR loops (dashed ellipses) are overlaid.*
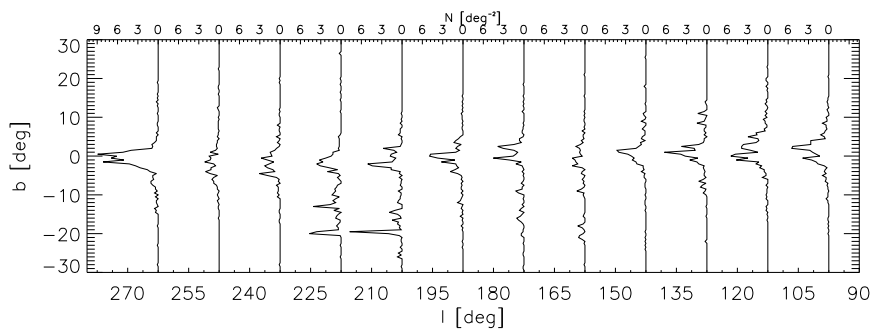
Figure 2: *Variation of the CTT candidate number density profile in 15deg wide sections in latitude. N is the number of CTT candidates per square degree in the given interval.*

T Tauri stars 614 (16%) are situated in the clusters. The effective radius of clusters vary between 1 arcmin and 105 arcmin, the mean value is 8 arcmin. The number of stars in a cluster ranges from 4 to 138 around the mean of 10. The distribution of CTT clusters plotted on the V band extinction map is shown in Fig. 1.

3.3 Star forming efficiency

Most clusters are related to high extinction regions, however some of such regions remained without any cluster found, while there are some clusters in moderate extinction positions. The mean extinction exceeds $1\,mag$ in positions of each cluster, moreover higher than $4\,mag$ for 36 (56%) of them the mean value is $4.8\,mag$. We compared the positions of clusters found to those of Galactic Infrared Loops, and 29 of them were found to be related to one or more catalogued GIRL shells (see Fig. 1).

4 Summary and outlook

We mapped the extinction of the 2nd and 3rd galactic quadrant within $\pm 30\,$deg using 2MASS near infrared stellar colours, searched the area for sources with T Tau like colour indices and examined the clustering of such sources. A catalogue of clusters found was also compiled. We showed relation between occur-

rence of such clusters, NIR based A_V extinction and shells of Galactic Infrared Loops.

Acknowledgement

References

Balázs, L.G. 1995, MemSocIt, 66, 689

Beichman, C. A., Myers, P. C., Emerson, J. P. et al. 1986, ApJ, 307,337

Cutri, R. M., Skrutskie, M. F., van Dyk, S. et al. 2003, yCat, 2246

Kiss, Z. T., Tóth, L. V. , Krause, O. et al. A&A, in Press

Kiss, Cs., Moór, A., Tóth, L. V. 2004, A&A, 418, 131

Kun, M., Vinkó, J., Szabados, L. 2000, MNRAS, 319, 777

Lombardi, M., Alves, J. 2001, A&A, 377, 1023

Meyer, M. R., Calvet, N., Hillenbrand, L. A., 1997, AJ, 114, 1

Paturel G., Petit C., Prugniel P. et al. 2003, A&A, 412, 45

How superdiffusion alters the fractional abundances in molecular clouds

G. Marschalkó

Eötvös University, Department of Astronomy, H-1518 Budapest, Pf. 32, Hungary

E-mail: `G.Marshalko@astro.elte.hu`

Abstract

The chemistry of molecular clouds is a complex system influenced by wide scale of different factors; amongst them one of the most important is the turbulent diffusion. Whilst the previous improved models laid emphasis on the chemistry, we wish to examine the turbulence with special regard to the superdiffusion.

Keywords: *turbulence, diffusion, ISM: clouds, ISM: abundances, ISM: molecules*

1 Introduction

The determination of fractial abundances of the constituents of molecular clouds has a long history. After the initial steady state gas-phase chemistry model of Herbst & Klemperer (1973) several (pseudo-)time-dependent models with fixed profiles of physical parameters were developed, considering more and more chemical reactions, however in the absence of photodissociation (Leung et al., 1984; Herbst & Leung, 1989; Millar & Herbst, 1990). Moreover, these models produced the observed fractional abundances (particularly in the case of C and complex organic molecules) too early and reaching the steady state these decreased notably below the expected values. However, the consideration of turbulence in later works solved these problems, significantly altering steady state abundances and radial profiles of the more important species (Xie et al., 1995).

Since then, these models have been refined: Willacy et al. (2002) demonstrated that HI is a tracer of turbulent diffusion and refined the ion-neutral reaction scheme, as well as took into account the gas-grains interaction and H_2 and CO self-shielding; Yate & Millar (2003) integrated in the model of Xie et al. (1995) the grain accretion effects and adsorption onto grains.

We examined the role of anomalous diffusion, namely how superdiffusion alters the evolved fractional abundances. After presenting a model with initial simplifying assumptions we conclude that the problem deserves the further studies.

2   Turbulence and anomalous diffusion

We would like to study the diffusive transport of certain species in a turbulent cloud using mixing length theory. Let n_{H_2} the number density of hydrogen, n_i the number density and f_i the fractional abundance of tracer i. Thus its diffusion equation is:

$$\frac{\partial n_i}{\partial t} = D\frac{\partial}{\partial r}[\frac{\partial}{\partial r}n_i - f_i\frac{\partial}{\partial r}n_{H_2}] + S_i, \qquad (1)$$

where S_i is the source and sink term, which comes from the chemistry reaction-scheme, and D is the diffusion coefficient, whose determination is fundamental.

It is known from the observations that there is an approximately power-low relation between the internal velocity dispersion and the size (or mass) of the cloud (Larson, 1980; Leung et al., 1982). Whilst the turbulent velocity is usually estimated to be approximately 1 km s^{-1} in the case of a typical molecular cloud, the values of the correlation length vary on a larger scale in the different papers. Xie et al. (1995) define about 10% of the cloud as the correlation length, which is approximately 0.1-0.5 pc. Yate & Millar (2003) prefer smaller values than 0.5 pc, what they reckon as an upper limit, while in highly fragmented clouds they figure that the mixing length is between 0.003 and 0.03 pc. Hence these authors get different values of diffusivity, 3x10^{22} - 2x10^{23} and 10^{21} - 10^{23} cm^{2}s^{-1}, respectively.

The diffusion velocity of each species, thus the diffusion timescale, too, depend on its density scale heights being altered continuously by the chemical reactions, moreover it depends on the cloud radius and is influenced by the external radiation field (Xie et al., 1995). Hence, in the case of diffusion timescales only an upper limit can be given by R^2/D. To estimate the timescales we need to define the turbulent flux of a tracer after Xie et al. (1995):

$$\phi_i = D n_i \frac{1}{H}, \tag{2}$$

where $H = (\frac{1}{H_i} - \frac{1}{H_{H_2}})^{-1}$ is the relative density scale height, which one can calculate by the density scale height of hydrogen H_{H_2} and the different tracers H_i ($H_j = -n_j(\frac{dn_j}{dr})^{-1}$, where $j = \{i, H_2\}$). Thus the diffusion velocity and the diffusion timescale are given on scale H $v_d \sim \frac{D}{H}$ and $\tau_c \sim \frac{H^2}{D}$, respectively. This timescale is comparable with the chemical timescale, both are around 10^6 years, but at higher densities the transport timescale exceeds the chemical timescale, so there is less effect of the turbulence (Scalo & Elmegreen, 2004).

It can be seen that the diffusion and the chemistry form a very complex system, so one needs to make some simplification, for example to use constant diffusivity over the whole cloud. We can take into account eddies with different sizes using superdiffusion, namely the eddies exceeding the separation r do not contribute to the further separation of fluid parcels at separation r.

The equation that describes the rms separation of two tracers

$$r = 2Kt^\zeta, \tag{3}$$

can be rewritten to get a unique relation between r and t ($r = 2K'(r)t^{1/2}$), so we can formally introduce a 'scale-dependent diffusion coefficient' (Petrovay, 2001):

$$D(r) = K'^2 = K^{1/\zeta} r^{2-1/\zeta}. \tag{4}$$

One can speak about a simple diffusion process if $\zeta = \frac{1}{2}$, while the case $\zeta \neq \frac{1}{2}$ corresponds to anomalous diffusion: superdiffusion if $\zeta > \frac{1}{2}$ and subdiffusion if $\zeta < \frac{1}{2}$.

3 Our results

At first we studied a simplified problem, neglecting the chemical processes and estimating the source term by means of the diffusionless solution based on relaxation timescales in referenced papers. Our cloud is spherically symmetrical, the density of H_2 is constant and we look for a stationary solution. Thus the equation of diffusion:

$$\frac{\partial n}{\partial t} = D\nabla^2 n + S, \quad \text{where} \quad S = \frac{n_0 - n}{\tau_c}, \tag{5}$$
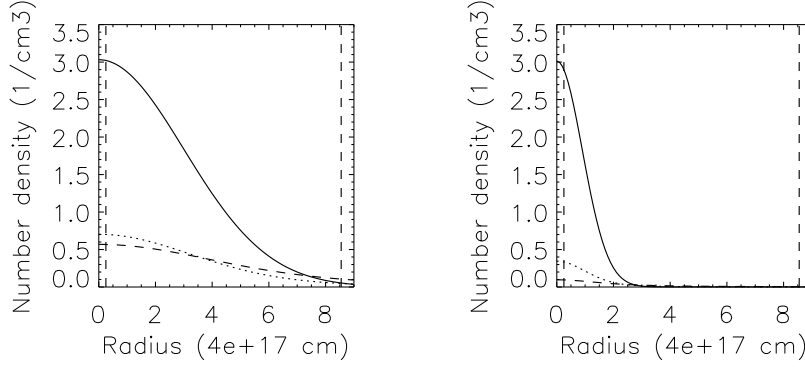
Figure 1: *Number density of a tracer as a function of the radius. The solid line represents the initial (or diffusionless) state, the dashed line the diffusive case and the dotted line the superdiffusive case. The upright dashed lines represent the inner and outer computational domain of the cloud. Left: Gaussian, $D = 10^{23} cm^2 s^{-1}$, $\tau_c = 10^6 year$ Right: Gaussian with lower standard deviation, $D = 1.2x10^{23} cm^2 s^{-1}$, $\tau_c = 10^6 year$*

n_0 is the diffusionless equilibrium solution of number density of the tracer and τ_c is the characteristic time. Transforming the initial partial differential equation into the Fourier space we get

$$\frac{\partial \hat{n}}{\partial t} = -Dk^2\hat{n} + \hat{S}, \quad \text{where} \quad \hat{S} = \frac{\hat{n}_0 - \hat{n}}{\tau_c}, \tag{6}$$

finally we find the stationary solution of this equation:

$$\hat{n} = \frac{\hat{n}_0}{1 + \tau_c Dk^2}. \tag{7}$$

To make the Fourier transform we apply the theorem that an n dimensional Fourier transform can be replaced a one dimensional Hankel transform, if the transformable function depends only on $r = \sqrt{\sum x_i^2}$ (Sneddon (1951)). So in the case of $n = 3$ the transformation formulae are:

$$\hat{n}(k) = \int_0^\infty r^{\frac{3}{2}} n(r) J_{\frac{1}{2}}(kr) dr \quad \text{and} \quad n(r) = \int_0^\infty k^{\frac{3}{2}} \hat{n}(k)) J_{\frac{1}{2}}(kr) dk. \tag{8}$$
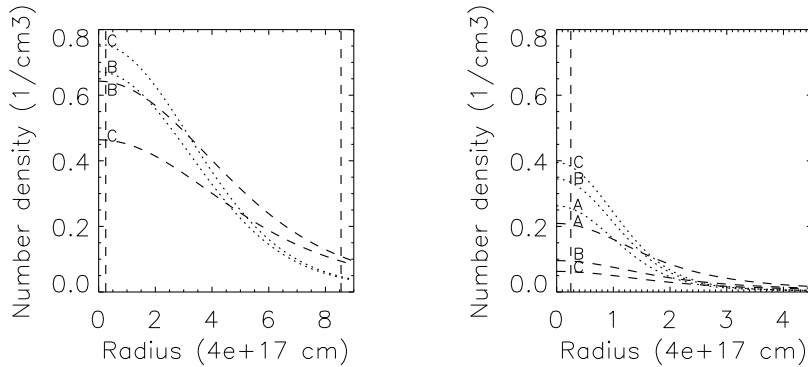
Figure 2: *Abundances of a tracer as a function of the radius. Line coding as in Fig. 1. $\tau_c = 10^6 year$, the diffusivities are $4x10^{22}$ (A), 10^{23} (B) and $1.6x10^{23}$ (C) $cm^2 s^{-1}$ Left: Gaussian Right: Gaussian with lower standard deviation*

In the superdiffusive case we assumed Kolmogorov spectra ($\zeta = \frac{3}{2}$) and scaled the turbulent diffusivity according to the formula $D = D_0(\frac{k}{k_0})^{-\frac{4}{3}}$. We only needed defining k_0 to know what size of eddies can assign to D_0, in the simple diffusive case used diffusion coefficient.

To simplify the calculations we made the equations dimensionless and approximated the initial density distribution of the tracer with Gaussian distributions. One of them has the same value at the outer border of the cloud like the real reciprocal distribution, but the total mass of it greater, the other has the same total mass, but its outer border is at the half of the real value. We performed our calculations with different diffusivities and characteristic times in both cases, concentrating particularly on the difference between the diffusive and superdiffusive case.

The results from the Gaussian distribution approximation show that further studies are warranted because the difference between these two cases approaches a factor of two in certain parts of the cloud. This can be seen better on the Gaussian distribution with lower standard deviation (see Fig. 1). It is also visible that with increasing diffusivity the difference between the diffusive and superdiffusive cases also increases (see Fig. 2). However this difference is the largest in the innermost part of the cloud; there, as we have mentioned above, the turbulence has little effect, so our approximation is less suitable within the
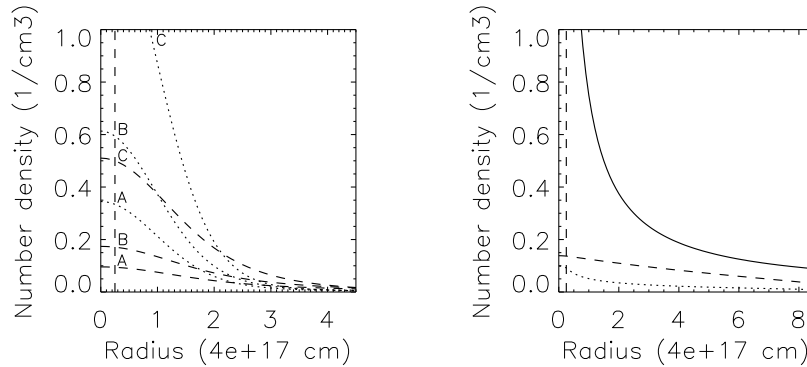
Figure 3: *Abundances of a tracer as a function of the radius. Line coding as in Fig. 1. Left: Gaussian with lower standard deviation, $D = 10^{23} cm^2 s^{-1}$, the characteristic times are 10^6 (A), 7.6×10^5 (B) and 1.2×10^5 (C) year. Right: real, $\tau_c = 10^6$ year, $D = 10^{23} cm^2 s^{-1}$*

radius 10^{17} cm. The difference between the two cases also increases with larger characteristic time (see Fig. 3 on the left side). Finally we made our calculations using a real reciprocal number density profile of a tracer, after Xie et al. (1995), within the above mentioned radius with constant density. The obtained results show that in this case also there are similar remarkable differences (see Fig. 3 on the right side).

4 Conclusion

We studied the effect of the superdiffusion on fractional abundances in molecular clouds using a simplified model. Approximating the initial tracer distribution with a Gaussian, and using constant density of H_2, the received results show that there are significant differences between the diffusive and superdiffusive case. In the future we plan to study this question dropping the assumption of a constant distribution of H_2 - since a gradient in the density of the main component affects the fractional abundance of a tracer (see Equation (1), where $f_i = n_i / n_{H_2}$) - looking for a non-stationary solution of the diffusion equation.

Acknowledgement

References

Herbst, E., Klemperer, W., 1973, ApJ, 185, 505

Herbst, E., Leung, C. M., 1989, ApJS, 69, 271

Leung, C. M., Kutner, M. L., Mead, K. N., 1982, ApJ, 262, 583

Leung, C. M., Herbst, E., Heubner, W. F., 1984, ApJS, 56, 231

Millar, T. J. Herbst, E., 1990, A&A, 231, 466

Petrovay, K., 1999, Space Sci. Rev., 95, 9

Larson, R. B. 1980, MNRAS, 194, 809

Scalo, J., Elmegreen, B. G., 2004, ARA&A, 42, 275

Sneddon, I. N., 1951, Fourier transforms (McGraw-Hill Book Company, New York), p. 62

Willacy, K., Langer, W. D., Allen, M., 2002, ApJ, 573, L119

Xie, T., Allen, M., Langer, W. D., 1995, ApJ, 440, 674

Yate, C. J., Millar, T. J., 2003, A&A, 399, 553

Evolution of Luminous Red Galaxies based on SDSS data

Dávid Koronczay[1]

[1] Eötvös University, Department of Physics, H-1518 Budapest, Pf. 32, Hungary

E-mail: [1]`koronczay@complex.elte.hu`

Abstract

We compared the broadband colors of different simulated galaxies with $\sim 10^5$ luminous red galaxies from the Sloan Digital Sky Survey to obtain constraints for the possible star formation histories of this type of galaxies. The simulation was done using the GALAXEV evolutionary stellar population synthesis code. Our results are consistent with these objects having solar metallicities, having formed 11 Gyr before present and evolving passively, without significant star formation since then.

Keywords: *Galaxies: evolution*

1 Introduction

The Sloan Digital Sky Survey (York et al., 2000) contains a large set of luminous, red galaxies. Their study can be important for a number of scientific goals. The evolution of these systems is a probe of galaxy formation theories. They are strongly correlated with clusters, making them an ideal tool for detecting and studying clusters. Finally, they are among the most luminous galaxies of the Universe, and sample large cosmological volumes, interesting for the study of large scale structure.

2   The data

The SDSS is a photometric and spectroscopic survey using a 2.5-m telescope, mapping π steradians of the sky. It has as of yet photographed 180 million objects using five broadband filters – u, g, r, i, z (Fukugita et al., 1996) – and took spectra of some of them, including 560 000 galaxies. Eisenstein et al. (2001) selected a sample of luminous red galaxies (LRGs) on the basis of color and magnitude to yield a sample of luminous intrinsically red galaxies. We used a sample of LRGs from the latest SDSS data (Adelman-McCarthy et al., 2006), using the same color cuts, that is *Cut I* for $z \lesssim 0.4$:

$$r_{\mathrm{Petro}} < 13.1 + c_{\parallel}/0.3 \tag{1}$$

$$r_{\mathrm{Petro}} < 19.2 \tag{2}$$

$$|c_{\perp}| < 0.2 \tag{3}$$

$$\mu_{r,Petro} < 24.2\,\mathrm{mag\ arcsec}^{-2} \tag{4}$$

$$r_{\mathrm{PSF}} - r_{model} > 0.3, \tag{5}$$

where (1) and (2) are luminosity tresholds, (3) selects the galaxy locus, (4) constrains the surface brightness and (5) is for star-galaxy separation, and

$$\mu_{r,Petro} = r_{Petro} + 2.5\log_{10}(2\pi R_{50}^2)$$

$$c_{\perp} = (r - i) - (g - r)/4 - 0.18$$

$$c_{\parallel} = 0.7(g - r) + 1.2((r - i) - 0.18).$$

Similarly the sample can be extended with an other color selection for $z \gtrsim 0.4$, *Cut II*:

$$r_{\mathrm{Petro}} < 19.5$$

$$c_{\perp} > 0.45 - (g - r)/6$$

$$g - r > 1.30 + 0.25(r - i)$$

$$\mu_{50} < 24.2\,\mathrm{mag\ arcsec}^{-2}$$

$$r_{\mathrm{PSF}} - r_{\mathrm{model}} > 0.5.$$

These selections, after rejecting some outliers, leave us with 120 000 LRGs, with redshifts $0 < z < 0.6$. However, since they are based on color cuts, and we're about to derive conclusions precisely from the colors of these objects, it

seems approproate to create a control sample with a different method. For not too far galaxies we can select a sample of early type galaxies using morphological and spectral criteria according to Bernardi et al. (2003):

- $C = r_{90}/r_{50} > 2.5$ in i (concentration index) [1]

- $L_{DeV} > 1.03 L_{Exp}$ (de Vaucouleurs fit vs. exponential fit likelihood)

- eClass < -0.1 (PCA classification typical of early type galaxies)

- zWarning $= 0$ (good spectroscopy)

- S/N > 10 (good signal-to-noise spectroscopy)

This sample extends out only to about $z \sim 0.3$ if we want to have reliable quality. The colors of these objects evolves with redshift, both because of that redshifting results in the filters sampling a different portion of the spectra and because of the evolution of the objects with time. Comparing the median colors in $g - r$, $r - i$ and $i - z$ as functions of redshift for the two sample shows that they agree fairly well. Figure 1 shows the two samples compared in $r - i$.
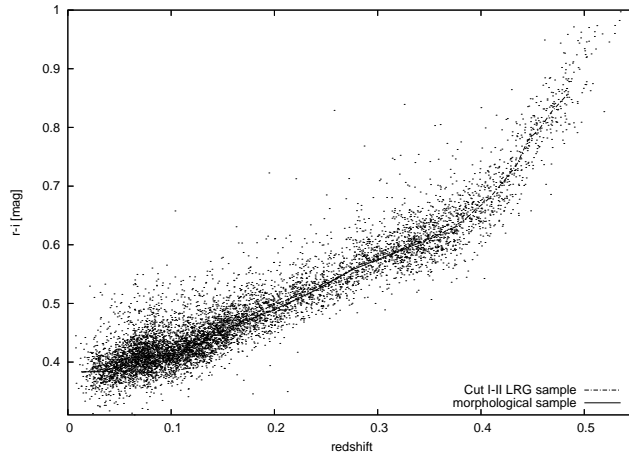
Figure 1: *Comparison of the two kind of samples' median colors ($r - i$ in this case) as a function of redshift. Dots are a random subsample of the individual objects.*

---

[1] According to Strateva et al. (2001), $C > 2.6$ are mostly early type systems.

3 Stellar population synthesis

In order to derive physical properties from the evolution of broadband colors of the sample, we compared them to the colors of simulated galaxies. For this purpose we used the GALAXEV stellar population synthesis code (Bruzual & Charlot, 2003). This is a semiempirical simulation based on the Geneva and Padova stellar evolutionary tracks, which allows one to compute the spectral evolution of single or multiple stellar populations, in wide ranges of metallicity and age. Dust content may also be varied, and different star formation histories can be chosen, apart from the "single burst" model, like exponentially declining star formation rate or multiple bursts.

We examined models with metallicities $0.4Z_\odot$, $1Z_\odot$, $2.5Z_\odot$, ages 7-13 Gyr, constant SFR, exponentially declining SFRs and a single burst model. After generating the spectra, redshift them by $0 < z < 0.5$, apply the SDSS filters, calculate $g-r$, $r-i$ and $i-z$ colors, thus constructing the color-redshift relation for each model. When we redshift an object to $z > 0$, we also place it back in time into the younger Universe, so its age has to be corrected with the light travel time corresponding to that redshift.

After having the curves of the photomtric evolution of the simulated galaxies, to test their agreement with the sample data, we calculated χ^2 between the median of the color-redshift relations of the sample and each model.

3.1 Results

The data are best fit with an 11 Gyr old solar metallicity ($Z_\odot$) single burst (passively evolving) model. Other metallicities (available in the synthesis code) are inconsistent with the data. Also, any significant star formation in the past 5 Gyr would distort their colors far from what we observe. The dust content should be $\mu < 0.1$ (see Bernardi et al. (2003) for the definition of μ).

However, a few problems should be noted here. The metallicity can only be varied in large steps, which prevents a better fit. Even worse is that we face the well known age-metallicity degeneration. Thirdly, the spectral synthesis is never perfect – actually, we could create better fits by adding some peaks to the model spectra "by hand".
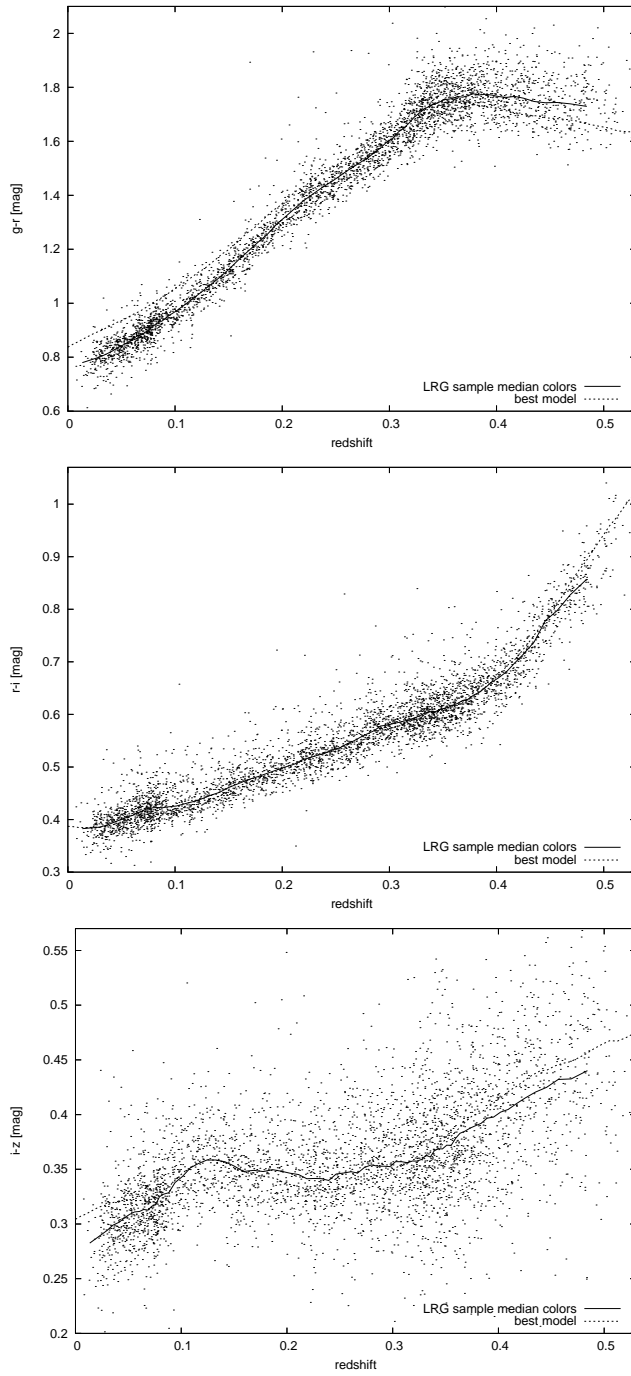
Figure 2: *Colors versus redshift, best fitting model copared to the LRG sample*

4 Distribution of physical properties

At a given redshift, the objects of our sample have significantly different colors, as opposed to what would be expected from a perfectly homogenous group of galaxies. This scatter of colors, which turns out to be gaussian, is clearly partly the result of instrumental errors, but it may also be caused by the difference between their physical properties such as age or metallicity. Since the SDSS database contains an estimation of the magnitude errors, we can test this scatter of colors in our sample against that of a simulated set of objects. In the simulated set, each object had identical physical properties, and they were spersed in redshift to have the same distribution as our sample data. Then we applied a random gaussian error to their photometric magnitudes, where the parameter of the gaussian was derived from the SDSS photometric errors in the database. The *color* errors are calculated from:

$$\delta(m_i - m_j)^2 = (\delta m_i)^2 + (\delta m_j)^2 - 2C_{ij}, \qquad (6)$$

where m_i and m_j are the ith and jth magnitudes that define the color, and C_{ij} is the covariance matrix of the magnitudes, should such a correlation exist (otherwise zero).

Figure 3 shows the scatter of colors as a function of redshift. The observational errors clearly don't explain fully the observed scatter.

Therefore we changed the simulation, and introduced a scatter in the input parameters of the simulation (while keeping adding the observational errors). We varied the amount of the scatter to find the best fit to the data.

4.1 Results

Figure 4 shows the observed scatters and the best fitting simulation. The observed scatter constrains the possible scatter of the formation ages of the LRG sample objects, to less than ± 1.5 Gyr. Unfortunately the value of metallicity can only be changed in discrete and large steps, so we couldn't repeat the same test for metallicities. But even if we could, there's a caveat here. We presumed that the physical parameters are independent. However, this doesn't necessarily be true – see "age-metallicity conspiracy", Worthey et al. (1995). If we can't account for the correlation term between them, we might misjudje the ranges of these parameters.
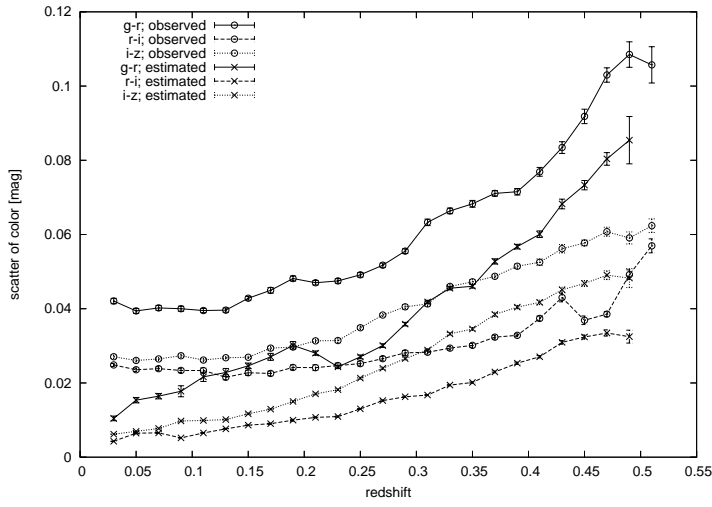
Figure 3: *The three pair of functions ($g - r$, solid; $r - i$, dashed; $i - z$, dotted) would ideally run together (pairwise), if the source of the observed scatter of colors (circles) was the photometric error (xs)*
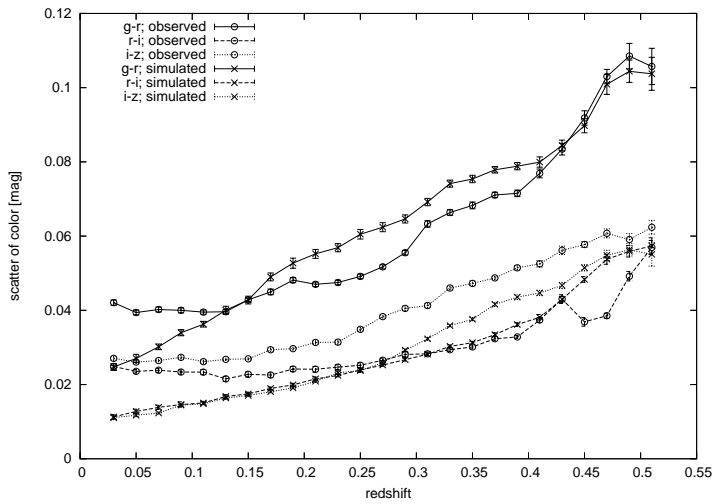
Figure 4: *Same as Figure 3, except that the ages of the simulated objects are also varied (before applying photometric errors).*

5   Summary

We showed that the LRGs in the SDSS data show broadband colors that are consistent with an 11 Gyr old, passively evolving population, having solar metallicity. The distribution of their physical properties are also limited by the observations.

According to (Scranton et al., 2005), the photometric errors in the SDSS may have to be revised. They found the magnitude errors to be slightly underestimated, while also measuring the correlation of the different color bands (which is not zero), which term (see equation (6)) can now be used to calculate proper color errors. Although their measurements don't extend to bright enough objects to be used with our samples right now, they point to the possibility that later a much tighter constraint may be given to the distribution of the physical properties.

The age-metallicity-dust degeneration can possibly be resolved either by calculating metallicity indices from the spectra, or other indices calculated from broader bandpasses of the spectra, such as in Kauffmann et al. (2003).

Acknowledgement

References

Adelman-McCarthy, J. K., et al. 2006, ApJS, 162, 38

Bernardi, M., et al. 2003, AJ, 125, 1817

Bruzual, G., & Charlot, S. 2003, MNRAS, 344, 1000

Eisenstein, D. J., et al. 2001, AJ, 122, 2267

Fukugita, M., Ichikawa, T., Gunn, J. E., Doi, M., Shimasaku, K., & Schneider, D. P. 1996, AJ, 111, 1748

Kauffmann, G., et al. 2003, MNRAS, 341, 33

Scranton, R., et al. 2005, astro-ph/0508564

Strateva, I., et al. 2001, AJ, 122, 1861

Worthey, G., Trager, S. C., & Faber, S. M. 1995, ASP Conf. Ser. 86: Fresh Views of Elliptical Galaxies, 86, 203

York, D. G., et al. 2000, AJ, 120, 1579

Interstellar Reddening of Type Ia Supernovae

Nikoletta Sipos[1], József Vinkó[2]

[1] Eötvös University, Department of Astronomy, H-1518 Budapest, Pf. 32, Hungary
[2] Department of Optics & Quantum Electronics, University of Szeged, H-6701, Pf. 406, Hungary

E-mail: [1]`niki@csoma.elte.hu`, [2]`vinko@physx.u-szeged.hu`

Abstract

We re-investigate the Lira-Phillips relation of Type Ia supernovae and its use for determination of reddening of individual SNe Ia. We use a more recent, more extensive dataset of SNe Ia with negligible reddening, and attempt to refine the prediction of the intrinsic B-V color index. We find that the Lira-Phillips relation is valid, but the dispersion of the intrinsic B-V colors is substantial. The present data may suggest slightly redder intrinsic colors, thus, the previously calculated total extinctions (and the corresponding distance moduli) should be decreased by ~ 0.19 mag.

Keywords: *supernovae: general, interstellar reddening*

1   Introduction

Type Ia supernovae (SNe) have been succesfully used as distance indicators, even to cosmological distances, due to their extreme brightness (Perlmutter et al. (1999), Riess et al. (2004)). Although their peak luminosities have significant dispersion, there is a relation between the peak luminosity and the decay rate of the light curve. This makes it possible to calibrate the luminosity of a given SN from its observed light curve, and reduce the light curve dispersion. In order to do so, one needs i) a large sample of SNe with independently known distances, observed in the same photometric system, and ii) information about all the effects that distorts the photons coming from the SNe while reaching the

Earth. One of the most important effects is due to the presence of interstellar dust: interstellar reddening (and extinction). Unfortunately, the measurement of reddening is quite difficult, mostly because our knowledge about the distribution and characteristics of dust in other galaxies is limited. It is usually assumed that the extragalactic dust has similar properties as that in the Milky Way, i.e. the total light absorption is related to the selective absorption via the galactic reddening law: $A_V = 3.1 \cdot E(B - V)$, and the selective absorption in different colors have the same ratio as in the Milky Way.

2   Determination of supernova reddenings

Reddening of supernovae has two components: $E(B - V)_{Gal}$ is caused by the dust present in our galaxy along the line of sight, $E(B - V)_{Host}$ is the result of the dust of the supernova's own galaxy. The first one can be relatively easily determined thanks to the reddening map of the Milky Way Galaxy made by Schlegel et al. (1998).

Obtaining host galaxy reddening values is considerably more complicated. Fortunately, SNe Ia do not occur in dense, dusty environment (unlike Type II SNe) indicated by the absence of lines originated from circumstellar matter in the spectra of SNe Ia. Thus, the reddening of SNe Ia is usually caused by the dust distributed along the line of sight.

To illustrate this general picture, we have computed a Monte Carlo simulation of the distribution of the reddening of SNe Ia. We have defined a model galaxy with similar (exponential) dust distribution such as in the Milky Way, and placed SNe randomly within the galaxy. The model galaxy has been put at random positions and distances with random inclination, and it was "observed" through the dust projected into the line of sight. Computing the total reddening both the dust in the Milky Way and in the host galaxy has been taken into account.

Fig. 1 shows the computed apparent magnitudes of model SNe Ia (open circles) with the observed data (SNe Ia before 2002) against the distance. The line indicates the true distance modulus of a fiducial SN Ia as a function of distance when there is no interstellar extinction. The distribution of the observed and computed points are very similar. This means that the scattering of the observed data in Fig.1 can be reasonably explained by interstellar extinction that varies from SN to SN.

If we had a large sample of *observed* SNe Ia, we could estimate the expected value of the reddening statistically, using the distribution in Fig. 1. However, in
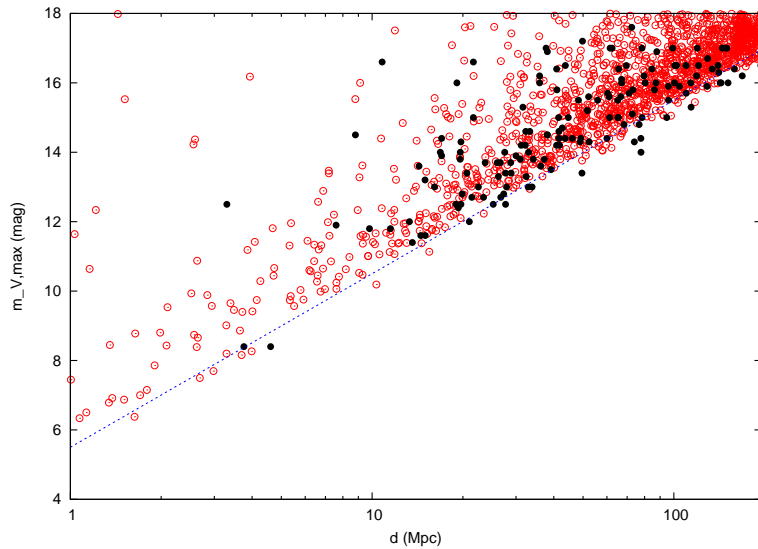
Figure 1: *Apparent magnitudes as a function of distance. Filled circles represent the observed data while the open circles are from the Monte Carlo simulation. The dotted line describes the extinction-free magnitude - distance relation (i.e. the true distance modulus) for SNe Ia with constant peak brightness. It is visible that the observed and computed data have the same distribution, thus, the dispersion of the observed data is mostly due to interstellar extinction.*

reality, such observational sample is not at our disposal. Therefore, it is important to determine the reddening of individual SNe directly from observations.

There are several methods to estimate individual reddenings. One is based on direct spectroscopic measurement of interstellar Na I D lines (Munari & Zwitter (1997)). The Multi-Color Light Curve Shape (MLCS) method (Riess et al. (1996)) determines the reddening of SNe Ia by comparing the observed magnitudes with template light curves. This method is based on the empirical correlation between the intrinsic color and the light curve shape of SNe Ia. The third method is the Lira-Phillips relation (Phillips et al. (1999)) that will be presented in detail in the next section.

2.1   The Lira–Phillips relation

Phillips et al. (1999) demonstrated that the $B - V$ color curves of SNe Ia that suffered negligible interstellar extinction evolve in an impressively similar fashion between $30 - 90$ days after their maximum light (measured in V filter). During this interval the $B - V$ color evolution seems to be independent of light curve shape and decline rate (which is connected with the similarity of the spectra at these phases). Thus, measuring the $B - V$ curve of a reddened SN Ia and comparing it with the expected color evolution, one can get good constraints on the amount of interstellar reddening for a particular SN.

Since it is a purely empirical method, it must be calibrated empirically. One needs many unreddened SNe Ia in order to get a fiducial $B - V$ curve between $30 \leq t \leq 90$ days. Phillips et al. (1999) applied three basic criteria for selecting such SNe:

1. the absence of interstellar Na I and Ca II lines in the spectra

2. the Hubble-type of the host galaxy is E or S0

3. the Hubble-type of the hist galaxy is S or SB, but the SN is located outside the spiral arms and dust lanes in the disk.

These criteria resulted in four SNe (1992A, 1992bc, 1992bo, 1994D) that Pillips et al. (1999) could use for calibration. The least-squares fit to their observed colors gave the following result for $30 \leq t \leq 90$ days past V maximum:

$$(B - V)_0 = 0.725 - 0.0118(t_V - 60), \tag{1}$$

where t_V is the elapsed time (in days) since V maximum.

2.2   Improving the Lira-Phillips relation

Since 1999 many more SNe Ia have been discovered, observed and published. Thus, it may be possible to improve the Lira-Phillips relation based on these more recent data. We have surveyed the literature and collected the data of potential SNe Ia. The original selection criteria listed above have been supplemented by a new one: the reddening is assumed to be negligible if it was below 0.03 according to the MLCS method (which is less than the uncertainty of the reddening determination in this method). These criteria resulted in the selection of 10 more SNe Ia beside the 4 one used by Phillips et al. (1999). The names and the basis of their selection are listed in Table 1.

Table 1: *The selected sample of SNe Ia with negligible reddening. The applied selection criteria are indicated in columns 2 - 5.*

SN	Selection criteria				References
	Morphology of host	Position of SN in host	Spectrum	MLCS	
1992A		+	+		1
1992bc		+	+		2
1992bo		+	+		2
1994D		+	+		1, 3, 4, 5
1992al		+		+	2
1993ae	+			+	6, 7
1995D	+		+		1, 6, 7
1996X	+		+		6, 8
1997cn	+			+	9, 10
1998de	+		+		9, 11
1998dx		+		+	9
1999ej	+			+	9
2000dk	+			+	9
2003du		+	+		12

References: (1) Altavilla et al. (2004), (2) Hamuy et al. (1996), (3) Richmond et al. (1995), (4) Patat et al. (1996), (5) Tsvetkov & Pavlyuk (1995), (6) Riess et al. (1999), (7) Ho et al. (2001), (8) Patat et al. (1996), (9) Jha et al. (2006), (10) Turatto et al. (1998), (11) Modjaz et al. (2001), (12) Anupama et al. (2005)

The color curves of the selected SNe are plotted in Fig. 2. A least squares fit to the same data range as above resulted in

$$(B - V)_0 = 0.781 - 0.0122(t_V - 60). \qquad (2)$$

This new relation has essentially the same slope as the original one (Eq. 1), but a slightly higher constant term.
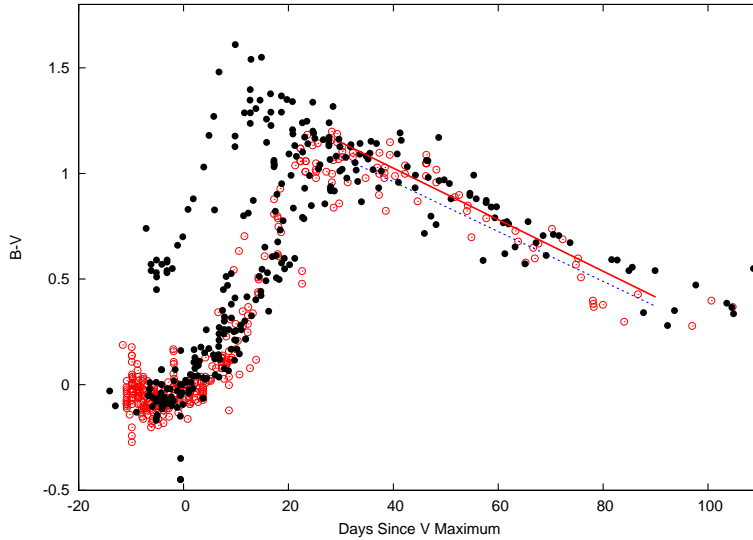
Figure 2: *B-V color evolution of the selected SNe. Open circles indicate the data used originally by Phillips et al. (1999), while filled circles represent the additional SNe (see Table 1 for references). The dashed line is the original relation (Eq. 1) and the solid line is the new calibration (Eq. 2).*

3   Discussion

From Fig. 2 it is visible that the new observational data of reddening-free SNe Ia confirm the existence of the Lira-Phillips relation. However, the data show considerable scatter (~ 0.3 mag) in the $30 \leq t \leq 90$ days interval that cannot be attributed purely to observational noise. This dispersion is significantly lower than during the early phases of the evolution of SNe Ia, thus, the original idea of the Lira-Phillips relation is still valid. But the $(B - V)$ color evolution of SNe Ia is clearly not as homogeneous as it was previously thought. There is a dispersion from SN to SN that causes a ~ 0.3 mag overall uncertainty in the intrinsic $(B-V)$ color, that propagates further into the reddening determination.

Based on the available data, the new relation (Eq. 2) predicts an intrinsic $(B - V)$ that is 0.06 mag redder than the one based on the original relation (Eq. 1). From the standard reddening law this corresponds to $\Delta A_V \sim 0.19$ mag increase of the extinction in the V band. If this is indeed true, then the SNe Ia

distance moduli that have been determined assuming the reddenings from Eq. 1, must be decreased by about 0.19 mag. It may also affect the calibration of the MLCS method, since it is based on individual reddenings such as those from the Lira-Phillips relation. Since many of the high-z SNe distances are based on the MLCS method, a reddening correction might further incorporate into the cosmological distances. However, this correction is not significant at present, because the difference between Eq. 1 and 2 is well below the 0.3 mag dispersion discussed above. Many more SNe Ia are needed to refine the reddening-free sample and further clarify this important issue.

Acknowledgement

References

Perlmutter, S., et al. 1999, ApJ, 517, 565

Riess, A. G., et al. 2004, ApJ, 607, 665

Schlegel, D. J., Finkbeiner, D. P., & Davis, M. 1998, ApJ, 500, 525

Phillips, M.M., Lira, P., Suntzeff, N. B., Schommer, R. A., Hamuy, M., & Maza, J. 1999, AJ, 118, 1776

Riess, A. G., Press, W. H., & Kirshner, R. P. 1996, ApJ, 473, 88

Munari, U., & Zwitter, T. 1997, A&A, 318, 269

Riess, A. G., et al. 1999, AJ, 117, 707

Jha, S., et al. 2006, AJ, 131, 527

Altavilla, G., et al. 2004, MNRAS, 349, 1344

Anupama, G. C., Sahu, D. K., & Jose, J. 2005, A&A, 429, 667

Hamuy, M., et al. 1996, AJ, 112, 2408

Richmond, M. W., et al. 1995, AJ, 109, 2121

Patat, F., Benetti, S., Cappellaro, E., Danziger, I. J., della Valle, M., Mazzali, P. A., & Turatto, M. 1996, MNRAS, 278, 111

Tsvetkov, D. Y., & Pavlyuk, N. N. 1995, Astronomy Letters, 21, 606

Ho, W. C. G., Van Dyk, S. D., Peng, C. Y., Filippenko, A. V., Leonard, D. C., Matheson, T., Treffers, R. R., & Richmond, M. W. 2001, PASP, 113, 1349

Salvo, M. E., Cappellaro, E., Mazzali, P. A., Benetti, S., Danziger, I. J., Patat, F., &
    Turatto, M. 2001, MNRAS, 321, 254

Turatto, M., Piemonte, A., Benetti, S., Cappellaro, E., Mazzali, P. A., Danziger, I. J.,
    & Patat, F. 1998, AJ, 116, 2431

Modjaz, M., Li, W., Filippenko, A. V., King, J. Y., Leonard, D. C., Matheson, T.,
    Treffers, R. R., & Riess, A. G. 2001, PASP, 113, 308

Irradiated closed Friedmann brane-worlds

Zoltán Keresztes[1], Ibolya Képíró[2]

[1] Departments of Theoretical and Experimental Physics, University of Szeged, 6720 Szeged, Dóm tér 9, Hungary
[2] Blackett Laboratory, Imperial College, Prince Consort Road, London SW7 2BW, UK
E-mail: [1]`zkeresztes@titan.physx.u-szeged.hu`, [2]`ibolya.kepiro@imperial.ac.uk`

Abstract
We consider the evolution of a closed Friedmann brane irradiated by a bulk black hole. Both absorption on the brane and transmission across the brane are allowed, the latter representing a generalization over a previously studied model. Without transmission, a critical behaviour could be observed, when the acceleration due to radiation pressure and the deceleration introduced by the increasing self-gravity of the brane roughly compensate each other. We show here that increasing transmission leads to the disappearance of the critical behaviour.
Keywords: *cosmology with extra dimensions, brane-worlds, radiating black holes*

1 Introduction

According to the original idea of Kaluza and Klein, new and compact spatial dimensions, commensurable with the Planck scale, can be introduced in the attempt to describe various fundamental interactions. The possibility of a non-compact extra dimension has been advanced only recently [Randall and Sundrum (1999)]. The so-called brane cosmological models contain our physical world as a hypersurface (the brane), embedded into a warped five-dimensional bulk space-time, in which gravity acts. Its dynamics in the bulk is determined by the Einstein-equation, however on the brane we see only a projection of this

dynamics. Consequently, on the brane, gravitational dynamics is modified as compared with general relativity. A modified Einstein equation for the most general case, allowing for both exotic energy in the bulk and asymmetric embedding, was given in [Gergely (2003)] (and for a more generic class of models, containing induced gravity contributions in [Gergely and Maartens (2005)]). The predictions of general relativity are recovered at low energies. With cosmological symmetries, the brane represents our observable universe. Branes with various other symmetries were found, like an Einstein static brane [Gergely and Maartens (2002)], a Kantowski-Sachs type homogeneous brane [Gergely (2004)] or a Gödel brane [Barrow and Tsagas (2004)].

Cosmological branes embedded in a bulk with radiation escaping from the brane were studied in [Langlois et al. (2002)], [Gergely et al. (2004)], [Jennings and Vernon (2005)] and [Langlois (2005)]. The scenario with a bulk black hole emitting Hawking radiation (its expression being derived for closed universes with $k = 1$ in [Emparan et al. (2000)], [Hemming and Keski-Vakkuri (2001)] and [Guedens et al. (2002)]) was studied in detail in [Gergely and Keresztes (2006)]. There, only one black hole was considered, with its radiation completely absorbed by the brane. (A somewhat similar model, but with $k = 0$ was considered in [Jennings et al. (2005)]. There a bulk black hole is placed on each side of the brane and the radiation is completely transmitted.)
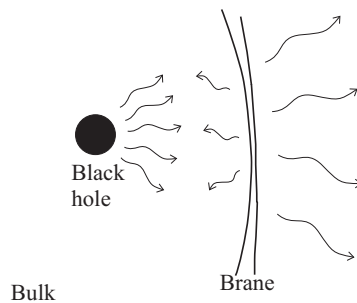
Figure 1: *The bulk contains an evaporating black hole. The radiation escaping this black hole is partially absorbed, partially reflected and partially transmitted across the brane.*

In [Gergely and Keresztes (2006)] the case of total absorption and no transmission was analyzed in detail. Two effects due to the radiation coming from the bulk were identified. First, radiation pressure on the brane accelerates its

outward motion, similarly as dark energy. Second, with the increasing amount of radiation absorbed, the self-gravity of the brane increases, contributing towards a recollapse. However both effects represent 10^{-4} order perturbations for the model without radiation. (We note that the asymmetry in the embedding produced by the presence of only one bulk black hole behaves as an other perturbation.)

In this paper we investigate the effect of including transmission into the model developed in [Gergely and Keresztes (2006)], cf. Fig. 1 (where the possibility of reflection is also raised). We keep a (partial) absorption on the brane, but continue to neglect the reflection, as in [Gergely and Keresztes (2006)], basically because there is no known exact solution with cosmological constant describing a cross-flow of radiation streams. Thus the five-dimensional Vaidya-anti de Sitter (VAdS5) spacetime describes both bulk regions, the one with, and the one without the black hole.

In order to distinguish among models with different transmissions, we introduce a transmission rate ε, zero for a total absorption, and one for a total transmission. The brane evolves cf. the energy balance, Friedmann- and Rachaudhuri equations [Gergely (2003)]. These equations, specified for the case $\varepsilon \neq 0$, are given in [Keresztes et al. (2006)]. In this paper we present some of the results of the numerical study on these equations, for different values of the transmission rate ε.

2   Numerical results

We assume that the brane is radiation dominated and its evolution stars at the apparent horizon of the bulk black hole. We choose the same initial data as in [Gergely and Keresztes (2006)].

Allowing the transmission across the brane, we encounter new features. First, the accumulated energy from the absorbed Hawking radiation on the brane will be smaller than in the case of total absorption. Second, the transmitted radiation does not contribute to the radiation pressure on the brane, which is also smaller.

In the case with zero transmission [Gergely and Keresztes (2006)], both the acceleration from the radiation pressure and the deceleration from the increase in the self-gravity of the brane were small perturbations of order 10^{-4}, which roughly cancel for the critical initial energy density. As in the presence of transmission the effects are even smaller, we again will plot only *differences*, taken in the radiating and non-radiating cases.

Figure 2 shows the evolution of the differences in the scale factor when the radiation is switched on and off, for vanishing transmission. The critical-like behaviour appears for $\widehat{\rho}_0 = 520$ (the quantity $\widehat{\rho}_0$ denotes a properly defined [Gergely and Keresztes (2006)] dimensionless initial brane energy density). For lighter branes the radiation pressure is the dominant effect, and the recollapse occurs later in the presence of the radiation. For heavier branes the increase in self-gravity dominates and the recollapse is speeded up.
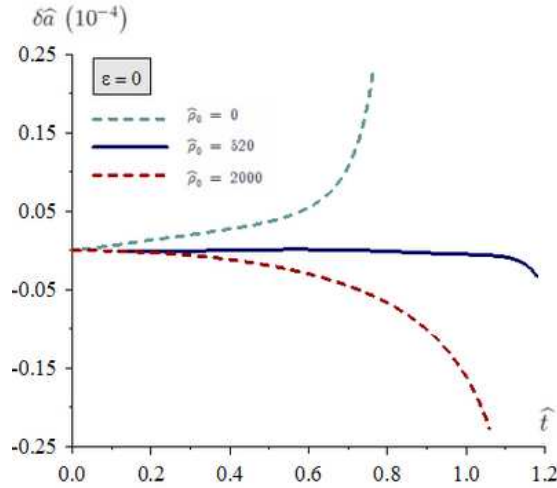
Figure 2: *The difference between the scale factors in the radiating and non-radiating cases for a fully absorbing brane. The critical-like behaviour is observed at $\widehat{\rho}_0 = 520$ (solid line). For small initial energy densities (e.g. $\widehat{\rho}_0 = 0$, upper dotted line), the pressure of the Hawking radiation is dominant. For high initial energy densities ($\widehat{\rho}_0 = 2000$, lower dotted line) the increase of self-gravity due to absorption overtakes the radiation pressure.*

On Figure 3, plotted for the transmission rate 0.2 we see similar behaviours. There are however two major differences, both due to the appearance of the transmission. First, the critical value of the initial brane energy density is decreased, as compared with the case of total absorption. Second, the sinusoidal-like pattern of the critical curve is much more accentuated, its amplitude is increased considerably.

Eventually, with increasing transmission rate the critical-like behaviour com-
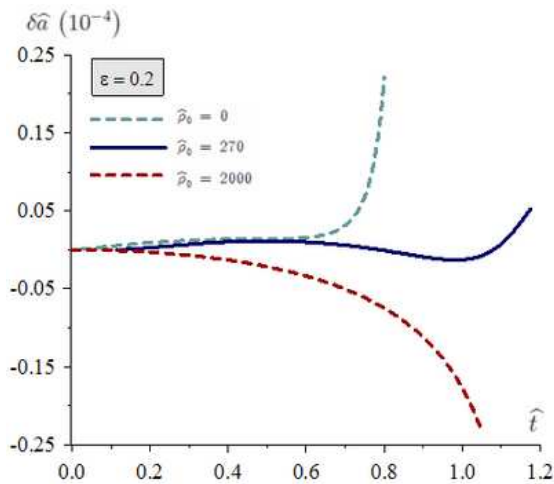
Figure 3: *For a higher transmission rate of $\varepsilon = 0.2$, the critical brane initial energy density is less ($\widehat{\rho}_0^{crit} = 270$) than for the case of total absorption. The amplitude of the sinusoidal evolution of $\delta\widehat{a}$ is higher.*

pletely disappears. This is illustrated on Figure 4 for $\varepsilon = 0.4$.

3   Concluding remarks

We have considered a brane-world scenario with a brane embedded into a bulk impregnated by radiation. The radiation is emitted by an evaporating bulk black hole. When this radiation hits the brane, it is partially absorbed and partially transmitted across the brane.

Since there is one black hole in the bulk, the embedding of the brane is asymmetric. It was shown in [Gergely and Keresztes (2006)], that this asymmetry is not able to change the recollapsing fate of the closed Friedmann brane. Neither does the completely absorbed Hawking radiation.

In this paper, we have generalized the above statements for branes allowing transmission. As was the case with total absorption, with a nonvanishing transmission rate the absorbed radiation keeps to increase the self-gravity of the brane, contributing towards deceleration, while the radiation pressure contributes towards the acceleration of the brane.
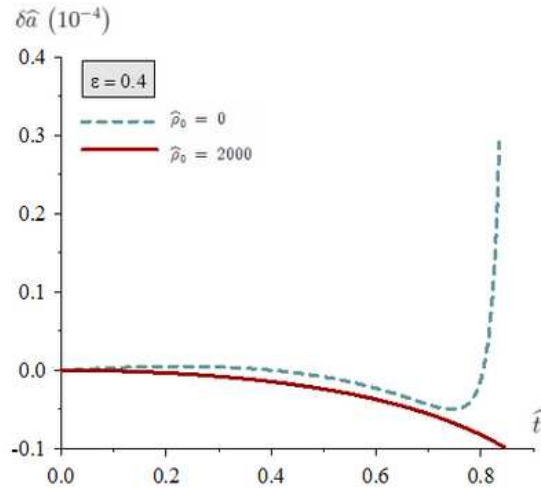
Figure 4: *For the transmission rate $\varepsilon = 0.4$ no critical-like brane evolution can be observed. For all values of the initial energy density the radiation drives the brane towards a faster recollapse.*

Our main result is that there are different behaviours depending on the actual value of ε. Whether the Hawking radiation contributes toward the recollapse of the brane-world universe or it speeds it up, depends on both the transmission rate and the brane energy density.

For small transmission rates and properly chosen initial brane energy density, the two effects can compensate each other. We have shown that by increasing the transmission rate, the critical-like behaviour disappears. In conclusion, a high transmission rate speeds up the recollapse, regardless of the value of the initial brane energy density.

4   Acknowledgement

References

Barrow, J. D., Tsagas, C. G. 2004 Phys. Rev. D, 69, 064007

Emparan, R., Horowitz, G. T., Myers, R. C. 2000 Phys. Rev. Lett., 85, 499

Gergely, L. Á., Maartens, R. 2002 Class. Quantum Grav., 19, 213

Gergely, L. Á. 2003 Phys. Rev. D, 68, 124011

Gergely, L. Á. 2004 Class. Quantum Grav., 21, 935

Gergely, L. Á., Leeper, E., Maartens, R. 2004 Phys. Rev. D, 70, 104025

Gergely, L. Á., Maartens, R. 2005 Phys. Rev. D, 71, 024032

Gergely, L. Á., Keresztes, Z. 2006 J. Cosmol. Astropart. Phys., JCAP01, 022

Guedens, R., Clancy, D. and Liddle, A. R. 2002 Phys. Rev. D, 66, 043513

Hemming, S., Keski-Vakkuri, E. 2001 Phys. Rev. D, 64, 044006

Jennings, D., Vernon, I. R. 2005 J. Cosmol. Astropart. Phys., JCAP07, 011

Jennings, D., Vernon, I. R., Davis, A.-C., van de Bruck, C. 2005 J. Cosmol. Astropart. Phys., JCAP04, 013

Keresztes, Z., Képíró, I., Gergely, L. Á. 2006 Semi-transparent brane-worlds, in preparation

Langlois, D., Sorbo, L., Rodríguez-Martínez, M. 2002 Phys. Rev. Lett.89, 171301

Langlois, D. 2005 [hep-th/0509231]

Randall, L., Sundrum, R. 1999 Phys. Rev. Lett., 83, 4690

WEAK GRAVITATIONAL LENSING IN BRANE-WORLDS

László Á. Gergely[1], Barbara Darázs[2]

Departments of Theoretical and Experimental Physics, University of Szeged, 6720 Szeged, Dóm tér 9, Hungary

E-mail: [1]gergely@physx.u-szeged.hu, [2]dbarbi@titan.physx.u-szeged.hu

Abstract
We derive the deflection angle of light rays caused by a brane black hole with mass m and tidal charge q in the weak lensing approach, up to the second order in perturbation theory. We point out when the newly derived second order contributions become important.

Keywords: *brane black holes and stars, gravitational lensing*

1 Introduction

The possibility of allowing gravitation to exist in a more than four-dimensional non-compact space-time [Randall and Sundrum (1999)], while keeping the other interactions locked in four space-time dimensions, has raised interesting new perspectives in the solvability of the hierarchy problem and in cosmological evolution. This hypothesis has led to alternative explanations for both dark energy (see for example [Deffayet (2001))] and dark matter ([Mak and Harko (2004)], [Pal at al. (2005)] and [Pal (2005)]). The simplest so-called brane-world model is five-dimensional. Gravitational dynamics on the four-dimensional brane is governed by a modified Einstein equation, derived in full generality in [Gergely (2003)].

Gravitational lensing is one of the means by which the existence of brane-worlds can in principle be tested. A recent review in the topic can be found in

[Majumdar and Mukherjee (2005)]. In the context of brane-worlds, both weak [Kar and Sinha (2003)], [Majumdar and Mukherjee (2004)] and strong [Whisker (2005)] gravitational lensing were discussed.

Black holes on the brane are described by the *tidal* charged black holes, derived in [Dadhich et al. (2000)]:

$$ds^2 = -f(r)\,dt^2 + f^{-1}(r)\,dr^2 + r^2\left(d\theta^2 + \sin^2\theta d\varphi^2\right)\,. \tag{1}$$

The metric function f is given as

$$f(r) = 1 - \frac{2m}{r} + \frac{q}{r^2}\,. \tag{2}$$

These black holes are characterized by two parameters: their mass m and their tidal charge q. The latter arises from the bulk Weyl curvature (more exactly, from its "electric" part as compared to the brane normal).

Formally the metric (1) is the Reissner-Nordström solution of a spherically symmetric Einstein-Maxwell system in general relativity. There, however the place of the tidal charge q is taken by the square of the *electric* charge Q. Thus $q = Q^2$ is always positive, when the metric (1) describes the spherically symmetric exterior of an electrically charged object in general relativity. By contrast, in brane-world theories the metric (1) allows for any q.

The case $q > 0$ is in full analogy with the general relativistic Reissner-Nordström solution. For $q < m^2$ it describes tidal charged black holes with two horizons at $r_h = m \pm \sqrt{(m^2 - q)}$, both below the Schwarzschild radius. For $q = m^2$ the two horizons coincide at $r_h = m$ (this is the analogue of the extremal Reissner-Nordström black hole). In these cases it is evident that the gravitational deflection of light and gravitational lensing is decreased by q. Finally there is a new possibility forbidden in general relativity due to physical considerations on the smallness of the electric charge. This is $q > m^2$ for which the metric (1) describes a naked singularity. Such a situation can arise whenever the mass m of the brane object is of small enough, compared to the effect of the bulk black hole generating Weyl curvature, and as such, tidal charge. Due to its nature, the tidal charge q should be a more or less global property of the brane, which can contain many black holes of mass $m \geq \sqrt{q}$ and several naked singularities with mass $m < \sqrt{q}$.

For any $q < 0$ there is only one horizon, at $r_h = m + \sqrt{(m^2 + |q|)}$. For these black holes, gravity is increased on the brane by the presence of the tidal charge [Dadhich et al. (2000)]. Light deflection and gravitational lensing are stronger than for the Schwarzschild solution.

The metric (1) also describes compact stellar objects. In this case one does not have to worry about the existence or location of horizons, as they would lie inside the star, where an interior solution should replace the metric (1). The generic feature that a positive (negative) tidal charge is weakening (strengthening) gravitation on the brane, is kept.

In this paper we derive the deflection angle of light rays caused by brane black holes with tidal charge (1). Generalizing previous approaches [Kar and Sinha (2003)], [Majumdar and Mukherjee (2004)], we carry on this computation up to the second order in the weak lensing parameters. As the metric (1) is static, we consider only the second order gravielectric contributions, but no gravimagnetic contributions, which are of the same order and would appear due to the movement of the brane black holes. Gravimagnetic effects in the general relativistic approach were considered in [Schäfer and Bartelmanm (2005)].

2 Light propagation

Light follows null geodesics of the metric (1). Its equations of motion can be derived either from the geodesic equations, or from the Lagrangian given by $2\mathcal{L} = \left(ds^2/d\lambda^2\right)$ [Straumann (2004)] (λ being a parameter of the null geodesic curve). Due to spherical and reflectional symmetry across the equatorial plane, $\theta = \pi/2$ can be chosen. Thus

$$0 = 2\mathcal{L} = -f\left(r\right)\dot{t}^2 + f^{-1}\left(r\right)\dot{r}^2 + r^2\dot{\varphi}^2 \,. \tag{3}$$

(A dot represents derivative with respect to λ.) The cyclic variables t and φ lead to the constants of motion E and L

$$E = f\dot{t}\,, \qquad L = r^2\dot{\varphi}\,. \tag{4}$$

By inserting these into Eq. (3), passing to the new radial variable $u = 1/r$ and introducing φ as a dependent variable, we obtain

$$\left(u'\right)^2 = \frac{E^2}{L^2} - u^2 f\left(u\right)\,, \tag{5}$$

where a prime refers to differentiation with respect to φ.

Unless $u' = 0$ (representing a circular photon orbit), differentiation of Eq. (5) gives

$$u'' = -uf - \frac{u^2}{2}\frac{df}{du}\,, \tag{6}$$

For $f = 1$, when there is no gravitation at all (the metric (1) becomes flat), the above equation simplifies to $u'' + u = 0$, which is solved for $u = u_0 = b^{-1} \cos \varphi$. The impact parameter b represents the closest approach of the star on the straight line orbit obtained by disregarding the gravitational impact of the star (this is the viewpoint an asymptotic observer will take, as the metric (1) is asymptotically flat). The polar angle φ is measured from the line pointing from the centre of the star towards the point of closest approach. With $u' = 0$ at the point of closest approach, given in the asymptotic limit by $u = b^{-1}$, Eq. (5) with $m = 0 = q$ gives $b = L/E$.

3 Perturbative solution

Eq. (6), written in detail, gives

$$u'' + u = 3mu^2 - 2qu^3 \ . \tag{7}$$

For studying weak lensing, we look for a perturbative solution in series of the small parameters

$$\varepsilon = mb^{-1} \qquad \text{and} \qquad \eta = qb^{-2} \tag{8}$$

in the form

$$u = b^{-1} \cos \varphi + \varepsilon u_1 + \eta v_1 + \varepsilon^2 u_2 + \eta^2 v_2 + \varepsilon \eta w_2 + \mathcal{O}\left(\varepsilon^3, \eta^3, \varepsilon \eta^2, \varepsilon^2 \eta\right) \ . \tag{9}$$

The index on the unknown functions u_1, u_2, v_1, v_2 and w_2 counts the perturbative order in which they appear. By inserting Eq. (9) into the weak lensing equation (7) we obtain the relevant differential equations for the unknown functions. Up to the second order in both small parameters these are:

$$\varepsilon \quad : \qquad u_1'' + u_1 = 3b^{-1} \cos^2 \varphi \ , \tag{10}$$

$$\eta \quad : \qquad v_1'' + v_1 = -2b^{-1} \cos^3 \varphi \ , \tag{11}$$

$$\varepsilon^2 \quad : \qquad u_2'' + u_2 = 3u_1 \left[u_1 \left(m - 2qb^{-1} \cos \varphi\right) + 2 \cos \varphi\right] \ , \tag{12}$$

$$\eta^2 \quad : \qquad v_2'' + v_2 = 3v_1 \left[v_1 \left(m - 2qb^{-1} \cos \varphi\right) - 2 \cos^2 \varphi\right] \ , \tag{13}$$

$$\varepsilon \eta \quad : \qquad w_2'' + w_2 = 6 \left[u_1 v_1 \left(m - 2qb^{-1} \cos \varphi\right) + v_1 \cos \varphi - u_1 \cos^2 \varphi\right] \tag{14}$$

The first order equations are solved for

$$u_1 \quad = \quad \frac{b^{-1}}{2} \left(3 - \cos 2\varphi\right) \ , \tag{15}$$

$$v_1 \quad = \quad -\frac{b^{-1}}{16} \left(9 \cos \varphi - \cos 3\varphi + 12\varphi \sin \varphi\right) \ . \tag{16}$$

Thus, both mu_1 and mv_1 are of order ε, while both $qb^{-1}u_1$ and $qb^{-1}v_1$ are of order η. In consequence, all these terms drop out from Eqs. (12)-(14), which are then solved for

$$u_2 = \frac{3b^{-1}}{16}\left(10\cos\varphi + \cos 3\varphi + 20\varphi\sin\varphi\right),$$ (17)

$$v_2 = \frac{b^{-1}}{256}\big(192\cos\varphi - 48\cos 3\varphi + \cos 5\varphi + 384\varphi\sin\varphi$$
$$-36\varphi\sin 3\varphi - 72\varphi^2\cos\varphi\big),$$ (18)

$$w_2 = \frac{b^{-1}}{16}\left(-87 + 40\cos 2\varphi - \cos 4\varphi + 12\varphi\sin 2\varphi\right).$$ (19)

With this, we have found the generic solution of Eq. (7), up to the second order in both small parameters.

Far away from the lensing object $u = 0$ and $\varphi = \pi/2 + \delta\varphi/2$, where $\delta\varphi$ represents the angle with which the light ray is bent by the object with mass m and tidal charge q. In our second-order approach it has the form:

$$\delta\varphi = \varepsilon\alpha_1 + \eta\beta_1 + \varepsilon^2\alpha_2 + \eta^2\beta_2 + \varepsilon\eta\gamma_2 + \mathcal{O}\left(\varepsilon^3, \eta^3, \varepsilon\eta^2, \varepsilon^2\eta\right).$$ (20)

A power series expansion of the solution (9) then gives the coefficients of the above expansion, and the deflection angle becomes:

$$\delta\varphi = 4\varepsilon - \frac{3\pi}{4}\eta + \frac{15\pi}{4}\varepsilon^2 + \frac{105\pi}{64}\eta^2 - 16\varepsilon\eta.$$ (21)

The first three terms of this expansion were already given in [Briët and Hobill (2005)] for the Reissner-Nordström black hole. There, however the argument that η is of ϵ^2 order was advanced. In brane-worlds there is no a priori reason for considering only small values of the tidal charge, thus we have computed the deflection angle (21) containing all possible contributions up to second order in both parameters.

The deflection angle however is given in terms of the Minkowskian impact parameter b. It would be useful to write this in term of the distance of minimal approach $r_{\min}$ as well. The minimal approach is found by inserting the values $u = 1/r_{\min}$ and $\varphi = 0$ in Eq. (9):

$$r_{\min} = b\left(1 - \varepsilon + \frac{1}{2}\eta - \frac{17}{16}\varepsilon^2 - \frac{81}{256}\eta^2 + 2\varepsilon\eta\right).$$ (22)

Inverting this formula gives to second order accuracy (the small parameters being now $m/r_{\min}$ and $q/r_{\min}^2$):

$$\frac{1}{b} = \frac{1}{r_{\min}} \left(1 - \frac{m}{r_{\min}} + \frac{q}{2r_{\min}^2} - \frac{m^2}{16r_{\min}^2} + \frac{47q^2}{256r_{\min}^4} + \frac{mq}{2r_{\min}^3} \right). \qquad (23)$$

As the deflection angle consists only of first and second order contributions, the above formula is needed only to first order for expressing $\delta\varphi$ in terms of the minimal approach:

$$\delta\varphi = \frac{4m}{r_{\min}} - \frac{3\pi q}{4r_{\min}^2} + \frac{(15\pi - 16)\, m^2}{4r_{\min}^2} + \frac{57\pi q^2}{64r_{\min}^4} + \frac{(3\pi - 28)\, mq}{2r_{\min}^3}. \qquad (24)$$

The first three terms again agree with the ones given in [Briët and Hobill (2005)], for $q = Q^2$.

4   Concluding remarks

In this paper we have computed the deflection angle caused by a tidal charged brane black hole / naked singularity / star, up to second order in the two small parameters, related to the mass and tidal charge of the lensing object.

As already remarked in [Sereno (2003)], the electric charge of the Reissner-Nordström black hole decreases the deflection angle, as compared to the Schwarzschild case. The same is true for a positive tidal charge. In brane-worlds, however there is no upper limit for q as compared to m. Thus for small mass brane black holes / naked singularities / stars the condition $16mr_{\min} = 3\pi q$ could be obeyed. In this case the first order contributions to the deflection angle cancel and the three second order terms of $\delta\varphi$ give the leading effect to the weak lensing.

Furthermore, $16mr_{\min} < 3\pi q$ could be obeyed, leading to a *negative* deflection angle, at least to first order. That would mean that rather than magnifying distant light sources, such a lensing object will demagnify them.

By contrast, a negative tidal charge can considerably increase the lensing effect. Therefore a negative tidal charge could be responsible at least for part of the lensing effects attributed at present to dark matter.

5   Acknowledgement

References

Briët, J., Hobill, D. 2005 Gravitational lensing by charged black holes, University of Calgary preprint

Dadhich, N., Maartens, R., Papadopoulos, P., Rezania, V. 2000 Phys. Lett. B, 487, 1

Deffayet, C. 2001 Phys. Lett. B, 502, 199

Gergely, L. Á. 2003 Phys. Rev. D, 68, 124011

Kar, S. Sinha, M. 2003 Gen. Rel. Grav. 35, 10

Majumdar, A. S., Mukherjee, N. astro-ph/0403405

Majumdar, A. S., Mukherjee, N. 2005 Int. J. Mod. Phys D, 14, 1095 [astro-ph/0503473]

Mak, M. K., Harko, T. 2004 Phys. Rev. D, 70, 024010

Pal, S., Bharadwaj, S., Kar, S. 2005 Phys. Lett. B, 609, 194

Pal, S. 2005 astro-ph/0512494

Randall, L., Sundrum, R. 1999 Phys. Rev. Lett.83, 4690

Schäfer, B. M., Bartelmann, M. 2005 astro-ph/0502208

Sereno, M. 2003 Phys. Rev. D, 67, 064007

Straumann, N. 2004 General Relativity (Springer), ch. 3

Whisker, R. 2005 Phys. Rev. D, 71, 064004

On the luminosity-redshift relation in brane-worlds with cosmological constant

Botond Nagy[1], Zoltán Keresztes[2]

Departments of Theoretical and Experimental Physics, University of Szeged, 6720 Szeged, Dóm tér 9, Hungary

E-mail: [1],`Nagy.Botond@stud.u-szeged.hu` [2]`zkeresztes@titan.physx.u-szeged.hu`

Abstract
In this paper we calculate the luminosity distance - redshift relation for a special type of flat Friedmann branes with cosmological constant. This special case is singled out by its simplicity, the luminosity distance being given in terms of elementary functions. We compare our analytical result with the expresssion of the luminosity distance for the flat Friedmann-Lemaitre-Robertson-Walker (FLRW) universe and discuss the differences.
Keywords: *luminosity - redshift relation, cosmology with extra dimensions, brane-worlds*

1 Introduction

[Randall and Sundrum (1999)] suggested a new model for the gravitational interaction acting in five non-compact dimensions, the fifth dimension being warped. In brane cosmological models, emerging as generalizations of [Randall and Sundrum (1999)], our observable universe is a four-dimensional space-time hypersurface (the brane), which has cosmological symmetries and is embedded in the warped five-dimensional bulk. The standard model interactions are confined to the brane, but gravitational dynamics is modified as compared with general relativity, at least at high energies (also at late times in the so-called

induced gravity models). Consequently, the luminosity - redshift relation is also changed.

The relation between the luminosity distance and redshift is a powerful tool of the cosmology and has a long history of its own [Perlick (2004); Padmanabhan (2004)]. In general relativity, a milestone was the work of Mattig [Mattig (1958)], in which this relation has been derived for the FLRW universe with vanishing cosmological constant.

In Section 2 we discuss various luminosity distance - redshift relations. Subsection 2.1 contains the definition of the radial coordinate distance. In Subsection 2.2 we use a standard method for the calculation of the luminosity distance [Starobinsky (2000)] in a FLRW universe with cosmological constant. The result cannot be represented by elementary functions as it contains elliptic integrals of the first kind.

In Subsection 2.3 we calculate the luminosity distance - redshift relation for the flat Friedmann brane embeded in Z_2 symmetrically into the five-dimensional Schwarzschild-anti de Sitter space-time (5D SADS). For a special value of the brane tension, this relation becomes even simpler than in general relativity, containing only elementary functions. We briefly discuss the assumptions which led to this special case. We compare the luminosity distance - redshift relations for flat Friedmann brane and for FRLW universe with cosmological constant in the Concluding Remarks.

2 Luminosity distance - redshift relations

We define the luminosity distance [Padmanabhan (2004)] in terms of the luminosity $\mathcal{L}$ and the flux $\mathcal{F}$ as:

$$d_L(z) = \left(\frac{\mathcal{L}}{4\pi\mathcal{F}}\right)^{\frac{1}{2}} = a_0(\eta_0 - \eta)(1 + z) . \tag{1}$$

Here a_0 represents the value of the scale factor at present time, $\eta_0 - \eta$ is the radial coordinate distance of the source, and z is the redshift. In order to find the luminosity distance - redshift relation, first we need to calculate the radial coordinate distance.

2.1 The radial coordinate distance

Current observational data indicates [Liddle (2003)] that the universe is spatially flat. Thus, in this subsection we calculate the radial coordinate distance for the

spatially flat Friedmann metric:

$$ds^2 = -c^2 d\tau^2 - a^2(\tau)[d\eta^2 - \eta^2(d\theta^2 + sin^2\theta d\varphi^2)] \ . \tag{2}$$

Light rays, perceived by Earth-based observers, travel along null radial geodesics:

$$ds^2 = d\theta = d\varphi = 0 \ . \tag{3}$$

Using (3) we can express the radial distance from the metric:

$$\eta_0 - \eta = \int_\eta^{\eta_0} d\eta = \int_t^{t_0} \frac{c\,d\tau}{a(\tau)} = \int_a^{a_0} \frac{c\,da}{a^2 H(a)} \ . \tag{4}$$

In the last equality we changed from the time variable t to the scale factor a as integration variable and H denotes the Hubble parameter. In the above formula the evolution of Hubble parameter is different in the FLRW universe and for a Friedmann brane.

2.2 The luminosity distance-redshift relation for flat FLRW universe with cosmological constant

For the flat FLRW, the Friedmann equation which gives to the evolution of the Hubble parameter is

$$H^2 = \left(\frac{\dot{a}}{a}\right)^2 = \frac{\kappa^2 \rho}{3} + \frac{\Lambda}{3} \ , \tag{5}$$

where ρ denotes the density of matter, Λ the cosmological constant, and $\kappa^2 = 8\pi G$. If we divide this equation with the square of the Hubble constant (the present value of the Hubble parameter) H_0^2, we obtain:

$$\frac{H^2}{H_0^2} = \Omega_\rho \frac{a_0^3}{a^3} + \Omega_\Lambda \ , \tag{6}$$

where we have introduced

$$\Omega_\rho = \frac{\rho_0}{3H_0^2} \ , \tag{7}$$

$$\Omega_\Lambda = \frac{\Lambda}{3H_0^2} \ . \tag{8}$$

Knowing the evolution of the Hubble parameter, Eq. (5) the luminosity is found as

$$d_L(z) = \frac{c(1+z)}{3^{\frac{1}{4}} H_0 \Omega_\Lambda^{\frac{1}{3}} \Omega_\Lambda^{\frac{1}{6}}} \cdot [\mathbf{F}(\varphi_0, \varepsilon) - \mathbf{F}(\varphi, \varepsilon)] \ , \tag{9}$$

where

$$\varphi_0 = arccos\frac{\left(1 - \sqrt{3}\right) \cdot \Omega_\Lambda^{\frac{1}{3}} + \Omega_\rho^{\frac{1}{3}}}{\left(1 + \sqrt{3}\right) \cdot \Omega_\Lambda^{\frac{1}{3}} + \Omega_\rho^{\frac{1}{3}}} \ , \tag{10}$$

$$\varphi = arccos\frac{\left(1 - \sqrt{3}\right) \cdot \Omega_\Lambda^{\frac{1}{3}} + \Omega_\rho^{\frac{1}{3}}\left(1 + z\right)}{\left(1 + \sqrt{3}\right) \cdot \Omega_\Lambda^{\frac{1}{3}} + \Omega_\rho^{\frac{1}{3}}\left(1 + z\right)} \ , \tag{11}$$

and

$$\varepsilon = \frac{1}{2} + \frac{\sqrt{3}}{4} \ . \tag{12}$$

The function $\mathbf{F}(\varphi, \varepsilon)$ is the elliptic integral of first kind, with the variable φ and the argument ε. We can see that even in the general relativistic case, the luminosity distance - redshift relation can be given only in terms of elliptic functions.

2.3   Flat Friedmann brane

The metric on the Friedmann brane is the same as in the case of FLRW universe, thus we can use the previous method for the calculation of the radial coordinate distance. Only the evolution of the Hubble parameter is different for a Friedmann brane embedded symmetrically into the 5D SADS space-time (for the most generic form of this equation see [Gergely (2003)]):

$$H^2 = \frac{\kappa^2 \rho}{3} \cdot (1 + \frac{\rho}{2\lambda}) + \frac{\Lambda}{3} + \frac{2\bar{m}}{a^4} \ . \tag{13}$$

New source terms arise as compared to (5) from the assumptions that our universe is a brane and there are identical black holes with mass $\bar{m}$ in both bulk regions. Here λ is the brane tension. We introduce the following notations:

$$\Omega_\lambda = \frac{\rho^2 \kappa^2}{6\lambda H_0^2} \ , \tag{14}$$

$$\Omega_d = \frac{2\bar{m}}{a_0^4} \ . \tag{15}$$

The radial distance, after a short rearrangement, is

$$\eta_0 - \eta = \frac{c}{H_0 \Omega_\Lambda^{\frac{1}{2}}} \int_a^{a_0} \frac{a \, da}{\left[\left(a^3 + \frac{\Omega_\rho a_0^3}{2\Omega_\Lambda}\right)^2 + \left(\frac{\Omega_\lambda}{\Omega_\Lambda} - \frac{\Omega_\rho^2}{4\Omega_\Lambda^2}\right)a_0^6 + \frac{\Omega_d}{\Omega_\Lambda}a_0^4 a^2\right]^{\frac{1}{2}}} \ . \tag{16}$$

Table 1: *The values of Ω_Λ and brane tension.*

Ω_Λ	$\lambda(10^{-60}TeV^4)$
0.704	41.065
0.025	1.509

In general, this integral leads to elliptic functions, however in the special case, when both the second and the third terms in the denominator vanish, is can be given in terms of elementary functions. For this, two conditions have to be satisfied. The first is

$$\Omega_d = 0 \ . \tag{17}$$

This assumption is realistic at late times because Ω_d is proportional to a_0^4. Its direct implication is that the brane, rather than being embedded into the 5D SADS space-time, is embedded into a five-dimensional anti de Sitter (5D ADS) bulk. The second assumption is

$$\Omega_\lambda = \Omega_\rho^2/(4\Omega_\Lambda) \ , \tag{18}$$

or equivalently

$$\kappa^2\lambda = 2\Lambda \ . \tag{19}$$

As observational evidence suggest $\Omega_\rho = 0.27$ and for flat universe, we have $\Omega_\Lambda + \Omega_\lambda + \Omega_\rho = 1$, a quadratic equation for Ω_λ emerges. Both solutions of this quadratic equation are positive. The values of Ω_Λ and λ are collected in *Table 1*. We note that these values of the brane tension are much below the minimal value of λ predicted to be $1(TeV)^4$ [Maartens (2004)]. However with the conditions (17) and (18) satisfied, the luminosity distance has a very simple expression:

$$d_L = \frac{1}{6} \frac{c(1+z)}{2^{\frac{-1}{3}} H_0 \Omega_\rho^{\frac{1}{3}} \Omega_\Lambda^{\frac{1}{6}}} \left\{ \left(ln \frac{(1-h+h^2)[1+h(1+z)]^2}{[1-h(1+z)-h^2(1+z)^2](1+h)^2} \right. + \right.$$

$$\left. + 2\sqrt{3}[arctan\frac{\sqrt{3}}{3}\left(\frac{2}{h}-1\right) - arctan\frac{\sqrt{3}}{3}\left(\frac{2}{h}(1+z)-1\right) \right\} \ , \tag{20}$$

where we have introduced:

$$h = \left(\frac{\Omega_\rho}{2\Omega_\Lambda}\right)^{\frac{1}{3}} \ . \tag{21}$$
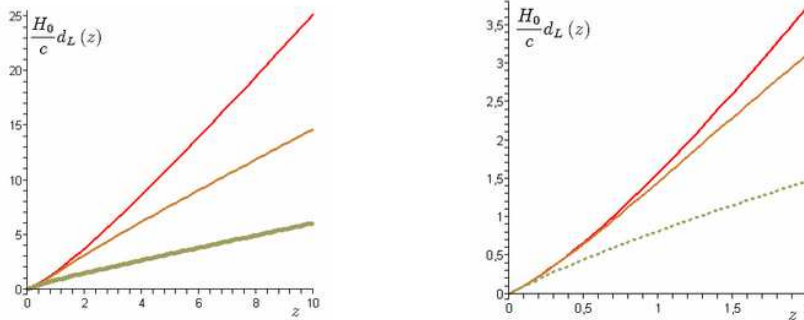
Figure 1: *Left: The luminosity distance plotted as function of redshift in the range $z = 0..10$. The upper curve represents the solution for FLRW universe, the middle and the lowest are for the Friedmann brane with $\Omega_\Lambda = 0.704$ and 0.025, respectively. Right: The same, in the range $z = 0..2$.*

3   Concluding remarks

We have derived the analytical expressions of the luminosity distances for both a flat FLRW universe with cosmological constant and a Friedmann brane embedded into 5D ADS bulk. These expressions are substantially different, as they depend on the Friedmann equation. In the case of the Friedmann brane we have imposed two simplifying assumptions yielding the luminosity distance in terms of elementary functions. There are two values of the cosmological constants and of the brane tension, which are in accordance with these assumptions. The higher value of the Ω_Λ (see: *Table 1*) is very close to today's preferred value [Liddle (2003)].

The luminosity distances as function of redshift for all three cases is represented in Fig. 1. On the two plots, d_L is represented from $z = 0$ to $z = 10$ and $z = 0$ to $z = 2$, respectively. The motivation for the second graph is that supernova observations extend nowadays up to $z = 2$. On the plots, we see that all three luminosity distances grow monotonically with increasing redshift. The steepest curve belongs to the FLRW universe. The middle curve is for the case of the brane with the higher value of the cosmological constant. This curve, in the range $z = 0..2$, is extremely close to one pertinent to a flat FLRW universe.

Since the values of both brane tensions are much below the theoretically predicted limit, our brane model qualifies as a "toy model". The constraints on

brane tension [see: Maartens (2004)] imply that Ω_λ should be small. Nowadays, Ω_d is also small, being proportional to a_0^4. Thus a perturbative treatment can give rise to a more realistic solution for the luminosity distance for Friedmann brane models [see: Keresztes et al. (2006)]. However, such realistic solutions for the luminosity distance will be more complicated than the correponding expressions in general relativity.

Acknowledgement

References

Gergely, L. Á. 2003 Phys. Rev. D68, 124011

Keresztes, Z., Nagy, B., Szabó Gy., Gergely, L. Á. 2006 in preparation

Liddle, A. 2003 An Introduction to Modern Cosmology , John Wiley & Sons

Maartens, R. 2004 Living Rev. Relativity 7, 7

Mattig, W. 1958 Astronomische Nachrichten, volume 284, 119

Padmanabhan, T. 2002 Theoretical Astrophysics, vol.3, Cambridge University Press

Perlick, V. 2004 Living Rev. Relativity 7, 9

Randall, L., Sundrum, R. 1999 Phys. Rev. Lett., 83, 4690

Starobinsky, A. A. 2000 Gravit. and Cosmology 6, 157 [astro-ph:9912054]

Canonical theory of the Kantowski-Sachs cosmological models

Zsolt Horváth[1], Zoltán Kovács[1,2]

[1] University of Szeged, Department of Theoretical Physics, H-6720 Szeged, Tisza Lajos krt. 84.-86., Hungary
[2] Max-Planck-Institut für Astronomie, Königstuhl 17. D-69117 Heidelberg, Germany

E-mail: [1]`zshorvath@titan.physx.u-szeged.hu`, [2]`kovacs@mpia-hd.mpg.de`

Abstract
We briefly discuss the Hamiltonian formalism of the Kantowski-Sachs space-times with vacuum, anisotropic fluid and two cross-streaming radiation field sources. For these models a cosmological time is introduced. New constraints are found in which the fluid momenta are separated from the rest of the variables. In consequence their Poisson brackets give an Abelian algebra.
Keywords: *Kantowski-Sachs cosmology, canonical gravity*

1 Introduction

The Kantowski-Sachs (hereafter KS) cosmologies have two symmetry properties, the spherical symmetry and the invariance under spatial translations. The vacuum solution for this line element is equivalent to the inner Schwarzschild space-time and exact solutions were also found in presence of some matter fields for homogenous cosmological models. Kantowski and Sachs [Kantowski and Sachs (1966)] provided solutions for dust space-times but later on KS geometries with other matter sources were found, such as scalar fields [Barrow et al. (1997)], prefect fluid [Collins (1977)] and anisotropic fluid [Gergely (1999)] and exotic fluid [Gergely (2002)] models. Here we give a short overview of the Hamiltonian theory of the KS cosmology in the case of vacuum and anisotropic fluid sources. We employ the equivalence of the latter with the model consisting of

two, in- and outgoing radiation streams in a stellar atmosphere. We introduce a cosmological time for the space-time containing colliding radiation streams and introduce new constraints. These results might represent an important step in carrying out a consistent canonical quantization and in building up KS quantum cosmologies.

2   Vacuum Kantowski-Sachs space-times

The line element of KS space-times is given by

$$ds^2 = -d\tau^2 + H(\tau)\,dh^2 + R^2(\tau)\,d\Omega^2 \ , \tag{1}$$

where τ is the cosmological time, h a radial coordinate and $d\Omega^2$ is the metric on the unit sphere. For vacuum this metric can be written the form

$$ds^2 = -d\eta^2 + b^2 \tan^2 \eta\, dh^2 + R^2 d\Omega^2 \ , \tag{2}$$

where we introduced the angle parameter η,

$$\tau = a\,(\eta + \sin\eta\cos\eta) + c \qquad a, b, c \in I\!\!R \ ,$$

usually employed in homogenous, spherically symmetric cosmologies. With the coordinate transformation $R(\eta) = a\cos^2\eta$ the solution (2) can be cast into the form of the Schwarzschild metric

$$ds^2 = -F(R)dT^2 + F^{-1}(R)dR^2 + R^2 d\Omega^2 \ , \qquad F(R) = (1 - 2M/R) \ , \tag{3}$$

where $R < 2M$ and $T = bh$ are the time- and space-like coordinates, respectively.

   The canonical formalism of KS space-times is therefore equivalent to that of the Schwarzschild solution. In the Hamiltonian theory of Schwarzschild black holes we use a foliation consisting of spherical surfaces characterized by a constant time parameter t, which is identified to the Schwarzschild time T [Kuchař (1994)]. The geometry induced on these three-spheres has the form

$$d\sigma^2 = \Lambda^2(r)dr^2 + R^2(r)d\Omega^2 \ ,$$

where the functions Λ and R were chosen as canonical coordinates. Then their conjugated momenta P_Λ and P_R are derived from the action specified for the

Schwarzschild space-time [Kuchař (1994)] written in terms of the canonical variables,

$$P_\Lambda = -N^{-1}R(\dot{R} - R'N^r) \ , \qquad P_R = -N^{-1}[\Lambda(\dot{R} - R'N^r) + R(\dot{\Lambda} - (\Lambda N^r)')] \ .$$

The Legendre transformation of the Lagrangian gives the Hamiltonian

$$\mathcal{H}^G = P_\Lambda\dot{\Lambda} + P_R\dot{R} + NH^G + N^r H_r^G \tag{4}$$

with super-Hamiltonian and supermomentum constraints

$$H^G = R^{-1}P_R P_\Lambda + R^{-2}\Lambda P_\Lambda^2/2 + \Lambda^{-1}RR''$$
$$- \Lambda^{-2}RR'\Lambda' - \Lambda^{-1}R'^2/2 - \Lambda/2 \ ,$$
$$H_r^G = P_R R' - \Lambda P_\Lambda' \ .$$

The basics of the Hamiltonian formulation do not change if we couple matter fields to gravity. We only have to enlarge the phase space of gravity by including the canonical variables of the matter sources. After decomposing the matter action we can derive the Hamiltonian for the matter fields as well. Then the constraint equations of gravity must be supplemented with those of the matter fields, which gives the full of set constraints on the total system.

3 Kantowski-Sachs cosmologies with anisotropic fluid

Exact solutions for KS space-times with anisotropic fluid sources have also been found in the form

$$ds^2 = -2ae^{L^2}RdL^2 + ae^{L^2}R^{-1}dZ^2 + R^2 d\Omega^2 \ , \qquad a = -1 \ , \tag{5}$$

where

$$-R = a(e^{L^2} - 2L\Phi_B) \ , \qquad \Phi_B = B + \int^L e^{x^2}dx \ ,$$

and L and Z are the time and the radial coordinates [Gergely (1999)]. The time dependence of the metric components shows that the KS cosmology with anisotropic fluid is not static. By considering the time evolution of the radial length $R(L)$ and the co-moving energy density of the Universe, we see that the KS Universe has a finite lifetime with an initial and a final singularity.

Anisotropic fluids can be considered as superpositions of two cross-flowing null dust streams [Letelier (1980)]. Thus the action of an anisotropic fluid with the co-moving density ρ, the four velocity U^α of the fluid particles and a vector field X^α describing the direction of the pressure forces is given by

$$S^F = -\frac{1}{2} \int dx^4 \sqrt{-g} \rho (U^\alpha U_\alpha + X^\alpha X_\alpha) \ , \tag{6}$$

which is both algebraically and dynamically equivalent to the action of the two colliding null dust flows with the four velocities u^α and v^α:

$$S^{2ND} = -\frac{1}{2} \int dx^4 \sqrt{-g} \rho (u^\alpha u_\alpha + v^\alpha v_\alpha) \ . \tag{7}$$

Here the same energy density is chosen for both the dust components so that the net flow should vanish for the static configuration.

Previously a canonical formalism was developed for two cross-flowing null dust streams coupled to the geometry by [Bičák and Hájíček (2003)]. This however did not solve the problem of the absence of a time standard for the colliding null dusts. However, the anisotropic fluid interpretation of two in- and outgoing null dust streams indicates there may be a possibility to use the same procedure as in the case of the incoherent dust in order to find an internal time for the canonical dynamics of colliding null dust streams.

The action with the constraint equations for the spherically symmetric vacuum solution is to be supplemented with those of the matter fields. If we write of the null vector fields in terms of the coordinates Z and L,

$$u_\alpha = WZ_{,\alpha}/\sqrt{2} + RWL_{,\alpha} \ , \qquad v_\alpha = WZ_{,\alpha}/\sqrt{2} - RWL_{,\alpha}$$

and make the same decomposition for the vector fields U^α and X^α,

$$U_\alpha = WZ_{,\alpha} \ , \qquad X_\alpha = \sqrt{2}RWL_{,\alpha}$$

with $W = (ae^{L^2}/R)^{1/2}$, the matter actions (6) and (7) can be expressed with these coordinates as well. By extremizing these actions with respect to the variables Z, L and the parameter ρ, we obtain equivalent equations of motion for the null dust and fluid models.

We use the coordinates $L(t,r)$ and $Z(t,r)$ as the canonical variables for the matter and derive the canonical momenta conjugated to them form the matter action:

$$P_L = 2a\sqrt{g}R^2 \frac{\rho W^2}{N}(\dot{L} - N^r L') \ , \qquad P_Z = a\sqrt{g}\frac{\rho W^2}{N}(\dot{Z} - N^r Z') \ .$$

As a result of the Legendre transformation of the Lagrangian in the matter actions (6) and (7), we obtain the same Hamiltonian for both types of matter sources

$$\mathcal{H}^M = P_L \dot{L} + P_Z \dot{Z} + N H^M + N^r H_Z^M \quad , \tag{8}$$

where the super-Hamiltonian and supermomentum constraints imposed on the matter variables are

$$H_\perp^M = \left[\frac{1}{2\sqrt{g}\rho W^2} \left(P_Z^2 + \frac{1}{2aR^2} P_L^2 \right) + \sqrt{g} \frac{\rho W^2}{2\Lambda^2} \left((Z')^2 + 2R^2(L')^2 \right) \right] \quad ,$$

$$H_r^M = Z' P_Z + L' P_L \quad .$$

The Hamiltonian (4) of the vacuum equations, together with Eq. (8) describe the KS space-time with two colliding null dust streams or equivalently, an anisotropic fluid source. The super-Hamiltonian and supermomentum constraints of the total system are given by

$$H_\perp := H_\perp^G + H_\perp^M = 0 \quad , \tag{9}$$

$$H_r := H_r^G + H_r^M = 0 \quad . \tag{10}$$

These constraints are replaced with an equivalent set by solving the old constraints with respect to P_Z and P_L. Hence the momenta associated with the matter can be separated from the other variables in the constraint equations (9)-(10):

$$H_\uparrow = P_L + h(r; \Lambda, R, L, Z, P_\Lambda, P_R) \quad ,$$

$$H_{\uparrow Z} = P_Z + h_Z(r; \Lambda, R, L, Z, P_\Lambda, P_R) \quad ,$$

where

$$h = \sqrt{2a} R L'^{-1} \left[\Lambda \sqrt{G} \frac{dZ}{dL} - \sqrt{2} a R^{-1} H_r^G P_L Z' \right] \left[\left(\frac{dZ}{dL} \right)^2 + 2aR^2 H_r^G \right]^{-1}$$

$$h_Z = -\sqrt{2a} R L'^{-1} \left[\Lambda \sqrt{G} - \left(\sqrt{2} a R \right)^{-1} h Z' \right] \quad , G^2 = (H^G)^2 - g_{ab} H_a^G H_b^G \quad .$$

Since the momenta P_L and P_Z are separated from the rest of the canonical variables, the algebra of the new constraints has strongly vanishing Poisson brackets and the Dirac algebra of the old constraints turns to an Abelian algebra of the new ones [Brown and Kuchař (1995)]. The time variable introduced here can be useful in the description of stellar atmospheres consisting of the in- and outgoing radiation streams. Our result might provide better prospects for the canonical quantization of KS cosmologies with cross-flowing null dust streams.

4 Conclusion

We have studied the Hamiltonian formulation of KS cosmologies. In the case of vacuum, the KS space-time is equivalent to the exterior Schwarzschild solution and we can use the canonical theory developed for Schwarzschild black holes. In static KS space-times with spherical symmetry, filled with an anisotropic fluid, the matter source is equivalent to two cross-streaming radiations. Thus the proper time of the dust particles used in the Hamiltonian treatment of the fluid space-times could also be introduced as a time variable in the canonical formalism of the colliding null dust streams. We have derived a new set of constraints for the fluid or colliding null dust variables as well, in which the canonical momenta of the matter are separated from the rest of the variables. As a result, we have obtained an Abelian constraint algebra. Our treatment could give new possibilities for the discussion of quantum KS cosmologies with anisotropic fluid of colliding null dust streams.

Acknowledgement

References

Barrow, J.D., Dabrowski, M.P. 1997, Phys. Rev. D, 55, 630

Bičák, J., Kuchař , K.V. 1997, Phys. Rev. D, 56, 4878

Bičák, J., Hájíček, P. 2003, gr-qc/0308013

Brown, J.D.,Kuchař, K.V. 1995, Phys. Rev. D, 51, 5600

Collins, C.B. 1977, J. Math. Phys. 18, 2116

Gergely, L. 1998, Phys. Rev. D, 58, 084030

Gergely, L. 1999, Phys. Rev. D, 59, 104014

Gergely L. 2002, Phys.Rev. D, 65, 127503

Kantowski, R., Sachs,R.K. 1966 J. Math. Phys. 7, 443

Kuchař, K.V. 1994, Phys. Rev. D, 50, 3961

Letelier, P. S. 1980, Phys. Rev. D, 22, 807

Gravitational Waveforms from Compact Binary Systems

János Majár

KFKI Research Institute for Particle and Nuclear Physics, Budapest 114, P.O.Box 49,
H-1525 Hungary

E-mail: `majar@rmki.kfki.hu`

Abstract
Here we present the basics of the method for determining the polarization states h_+ and $h_\times$ of the detectable gravitational waves emitted by a compact spinning binary system. The waveform and the dynamics of the binary are described with the use of the post-Newtonian (PN) approximation up to 1.5 PN relative order, related to the leading order newtonian expressions. Beyond point mass effects we investigate the influence of the rotation of the bodies on the waveform to linear order, in the case of eccentric orbits.
Keywords: *gravitational waves, PN, compact binary*

1 Introduction

Compact stars forming binary systems are promising sources of gravitational radiation which detection is expected by the gravitational wave observatories, i.e. LIGO, LISA, VIRGO, TAMA and GEO600. For the extraction of the true signal from the noisy output of the detectors accurate knowledge of the gravitational waveforms emitted by the binary is required. Thus, the construction of ready to use templates for gravitational waves is an important challenge in the investigation of detectable wave signals.

Many works have determined the form of the detectable gravitational wave signals emitted by compact binaries formally in terms of the dynamical properties of motion (Kidder, 1995; Will and Wiseman, 1996; Apostolatos et al.,

1994; Blanchet, 2001), but there exist fewer results in the literature where the detectable waveform is computed explicitly in terms of time or a useful parameter.

Here we present the method to describe the time evolution of the detectable gravitational waveform of a binary system. To fully integrate the problem one can use the so-called generalized true anomaly parametrizaton of the orbit (for further details see (Gergely et al., 2000)). Using this parametrization of the radial motion one can express the contributions to the gravitational wave polarizations h_+ and $h_\times$ up to 1.5 PN order in the case of eccentric orbits.

Sec.II is an introduction to the world of detectable gravitational waves. We introduce the basic quantities and the formalism used by the theory of detection of these gravitational waves. The description of the motion is shown in Sec.III, where we present the method to determine the evolution of the elements of the motion. In Sec.IV we show how to evaluate the polarizaton states of the detectable gravitational waves. In the last section we collect the steps needed to determine explicitly the dynamics of the waves. We use the $c = G = 1$ convention.

2 Gravitational waves in linearized gravity

The true signal of a laser-interferometric gravitational wave detector can be expressed by the linear combination of two polarization states h_+ and $h_\times$:

$$h(t) = F_+(\alpha, \beta, \xi)h_+(t) + F_\times(\alpha, \beta, \xi)h_\times(t) , \tag{1}$$

where F_+ and $F_\times$ are the so-called beam-pattern functions depending on the direction of the source (angles α, β) and the polarization angle (ξ).

The polarization states h_+ and $h_\times$ can be projected from the transverse-traceless tensor h_{TT}^{ij} describing the perturbations of the metric using an appropriate gauge. To be able to describe this projection we introduce the orthonormal triad ($\mathbf{N}, \mathbf{p}, \mathbf{q}$). Vector $\mathbf{N}$ is the direction of the line of sight, and we choose $\mathbf{p}$ to lie in the direction of the node line (the intersection of the orbital plane of the source and the so-called plane of the sky, the plane perpendicular to $\mathbf{N}$), and $\mathbf{q} = \mathbf{N} \times \mathbf{p}$. This way

$$h_+ = \frac{1}{2}(p_i p_j - q_i q_j)h_{TT}^{ij} , \qquad h_\times = \frac{1}{2}(p_i q_j - q_i p_j)h_{TT}^{ij} . \tag{2}$$

In this work we present the basics of the method of this projection and the determination of h_+ and $h_\times$ in terms of time or an appropriate parameter.

3   Description of the motion

The description of the projection method leads to the clearest expressions in the comoving system fixed to the orbital plane and the separation vector $\mathbf{r}$. The z axis of this coordinate system is fixed to the direction of the Newtonian angular momentum $\mathbf{L}_N := \mu \mathbf{r} \times \mathbf{v}$ ($\mathbf{v}$ denotes the relative velocity vector) which is perpendicular to the orbital plane, and the x axis to the separation vector.

To be able to determine the dynamics of the elements of motion needed we introduce an invariant coordinate system which do not move. Since the total angular momentum $\mathbf{J}$ is constant up to $2\,\mathrm{PN}$ order we fix the z axis of this system to it. We choose the x and y axes of the invariant system in a way that the form of the vector $\mathbf{N}$ is

$$\mathbf{N} = \begin{pmatrix} \sin\gamma \\ 0 \\ \cos\gamma \end{pmatrix} \tag{3}$$

in this system, where γ is the constant angle between $\mathbf{J}$ and $\mathbf{N}$.

The transition between the comoving and invariant systems is described with so-called Euler-angles. With these angles the separation vector in the invariant system has the form

$$\mathbf{r} = r \begin{pmatrix} \cos\Phi\cos\Psi - \cos\iota\sin\Phi\sin\Psi \\ \sin\Phi\cos\Psi + \cos\iota\cos\Phi\sin\Psi \\ \sin\iota\sin\Psi \end{pmatrix} \;, \tag{4}$$

where r is the length of the separation vector, ι is the angle between $\mathbf{L_N}$ and $\mathbf{J}$ and Φ shows the direction of the intersection of the orbital and invariant planes (determined by $\mathbf{L_N}$ and $\mathbf{J}$). This way Φ represents the precession of $\mathbf{L_N}$ over $\mathbf{J}$. Ψ describes the evolution of the separation vector in the orbital plane.

In this case every vector $\mathbf{u}$ which is given in the invariant system, in the comoving system will become

$$\mathbf{u}' = R_z(\Phi)R_x(\iota)R_z(\Psi)\mathbf{u} \;, \tag{5}$$

where the matrix $R_{x_i}(\alpha)$ denotes the rotation about the x_i axis with angle α. To be able to determine the dynamics of the system we have to evaluate the equations for the length of the separation vector and the Euler-angles.

The basic equation of the description of the motion is the radial equation of the motion evaluated from the Lagrangian formalism

$$\dot{r}^2 = \frac{2E}{\mu} + \frac{2m}{r} - \frac{L^2}{\mu^2 r^2} + \frac{2E\mathbf{L}\sigma}{m\mu^2 r^2} - \frac{2(2\mathbf{LS} + \mathbf{L}\sigma)}{\mu r^3} \tag{6}$$

where E and L are constants of the motion, μ is the reduced and m is the total mass of the system, and $\mathbf{S} := \mathbf{S}_1 + \mathbf{S}_2$ and $\sigma := m_2/m_1\mathbf{S}_1 + m_1/m_2\mathbf{S}_2$.

To describe the time evolution of the elements of the motion up to $1.5\,\mathrm{PN}$ order one has to integrate the spin precession equations linearly in spin

$$\dot{\mathbf{S}}_1 = (4 + 3\frac{m_2}{m_1})\frac{G}{2c^2r^3}\mathbf{J} \times \mathbf{S}_1 \tag{7}$$

$$\dot{\mathbf{S}}_2 = (4 + 3\frac{m_1}{m_2})\frac{G}{2c^2r^3}\mathbf{J} \times \mathbf{S}_2 \ . \tag{8}$$

From the Lagrangian formalism of the motion one can determine the form of the total angular momentum

$$\mathbf{J} = \mathbf{L}_N + \mathbf{L}_{SO} + \mathbf{S}_1 + \mathbf{S}_2 \tag{9}$$

where the explicit form of the spin-orbit angular momentum can be found in (Gergely et al., 1998).

Using the form of the relative velocity vector in the comoving system and the components of the total angular momentum in the invariant system (since in the invariant system its first and second components vanish and the third one is constant) one can determine all the equations needed to evaluate the time evolution of every elements of the motion which is needed to determine the time dependence of the polarization states.

We choose a parametrization of the orbit $\mathbf{r} = \mathbf{r}(\chi)$, which gives a generalization of the Keplerian true anomaly parametrization, see (Gergely et al., 2000). With the use of this parametrization we can integrate r, solve the spin precession equations, evaluate the length and the components of the relative velocity and the total angular momentum vectors too. After all we can determine the parameter dependence of the angular variables.

4   Determining waveform polarization states

To be able to evaluate the projection of the polarization states we need to determine the components of the $\mathbf{N}$, $\mathbf{p}$, $\mathbf{q}$ triad in terms of the elements of the motion.

At first we take a look at vector $\mathbf{N}$. Its form in the invariant system is given before, see Eq.(3), and in the comoving one it changes to

$$\mathbf{N} = \begin{pmatrix} \cos\Psi\cos\Phi\sin\gamma - \sin\Psi\cos\iota_N\sin\Phi\sin\gamma + \sin\Psi\sin\iota_N\cos\gamma \\ -\sin\Psi\cos\Phi\sin\gamma - \cos\Psi\cos\iota_N\sin\Phi\sin\gamma + \cos\Psi\sin\iota_N\cos\gamma \\ \sin\iota_N\sin\Phi\sin\gamma + \cos\iota_N\cos\gamma \end{pmatrix} , \tag{10}$$

where we used the inverse of the transformation law Eq.(5).

Since there are three conditions for the vector $\mathbf{p}$, it can be determined easily in the comoving system. It is a unit vector which is perpendicular to $\mathbf{N}$ and $\mathbf{L}_N$. After using all the conditions, the form of $\mathbf{p}$ becomes

$$\mathbf{p} = \frac{1}{N} \begin{pmatrix} \sin\Psi\cos\Phi\sin\gamma + \cos\Psi\cos\iota_N\sin\Phi\sin\gamma - \cos\Psi\sin\iota_N\cos\gamma \\ \cos\Psi\cos\Phi\sin\gamma - \sin\Psi\cos\iota_N\sin\Phi\sin\gamma + \sin\Psi\sin\iota_N\cos\gamma \\ 0 \end{pmatrix} , (11)$$

where

$$N = \sqrt{N_x^2 + N_y^2} = \sqrt{1 - N_z^2} = \sqrt{1 - (\sin\iota_N\sin\Phi\sin\gamma + \cos\iota_N\cos\gamma)^2} , \quad (12)$$

and we can calculate the components of vector $\mathbf{q}$ with

$$\mathbf{q} = \mathbf{N} \times \mathbf{p} . \tag{13}$$

In the post-Newtonian approximation the transverse-traceless tensor can be decomposed into terms corresponding to different PN orders and effects, see Eqs.(3.21) in (Kidder, 1995). Using this result and Eqs.(2) we can evaluate the contributions to the polarization states. Our notation is similar to the one given in (Kidder, 1995):

$$h_{\substack{+\\\times}} = \frac{2\mu}{D} \left[h_{\substack{+\\\times}}{}^N + h_{\substack{+\\\times}}{}^{0.5} + h_{\substack{+\\\times}}{}^1 + h_{\substack{+\\\times}}{}^{1SO} + h_{\substack{+\\\times}}{}^{1.5} + h_{\substack{+\\\times}}{}^{1.5SO} \right] , \tag{14}$$

where D is the distance between the detector and the source. h^N terms denote the quadrupole (or Newtonian) expressions, $h^{0.5}$, h^1 and $h^{1.5}$ are corrections corresponding to higher PN orders, h^{1SO} and $h^{1.5SO}$ are the spin-orbit terms. These contributions can be derived with the use of the formal expressions given in (Kidder, 1995) and (Will and Wiseman, 1996).

Since the expressions of the terms according to different orders and effects are rather long we give only two examples of them, namely the Newtonian and the lowest order spin-orbit contributions in the case of the "plus" polarization state:

$$h_+^N = \left(\dot{r}^2 - \frac{M}{r} \right) (p_x^2 - q_x^2) + 2v_\perp \dot{r}(p_x p_y - q_x q_y) + v_\perp^2 (p_y^2 - q_y^2) ,$$

$$h_+^{1SO} = \frac{m_2 + m_1}{r^2 m_2} [(\mathbf{q}\mathbf{S}_1)p_x + (\mathbf{p}\mathbf{S}_1)q_x] - \frac{m_2 + m_1}{r^2 m_1} [(\mathbf{q}\mathbf{S}_2)p_x + (\mathbf{p}\mathbf{S}_2)q_x] . \tag{15}$$

5 Conclusions and remarks

After all the method is the following. After determining and solving the equations of motion the results can be inserted into the components of the **N**, **p**, **q** triad. With the evaluation of the components of the relative velocity and spin vectors we have all the quantities which are to be substituted into the expressions of h_+ and $h_\times$. This way (neglecting higher-order spin corrections) we get the evolution of the polarization states of the detectable gravitational waveform.

To be able to find the effects of the rotation of the bodies and the eccentricity of the orbit one may use this method in the spinless and circular orbit cases too. The circular orbit case has the advantage that it can be integrated explicitly in time, however the meaning of the circular orbit is highly nontrivial in a perturbative sense.

In the future the knowledge of the form of the detectable gravitational waves emitted by a compact binary can be a starting point of a measurement method for determining the main features of such compact binaries with gravitational wave spectroscopy. Besides astronomy and radioastronomy the detection of these gravitational waves may become an important tool in the exploration of our universe.

Acknowledgement

References

L.E.Kidder, Phys. Rev. D**52**, 821 (1995).

C.M.Will and A.G.Wiseman, Phys. Rev. D**54**, 4813 (1996).

T.A.Apostolatos, C.Cutler, G.J.Sussman, K.S.Thorne, Phys. Rev. D**49**, 6274 (1994).

L.Gergely, Z.Perjés, M.Vasúth, Phys. Rev. D**58**, 124001 (1998).

L.Gergely, Z.Perjés, M.Vasúth, ApJS 126, **79** (2000).

L.Blanchet, Proc. of the Como School on Gravitational Waves in Astrophysics (2001).

On anthropic principles fine tuning and chaos

Zsolt Hetesi[1], László Végh[2]

[1] Eötvös University, Department of Astronomy, H-1518 Budapest, P.O.Box 32., Hungary
[2] Institute of Nuclear Research of the HAS, H-4001 Debrecen, P.O. Box 51., Hungary

E-mail: [1] zs.hetesi@astro.elte.hu, [2] vl@atomki.hu

Abstract
Anthropic principles were grown from the problem of fine tuning. Although anthropic principles have been discussed in cosmology for years there are no exact definitions for fine tuning. To define the fine tuning quantitatively we investigate how one can use Lyapunov indicator in the definition of fine tuning. Our result is an alternative Lyapunov indicator, which shows how fine tuned is a possible Universe with physical constants different from ours.
Keywords: *anthropic principles, fine tuning, Lyapunov indicator, chaotic systems, cosmology*

The Universe and life are connected. Man exists because the Universe is governed by delicately balanced laws that have led to a very high level of organization of matter called life. There are apparent coicidences in the dimensionless basic constants of nature. These basic numbers of nature not only allow the existence of stable atoms from which matter is built but also lead to the formation of galaxies and stars and even more complex stuctures all are necessary for the existence of life. A small change in the basic constants would result a universe without life-supporting conditions. We can say that the Universe is finely tuned for life.

Anthropic principles address the question why has the Universe the fine-tuning. Is this a fortunate condition, inevitable or it is expected. The weak anthropic principle stresses that we, intelligent observers, may observe only very

special properties being compatible with our existence. The strong anthropic principle claims that the Universe must have those features which are necessary for life to develop at some stage of its history. The immediate consequence of SAP is that the physical laws and constants must be such as to allow the emergence of life. There exist several different versions or supplements of SAP. The most known is the design argument which states that life can occur because of some purposive design. That is the values of physical constants were selected purposively. For more specific anthropic definitions see Barrow-Tipler (1996) and Balázs (2005).

To state that the physical constants of the universe derive specific values from an ensemble of different values, we have to suppose the (i) conceptual or (ii) real existence of the numerical ensemble. The design argument has chosen the first solution (i), when the other possibilities exist only as possibilities in the mind of the Designer. The represents the second version (ii), supposing that an ensemble of other different existing universes is necessary for the existence of our Universe (Barrow-Tipler, 1996) There exist some alternative definiton (Müller, 2001), (Smolin, 2004) but their common feature is the lack of using mathematical methods.

A mathematical expression of fine tuning may help discussing anthropic arguments. Our aim is to construct a simple mathematical definiton of fine tuning similar with the one used in the chaos theory. This defintion can be testable therefore arguments of Smolin (2004) about the unfalsificability of anthropic principless are avoidable.

Both design argument and many-words-hypothesis is created to explain the fine tuning of physical constants. Physically say, fine tuning arguments state that there exist such a domain in the n-dimension parameter space of physical constants that if a universe is in this domain it may contain life.(Fig. 1)

The starting point of anthropic arguments that this fine tuning is very strong, that is the probability of life which equals with the fraction of the volume of m nad M domains is small, i.e.

$$p_{life} = \frac{m}{M} = \epsilon \tag{1}$$

is true. Arguments against the fine tuning concept are formulated (Manson, 2001) and say that (i) there are no *a priori* probabilities, the value of the probability of a phenomenon is a result of our empiric experience. E.g. if we throw a dice and we see that every side is equally probable as a result we will say that our dice is symmetric. To say that every side's probability is 1/6 it is an *a posteriori* statement; (ii) there is not *a priori* gauge and *a priori* topology on
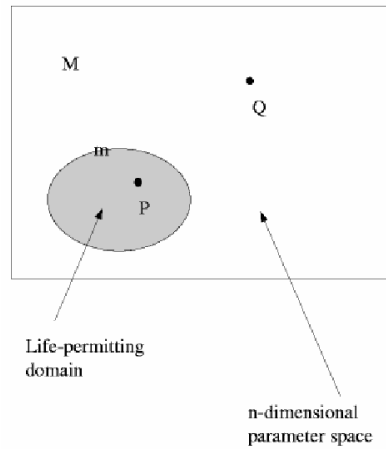
Figure 1: *In the M-multitude of physical parameters there exist such an m domain of phyiscal parameters that if a universe is in this domain it will permit life. **P** and **Q** are typical points in and out of the m life-permitting domain.*

M parameter-space (Fig. 1). Therefore it is meaningless to say that Universes signed by **P** and **Q** are near or far from each other on M parameter-space. Hence there is no reason to say that "if gravitation were $(1 + 10^{-40})$ stronger" something would happen with conditions of life.

Neither (i) nor (ii) arguments are indisputable. They may mirror rather an opinion than strict fact. A possible explanation of argument (i) will not be detailed here, but argument (ii) is investigated.

A mathematical expression of fine tuning may help the discussion of anthropic arguments. Our aim is to construct a simple mathematical definiton of fine tuning analogue to the Lyapunov-indicator in the chaos theory. Such a definition can lead to testable statements therefore arguments of Smolin (Smolin, 2004) about the unfalsificability of anthropic principless are avoidable.

Life depends on the presence of the proper chemical elements as building blocks and the existence of stars which can radiate enough energy for long time for evolution of life. If the abundance of carbon and other essential elements are lower or the number of properly radiating stars are smaller then we have a smaller probability for the evolution of intelligent life in a universe. To define fine tuning in a more quantitative way we can study the probability function

for intelligent life of a universe. The form of this probability function can be regarded as an anthropic adaptation of the Drake equation (Ellis et al., 2004). Physical constants are regarded here as variables. Therefore we can present a probability distribution of life-bearing potentiality for universes as a function of the basic constans of the physics.

In order to characterize fine-tuning we introduce a quantity like to the one used to describe the chaotic behavior. Chaos in a dynamical system can be characterized by the Lyapunov indicator γ. It gives a number as result if the motion is chaotic and gives zero if not. Let us consider two trajectories not far from each other. The initial distance is d_0 and after Δt the final distance is d. If the distance is groving exponentially, i.e. $d(t) = d_0 exp(\alpha t)$ is true, then the Lyapunov indicator γ tends to α:

$$\gamma = \frac{\ln d/d_0}{\Delta t} \to \alpha \tag{2}$$

For the case $\gamma > 0$ the system is chaotic. If the increase of distance is smaller, e.g. $d(t) = d_0(\beta t)$ then γ tends to zero.

In the extreme limit of fine tuning, the probability function can be represented by a Dirac-delta function taken at the point of the parameter space of physical constants which corresponds to the single life-bearing universe. The Dirac-delta function $\delta(Q - Q_0)$ can be represented as the $n \to \infty$ limit of the Gaussian function

$$\delta(Q - Q_0) = \lim_{n \to \infty} \frac{n}{\sqrt{\pi}} exp\left(-n^2(Q - Q_0)^2\right) \tag{3}$$

Now we assume that if there is a fine tuning in the parameter Q around the maximum probability at Q_0 then the probability function for the life-bearing of universes can be approximated by the Gaussian form:

$$p_{\text{life}}(q) = \frac{n}{\sqrt{\pi}} exp(-n^2 q^2) \tag{4}$$

where $q = |Q - Q_0|$. The measure of fine tuning can be defined as

$$\gamma_{\text{fine-tuning}} = -\frac{(\ln p/p_0)^{1/2}}{\Delta Q} \to n \tag{5}$$

According to this definition, we have fine tuning, if $\gamma_{\text{fine-tuning}} > 0$. Fine tuning is stronger if $\gamma_{\text{fine-tuning}}$ is larger.

Discussing the production of the carbon and oxigen in the Universe, the position of the famous resonance in C_{12} nuclei plays a crucial role. According

to (Oberhummer et al., 2000) outside a narrow window of 0.5 and 4 % of the values of the strong and nuclear forces, respectively, the stellar production of carbon or oxigen is reduced by factors of 30 to 1000. These production functions express Gaussian-like form. We can guess that the probability to find planets with a proper life-bearing mass would have even a higher decrease. Now the $\gamma_{\text{fine-tuning}}$ indicator of Eq. (5) has a definite nonzero value.

Acknowledgement

References

Balázs B. (2005):The cosmological replication cycle, the extraterrestrial paradigm and the final anthropic principle. Diotima (Review of philosophical research) **33** 44-53. (2005)

Barrow J.- Tipler F. (1996):The anthropic cosmological principle. Oxford University Press New York, 1996 2nd ed.

H. Oberhummer, A. Csótó and H. Schattl, Science, **289** 88 (2000).

Ellis G., Kirchner U. and Stroeger W. (2004):Multiverses and physical cosmology. MNRAS **3**47 921-936. (2004)

N. A. Manson, Inquiry **43**, 341 (2000).

Müller B. (2001): The anthropic principle revisited. astro-ph/0108259.

Smolin L. (2004): Scientific alternatives to the anthropic principle. astro-ph/0407213.